PROBING THE CENTRAL ENGINE OF

ACTIVE GALACTIC NUCLEI

USING TIME DELAY STUDIES

WILLIAM ALSTON

DEPARTMENT OF PHYSICS AND ASTRONOMY

UNIVERSITY OF LEICESTER

THIS THESIS IS FOR THE DEGREE OF

Doctor of Philosophy

OCTOBER 2013

Abstract

Understanding the physics of accretion onto black holes, and the role these cosmic engines play in shaping the universe, is one of the major challenges of contemporary astrophysics research. In this thesis I present several studies, aiming to better understand the variable emission we observe in accreting black holes. The focus of these studies are highly variable Narrow Line Seyfert 1 galaxies in the nearby universe. I start by summarising the current field of research in an introductory chapter. This is followed by a more technical chapter, outlining the analysis methods used in any subsequent chapters. This thesis contains five science chapters which are summarised below. I end with some concluding remarks and a discussion about the future prospects of the field.

In chapter 3 we present a study of correlated UV and X-ray variability in the NGC 4051, where we found evidence for the reprocessing of X-ray photons in the disc. In chapter 4 we present a study of the time delays between a soft and hard X-ray band as a function of source flux in NGC 4051. We found a strong flux dependence on the time delays, and through analytical modelling we found reprocessing of the primary power law emission close to the central source. In chapter 5 we study the X-ray time delays in a sample of objects, and found a significant flux dependence in only one other source, Ark 564. In chapter 6 we study the energy and flux dependence of the X-ray timing properties in NGC 4051. A strong flux dependence on the lag energy is found and simple modelling performed. In chapter 7 we study the frequency and energy dependent lags in PG 1244+026, and found high frequency lags from both reflection and thermal reprocessing.

I dedicate this thesis to the loving memory of my grandfather,
William "Bill" Robertson Pierce (1932–1998)

Declaration

I hereby declare that no part of this thesis has been previously submitted to this or any other University as part of the requirement for a higher degree. The work herein was conducted by the undersigned except for contributions as acknowledged in the text. Various figures have been reproduced from the literature to aid the discussion, and have been properly cited. This thesis conforms to the word limit of 50,000 words.

William Alston
October 29, 2013

List of Publications

A significant amount of work contained in this thesis is due to be or has already been published in the following papers:

- Chapter 3 was published as:
  Alston W. N., & Vaughan S. & Uttley P.
  Ultraviolet and X-ray variability of NGC 4051 over 45 days with XMM-Newton and Swift
  MNRAS, 429, 75–84 (2013)

- Chapter 4 was published as:
  Alston W. N., & Vaughan S. & Uttley P.
  The flux dependent X-ray time lags in NGC 4051
  MNRAS, 435, 1511 (2013)

- Chapter 7 was published as:
  Alston W. N., & Done C & Vaughan S.
  X-ray time delays in the Narrow Line Seyfert 1 galaxy PG 1244+026
  MNRAS, 439, 1548 (2014)

Acknowledgements

I am forever indebted to my supervisor Simon Vaughan, who introduced me to the exciting field of accreting black holes. Without your continued guidance and support throughout the last 3 years this thesis would not have been possible. Thank you.

I am sincerely grateful to my collaborators Phil Uttley and Chris Done for their valuable input and enthusiasm along the way. And to my co-supervisor Graham Wynn for his encouragement and useful discussions.

I would like to thank those who taught me physics and astrophysics throughout my undergraduate and masters course at the University of Sheffield. Without the inspiration and support from many people along the way, in particular Prof. Paul Crowther and the late Dr. Tim Richardson, I would not have made it onto the Ph.D course.

To the numerous office mates I have shared G24a with, in particular Beatriz "Mrs Bingo" Mingo, Vicky "Mercedes" Heard, Conor "The Wrecking Ball" Wildy, and Andrew "Blobban" Lobban. Thank you for interesting discussions, both astronomical and non-astronomical in nature. To the physics football team and those I played squash with I will sincerely miss sharing this stress relief with you. I can only hope to be in as physical condition in later life as some of you.

I would not have survived the last 3 years without the friendship and comradery of James O'Donoghue, Andrew Lobban and Fleur Stewart. I have thoroughly enjoyed our jaunts, those both cerebral and uncultivated in nature.

Lastly, I am forever grateful to Marion: Mon Chouchou d'amour. "Merc" de porter un grand intérêt à ce que je fais et d'être autant passionnée que moi, par la vie. Sans ton soutien ni ta patience, particulièrement lors de la rédaction de cette thèse, je ne serais pas là où je suis maintenant. Je me réjouis de notre avenir ensemble.

Contents

List of Tables

List of Figures

List of Abbreviations

ACF	Auto-Correlation Function
ADAF	Advection Dominated Accretion Flow
AGN	Active Galactic Nuclei
AU	Astronomical Unit
BBB	Big Blue Bump
BB	Blackbody
BH	Black Hole
BH-XRB	Black Hole X-ray Binary
BLR	Broad-Line Region
BLS1	Broad Line Seyfert 1
CCD	Charge Couple Device
CCF	Cross-Correlation Function
CL	Coincidence Loss
DC	Direct Component
DCF	Discrete Correlation Function
DFT	Discrete Fourier Transform
DT	Deadtime
EPIC	European Photon Imaging Camera
ESA	European Space Agency
FOV	Field Of View
FWHM	Full-Width-Half-Maximum
GBH	Galactic Black Hole
GR	General Relativity
HS	High/soft State
IMBH	Intermediate Mass Black Hole
ISCO	Innermost Stable Circular Orbit
ISM	Interstellar Medium
LH	Low/Hard state
LINER	Low Ionisation Nuclear Emission Region
MCMC	Markov-Chain Monte Carlo

MOS   Metal Oxide Semi-conductor
NLS1   Narrow Line Seyfert 1
ODF   Observation Data File
OM   Optical Monitor
PL   Power-law
PSD   Power Spectral Density
PSF   Point Spread Function
QPO   Quasi Periodic Oscillation
RGS   Reflection Grating Spectrometer
RXTE   Rossi X-Ray Timing Explorer
SAS   Science Analysis System
SMBH   Supermassive Black Hole
TDS   Time-dependent Sensitivity Degradation
TH   Top Hat
ULX   Ultraluminous X-ray source
UVOT   UltraViolet and Optical Telescope
VHS   Very High/intermediate State
VLBI   Very Long Baseline Interferometry
XMM   X-ray Multi-Mirror Mission
XRB   X-ray Binary
XRT   X-ray Telescope
XSA   XMM-Newton Science Archive

1

Introduction

This thesis forms part of a continuing effort to understand the physics of accretion onto black holes, and the role these cosmic engines play in shaping the universe. In this introductory chapter, I will briefly review the theoretical and observational framework that has led to the current paradigm for the existence of black holes and the class of objects in which these extreme phenomena reside. I will highlight our current understanding of the physics of accretion and how, in turn, this can improve our understanding of black holes. I will then discuss the current challenges in the field of black hole accretion, providing context for the detailed work that will be presented in later chapters.

Specifically, this work is aimed at answering the questions:

- What is the origin of the variability seen across the energy spectrum
- What is the geometry of the disc—corona system
- Which X-ray components dominate the spectral variability
- What is the nature of the inner accretion flow
- What is the origin and geometry of X-ray emission

The emission from accreting black hole systems is highly variable. Time- and Fourier-domain techniques will be utilised throughout to disentangle the variable emission components.

1.1 Black holes

Black holes are the most extreme objects found in the universe, providing a one-way passage to the unknown. Pioneering work over the last century has transformed black holes from theoretical curiosities, into the domain of the observational astronomer.

The concept of a body with an extreme gravitational field such that light cannot escape its surface was first discussed by Michell (1784) and de Laplace (1796). Only after Einstein had published his theory of general relativity in a series of papers (e.g. Einstein 1915) did physicists begin to understand the effect a gravitational field has on light. The first analytical solution to Einstein's vacuum field equation was derived by Schwarzschild (1916), which describes the gravitational field around a non-spinning, spherically symmetric point mass. Kerr (1963) published a solution describing the spacetime curvature outside a spinning star, which was soon after realised described a more general description for the gravitational field around any spherically symmetric point mass with non-zero spin (e.g. Carter 1968). However, the term 'black hole' was not used until 1967 by John wheeler.

Work done by Chandrasekhar (1931a,b) and Baade & Zwicky (1934), amongst others, showed white dwarfs and neutron stars to be the compact-object end products of stellar evolution. Oppenheimer & Volkoff (1939) showed that neutron stars must have a maximum mass, making the existence of black holes as the end products of stellar evolution seem unavoidable.

The 'no-hair' theorem states that all information about the progenitor will be lost once the black hole has formed, except for three fundamental properties: black hole mass (M_{BH}), charge (Q) and angular momentum (J; Bardeen et al. 1972), which is commonly described by the dimensionless spin parameter $a = Jc/GM^2$. The mass of the black hole determines the 'warpage' of the surrounding spacetime, whereas spin determines how 'twisted' the surrounding spacetime is (see e.g. Misner et al. 1973 and Schutz 2003 for more on the gravitational effects of black holes). The spin parameter for a black hole being spun-up by any realistic accretion process was shown to satisfy the condition $0<a<0.998$ (Thorne 1974). Values of a can also be negative, to allow for retrograde spin with respect to the accretion flow. Astrophysical black holes are expected to be charge neutral, and Q will not be considered further.

The Schawrzschild radius represents the invisible boundary known as the 'event horizon', within which no electromagnetic wave or particle can escape.

$$R_{\mathrm{s}} = \frac{2GM_{\mathrm{BH}}}{c^2} \approx 3\left(\frac{M_{\mathrm{BH}}}{\mathrm{M_\odot}}\right)\,\mathrm{km}. \tag{1.1}$$

However, it is common to use the gravitational radius $R_{\mathrm{g}} = GM/c^2$, which serves as a

natural unit of distance from a black hole singularity, where $R_{\rm s} = 2R_{\rm g}$.

A location of particular importance is the innermost stable circular orbit (ISCO), within which test-masses on circular orbits become unstable, and fall radially towards the centre of the black hole. The location of $R_{\rm ISCO}$ is highly dependent on a. For a Schwarzschild black hole $R_{\rm ISCO} = 6R_{\rm g}$ and for a maximally spinning Kerr black hole $R_{\rm ISCO} \approx 1.24R_{\rm g}$ (e.g. Misner et al. 1973 and Schutz 2003).

Aside from the extremely faint Hawking radiation (Hawking 1974) black holes emit no light themselves. We are therefore restricted to studying the light emitted from matter within the immediate vicinity of the black hole. This light contains information about the spacetime distortions around the black hole, allowing us to use electromagnetic radiation to test Einstein's theory of General Relativity (GR) in the strong gravity domain (e.g. Cunningham 1975). This requires both accurate mass and spin determinations (e.g Brenneman 2013).

1.1.1   Astrophysical black holes

Evidence for the existence of black holes has grown substantially in recent years (see e.g Begelman 2003; McClintock & Remillard 2006 and Kormendy & Ho 2013 for a review). The types of black holes that are important astrophysically, that is, there is consistent observational evidence for their existence, are; stellar-mass Galactic black holes (GBH) with masses between $4 - 20$ $M_\odot$, supermassive black holes (SMBH) with masses in the range $10^5 - 10^9$ $M_\odot$ and intermediate-mas black holes (IMBH) with masses $\sim 10^2 - 10^5$ $M_\odot$.

Stellar-mass black holes are the evolutionary end product of massive stars (i.e stars with initial mass $\gtrsim 20M_\odot$, e.g. Smartt 2009). They are observed as black hole X-ray binaries (XRBs), when they are formed in a gravitationally-bound system with a companion star, which acts as a donor for accreting matter. Cygnus X-1 (hereafter Cyg-X1) was the first GBH candidate following the detection of short timescale X-ray variability and dynamical mass measurements (Schreier et al. 1971; Webster & Murdin 1972). There are currently ~ 40 black hole candidate XRBs (McClintock & Remillard 2006), of which ~ 25 known to have a compact object with mass greater than the $\sim 3M_\odot$ upper limit for a neutron star (Kalogera & Baym, 1996).

Intermediate mass black holes may bridge the gap between GBH and SMBH, however their existence is far less certain. There is evidence to suggest they are associated with the point like, off nuclear, extra-galactic ultra-luminous X-ray sources (ULXs), with X-ray luminosities $L_{\rm x} > 10^{39}$ erg s^{-1} (e.g. Colbert & Mushotzky 1999). If the emission is isotropic and sub-Eddington, then ULXs must be powered by accretion onto a black hole with mass $100 - 10^5$ $M_\odot$ (Gladstone 2013). Recent X-ray spectral studies suggest
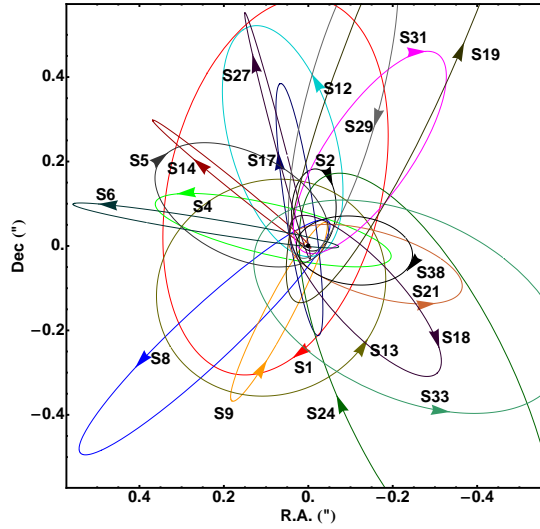
Figure 1.1: The orbital motion of the stars in the Galactic centre (from Gillessen et al. 2009). The orbits indicate an unseen mass of $\sim 4 \times 10^6 \mathrm{M}_\odot$, and these form one of the strongest pieces of evidence for the existence of SMBHs.

ULXs are in a super-Eddington accretion state, which is mildly beamed and comprise a black hole with masses $10 - 100 \ \mathrm{M}_\odot$ (e.g. Gladstone et al. 2009; Middleton et al. 2011).

Supermassive black holes are believed to reside in the dynamical centre of most galaxies. Accretion of matter onto a SMBH (see Section 1.2) is believed to be the central engine in active galactic nuclei (AGN). The masses of SMBH are harder to determine. Several methods are employed, which also provide evidence for a compact mass. These depend on measuring radiation emitted far from where the energy output is dominated, and include: reverberation mapping of the high velocity clouds surrounding the SMBH (Blandford & McKee 1982, Peterson 2008); VLBI observations of water masers (e.g. Miyoshi et al. 1995); tracing the motions of gas in the central regions (Dressler & Richstone 1988); and a number of relations based on properties of the host galaxy (see Section 1.1.2).

The strongest evidence for the existence of SMBHs comes from measuring the velocities of stars in the Galactic centre (see Fig. 1.1; Gillessen et al. 2009). These results imply an unseen mass of $\sim 4 \times 10^6 M_{\mathrm{BH}}$ within ~ 100 AU radius (Eckart & Genzel 1997; Ghez et al. 2008; Genzel et al. 2010).

1.1.2 Gravity engines

Black holes play a key role in shaping the evolution of the universe. Their study is therefore of more interest than mere bizarre curiosity.

The existence of a SMBH in the centre of most galaxies is attributed to a number of observed strong correlations between measured black hole mass and host galaxy proper-

ties. These include a correlation between: the black hole mass and galaxy bulge luminosity $M_{\text{BH}} - L_{\text{bulge}}$ (Kormendy & Richstone, 1995); the black hole mass and mass of the galaxy bulge $M_{\text{BH}} - M_{\text{bulge}}$ (Magorrian et al. 1998); and the black hole mass and stellar velocity dispersion of the galaxy bulge, the $M_{\text{BH}} - \sigma$ relation (Ferrarese & Merritt 2000, Gebhardt et al. 2000). These strong correlations between SMBH on sub-parsec scales and stars on kilo-parsec scales tell us that galaxy formation and black hole growth are intrinsically linked (see Kormendy & Ho 2013 for a review).

SMBHs grow through either accretion of material and black hole mergers, and most likely a combination of both processes (e.g. Volonteri & Rees 2005). The masses and spins of black holes therefore evolve over the billions of years since their formation. As the SMBH grows it goes through periods where powerful winds, outflows and jets, releasing vast amounts of kinetic and radiative energy into the surroundings (see Fabian 2012 for a review). This is known as AGN feedback (Silk & Rees 1998) and is the likely cause of the above observed correlations, through regulation of the star formation rate (Kormendy & Ho 2013). Depending on redshift, AGN are observed in 5–10 % of galaxies. The number density of AGN suggests that every galaxy typically goes through this accretion phase (e.g. Beckmann & Shrader 2012b).

The powerful jets observed in many XRBs and AGN are could be powered by the Blandford-Znajeck process, where rotational energy of the black hole ergosphere is extracted by magnetic field lines (Blandford & Znajek 1977), if the black hole spin is large enough ($a \geq 0.93$; Agol & Krolik 2000). Spin measurements therefore tells us about the black hole and jet power (e.g. Narayan & McClintock 2012). Accurate spin measurements ($\Delta a \leq 10\%$) for a sample of black holes allow us to understand the gas accretion and merger history of galaxies (Berti & Volonteri 2008), as well as probing the nature of spacetime in the strong gravity regime (Fabian et al. 1989; Laor 1991).

It is currently not possible to determine spin in a model independent manner, with 3 viable methods in use: (1) inner disc reflection modelling (e.g. Fabian et al. 2000; Reynolds & Nowak 2003), (2) thermal continuum fitting of disc component (e.g. Remillard & McClintock 2006) and lastly (3) high-frequency quasi-periodic oscillations (e.g. Strohmayer 2001). These methods therefore depend highly on understanding the timing properties of accreting black holes, and the causal between different emission components.

Another argument for the compact emission region in AGN is the fast variability of the X-ray emission (e.g. Mushotzky et al. 1993). Variations within a region of size R must be varying coherently (i.e. causally connected), otherwise the variations would be smoothed out due to the difference in the light travel time between the two regions and the distant observers. Variability observed on timescales Δt tells us the size of the

emission region must be of order $R \sim c\Delta t$. For the fast variability observed in XRBs and AGN, the X-ray emission must be coming from a compact region of order $\lesssim 10R_{\mathrm{g}}$ (e.g. Mushotzky et al. 1993; Edelson et al. 1996).

1.2 Black hole accretion

It was realised in the 1960s that accretion onto a supermassive ($\gtrsim 10^6$ M$_\odot$) but compact object could explain the vast amounts of radiative energy required for the cosmological interpretation of quasars (Salpeter 1964; Lynden-Bell 1964). This highly efficient process converts the gravitational potential energy of in-falling streams of gas into kinetic and thermal energy, resulting in emission from radio to hard X-rays.

The sine qua non of accretion is that self-gravity of the source must exceed the outward radiation pressure, in order for the source to maintain its outward energy flux, i.e. $F_{rad} < F_{grav}$). Under the assumption of spherical accretion, the highest luminosity a source can have whilst maintaining stability against isotropic radiation pressure is known as the 'Eddington luminosity':

$$L_{\mathrm{Edd}} = \frac{4\pi G M_{\mathrm{BH}} m_{\mathrm{p}} c}{\sigma_{\mathrm{e}}} = 1.26 \times 10^{38} (M/\mathrm{M}_\odot) \text{ erg s}^{-1} \tag{1.2}$$

where $\sigma_{\mathrm{e}} = 6.65 \times 10^{-25} \mathrm{cm}^2$ is the Thomson cross-section for electron scattering. Assuming that matter is completely ionised the proton scattering cross-section can be ignored, due to the $\sim q^4/m^{-2}$ dependence. The rate at which matter is accreted to maintain a given luminosity is given by

$$L = dE/dt = \eta \dot{m} c^2 \tag{1.3}$$

where $\dot{m} = dM/dt$ is the mass accretion rate and η is the efficiency of converting to radiation the rest mass energy, $E = \eta M c^2$. The accretion efficiency η depends on the location of the innermost stable orbit, R_{ISCO}, which in turn is dependent on the black hole spin. For spin zero Scwarzschild black hole this is predicted to be as high as $\eta = 0.057$ (the Novikov-Thorne emissivity). For a maximally spinning Kerr black hole this can be as high as $\eta = 0.42$, neglecting the fact that some liberated energy close to the horizon will be lost to the black hole. Including this effect a more realistic value would be $\eta = 0.3$ (Thorne 1974).

It is often convenient to use the 'Eddington ratio', the ratio between actual bolometric luminosity and Eddington luminosity (i.e. $\lambda_{\mathrm{Edd}} = L/L_{\mathrm{Edd}}$), or the ratio between actual accretion rate and Eddington rate (i.e $\dot{m} = \dot{M}/\dot{m}_{\mathrm{Edd}}$). For example, an XRB with $M_{\mathrm{BH}} \sim 10\mathrm{M}_\odot$ has $L_{\mathrm{Edd}} \sim 10^{39}$ erg s^{-1}, whilst for an AGN with $M_{\mathrm{BH}} \sim 10^6 \mathrm{M}_\odot$, it is 10^5 times larger, with $L_{\mathrm{Edd}} \sim 10^{44}$ erg s^{-1}.

The in-falling gas must lose almost all of its angular momentum before it can be accreted onto the black hole. Conservation of angular momentum ensures the gas collapses down to form a disc structure, transporting angular momentum outwards and allowing mass to flow inward. Some form of viscous dissipation is required to transport angular momentum (Pringle 1981), the details of which are still not fully understood.

The standard small-scale viscosity of kinetic theory is many orders of magnitude too small to provide the viscosity required in accretion discs. The best candidate mechanism provides an 'effective viscosity' through the process of Magneto-Rotational Instability (MRI; Balbus & Hawley 1991, 1992). Here, weak magnetic fields threading the axial component of the disc render the differential rotation susceptible to a local magneto-hydrodynamical shear instability. The turbulence from such an instability provides the necessary sheer stress to transport angular momentum outwards. For a discussion on this, and other candidates for viscosity see the review by Blaes (2013).

The simplest form of accretion disc structure is the geometrically thin, optically thick disc with constant accretion rate (steady state), proposed by Shakura & Sunyaev (1973). The authors introduced the α prescription for the unknown viscosity, such that $v = \alpha c_s h$, where c_s is the sound speed and h is the scale height of the disc. α is a dimensionless quantity between 0 and 1, which describes our ignorance of the exact mechanism producing the shear stress, and allows us to calculate the disc structure using the equation of hydrostatic equilibrium. Typical values of α are of the order $0.01 - 0.1$.

In the α-disc model gravitational potential energy (GPE) is converted to kinetic (thermal) energy through viscous dissipation. Assuming local equilibrium and that no convection occurs, the virial theorem tells us that half the GPE is converted to kinetic energy and radiated away. (e.g. Frank et al. 2002). The temperature profile of such as disc is given by (e.g. Frank et al. 2002)

$$T(r) = \frac{3GM_{\mathrm{BH}}\dot{M}}{8\pi\sigma r^3}\left(1 - \frac{R_{\mathrm{in}}}{r}\right) \tag{1.4}$$

where R_{in} is the inner disc radius. For $r \gg R_{\mathrm{in}}$, we can write

$$T(r) \approx 3.7 \times 10^5 \left(\frac{\dot{M}}{\dot{M}_{\mathrm{Edd}}}\right)\left(\frac{r}{R_g}\right)K \tag{1.5}$$

The nature of the accretion disc is determined by the efficiency at which it can radiate. If this efficiency is high, it suggests the matter has no significant dynamical pressure, so that the circular orbits of disc gas have Keplerian velocity, $\nu_{\mathrm{K}} = (GM/R)^{\frac{1}{2}}$. Accretion discs are believed to be present in numerous classes of objects. These include, active galctic nuclei (AGN); black-hole and neutron-star X-ray binaries; accreting white dwarfs (cataclysmic variavle; CVs); planetary formation. A full discussion about the physics of disc accretion can be found in Pringle (1981) and Frank et al. (2002).

1.2.1 Disc timescales

For the geometrically thin α-disc we can calculate the relevant timescales on which we expect significant changes to happen (e.g Czerny 2006). The dynamical timescale is equal to the orbital period and characterises the timescale for vertical perturbations to return to hydrostatic equilibrium:

$$t_{\mathrm{dyn}} \sim \frac{R}{\nu_{\mathrm{K}}} = \left(\frac{R^3}{GM} \right)^{\frac{1}{2}}. \tag{1.6}$$

The free-fall timescale, t_{ff}, of matter from radius r to the centre of the black hole is of the same magnitude. The thermal timescale, t_{th}, is defined as the ratio of internal energy to the rate of heating or cooling. The viscous timescale t_{visc} defines the characteristic timescale of mass flow. These timescales are related via $t_{dyn} \sim t_{\mathrm{ff}} \sim \alpha t_{th} \sim \alpha(h/R)^2 t_{visc}$, such that $\mathrm{dynamical} < \mathrm{thermal} < \mathrm{viscous}$. The light-crossing timescale is $t_{lc} = R/c$.

Assuming e.g. $\alpha = 0.1$, $h/R \sim 0.01$ ('thin') and $R = 6R_{\mathrm{g}}$, the dynamical timescale for $M_{\mathrm{BH}} \sim 10 \mathrm{M}_\odot$ is $t_{dyn} \sim 1$ ms, and $t_{visc} \sim 1000$s. For $M_{\mathrm{BH}} \sim 10^6 \mathrm{M}_\odot$, $t_{dyn} \sim 100$ s and $t_{visc} \sim$ months—years.

1.2.2 Other accretion flows

In accreting black hole systems the standard thin α-disc model may break down if, for example, $\lambda_{\mathrm{Edd}} \gtrsim 1$, or the disc cooling becomes highly inefficient. This produces a high viscosity parameter α and the accretion flow can no longer be vertically confined (e.g. Frank et al. 2002). The accretion flow may form a *toroidal* or *thick-disc* geometry depending on whether radiation or gas pressure dominates (e.g. Abramowicz 1988). A variety of solutions exist for accretion flows that in which the gas opacity is too low or too high for the internal energy of the plasma to be radiated away. These include, the two-temperature plasma at the Eddington rate (Shapiro et al. 1976); optically-thick advection dominated accretion flow (ADAF) accreting at super-Eddington rate (e.g. Narayan & Yi 1995); and an optically-thin ADAF consisting of a two-temperature plasma accreting at sub-Eddington rate.

Evidence for such sub-Eddington rate ($\lambda_{\mathrm{Edd}} \sim 0.01$) accretion flows comes from low-luminosity AGN such as Low Ionisation Nuclear Emission Regions (LINERS; e.g. Heckman 1980), which show no big blue bump (BBB; see Section 1.3.1) component (Lasota et al. 1996; Quataert et al. 1999; Nemmen et al. 2010). Galactic XRBs are observed to go through state transitions with corresponding changes in jet activity (e.g. Fender 2010). The state transitions are believed to correspond to a change in disc configuration
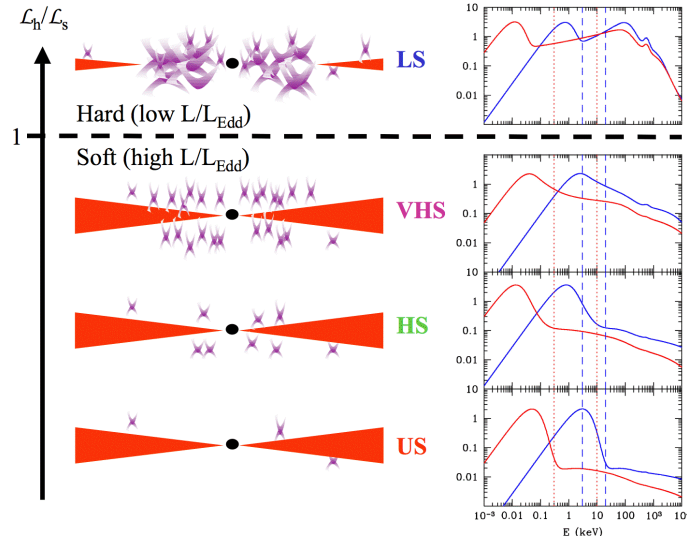
Figure 1.2: The expected accretion flow geometries for different black hole X-ray binary (XRB) and active galactic nuclei (AGN) *states*. The right hand panels show the spectra for XRBs (blue) and AGN (red). Figure taken from Done & Gierliński (2005).

from a standard α-disc to a recessed disc with a central ADAF, with associated radio jet. This transition appears to occur around $\lambda_{\mathrm{Edd}} \sim 0.01 - 0.1$ (or $M_{\mathrm{crit}} < \dot{m} \sim 0.01 - 0.1$), where M_{crit} is the critical accretion rate dividing the two accretion regimes (Courvoisier 2013). State transitions are expected to occur on much longer timescales in AGN, so ensembles of AGN subclasses must be compared in a statistical sense. The radio-loud FR-I and FR-II objects are possibly the analogues of jet dominated XRBs (Beckmann & Shrader 2012b).

1.3 Active Galactic Nuclei

Active Galactic Nuclei (AGN) are the most luminous persistent sources observed in the universe, with typical bolometric luminosities $L_{\mathrm{bol}} \sim 10^{41} - 10^{47}$ erg s^{-1}. A variety of AGN subtypes are observed and are classified based on their broadband spectral energy distribution (SED) properties.

It is generally believed that the various AGN phenomenon are part a distinct class of objects, with the differences between AGN subclasses are explained by differences in orientation, obscuration and radio loudness (Barthel 1989; Antonucci 1993). Fig. 1.3 shows this simplified unification model. Type 1 AGN show broad (FWHM $\sim 5000\,\mathrm{km\,s^{-1}}$) permitted optical/UV emission lines (such as the Balmer lines) in their spectra, along with narrow (FWHM $\sim few \times 100\,\mathrm{km\,s^{-1}}$) forbidden lines such as [OIII] $\lambda 5007$, $\lambda 4995$. Type 2 objects show only narrow permitted and forbidden lines. This is believed to be a result of the viewing angle, where a dusty and possibly clumpy torus obscures the broad line
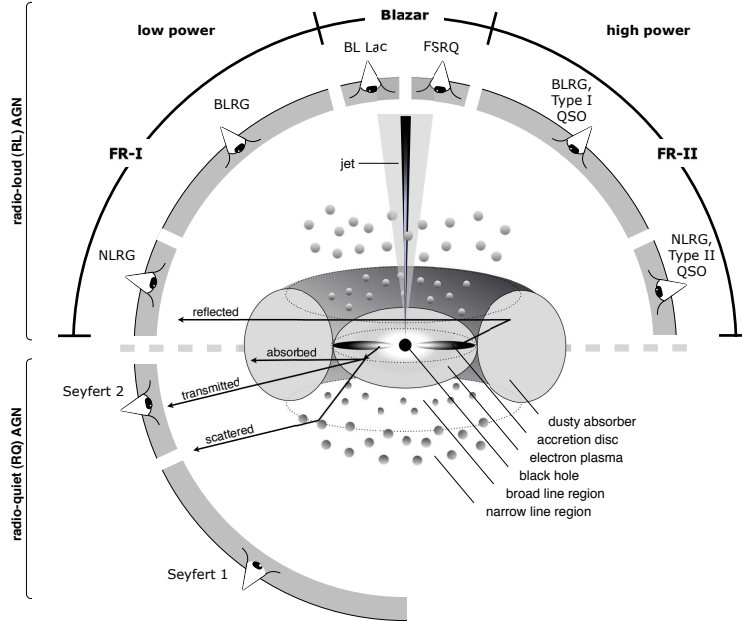
Figure 1.3: The *unified model* of active galactic nuclei (AGN). In this simplified model, AGN are characterised by their radio power and viewing angle. Figure reproduced from Beckmann & Shrader (2012a).

region (BLR) in the low inclination type 2 objects.

In support of this argument are observations of polarised optical light, which reveal hidden broad emission line regions in some Seyfert 2 galaxies, whilst the narrow forbidden lines show little or no polarization (Antonucci & Miller 1985). X-ray observations reveal that $\lesssim 10\%$ of Seyfert 1 objects are obscured ($N_{\mathrm{H}} < 10^{22} \ \mathrm{cm}^{-2}$), whereas $\gtrsim 90\%$ of Seyfert 2 are obscured (e.g. Lawrence & Elvis 1982; Awaki et al. 1991).

Quasars are believed to be the higher luminosity, higher redshift (z) analogues of Seyfert galaxies. The latter are predominantly found in the local universe. Narrow Line Seyfert 1 (NLS1) galaxies are a subclass which exhibit narrower broad emission lines (FWHM(Hβ) $< 2000 \, \mathrm{km \, s^{-1}}$), compared to Broad Line Seyfert 1 galaxies (BLS1s). NLS1s also show a FeII/Hβ ratio approximately twice as strong compared to other Seyferts, with a strong correlation with optical luminosity in the former (Zhou et al. 2006). NLS1s appear to be less massive on average compared to other Seyferts, with $M_{\mathrm{BH,NLS1}} \sim 10^5 - 10^7 \mathrm{M}_\odot$. This suggest that NLS1 have a higher Eddington ratio (Collin & Kawaguchi 2004) and may be the analogues of XRBs in the high/soft state (Pounds et al. 1995; Boller et al. 1996). This interpretation is still open for discussion, with some authors explaining the peculiar properties of NLS1s by low inclination angles (e.g. Peterson 2011). NLS1s are the main focus of this thesis as they offer a clean, relatively unabsorbed view of the accretion disc. The low masses mean the variability timescales are shorter so we can get to comparatively lower frequency behaviour than higher mass
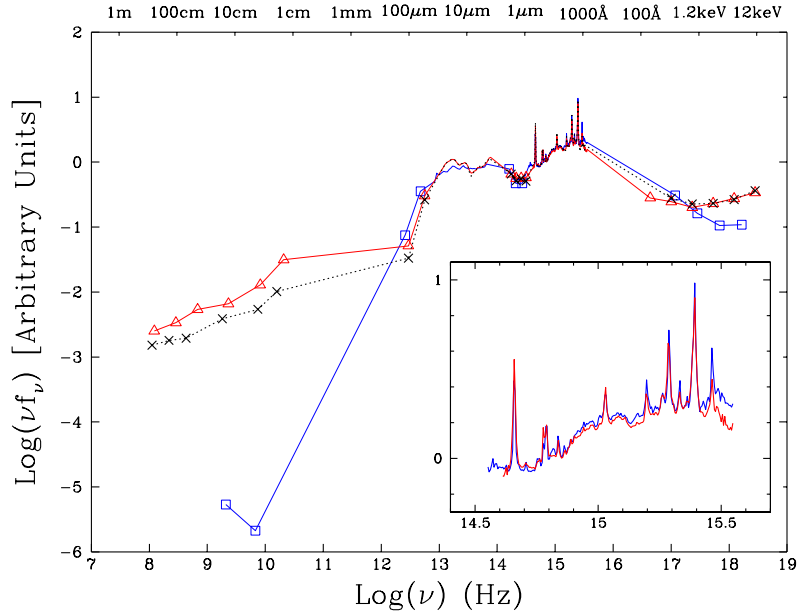
Figure 1.4: A mean AGN spectral energy distribution (SED) for a sample of 58 radio-loud (red) and 27 radio-quiet objects, from Shang et al. (2011). Shown in black is the mean SED for 21 radio-loud objects with redshift $z < 0.5$. The optical-UV region is expanded in the inset.

systems (see Section 1.4).

The radio-loud constitute $\sim 10\%$ of AGN, and have an associated jet component (for a review on jets see Meier 2003 and Worrall 2009). The distinction between radio loud and radio quiet sources is still a debated topic. Accretion efficiency (e.g. Gallo et al. 2010) and black hole spin (e.g. Garofalo et al. 2010) have been proposed to explain the apparent differences.

For a historical perspective on the classification and unification of AGN, see the texts by Peterson (1997), Beckmann & Shrader (2012b) and the review article by Tadhunter (2008).

1.3.1 Disc continuum emission

The SED of Seyferts and quasars typically peak in the UV or extreme-UV (e.g Shang et al. 2011; see Fig. 1.4). Approximately half the bolometric luminosity is emitted in the broad feature known as the Big Blue Bump (BBB), believed to be the thermal emission from an optically thick accretion disc (see review by Koratkar & Blaes 1999). Each annular segment of the disc can be assumed to radiate as a blackbody (BB) with luminosity $2\pi r \delta r \sigma T^4$, with $T(r)$ from Equation. 1.5. The emergent spectrum can then be

approximated by integrating the Plank function, yielding

$$f_\nu = \frac{4\pi h \cos i \nu^3}{c^3 d^2} \int_{R_{in}}^{R_{out}} \frac{R dR}{exp(h\nu/kT) - 1} \tag{1.7}$$

where d is the distance to the observer and with inclination i (Frank et al., 2002). For low frequencies ($\nu \ll kT(R_{out})$) the continuum shape is $f(\nu) \propto \nu^2$ and for high frequencies ($\nu \gg kT(R_{in})$) it becomes $f(\nu) \propto \nu^3 \exp(h\nu/kT)$, the 'Wein tail' of the BB spectrum. The central, relatively flat portion of the distribution has the characteristic $\nu^{\frac{1}{3}}$ slope.

The observed spectrum deviates from this simple picture, as the discs are likely to have atmospheres, so won't act as simple blackbodies (e.g. Hubeny et al. 2000). In addition, the disc continuum shape will be altered by dust reddening, contamination with any underlying spectral components, and host galaxy contributions. The intrinsic disc continuum shape will likely be more complicated than a simple $\nu^{\frac{1}{3}}$ relation when the effects of inclination, rotation, inclination magnetic fields, relativistic effects, etc. are considered (e.g Czerny & Elvis 1987; Laor & Netzer 1989; Sun & Malkan 1989). If the accretion flow has a thick-disc geometry, the peak in the spectrum is expected to occur at $\sim 5R_{\rm g}$ (Beckmann & Shrader 2012b).

1.3.2 X-ray spectra

X-ray emission makes up a large portion ($\sim 5 - 10$ per cent) of the bolometric luminosity, with $L_{\rm x} \sim 10^{41} - 10^{45}$ erg s^{-1}. The observed rapid variability suggests the X-ray emission region is very compact, making them direct probes of the immediate vicinity (spacetime curvature) around the black hole. A number of emission and absorption processes constitute the X-ray spectra. The principle components are outlines below:

Primary power-law emission

Early observations found the $2 - 20$ keV band could be modelled with a power-law of photon index $\Gamma \sim 1.7$ (e.g Mushotzky et al. 1980). This power law was later observed to have an exponential cut-off at ~ 100 keV (Zdziarski et al. 1995). The currently favoured model for the primary power-law continuum is the inverse Comptonisation of optical/UV disc photons in an optically thin 'corona' of (possibly relativistic) electrons (Haardt & Maraschi 1991; Zdziarski et al. 1994). The electrons are in thermal equilibrium and have a Maxwellian distribution with characteristic temperature $kT_{\rm e} \sim 100$ keV ($T_{\rm e} \sim 10^9$ K), whilst the seed photons have initial energy $E \ll T_{\rm e}$.

For an electron temperature $kT_{\rm e} \ll m_{\rm e}c^2$ and $E < 4kT_{\rm e}$ the average energy gain for a

photon of initial energy E per scattering is given by

$$\frac{\Delta E}{E} \approx \frac{4kT_{\rm e} - E}{m_{\rm e}c^2} \tag{1.8}$$

(Rybicki & Lightman 1979, eq. 7.36). The average gain of each photon is given by the Compton amplification factor $A = 4kT_{\rm e}/m_{\rm e}c^2 = 4\Theta$. In the relativistic case this becomes $A = 4\Theta + 16\Theta^2$. The total energy gain of the photon propagating through the scattering medium with optical depth $\tau_{\rm e} = n_{\rm e}\sigma_{\rm T}R$, where $n_{\rm e}$, is the electron number density, $R = ct$, can be approximated by multiplying the average number of scatterings (each with probability $e^{-\tau}$) by the average energy gain per scattering. The number of scatterings follows a random walk with $n_{\rm scat} = \max(\tau_{\rm e}, \tau_{\rm e}^2)$. If Compton recoil can be neglected, then the total energy gain of the photon after n scatterings is given by the Compton-y parameter (Rybicki & Lightman 1979):

$$y = \frac{4kT_{\rm e}}{m_{\rm e}c^2}\max(\tau_{\rm e}, \tau_{\rm e}^2). \tag{1.9}$$

For a $\tau \ll 1$ plasma and $kT_{\rm e} \ll m_{\rm e}c^2$ seed photons the probability of n scatterings is $p \sim \tau^n$, whilst the photon will emerge with $E \sim E_0 A^n$. Assuming the distribution of $kT_{\rm e} \ll m_{\rm e}c^2$ seed photons the intensity of the emerging photons at energy E after n scatterings is a power-law, given by

$$I(E) \sim I(E_0 p(E_0 \rightarrow E)) \sim I(E_0)\tau^n \sim I(E_0)\left(\frac{E}{E_0}\right)^{ln\tau/lnA} \tag{1.10}$$

(Rybicki & Lightman 1979, eq. 7.45), which has an exponential turn-over at $E \sim kT_{\rm e}$.

In addition to the primary power-law continuum, the resultant X-ray spectrum is shaped by a variety of emission and absorption components (see Fig. 1.5).

X-ray reprocessing

A large fraction of the primary hard power-law emission is expected to irradiate the cold ($kT \lesssim 0.5\,{\rm keV}$) accretion flow, and any other gas. The fraction of the photons that reach the disc is proportional to the solid angle subtended by the disc as seen by the 'corona'. A fraction of the irradiating photons are absorbed, heating the disc, followed by subsequent re-radiation of a black-body, in a process known as *reprocessing* (Guilbert & Rees 1988). On top of this, a combination of scattering, fluorescence, recombination, and other emissions modify the spectrum further, producing a reflection spectrum (Lightman & White 1988).

Photons with energies below $\sim 10\,{\rm keV}$ will preferentially be the photo-absorbed by the disc as the cross-section for photo-absorption ($\propto Z^5 E^{-3}$) is larger than the cross-section for electron scattering. At energies $\gtrsim 10\,{\rm keV}$ Compton scattering dominates,
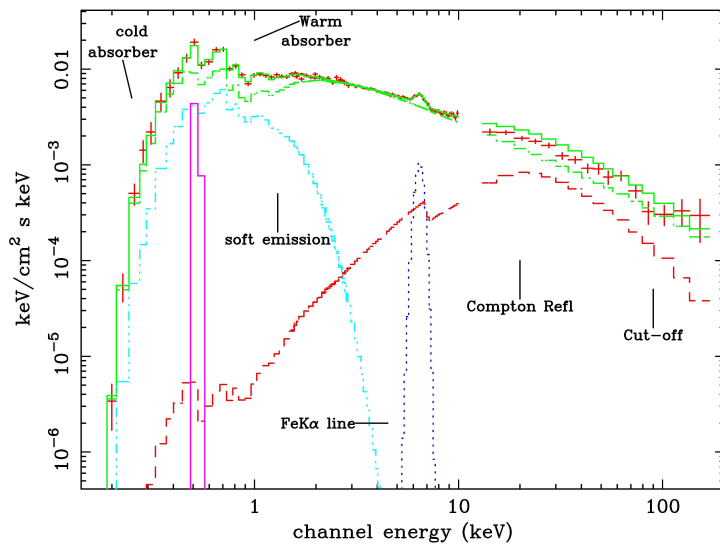
Figure 1.5: Example X-ray spectra for Narrow Line Seyfert 1 galaxy. The plot shows the 'unfolded' model fit NGC 3783 with the important spectral components labeled (De Rosa et al. 2002).

increasing the reflection fraction. At higher energies still, the scattering is inelastic so the photons emerge at lower energies than before. Photon number is conserved in the scattering process, so the neutral reflection spectrum has a peak between $20 - 50 \, \mathrm{keV}$, known as the *Compton hump* (see Fig. 1.6; Lightman & White 1988; George & Fabian 1991; Matt et al. 1991).

The accreting material, and at least the surface layers of the disc, is likely to be ionised by the illuminating continuum or from the inner disc blackbody (e.g. Ross & Fabian 1993; Ross et al. 1999; Fabian 2005). The shape of the reflection spectrum is highly dependent on the ionisation state of the material, which is characterised by the ionisation parameter $\xi = 4\pi F/n_{\mathrm{H}}$, where F is the incident flux and n_{H} is the hydrogen number density. Examples of reflection spectra produced by the XSPEC code REFLIONX for a variety of ionisation states is shown in Fig. 1.6 (Ross & Fabian 2005). This model predicts sharp emission features in the $0.2 - 2 \, \mathrm{keV}$ band, which then require relativistic blurring in order to match the smooth appearance of the data (e.g. Crummy et al. 2006).

Fe Kα

The fluorescent / recombination iron Kα line at 6.4 keV (see Fig. 1.6) is another signature of reflection. The line is present in most Seyfert spectra, with an average equivalent width of $\sim 50 - 100 \, \mathrm{eV}$ (Matt et al. 1991; Nandra et al. 1997; Nandra et al. 2007; Shu et al. 2010). Broadened Kα lines are one of the main pieces of evidence for a relativistic accretion disc extending deep into the gravitational well of a black hole (e.g.
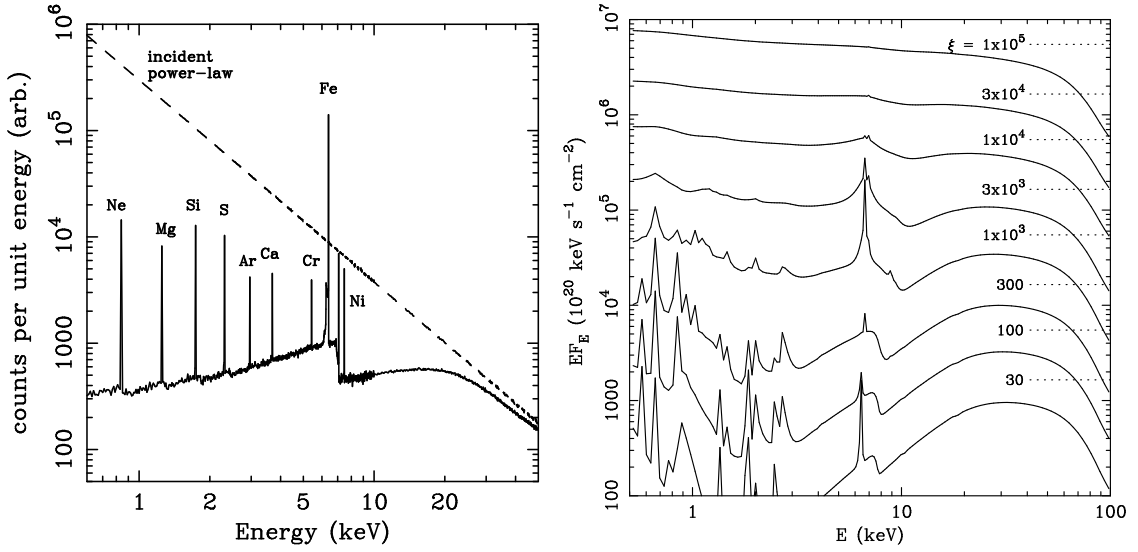
Figure 1.6: Left: Reflection features expected from power-law emission illuminating the disc (from Reynolds & Nowak 2003). Right: Reflection spectrum expected for a range of ionisation states (from Ross et al. 1999).

Tanaka et al. 1995; Fabian et al. 2000; Reynolds & Nowak 2003; Życki 2004; Miller 2007). A combination of Doppler and relativistic effects alter the shape of the emitted line feature (Fabian et al. 1989; Laor 1991). In particular, the strength of the gravitational redshift determines the redward extent of the emission line. This allows us to determine the innermost disc radius, and if this is identical to R_{ISCO} it provides an estimate of black hole spin (Bardeen et al. 1972; Reynolds & Fabian 2008). The blue 'horn' is caused by Doppler boosting (relativistic aberration), and tells us about inclination of the disc-black hole system (Fabian et al. 2000). A combination of high cosmic abundance and fluorescent yield mean the Fe Kα line is often the strongest emission line in the X-ray band (see Fig. 1.6).

There is ongoing debate about the general-relativistic origin for the red wing of the broadened Kα line. Miller et al. (2008; 2009) argued that an apparent broad line in the NLS1 MCG-6-30-15 could be explained in terms of several complex ionised absorbers partially covering the source (see also, Miyakawa et al. 2009; Reynolds et al. 2009; Yaqoob et al. 2010). However, this *partial-covering* model has many free parameters and is able to fit a wide range of spectral shape if enough absorbing components are included. Furthermore, the partial-covering scenario has great difficulty explaining many of the variability properties (see Section 1.4.1), a topic to be discussed throughout this thesis.

The observed Fe Kα line appears to remain relatively constant on timescales where the continuum shows significant variability (e.g. Reynolds 2000; Vaughan & Edelson 2001). The red-wing is expected to vary in phase with the continuum in the general-

relativistic origin of the broadened line (Stella 1990; Matt & Perola 1992; Reynolds et al. 1999; Inoue & Matsumoto 2003). The lack of variability in the red-wing and the high reflection fractions (ratio of reflected to primary emission) have been explained as a consequence of light-bending effects close to the black hole (Fabian & Vaughan 2003; Miniutti et al. 2003; Miniutti et al. 2004). The *light bending* model places the primary X-ray emission above the black hole (possibly the base of a jet), which can move closer/further from the BH. The illumination of the disc increases as more of the primary emission is focused by gravitational light bending down as the source moves closer to the disc. However, this picture requires significantly centrally concentrated emission, and extreme relativistic blurring to smooth out the predicted Fe L line in the soft excess (see below).

A recent *XMM-Newton* study of 26 Seyfert galaxies found that $\sim 60\%$ of Seyfert 1s showed a feature below 6 keV, consistent with a broadened red wing of the Fe Kα line (Nandra et al. 1997). A broadened Fe-L feature below 1 keV has also been claimed in the NLS1 1H0707-495 (Fabian et al. 2009). A recent *Suzaku* study by Patrick et al. (2011) found the presence of relativistically broadened Fe Kα in several objects, but with only moderate spin parameters.

Soft Excess

The launch of *EXOSAT* in the 1980s extended the X-ray coverage down to $0.1\,\mathrm{keV}$, and revealed that many AGN shown an excess of emission below $2\,\mathrm{keV}$ over the extrapolated power-law component at higher energies (Arnaud et al. 1985; Pounds & Turner 1989; Saxton et al. 1993). The origin of this 'soft excess' is still an open issue. The component has a very smooth spectrum, often without any strong features even at high resolution, as shown by (Vaughan et al. 2002; Marshall et al. 2003; Vaughan et al. 2004), with $\Gamma \sim 2 - 3$, compared to the primary power-law with $\Gamma \sim 1.7 - 2.0$. The soft-excess was originally associated with the high-energy tail of the thermal disc blackbody. However, this would suggest the inner-disc temperature ($kT \sim 0.1 - 0.2\,\mathrm{keV}$) to be independent of black hole mass, luminosity and accretion rate (Czerny et al. 2003; Gierliński & Done 2004). There are currently three plausible explanations (Vaughan et al. 2002 discussed several of these) for the soft excess: additional Comptonisation component (Dewangan et al. 2007), ionized reflection from disc (Crummy et al. 2006), complex and/or ionized absorption (Gierliński & Done 2004; Done 2007).

The reflection origin requires extreme relativistic blurring in order to smooth out the soft X-ray emission features. This requires small R_{in}, and hence implies high spin. However, much of the disc photosphere needs to be ionised. Yet only part of the disc pho-

tosphere can be, otherwise the disc cannot remain in hydrostatic equilibrium, requiring support from magnetic fields (Done & Nayakshin 2007).

The excess could be formed of the emission from partially ionised material which is then absorbed by optically thin material Gierliński & Done 2004; Schurch & Done 2006). A highly relativistic outflow velocity ($v \lesssim c$) is required to smooth out the expected absorption lines of Fe, C and O to produce a pseudo-continuum component (Schurch & Done 2008). Such a component would produce strong absorption signature, which is not observed (Done 2010).

Absorption

The primary X-ray continuum is modified by neutral and ionised absorption along the line of sight, which scales as $\sim \exp(-\tau) = \exp(-N_{\mathrm{H}})\sigma(E)$. Cold absorption from the host galaxy or Galaxy ISM dominates below 0.5 keV.

X-ray CCD and grating spectroscopy at soft energies (< 1 keV) has revealed the presence of multiple ionised absorption zones known as *warm absorbers* (Halpern 1984, predominetly from OVII 0.76 keV and OVIII 0.87 keV (Nandra & Pounds 1992; Reynolds 1997; Sako et al. 2001; Kaspi et al. 2001; Lee et al. 2001). The ionisation states and inferred temperatures (typically $\lesssim 10^5$ K) suggest the gas is photo-ionised by X-rays from the central engine, rather than being a collisionally ionised thermal plasma.

1.4   Variability

Aperiodic variability is observed at all wavelengths and on all timescales probed thus far (e.g. Gaskell et al. 2006). Strong UV and X-ray variability is common to AGN on a wide range of timescales (e.g. Collin 2001), with the most rapid variations seen in X-rays (e.g. Mushotzky et al. 1993).

Variability and spectral-variability studies add a complimentary dimension to spectral studies, and reveal the dynamical processes involved and the causal-connections between separate emission components. X-ray and optical/UV variability is the best probe of accretion processes, so will be discussed it detail.

1.4.1   X-ray Variability

Over the last 20 years, the *RXTE* and *XMM-Newton* satellites have dramatically improved our understanding of the X-ray variability. It too became clear that the variability process in AGN have much in common with XRBs, scaled by mass and $\dot{m}_{\mathrm{Edd}}$ (see e.g. McHardy
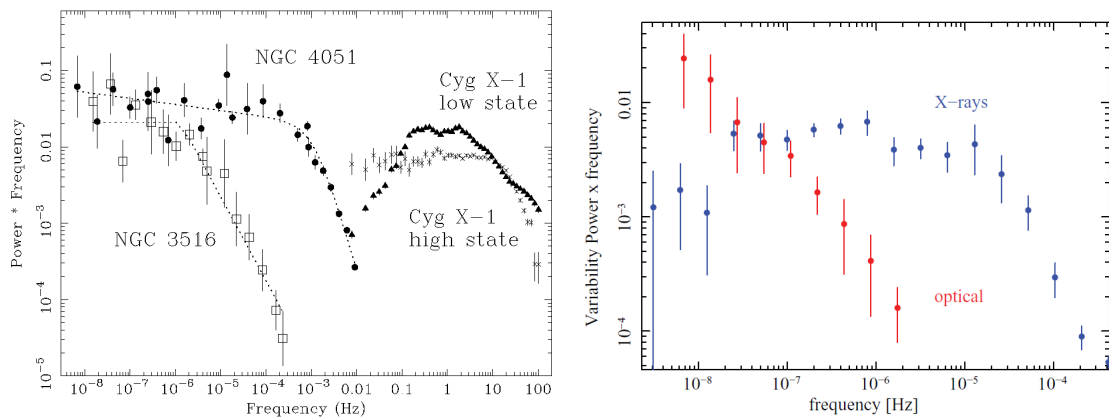
Figure 1.7: Left: Power spectral density of accreting black hole systems, spanning 10 decades in frequency (from McHardy et al. 2004). Cyg X-1 is a stellar mass BH-XRB with $M_{BH} \sim 10 M_\odot$ and NGC 4051 is a Seyfert 1 with a $M_{BH} \sim 2 \times 10^6 M_\odot$. Right: Optical and X-ray PSD for the Seyfert 1 galaxy NGC 3783 (Arévalo 2013). At high frequencies the X-ray variability power dominates, whereas at lower frequencies more power is seen in the optical.

2010). If true, then understanding the variability process in one, will aid our understanding in the other. XRBs have a higher flux and so higher count rates, so are less affected by photon counting noise. However, more photons per characteristic timescale are typically received from nearby AGN. This allows us to probe the variability on higher characteristic timescales in AGN, timescales that are most affected by photon counting noise in XRBs.

XRBs are observed to transition through 'states' on timescales of months to years, characterised by their spectral hardness and $0.2 - 10$ keV X-ray flux (see Belloni 2010 and Fender 2010 for a review). The most commonly observed states are the low/hard (LH), high/soft (HS) and the very high/intermediate (VHS). The variability properties also change between the different states, and may offer a cleaner way of determining the state of the accreting black hole (see the review by McHardy 2010). If state transitions occur in AGN, the timescale will be much longer, of the order of ∼thousands of years for $M_{BH} \sim 10^6 M_\odot$. A statistical analysis is therefore required to understand AGN states.

Power spectral density

A variety of methods for characterising the variability exist in both the *time* and *Fourier* domain (see Section 2.2). One such univariate Fourier method routinely applied to XRBs and AGN is the power spectral density (PSD) of the light curve (see e.g. Vaughan et al. 2003. This provides information about the variability amplitude as a function of Fourier frequency ($1/timescale$). An example AGN and XRB PSD is shown in Fig. 1.7, where

the similarities in PSD shape between the two classes of objects can be seen. The PSDs in most AGN show a high frequency bend, which is similar to soft state XRBs. The variability is that of broadband noise with the PSD shape well described by a bending power-law, $P(f) \propto f^{-\alpha}$ with $\alpha \sim 2$ at frequencies above the break ν_B, and $\alpha \sim 1$ below ν_B (e.g. González-Martín & Vaughan 2013).

The PSD is not always well described by a simple power-law or bending power-law model, with some objects displaying a 'clumpy' or peaked structure (e.g. Ark 564; McHardy et al. 2007, PG 1244+026; Jin et al. 2013). In Ark 564 the PSD was well described by a combination of broad Lorentzian profiles (McHardy et al. 2007). This observation, together with the hardening of the PSD with energy at high frequencies, supports the idea of two variability process, with one dominating at high or low frequencies.

In XRBs, superimposed on the PSD are sharp peaked features known as quasi periodic oscillations (QPOs). These are observed for XRBs in the hard state and during state transitions. Their origin in XRBs is still not understood, but can be used to characterise states in XRBs (see Belloni 2010 for a review). The high frequency QPOs ($\nu > 40\,\mathrm{Hz}$) have variations which are close to the Keplerian frequency at R_{ISCO}, and so may be associated with the effects of GR (e.g. Remillard et al. 2002). One reliable detection of a QPO has been seen in an the NLS1, REJ 1034+396 (Gierliński et al. 2008). However this provides a limited diagnostic, as the feature is only present in one out of several long observations.

Coherence / Time lags

Additional information on the variability process and the causal connection between emission mechanisms is provided by multivariate techniques such as the cross-spectrum (van der Klis 1989; Vaughan & Nowak 1997), from which we get the coherence and phase difference (time lags) between the two light curves (see Section 2.4). The time delays and coherence provide an powerful diagnostic for emission mechanisms and constraining the geometry of the X-ray emission region.

XRBs in the hard state, show coherence between a soft and hard band that is very high ($\gamma^2 \sim 1$) at frequencies $\lesssim 10\,\mathrm{Hz}$ (e.g. Vaughan & Nowak 1997; Nowak et al. 1999). High coherence at a given frequency is produced if the one variability process dominates, and the X-ray emission source has a small spatial extent. At high frequencies, where the coherence is observed to drop, this is consistent with another independent variability process beginning to dominate the variability. AGN too, show high coherence at low frequencies, which drops at higher frequencies (e.g. Vaughan et al. 2003).
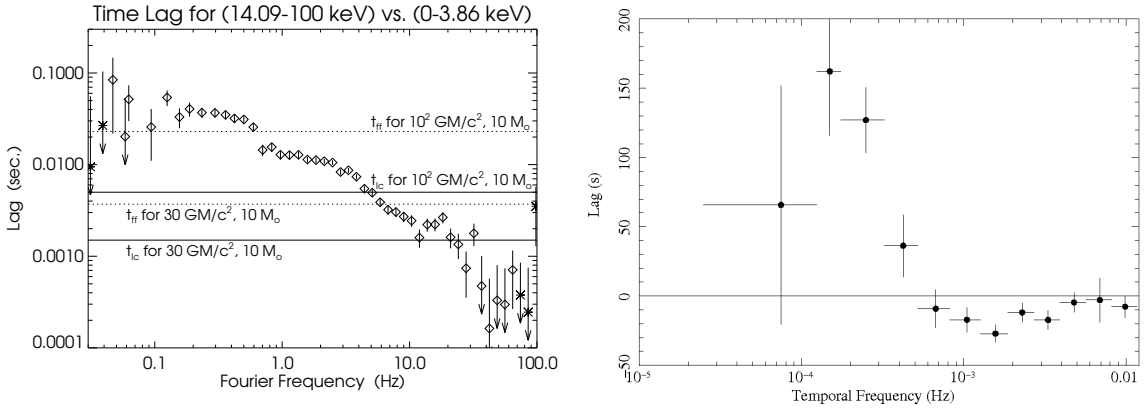
Figure 1.8: Left: Lag frequency spectrum of Cyg-X1, showing the hard band time delay (from Nowak et al. 1999). Right: Lag frequency spectrum for the NLS1 1H0707+496. A hard (positive) lag is seen at low frequencies, switching to a soft (negative) lag at higher frequencies (from Fabian et al. 2009).

Frequency dependent phase (or time) lags are seen in XRBs in the $1 - 100$ keV range, where the hard energy bands lag the softer bands (Miyamoto et al. 1988; Miyamoto & Kitamoto 1989). The time lag $\tau(f) \propto f^{-\alpha}$, where $\alpha \sim -1$, and has an approximately logarithmic dependence on energy (Miyamoto & Kitamoto 1989; Cui et al. 1997; Nowak et al. 1999). At the lowest frequencies the time lag is ~ 1 s, ruling out the Comptonisation origin of the time lag, as this implies the corona to be $\sim 10^4 R_g$.

Very short time lags ($\lesssim 100$ s) between soft and hard X-ray bands, where the soft band variations lag the hard band variations, may allow us to probe the X-ray emission region and inner accretion flow (e.g. McHardy et al. 2007; Fabian et al. 2009). The soft lag is thought to represent the 'reverberation' signal as the primary X-ray emission is reprocessed by relatively nearby material, one candidate for which is the inner accretion disc itself (e.g. Fabian et al. 2009). These subtle signals directly encode the physical scales of the reflection region (by light travel time arguments). The X-ray emission illuminates the optically thick disc material, which responds to variations in the X-ray luminosity with a short time lag set by the light travel time between the emission sites ($10R_g$ is ~ 100 s for $M_{BH} \sim 2 \times 10^6$ M$_\odot$).

Another model for the time lags has the X-rays scattering off a shell of circumnuclear material located at tens to thousands of R_g from the central source of X-ray emission Miller et al., (2010a; 2010b, hereafter M10a and M10b respectively). Electron scattering within this region produces a delayed, reprocessed X-ray continuum. Absorption within the shell (bound-free and bound-bound transitions) means that, at large distances (hence longer time lags) soft X-rays are preferentially more likely to be absorbed than scattered out of the shell, relative to harder X-rays. Including only the hard-band reprocessing, such a model can reproduce a (positive) hard lag at low frequencies, and if the edges

of the shell are quite sharp it can also reproduce a (negative) soft lag in a narrow, higher frequency band, as a 'ringing' artefact of the sharp impulse response function (a manifestation of the Gibbs phenomenon). M10a extended the model to include reprocessing of the softer X-rays, from only inner regions of the shell, this reproduces a broader negative (soft) lag.

RMS-flux relation

An important diagnostic of the underlying variability process is the linear rms-flux relation (e.g. Uttley & McHardy 2001; Uttley et al. 2005). Here, a linear scaling is observed between the root-mean-square (rms) amplitude and the mean X-ray flux over a given time interval. The non-zero offset in the relation indicates an additional component with constant flux, rms or both (Vaughan & Uttley 2007). This relation appears to hold for all timescales, and implies the model describing the underlying noise process is non-linear and predicts a log-normal distribution of fluxes. The non-linear behaviour means the model must be multiplicative (rather than additive) and couple on all time scales (Uttley et al. 2005; Vaughan & Uttley 2007).

1.4.2 Underlying variability process

The leading model for X-ray variability of AGN and XRBs is based on the inward propagation of random accretion rate fluctuations coupled at each radius in an accretion disc (e.g. Lyubarskii 1997; Kotov et al. 2001; King et al. 2004; Zdziarski 2005; Arévalo & Uttley 2006; Ingram & Done 2010; Kelly et al. 2011), where the local mass accretion rate through the inner regions of the disc modulate the X-ray emission. This multiplicative model reproduces many of the currently known spectral variability patterns in AGN and XRBs (Arévalo & Uttley 2006), e.g. the linear rms-flux relation; the change in PSD shape with energy due to the radial dependence on emissivity; break frequency dependence on energy; and energy dependent time lags.

1.4.3 Optical/UV variability

Optical variability in quasars has been known for some time (e.g. 3C 273; Press 1978). Many Seyferts show UV and optical variability, although with a weaker variability amplitude at higher frequencies than is observed in the X-rays (see right panel of Fig. 1.7). However, the origin of the optical and UV variability is still unclear. The location of the UV emitting region (optical and UV emission will be considered the same thing for the remainder of this section) depends on the details of the accretion flow, and these

in turn depend on the black hole mass and accretion rate (see Fig.1.9), but is typically $\sim 10 - 1000 \, R_{\mathrm{g}}$. By contrast, the optically thin corona of hot electrons producing the primary X-ray spectrum is located in the central few tens of R_{g} from the black hole (e.g. Haardt & Maraschi 1991). The causal connections between these processes are still unclear but can in principle be investigated by studying the time variations in the luminosity across different wavebands. If the emission mechanisms are coupled the UV and X-ray variations should be correlated, in which case the direction and magnitude of time delays should reveal the causal relationship. Two favoured coupling mechanisms are:

1. *Compton up-scattering* of UV photons — produced in the disc — to X-ray energies in the corona (Haardt & Maraschi, 1991). Here, any variations in the seed photons being upscattered will directly translate into variatons in the X-ray emission.

2. *Thermal reprocessing* in the disc of X-ray photons produced in the corona (Guilbert & Rees, 1988). Reprocessing in a cold disc is observed in X-ray reflection features of AGN spectra (e.g. Nandra & Pounds 1994; Fabian et al. 2002). The wavelength the reprocessed photons emerge at and their contribution to the energy radiated by the disc can be tested in multi-wavelength variability studies. Of course, the X-rays will irradiate a significant portion of the disc, but we are only interested in the region — or annulus — of the disc that reprocesses the X-rays photons to UV energies.

The coupling mechanisms are shown in Fig. 1.9. The interaction timescale for these two processes is approximately the light crossing time between the two emitting regions, and will be in the region of minutes to days for black hole masses $M_{\mathrm{BH}} \sim 10^6 - 10^8 \mathrm{M}_\odot$.

Both emission regions are also likely to be correlated at some level if they are both modulated by their local accretion rate, which varies as accretion rate fluctuations propagate through the flow (e.g. Arévalo & Uttley 2006). In a standard accretion disk the timescale for propagation of fluctuations between the two emission regions is governed by the viscous timescale of the disc. For $M_{\mathrm{BH}} \sim 10^6 - 10^8 \mathrm{M}_\odot$ this timescale will be in the region of weeks to years (Czerny, 2006). If any of these processes are significant, their effects should be apparent from time series analysis of light curves from both wavebands. However, a combination of these processes occurring at the same time could make individual reprocessing models harder to detect.

Studies of correlations between variations in different wavebands are a potentially powerful tool for investigating the connections between different emission mechanisms (see Uttley 2006 for a short review). Done et al. (1990) performed the first simultaneous optical/X-ray study, searching for correlated emission in the NLS1 galaxy NGC 4051 over two days. The X-ray flux varied by a factor of two over this period, whilst the
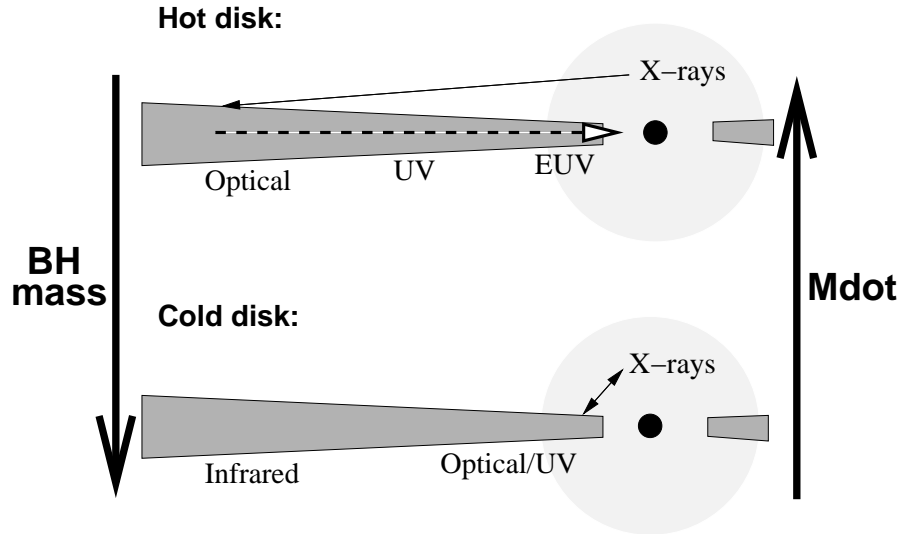
Figure 1.9: The possible coupling mechanisms between the UV and X-ray emission regions. The Compton up-scattering and thermal reprocessing scenarios are shown by the solid arrows. The coupling of the two emission regions due to propagation of accretion rate fluctuations is shown by the dashed arrow. The dependence of M_{BH} and $\dot{M}$ on the location of the optical and UV emission regions is shown. This figure is taken from Uttley 2006.

optical variations were $\lesssim 1\%$. This demonstated that optical and X-ray emission was produced by separate processes. X-ray/optical correlations on long timescales have been seen in radio-quiet AGN (e.g. Uttley et al. 2003; Arévalo et al. 2008; Arévalo et al. 2009; Breedt et al. 2009). Together with the optical-optical lags (e.g. Cackett et al. 2007) they imply that a combination of accretion fluctuations and reprocessing produces much of the optical variability. X-ray/UV correlations have been seen in e.g. Nandra et al. (1998); Cameron et al. (2012), however, there are currently fewer examples than the X-ray/optical correlation studies.

Given a black hole mass estimate, it is possible to make predictions time delays for the possible coupling mechanisms using simple toy models. In the *Compton up-scattering* scenario we assume that the disc temperature profile is created solely by viscosity of the disc itself. Using Wien's Law to derive a temperature for a UV wavelength, a radius for the UV emitting region can can be estimated from Equation 1.5. The X-rays are assumed to come from close to the black-hole ($R \approx 0$) and the light travel time is taken as a reasonable approximation for the time-lag.

In the reprocessing scenario we assume the disc is heated entirely by the external X-rays. If 50 percent of the X-ray flux irradiates the disc the UV luminosity is approximately equivalent to the observed X-ray luminosity (L_{x}). Using the temperature as calculated Equation 1.5 we can estimate the radius to the UV emitting region using Stefan's

Law:

$$L_{\mathrm{UV}} \approx L_{\mathrm{X}} = 4\pi r^2 T^4 \tag{1.11}$$

For $M_{\mathrm{BH}} \sim 10^6 - 10^8 \mathrm{M}_\odot$ these timescales are on the order of $\sim$ minutes–days. This is well within the sampling capability for many current ground- and space based observatories (see Section 2.1).

Science is not an exact science

Dr. Tim Richardson

2

Instrumentation and analysis methods

In this chapter I will describe the instrumention and data reduction methods used in the proceeding chapters. I will also describe the time- and Fourier-domain methods used in the subsequent variability analysis.

2.1 Instrumentation

2.1.1 The *XMM-Newton* Space Observatory

The European Space Agency (ESA) X-ray Multi-Mirror Mission (*XMM-Newton*, Jansen et al. 2001) satellite has been in operation since 1999. It occupies a ~ 48 hour, highly elliptical orbit (perigee of 7,000 km; apogee of 114,000 km), allowing for up to ~ 40 hours of uninterrupted scientific observations. On-board are three co-aligned X-ray telescopes and an optical/UV telescope (described below), which can all be operated simultaneously and independently.

The three X-ray mirror modules each contain 58 Wolter–1 high-precision concentric mirrors (see Fig. 2.3), each having an effective area of $1550\,\mathrm{cm}^2$ at $1.5\,\mathrm{keV}$. With a total geometric effective area of $4650\,\mathrm{cm}^2$, *XMM-Newton* achieves high sensitivity and has the largest ever effective area for an X-ray focusing telescope.

Each telescope has a different CCD detector in its focal plane, known collectively as the European Photon Imaging Cameras (EPIC). EPIC consists of two front illuminated Metal Oxide Semi-conductor (MOS) CCD arrays (MOS-1 and MOS-2; Turner et al.
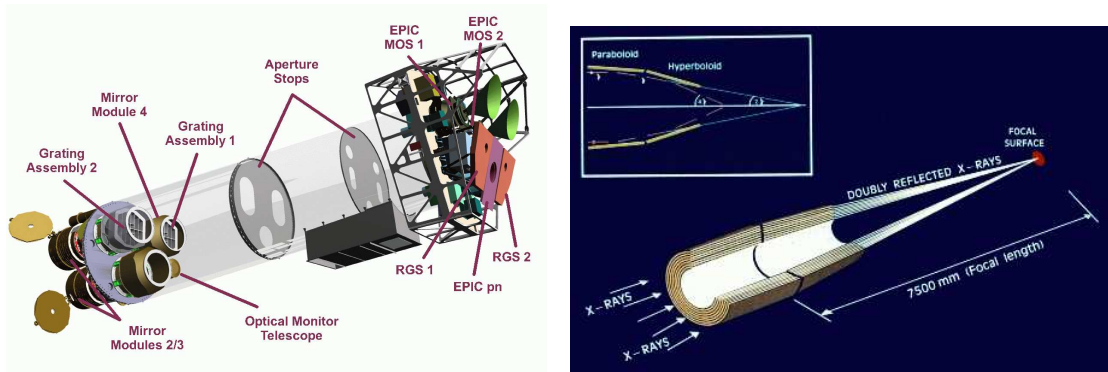
Figure 2.1: Left: Schematic of the *XMM-Newton* telescope, including X-ray mirror modules and scientific instruments. Right: Schematic of the Wolter-1 X-ray mirrors used on *XMM-Newton* and other focusing X-ray spacecraft. Both figures taken from[2].

2001) and a back illuminated silicon pn-junction CCD array (pn; Strüder et al. 2001). The modules containing the MOS cameras also house Reflection Grating Spectrometers (RGS-1 and RGS-2; den Herder et al. 2001) for high resolution X-ray spectroscopy. EPIC provides sensitive imaging over a 30 arc-minute field of view (FOV) and $0.15 - 15\,\mathrm{keV}$ energy range. In practice it is the 0.2–10 keV data that are useful. Above 10 keV the data usually are dominated by background and below 0.2-0.3 keV there are few source photons due to absorption. Near the telescope aimpoint the point spread function (PSF) has a FWHM of ~ 6 arcsec. Fig. 2.2 shows the fraction of counts as function of aperture radius derived from a real observation (revolution 0541 of the AGN NGC 4051).

The EPIC CCDs are photon counting devices. The CCDs are read out at a high frame rate such that the properties of individual photons can be measured. The output is an *event list* — a list of photon events in each detector, including time, energy and position of each photon detected. Observation data is downloaded from the *XMM-Newton* Science Archive (XSA) and can be processed using the *XMM-Newton* Science Analysis System (SAS[2]).

2.1.1.1 The Optical Monitor

XMM-Newton is also equipped with a 30 cm Ritchey-Chretien optical/UV telescope (OM; Mason et al. 2001) co-aligned with the X-ray instruments. A choice of 6 filters allows for total coverage between $1700 - 6500\,\mathrm{\AA}$ of the central 17 arc-minutes square of the X-ray detectors FOV. Unlike on most optical telescopes, the OM detector is also a photon-counting detector, with a micro-channel plate intensified CCD. The OM can operate in either Imaging Mode, with the emphasis on spatial coverage, or Fast Mode

---

[1]http://xmm.esac.esa.int/external/xmm_user_support/
[2]http://xmm.esa.int/sas/
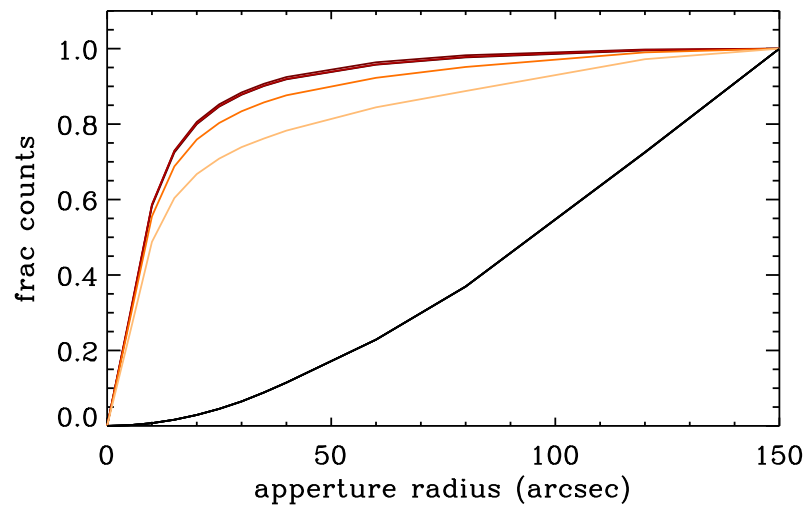
Figure 2.2: *XMM-Newton* source counts as a function of aperture radius derived from a real observation (revolution 0541 of the AGN NGC 4051) for the 0.2–0.7 keV (dark red), 0.7–1.2 keV (red), 1.2–2 keV (orange) and 2–10 keV (yellow) energy bands. The black line shows the fraction of background counts in the aperture.

to emphasize timing information. Imaging mode with 2x2 binning factor results in a 488x480 pixel image, with a resolution element of ~ 1.0 arc seconds per pixel. The Imaging Mode exposure length can be set in the range 800–5000 s. OM imaging and fast mode data are processed with the SAS pipelines OMICHAIN and OMFCHAIN respectively.

Accurate count rates from aperture photometry of the OM images (using e.g OMDE-TECT) can only be produced once 5 instrumental corrections have been applied: The point spread function (PSF1) correction must be applied in order to scale the count rates to those of a 6 arc seconds radius aperture. Coincidence loss (CL) is the loss of photons being counted when more than one photon is collected within the same pixel in a single CCD readout frame. Multiple photons therefore register as one event causing a reduction in the observed counts. The CL correction has been calibrated empirically for an aperture radius of 6 arc second and hence follows the PSF1 correction. There is a short amount of time, the frame transfer time, when the CCD is read out and any incident photons will not register as events. The deadtime (DT) correction is a simple scaling factor correcting for this effect. When using the UV filters, the Gaussian wings of the PSF extend further than the aperture radius so a further correction (PSF2) must be applied to account for the loss of counts from the wings. As the performance of the OM detector decreases over time, the time-dependent sensitivity degradation (TDS) correction must be applied.

2.1.2   The Swift satellite

Launched in 2004, the NASA *Swift* satellite (Gehrels et al. 2004) occupies a Low Earth Orbit at an altitude of 600 km with a ~ 96 minute orbital period. Designed as a rapid
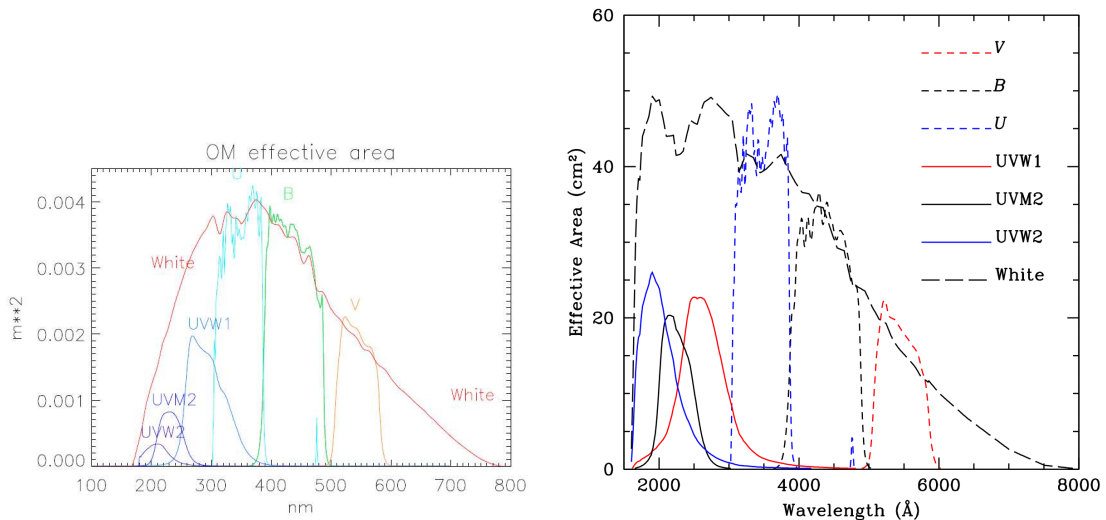
Figure 2.3: Left: The effective are of the *XMM-Newton* OM filters. The curves represent the filter throughput after folding in the detector sensitivity[3]. Right: The effective are of the *Swift* UVOT filters [4].

response gamma-ray burst mission, *Swift* consists of 3 science instruments — the Burst Alert Telescope (BAT; Barthelmy et al. 2005, the X-Ray Telescope (XRT; Burrows & The Swift XRT Team 2004) and the Ultraviolet/Optical Telescope (UVOT; Roming et al. 2005) — which allow for X-ray and UV monitoring on longer timescales. The XRT has a $23.6'$ × $23.6'$ FOV with a pixel scale of 0.236 arc seconds. Its detector is identical to a single EPIC MOS chip, unlike the EPIC MOS which are 7 chips, and can operate in *photon-counting* and *imaging* mode in the energy range $0.2 - 10$ keV.

Similar to the OM, the UVOT is a modified 30 cm Ritchey-Chretien telescope with a 17 arc second squared FOV and operates in the $1600 - 6000$ Å range. The detector operates as a photon counting instrument with a pixel scale of 0.5 arc seconds. The wavelength coverage and broadband filters of the UVOT and OM are approximately the same in both the optical and UV regimes (Poole et al. 2008).

2.2 Time-series analysis

Time-series analysis is a branch of statistics, and is routinely applied throughout economics, the sciences and astronomy (e.g. Feigelson 1997; Vaughan 2013). The terms *time series* and *lightcurve* are used interchangeably to mean a finite sequence $x(t_i)$ of N data points of some measured quantity (e.g. photon counts, flux, etc.). X-ray detectors are typically photon counting devices, recording a discrete number of counts c_i in the

---

[3]http://xmm.esac.esa.int/external/xmm_user_support/
[4]http://swift.gsfc.nasa.gov/about_swift/uvot_desc.html

time interval $[t_i, t_{i+1}]$, hence $x(t_i) = c_i/\delta t$, where $i\epsilon[0, N-1]$ and the length of the light curve is given by $T = N\delta t$. In the following sections the subscript i will be dropped from much of the notation.

In this thesis we make use of X-ray and optical/UV light curves from AGN and apply methods of time series analysis. An implicit assumption in many methods is that the process generating the time series under consideration is stationary. The measured flux is treated as a stationary stochastic (random) noise process, where each observation is one realization of the stochastic process (e.g. Priestley 1981; Percival & Walden 1993). A stochastic process is considered stationary when its probabilistic structure is time invariant. In practice, the stochastic process is considered to be only *weakly stationary*, where only the second order moments are time invariant, e.g. the variance or rms, power spectrum, cross-correlation and cross-spectrum which are used extensively in this work.

2.2.1 Poisson noise

The photon counting nature of X-ray detectors means that the observed signal in a given energy band, $x(t)$, comprises the 'true' underlying physical signal $s(t)$ plus some Poisson counting noise $n(t)$, such that

$$x(t) = s(t) + n(t) \tag{2.1}$$

where $n(t)$ has mean 0 and sigma (rms) of $\sqrt{s(t)}$. If the true flux is $s(t)$ (in time interval dt) then we will observe random values $X \sim Pois(s)$, i.e. each measurement is drawn from a Poisson distribution. But in the limit of moderately high counts/interval we approximate the Poisson distribution as a Normal distribution and treat the observed signal as the sum of the true signal $s(t)$ plus a noise term, $n(t)$. We can thus approximate variance$(n) \sim s(t)$. The noise is uncorrelated with the signal, however, since the amplitude of Poisson noise is $\sqrt{flux}$, it is not independent.

2.2.2 Quantifying variability

For a time series, $x(t)$, variability can be quantified using a number of statistical tests. In an observed light curve, some of the total variance, S^2, will be intrinsic to the source σ_{XS}^2, and some will come from the measurement uncertainties, $\overline{\sigma_{err}^2}$ (Vaughan et al. 2003). The 'excess variance' can be used to estimate the intrinsic source variance for N_x data points using:

$$\sigma_{XS}^2 = S^2 - \overline{\sigma_{err}^2} \tag{2.2}$$

where $S^2 = \sum_{i=1}^{N}(x_i - \bar{x})^2/(N-1)$ is the unbiased sample variance, and $\overline{\sigma_{err}^2} = \frac{1}{N}\sum_{i=1}^{N}\sigma_{err,i}^2$ is the mean square error (mse). $\sqrt{\sigma_{XS}^2}$ gives the root mean squared (rms) variability amplitude. The fractional rms variability amplitude (F_{var}; Edelson et al. 1990) is the normalised version of the excess variance defined as:

$$F_{var} = \sqrt{\frac{S^2 - \overline{\sigma_{err}^2}}{\bar{x}^2}} \tag{2.3}$$

2.2.3 Time evolution

For the statistics desribed in Section 2.2.2 the time ordering of the measured quantities is irrelevant, hence they provide no information about the time evolution of the process. For a univariate time series we can gain such information from the autocorrelation function

$$\rho_{xx}(\tau) = \frac{E[(x_t - E[x_t])(x_{t-\tau} - E[x_t])]}{\sigma_x^2} \tag{2.4}$$

where E is the expectation value and $x_{t-\tau}$ is a lagged version of the time series, $x(t-\tau)$. The autocorrelation function is symmetric ($\rho_{xx}(\tau) = \rho_{xx}(-\tau)$.

For multivariate data, where we have two simultaneously sampled time series $x(t)$ and $y(t)$ - such as observations of the same target in two different energy bands - we have the cross-correlation function:

$$\rho_{xy}(\tau) = \frac{E[(x_t - E[x_t])(y_{t-\tau} - E[y_t])]}{\sigma_x\sigma_y}. \tag{2.5}$$

The numerator in Equation 2.5 is the cross-covariance function.

The use of the CCF and other statistical tools that require evenly sampled data are often hampered by the irregular sampling nature of astronomical data. Interpolating between the gaps is commonly performed, but is likely to introduce spurious correlations when the PSD has substantial amplitude at frequencies higher than the mean sampling rate. Edelson et al. (1990) devised the discrete correlation function (DCF) which is defined for lags between each pair (a_i, b_j) of measured data points, and hence does not invent data.

$$DCF_{xy}(\tau) = \frac{1}{M}\sum \frac{(x_i - \bar{a})(b_j - \bar{b})}{\sqrt{(\sigma_a^2 - e_a^2)(\sigma_b^2 - e_b^2)}} \tag{2.6}$$

where the sum is over all pairs within the time interval $\Delta t_{ij} = t_j - t_i$, defined by time lag τ for $\tau - \Delta\tau/2 \leq \Delta t_{ij} \leq \tau + \Delta\tau/2$. Here, e are the measurement errors and M is the number of pairs within $\pm\Delta\tau$ of each time lag τ.

The Bartlett formula can be used to estimate the variance on the CCF estimates, and can therefore be used like an error bar (Bartlett 1948):

$$\sigma^2\{CCF(\tau)\} = \frac{1}{N} \sum_i \text{ACF}_x(\tau)\text{ACF}_y(\tau) \tag{2.7}$$

where N is the number of data points contributing to each time lag τ. This formula can also be applied to the DCF if the ACF is formed from the DCF of the uneven time series with itself.

2.3 Estimating the power spectrum

The power spectrum (or power spectral density: PSD) describes the amount of variability *'power'* (squared variability amplitude) as a function of Fourier (temporal) frequency ($\sim 1/timescale$). The power spectrum is the Fourier counterpart of the ACF.

The standard method for estimating the power spectrum in astronomical time series data is to use the Bartlett method (Bartlett 1948). An evenly sampled and contiguous time series $x(t_i)$ with time bin size Δt and sampling length $N\Delta t$, can be broken into M non-overlapping segments of length N (where $i = 1, 2, \cdots, N$). The periodogram (Priestley 1981) of each segment is computed and the average of the M periodograms is taken. The periodogram $P(f)$ is the normalised modulus-squared of the discrete Fourier transform (DFT), which is a discrete estimator of the underlying continuous PSD, $\mathcal{P}(f)$. The DFT of $x(t_i)$ is defined as

$$X(f_j) = \mathcal{F}[x(t_i)](f) = \sum_{i=1}^{N} x(t_i)e^{-i2\pi f_j t_i} = \Re[X(f_j)] + \Im[X(f_j)] \tag{2.8}$$

with

$$\Re[X(f_j)] = \sum_{i=1}^{N} x(t_i) \cos 2\pi f_j t_i$$
$$\Im[X(f_j)] = \sum_{i=1}^{N} x(t_i) \sin 2\pi f_j t_i \tag{2.9}$$

where $\Re(\cdot)$ and $\Im(\cdot)$ indicate the real and imaginary components of some variable. $X(f)$ is calculated at $N/2$ evenly spaced frequencies $f_j = j/N\Delta t$ (where $j = 1, 2, \cdots, N/2$). The highest frequency that can be sampled is the Nyquist frequency: $f_{N/2} = f_{Nyq}$. Because astronomical time series are real valued, the resulting complex Fourier transform is symmetric around $f_{j=0}$ (i.e. $X(f_{+j}) = X^*(f_{-j})$), meaning the Fourier transform of the negative frequencies provide no additional information. The Fourier transform at $f_{j=0}$ is

Table 2.1: Commonly used periodogram normalisations for input light curves in cts^{-1} with Poissonian errors. The Poisson noise level is different for light curves with Gaussian errors $\sigma_{err,i}$ (e.g. Vaughan et al. 2003).

Normalisation	ordinate	Integrated	Poisson noise
$A_{\mathrm{abs}} = 1$	$[\mathrm{ct\ s}^{-1}]^2 \mathrm{Hz}^{-1}$	$[\mathrm{ct\ s}^{-1}]^2$	$P_{\mathrm{noise}} = 2\Delta t \sigma_{\mathrm{err}}^2$
$A_{\mathrm{Leahy}} = 1/\bar{x}$	$\mathrm{ct\ s}^{-1} \mathrm{Hz}^{-1}$	$\mathrm{ct\ s}^{-1}$	$P_{\mathrm{noise}} = 2$
$A_{\mathrm{rms^2}} = 1/\bar{x}^2$	$[\mathrm{rms/mean}]^2 \mathrm{Hz}^{-1}$	$[\mathrm{rms/mean}]^2$	$P_{\mathrm{noise}} = \frac{2(\bar{x}+B)}{\bar{x}^2} \frac{\Delta t}{\Delta t_{\mathrm{bin}}}$

known as the direct component (DC) and represents the non-variable part of the signal (i.e. the mean level). The Fourier transform $X(f_{j\leq 0})$ are generally neglected from variability studies. Additionally, the constant power from the DC component may leak into neighbouring frequencies. It is therefore standard practice to subtract the mean $\langle x_t \rangle$ from each segment M before computing the DFT.

The periodogram can then be calculated choosing an appropriate normalisation:

$$P(f) = A\frac{2\Delta t}{N}|X(f)|^2 = A\frac{2\Delta t}{N}X^*(f)X(f) \tag{2.10}$$

where $*$ denotes the complex conjugate and for brevity the subscript j has been dropped. The factor of 2 in Equation 2.10 makes the periodogram 'one-sided' meaning that the original signal power (variance) is recovered when integrating over only positive frequencies. The factor $(\Delta t/N)$ ensures that the amplitudes at each f_j are independent of the sampling length of the time series.

Three commonly used normalisations in astronomy ($A_{\mathrm{abs}} = \bar{x}_t A_{\mathrm{Leahy}} = \bar{x}_t^2 A_{\mathrm{rms^2}}$) are shown in Table 2.1, along with the periodogram ordinate units and the result of integrating the periodogram between f_a and f_b (i.e. the sum $S_{b-a} = \sum_a^b P(f)\Delta f$). The A_{abs} normalisation gives the periodogram in absolute units and the integrated periodogram gives the total variance in absolute units. Using the A_{Leahy} normalisation (Leahy et al., 1983), the integrated periodogram gives the total rms amplitude. The $A_{\mathrm{rms^2}}$ normalisation (van der Klis 1997; Miyamoto et al. 1991) is the most commonly used for AGN and XRB analysis due to the integrated periodogram giving the fractional variance of the data for a given range of frequencies.

The effect of Poisson noise is to add a continuous floor to the power spectrum, as the power spectrum of Poisson noise is constant at all frequencies (white noise).

2.3.1 Scatter and bias in the PSD estimate

The stochastic nature of accreting black hole light curves means that each periodogram, $P(f)$, measured from a single realisation of the noise process shows a large amount of

scatter around the true underlying PSD, $\mathcal{P}(f)$:

$$P(f) = \frac{1}{2}\mathcal{P}(f)\chi_2^2 \qquad (2.11)$$

where χ_2^2 is a random variable following a chi-square distribution with 2 degrees of freedom. The expectation value and variance of χ_ν^2 are ν and 2ν respectively, so the measured periodogram exhibits a large amount of scatter around the underlying PSD (e.g. van der Klis 1989; Uttley et al. 2002; Vaughan et al. 2003). This intrinsic scatter does not decrease by adding more points to the light curve as the standard deviation of the PSD is insensitive to the length of the observation.

Under the assumption of stationarity, averaging over M independent light curve segments or by binning over N adjacent frequencies produces a consistent estimate of the PSD with Gaussian errors for $n = M \times N \gtrsim 50$ (Vaughan et al. 2003). The error in the estimate of the true PSD is now:

$$\delta\mathcal{P}(f) = \frac{\langle P(f)\rangle}{\sqrt{n}} \qquad (2.12)$$

where $\langle \cdot \rangle$ indicates the overage over M periodograms. The frequency binning can be done e.g. geometrically or logarithmically.

Another method for reducing the scatter in red noise light curves is to bin the logarithm of the periodogram (Papadakis & Lawrence 1993; Stella et al. 1994). Here, the errors converge to a Gaussian distribution with fewer ($n \geq 20$) points in each frequency bin.

Each periodogram measurement is biased away from the true PSD due to the finite sampling window. A finite time series can be written in terms of an infinite, continuous function $l(t)$ and a window or sampling function $w(t)$ that is non-zero only over a finite range and encodes the time sampling of the observed light curve $o(t)$:

$$o(t) = l(t) \cdot w(t) \Longleftrightarrow O(f) = L(f) \cdot W(f) \qquad (2.13)$$

where as this is a multiplication in the time domain, it gives a convolution in the Fourier domain (by the convolution theorem). The periodogram (formed from $O(f)$) is distorted due to the convolution of the FT of the true light curve $L(f)$ with the spectral window function $W(f)$ (see e.g. van der Klis 1989; Vaughan et al. 2003). The two main effects of this distortion are *aliasing* and *leakage*.

If the light curve is not continuously and contiguously sampled then power from above the Nyquist frequency ($f_{N/2} = f_{Nyq}$) is reflected back (*aliased*) about f_{Nyq}. Fortunately, aliasing is negligible for continuous binned light curves, and in all but the steepest AGN PSDs, the Poisson noise level dominates at f_{Nyq}. See Uttley et al. (2002) for a discussion on correcting for aliasing when it presents a problem.
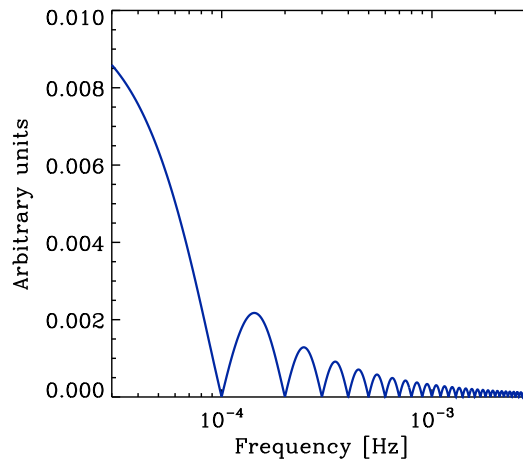
Figure 2.4: An example of the Fejer kernel illustrating the effect of convolution of the spectral window function $W(f)$ on the true light curve $L(f)$. A window function with width 10 ks was used, to represent a typical segment length.

Leakage or red-noise leak results from the finite duration of the sampling window, $w(t)$. Here, variability power is transferred (*leak*) from frequencies below the lowest sampled frequency through the lobes of the spectral window function (i.e. the *Fejer kernel*, an illustration of which is shown in Fig. 2.4). Lower frequency power (i.e. below the bandpass) is apparent as quasi-linear (i.e. very slow/smooth) trends; these cause leakage because they add variance to the observed frequency bandpass, which adds a constant component to the variance in $P(f)$, biasing the slope of the PSD towards $\alpha = 2$ (Vaughan et al. 2003).

2.4 The cross spectrum

The properties of two simultaneous and time series can also be compared in the Fourier domain using the cross-spectrum (Priestley 1981; Bendat & Piersol 2010). From two evenly sampled time series $x(t), y(t)$ we can compute the Fourier transforms $X(f) = |X(f)|e^{i\phi_x(f)}$ and $Y(f) = |Y(f)|e^{i\phi_y(f)}$, in terms of amplitude and phase. We can estimate the power spectrum for each time series using $|X(f)|^2$ and $|Y(f)|^2$, after subtracting the Poisson noise and applying some normalisation factor. The complex-valued cross-spectrum can be written

$$C_{xy}(f) = X^*(f)Y(f) = |X(f)||Y(f)|e^{i(\phi_y(f) - \phi_x(f))} \qquad (2.14)$$

following Vaughan & Nowak (1997) and Nowak et al. (1999) this is usually averaged over M non-overlapping segments, just as with the power spectrum.

2.4.1 Coherence

We can define the coherence or squared coherency as

$$\gamma^2_{xy}(f) = \frac{|\langle C_{xy}(f)\rangle|^2}{\langle |X(f)|^2\rangle\langle |Y(f)|^2\rangle} \tag{2.15}$$

The coherence is a measure of the linear correlation between two time series as a function of Fourier frequency (Vaughan & Nowak, 1997) and takes on values in the range [0,1], where 1 is perfect coherence. In the absence of observational (Poisson) noise the coherence can be estimated using M segments with a standard deviation of $\delta\gamma^2(f) = \sqrt{2/M}(1 - \gamma^2(f))/|\gamma(f)|$ (e.g Bendat & Piersol 2010).

The linearity property of the FT means that Equation 2.1 can be written for each energy band

$$X(f) = S_x(f) + N_x(f) \tag{2.16}$$
$$Y(f) = S_y(f) + N_y(f) \tag{2.17}$$

Allowing for the noise contribution to the measured signal, the cross-spectrum in Equation 2.14 can now be expressed as

$$|\langle C_{xy}\rangle|^2 = |\langle (S_x^* + N_x^*)(S_y + N_y)\rangle|^2 \tag{2.18}$$
$$= |\langle S_x^* \cdot S_y\rangle + \langle S_x^* \cdot N_y\rangle + \langle N_x^* \cdot S_y\rangle + \langle N_x^* \cdot N_y\rangle|^2 \tag{2.19}$$

where we have dropped the f subscript for brevity. The quantities $s_{xy} = \langle S_x^* \cdot S_y\rangle$ and $n_{xy} = \langle S_x^* \cdot N_y\rangle + \langle N_x^* \cdot S_y\rangle + \langle N_x^* \cdot N_y\rangle$ can be understood in terms of the intrinsic signal and the noise contribution of the measured cross-spectrum $\langle C_{xy}(f)\rangle$. As the signal in each band is uncorrelated with the noise component in either band, $\langle\Re(n_{xy}(f))\rangle = \langle\Im(n_{xy}(f))\rangle = 0$ for sufficiently large M (Vaughan & Nowak 1997).

For the case of high measured coherence, the quared amplitude of the cross-spectrum can be written as $|\langle C_{xy}(f)\rangle|^2 = |\langle S_x^*(f) \cdot S_y(f)\rangle|^2 + n^2_{xy}(f)$ (Vaughan & Nowak 1997). The Poisson noise corrected coherence then becomes:

$$\gamma^2_{cor,xy}(f) = \frac{|\langle C_{xy}(f)\rangle|^2 - n^2_{xy}(f)}{\langle P_x(f) - |N_x(f)|^2\rangle\langle P_y(f) - |N_y(f)|^2\rangle} \tag{2.20}$$

where $P_x = |X(f)|^2 = |S_x(f)|^2 + |N_x(f)|^2$ and $P_y = |Y(f)|^2 = |S_y(f)|^2 + |N_y(f)|^2$ are the noisey PSDs. The error on the Poisson-noise corrected coherence depends on the amplitude of $S_x(f)$ and $S_y(f)$ and the measured coherence, and are given in equations 8 and 9 of Vaughan & Nowak (1997).

There are several possible sources of bias on the coherence. The coherence is a squared quantity and so cannot take values below zero. A result of this is that the average of several coherence estimates tends to be biased upwards slightly, although this effect is only significant when the intrinsic coherence is low (and so the true coherence values are close to zero). This is given by $B[\gamma^2] = 1/M(1 - \gamma^2)^2$ where γ^2 is the coherence and M is the number of segments (Bendat & Piersol 1986, Sec. 9.2.3). When the coherence is low the bias dominates and acts to shift up the observed coherence value and must be subtracted from the computed value.

2.4.2 Time delays

From the complex-valued cross-spectrum estimate (Equation 2.14) we obtain a phase difference (or phase lag) between two signals $x(t), y(t)$:

$$\Delta\phi(f) = \arg\langle C_{xy}(f)\rangle = \arctan\frac{\Im(\langle C_{xy}(f))}{\Re(\langle C_{xy}(f))} \tag{2.21}$$

where $\Delta\phi(f)$ is limited to $[-\pi, +\pi]$ (or $[0, 2\pi]$ depending on convention) so cannot distinguish $\pi/2$ from $-3\pi/2$. $\Delta\phi(f)$ can be transformed into a corresponding time lag

$$\Delta\tau(f) = \frac{\Delta\phi(f)}{2\pi f} \tag{2.22}$$

This recovers the (time averaged) frequency dependent time lags between any correlated variations in $x(t)$ and $y(t)$. The standard deviation of phase lag estimates, when computed using M non-overlapping segments, are estimated following e.g. (Nowak et al. 1999; Bendat & Piersol 2010):

$$\delta\phi(f) = \frac{(1 - \gamma^2(f))^{1/2}}{\gamma\sqrt{2M}} \tag{2.23}$$

with the error on time lag at each frequency naturally given by

$$\delta\tau(f) = \frac{\delta\phi(f)}{2\pi f}. \tag{2.24}$$

Binning over N frequencies which are e.g. geometrically spaced and averaging over M segments gives $N \cdot M$ measurements. This improves the error $\delta\tau$ by a factor $1/\sqrt{NM}$.

2.5 Transfer functions

Two continuous time series $x(t)$ and $y(t)$ may be related via

$$y(t) = \int_{-\infty}^{+\infty} \psi(t-\tau)x(\tau)\mathrm{d}\tau = \psi(t) \otimes x(t) \tag{2.25}$$

where the function $\psi(t)$ relating the two signals is the 'response function'[5], i.e. the response to an instantaneous impulse. The response function can be thought of in terms of the filter causing any delay or smoothing between the input and output signals. In principle, this can provide valuable information about the spatial extent of the reprocessing medium which is acting as the filter between the two signal emitting regions.

Using the convolution theorem we can re-write this in the Fourier domain as

$$Y(\omega) = \Psi(\omega) \cdot X(\omega) \tag{2.26}$$

where $\omega = 2\pi f$ and

$$\Psi(\omega) = \int_{-\infty}^{+\infty} \psi(t)\mathrm{e}^{-\mathrm{i}\omega t}dt \tag{2.27}$$

is referred to as the 'transfer function' in the Fourier domain. If $\Psi(f)$ is linear and independent of the time series used to estimate it, then the two signals $X(f)$ and $Y(f)$ will have unity coherence (Equation 2.15). The phase difference between $X(f)$ and $Y(f)$ (Equation 2.21) is contained within $\Psi(f)$, therefore we can get the frequency dependent time delay from the Fourier transform of the response function

$$\tau(\omega) = \frac{1}{\omega} \arg \left(\int_{-\infty}^{+\infty} \psi(t)\mathrm{e}^{-\mathrm{i}\omega t}dt \right) \tag{2.28}$$

2.5.1 Top hat response function

One of the simplest forms of response function is the 'top hat', which has width a and is centred on $t = b$, such that

$$\psi(t) = TH(t; a, b) = \begin{cases} 1/a & \text{if } b - a/2 \leq t \leq b + a/2 \\ 0 & \text{elsewhere} \end{cases} \tag{2.29}$$

which is normalised to unity. Substituting this into egn. 2.27 we can find the Fourier transform of this function

$$\Psi(w) = \mathrm{e}^{-\mathrm{i}\omega b}\mathrm{sinc}\left(\frac{a\omega}{2}\right) \tag{2.30}$$

---

[5]we note that in signal processing parlance: 'impulse response function' is used for time domain, and 'transfer function' for Fourier domain
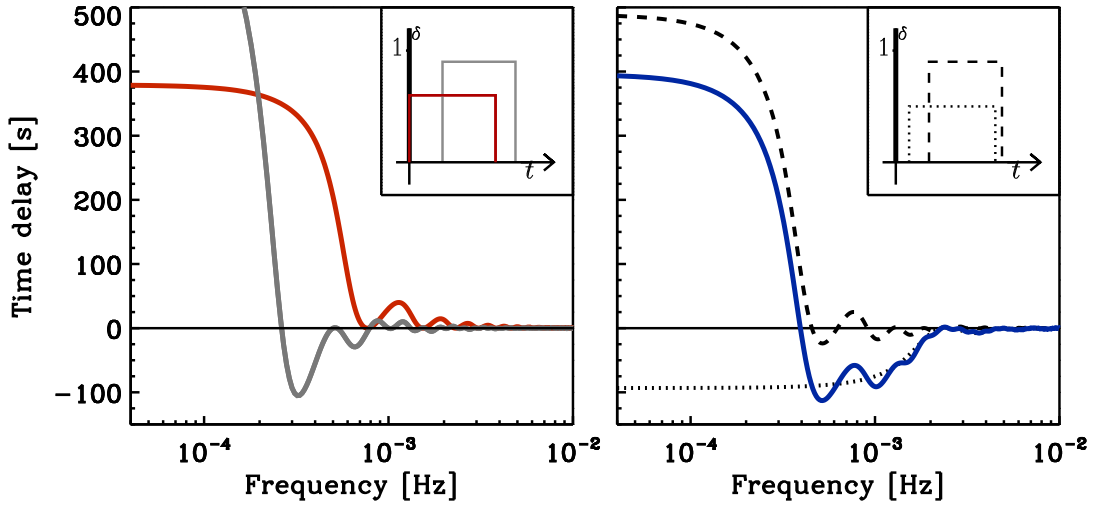
Figure 2.5: Examples of transfer functions in the lag-frequency plot. (a) A single top hat plus delta function response function between the two time series, with the top hat starting at $t_0 = 0$ (red) and $t_0 > 0$ (grey). (b) A top hat plus delta function response function is present in each time series, with the overall transfer function (blue) resulting from the difference between the transfer function in each time series (see Section 2.5.1 for details). The insets show the time domain representation of the response functions.

To get the time delay we compute the argument of $\Psi(w)$

$$\tau(\omega) = \frac{1}{\omega} \arg\left[e^{-i\omega b} \mathrm{sinc}\left(\frac{a\omega}{2}\right) \right] = \frac{1}{\omega} \arg\left[e^{-i\omega b} \right] = \frac{1}{\omega}(-\omega b) = -b \qquad (2.31)$$

The sinc function is real so is dropped from the argument. This now produces a constant time delay $-b$ at all frequencies.

Since the Fourier transform is linear, we can compute the phase shift produced by a response function that is a combination of a δ-function and a top hat. The combined response has the form

$$\psi(t) = f \times TH(t; a, b) + \delta(t - c) \qquad (2.32)$$

where f is a simple scaling factor that sets the fraction of the TH in the combined response. Taking a zero-centred δ-function (i.e. $c = 0$) the Fourier transform of the combined response is now

$$\Psi(w) = 1 + f e^{-i\omega b} \mathrm{sinc}\left(\frac{a\omega}{2}\right) \qquad (2.33)$$

Following Equation 2.24 we can find the argument of the transfer function, yeilding the time lag as a function of frequency (or lag-frequency spectrum):

$$\tau(w) = \frac{1}{\omega} \arctan\left(\frac{-f \sin(b\omega)\mathrm{sinc}(a\omega/2)}{1 + f \cos(b\omega)\mathrm{sinc}(a\omega/2)} \right) \qquad (2.34)$$

The left side of Fig. 2.5 show the lag-frequency spectrum of the top hat plus delta response model for a variety of parameter values. When the top hat start time $t_0 = 0$ (i.e. $a = 2b$) no negative delay is observed and the first oscillation with zero delay occurs at $\sim 1/\tau(\mathrm{max})$. In contrast, when $t_0 > 0$ (i.e. $a < 2b$) the time delay now goes negative at certain frequencies, with the first oscillation again corresponding to $\sim 1/\tau(\mathrm{max})$. This is the 'ringing' effect, related to the Gibbs phenomenon, which arises due to the separation of the delta function and t_0 changing the frequency at which the phase wrapping occurs. The negative time delay oscillation covers a very narrow range of frequencies, with width $\sim 1/\tau(\mathrm{max})$.

The measured time series in a given energy band is related to some underlying 'source' variability, $z(t)$, via

$$x(t) = \psi_x \otimes z(t) \Longleftrightarrow X(f) = \Psi_x(f) \cdot Z(f)$$
$$y(t) = \psi_y \otimes z(t) \Longleftrightarrow Y(f) = \Psi_y(f) \cdot Z(f) \tag{2.35}$$

where it is assumed that $z(t)$ is some unseen variations occurring before both $x(t)$ and $y(t)$. Each measured time series now has a response function relative to $z(t)$, which itself is not observed. The phases obtained from the cross-spectrum $C_{xy}(f)$ of the observed time series, which give the time lag-frequency spectrum, are (on average) the differences between the phases of the Fourier transforms of each response, i.e. $\phi(f) = \arg \Psi_y(f) - \arg \Psi_x(f)$. This is illustrated in Fig. 2.5(b), where the overall transfer function results from the difference between the transfer function in each time series. Here, the negative time delay is much broader in frequency than in the single transfer function case, due to a genuine response function component present in each time series.

2.6 Covariance spectrum

The covariance spectrum (Wilkinson & Uttley 2009) acts as a 'matched filter', picking out the correlated variability between a comparison energy band $x(t)$ and broad reference band $y(t)$. This method is similar to the rms spectrum, except the any uncorrelated white noise is removed, providing a less noisy estimate of the variability spectrum, particularly at higher energies. Wilkinson & Uttley 2009 presented a definition of the zero-time lag covariance spectrum in the time-domain. The covariance between $x(t)$ and $y(t)$ can be computed in the frequency domain for a given frequency range Δf_j. Cassatella et al. (2012) give a Fourier domain definition, but their equations contain several typographical mistakes. The corrected version (Phil Uttley, prov comm. July 2013) can be written in

terms of the coherence as

$$cov(\Delta f_j) = \sqrt{\gamma_{xy}^2(f)\langle|X(f)|^2\rangle\Delta f_j} \tag{2.36}$$

which has an error

$$\delta cov(\Delta f_j) = \sqrt{\frac{n_{xy}^2\Delta f_j}{2\langle|Y(f)|^2\rangle}}. \tag{2.37}$$

2.7 Simulating time series data

Simulating time series with the statistical properties of observed time series allows us to perform parametric tests of the spectral estimates.

The method of simulating time series depends on the desired PSD properties, which are typically approximated with a $\sim 1/f^\beta$ spectrum. A time series with constant power at each frequency (white noise; $\beta = 0$) can be simulated by randomly sampling numbers from a Gaussian distribution. Red noise ($\beta = 2$) can be simulated using a random walk, where each time series point is drawn from a Gaussian distribution and added to some fraction of the previous time series value.

For a more complicated PSD shape (e.g. a bending power-law) the algorithm of Timmer & König (1995) is commonly used. For a desired power spectral shape we sample random complex phase and amplitudes from a Normal distribution. These are then inverse Fourier transformed back into the time domain to produce a simulated time series with the properties of the defined power spectrum.

The effects of leakage can be accounted for using Monte Carlo simulations of light curves with duration much longer (e.g. $50\times$) than the observed light curve (e.g. Uttley et al. 2002). Observational noise can be added to each simulated light curve by drawing a Poisson random deviate with mean equal to the mean count per bin in the real light curves. To produce the log-normal distribution of fluxes (as observed in the rms-flux relation) we compute the exponential function (i.e. $y = e^x$) at each point (Uttley et al. 2005; Vaughan & Uttley 2008).

2.8 Markov Chain Monte Carlo

Markov Chain Monte Carlo (MCMC) is a class of algorithms used for calculating the integrals required in determining the probability density of the model parameters (e.g. Metropolis et al. 1953; Hastings 1970; Gelman & Rubin 1992, see Brooks 1998 for a review).

A Markov Chain is a random, memoryless process, meaning the next state only depends on the current state, and not the sequence of states that preceded it. The sequence of states converges to an equilibrium distribution of samples in parameter space, which is proportional to the target probability distribution. The state of each chain is taken as a sample of the desired probability distribution.

In Chap. 5 we shall use the Metropolis-Hastings algorithm, one of the simplest implementations of MCMC. For a large chain (number of iterations) this provides the target probability distribution $P(X|D, M, I)$, where D is the data, M is the model, X is the set of model parameters, and I is the prior. The prior allows us to set some constraint on the parameter search, given some a priori knowledge. At each state in the chain, a sample is drawn from a Gaussian proposal distribution.

Chains of e.g. $N = 20,000$ iterations are ran, with a large fraction (e.g. 20%) of the beginning portion of the chain being discarded, known as the 'burn-in period'. This removes the effect of the initial position when starting the chain. Convergence is tested for using the Gelman-Rubin statistic (Gelman & Rubin 1992) on parallel sets of chains, to see if they are converging to the same distribution. The parameter should be close to 1 for convergence.

The post burn-in samples for each parameter can then be histogrammed, which should approximate the true distribution for each parameter. From the histograms we can then determine the best model values and confidence intervals on each parameter.

3

Correlated UV/X-ray emission in NGC 4051

In this chapter I explore the relation between the UV and X-ray emission in the low-mass Narrow line Seyfert 1 (NLS1) galaxy NGC 4051. Using simultaneous UV and X-ray observations, the causal connection between the two emission components can be investigated (see Section 1.4.3).

NGC 4051 is a nearby ($z = 0.0023$) NLS1 galaxy with black hole mass, $M_{BH} \approx 1.7\pm 0.5 \times 10^6 M_\odot$ (Denney et al., 2009), at a Tully-Fisher distance, $D \approx 15.2$ Mpc (Russell, 2002), and has been the subject of several such studies. Done et al. (1990) obtained ~ 3 days of contemporaneous X-ray, UV, optical and IR data, but found little variability at longer wavelengths despite strong, rapid X-ray variations. Using light curves spanning ~ 1000 days in the optical and X-rays, Peterson et al. (2000) revealed significant optical variability on longer timescales that appeared to be correlated with the (longer timescale) X-ray variations. Shemmer et al. (2003) and Breedt et al. (2010) also found a significant X-ray/optical correlation, the latter using ~ 5000 days of monitoring data. On shorter timescales Mason et al. (2002) and Smith & Vaughan (2007) used ~ 2 day *XMM-Newton* observations to search for X-ray/UV correlations, with inconclusive results.

The rest of this chapter is organised as follows. Section 3.1 discusses the observations of NGC 4051 and extraction of the X-ray and UV light curves. Section 3.2 gives an analysis of the variability amplitudes and UV power spectral density, cross-correlations are discussed in Section 3.3, and the implications of these results are discussed in Section 3.4.

3.1 Observations and Data Reduction

3.1.1 Observations

NGC 4051 was observed by *XMM-Newton* in 15 separate observations over a period of 45 days during May-June 2009. Each observation lasted ~ 40 ks giving a total of ~ 580 ks of usable data. Individual observation details are listed in Table 3.1. With roughly the same start and end time as the OM, this gives a total of ~ 530 ks of simultaneous UV and X-ray data.

All of the OM observations were taken in *Imaging Mode* in the UVW1 filter (central wavelength 2910 Å) with 2×2 pixel binning. This gives a field-of-view of 8×8 arcmin and a spatial resolution of 0.95 arcsec/pixel. The exposure length varied between 1000–1400 sec from observation to observation, giving ~ 30 exposures per observation and a total of 406 across all 15 observations.

To compliment the *XMM-Newton* data set, 51 *Swift* ToO observations were made covering the same epoch. The observations are separated by ~ 1 day and typically ~ 1.5 ks long, with 1–3 UVOT exposures per observation, giving a total of 71 frames. The UVOT exposures were taken in the *uvw*1 filter, which has approximately the same bandpass as the OM UVW1, with a field-of-view of 17×17 arcmin and pixel scale of 0.5 arcsec. The XRT has a 23×23 arcmin field-of-view with a pixel scale of 0.236 arcsec and covers the energy range 0.2–10.0 keV, similar to EPIC-pn.

3.1.2 OM light curves

The Observation Data Files (ODFs) for our target were extracted from the XMM-Newton Science Archive (XSA) and processed using *XMM-Newton* Science Analysis System (SAS v11.0.0) routine OMICHAIN. Custom made IDL[6] scripts were made to perform source photometry and apply instrumental corrections (see Section 2.1.1.1). Source counts were extracted in a 6 arcsec radius aperture for the galaxy nucleus and 3 field stars present in the images (see Fig. 3.1). Background counts were extracted in a 30 arc second radius aperture, placed in a region away from the host galaxy and field stars. The concatenated background subtracted light curves for the *XMM* OM sources and background region are shown in Fig. 3.2.

In the UVW1 filter there will be a significant contribution to the observed nuclear light from the host galaxy. This should be constant (to within the random and systematic

---

[6]http://www.exelisvis.com

Table 3.1: *XMM-Nexton* observation summary. The columns list (1) the spacecraft revolution number, (2) the start date of the observation, (3) the EPIC-pn observation duration, (4) the OM observation duration, (5) the number of OM images in each observation.

XMM rev. no.	Observation Date [Y-M-D]	EPIC-pn On time [s]	OM On time [s]	No. OM images
1721	2009-05-03	45717	45105	33
1722	2009-05-05	45645	45103	33
1724	2009-05-09	45548	45003	33
1725	2009-05-11	45447	44903	33
1727	2009-05-15	32644	31340	21
1728	2009-05-17	42433	37367	26
1729	2009-05-19	41813	41267	26
1730	2009-05-21	41936	40894	26
1733	2009-05-27	44919	39168	22
1734	2009-05-29	43726	43182	27
1736	2009-06-02	44946	44164	22
1737	2009-06-04	39756	34574	23
1739	2009-06-08	43545	43000	27
1740	2009-06-10	44453	43909	28
1743	2009-06-16	42717	42116	26

errors of the aperture photometry) and so we have not tried to remove it, but as such it should not affect the PSD or correlation analysis in any important way.

As a test of the background subtraction and photometry procedure we tested for (zero lag) correlations between the background subtracted light curves of the sources and a second background region for all 15 observations. For ~ 400 data points a Pearson linear correlation coefficient $r \geq 0.13$ indicates a weak but statistically significant correlation ($p < 0.01$). We find no significant correlation between each of the background subtracted sources, but in the source vs background tests, values of r up to 0.3 are observed. The strength of this correlation is also observed to change between 0.0 and 0.3 when using a different background region. The mean correlation coefficient between source vs source and source vs background for individual observations is very low ($-0.1 \lesssim r \lesssim 0.1$). This indicates that the correlation is caused by changes in the background over the course of the 15 observations. We are cautious of this fact during the rest of the analysis and use source light curves subtracted using various background regions. We find that the choice of background region has no effect on any subsequent analysis.

3.1.3 EPIC-pn light curves and spectra

The EPIC-pn light curves used in this analysis are the same as those used in Vaughan et al. 2011. The raw EPIC-pn data were processed from the ODFs using the SAS (v11.0.0).
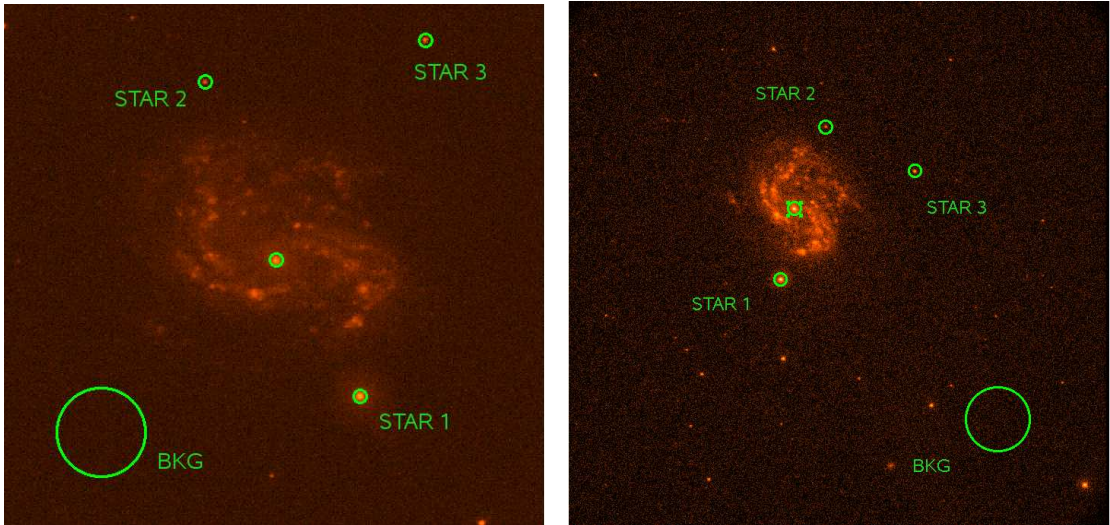
Figure 3.1: Left: *XMM-Newton* OM UVW1 image of NGC 4051. The apertures used for photometry for the central source, field stars and background region are shown in green. Right: *Swift* UVOT *uvw*1 image of NGC 4051. The apertures used for photometry for the central source, field stars and background region are shown in green.

Events lists were filtered using PATTERN 0–4, FLAG = 0 and were visually inspected for background flaring. Light curves were extracted from the filtered events files using a source aperture of radius 35 arcsec and a non-overlapping larger background region on the same chip. Light curves were extracted with bin size of $\Delta t = 5$ s and an energy range of 0.2–10.0 keV. The background subtracted EPIC-pn light curves are shown in the bottom panel of Fig. 3.4. Spectra were extracted and binned to a minimum of 25 counts per bin. Response files were created using RMFGEN v1.55.2 and AFRGEN v.1.77.4.

3.1.4 UVOT and XRT light curves

Visual inspection of the 71 UVOT exposures revealed considerable target movement in 40, leaving 31 usable frames. The exposure time varied slightly across the observations but is typically ~ 500 s. The HEAsoft (v6.10) tasks UVOTSOURCE was used to extract source counts from the galaxy nucleus and the same field stars used in the OM photometry. The optimum extraction radius is 12.5 pixels (~ 6 arc seconds) for the *uvw*1 filter (Poole et al., 2008). A 60 pixel radius background aperture fixed in sky co-ordinates in a blank region of the sky was also extracted. Similar to the OM, instrumental corrections — PSF1, CL, DT, PSF2 and TDS — must be applied to the counts extracted in each aperture on the UVOT images. UVOTSOURCE automatically performs background subtraction and applies these corrections based on the most up-to-date instrument calibration database (CALDB 4.1.2). The background subtracted UVOT light curves are shown in the lower panel of Fig. 3.4. We extract XRT counts in the 0.2–10 keV range using
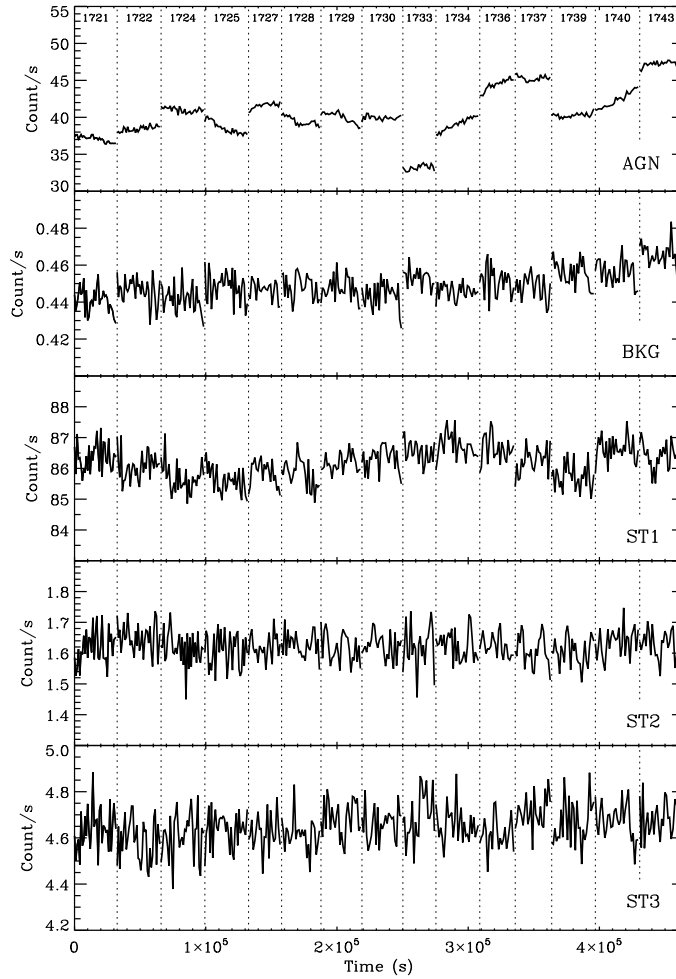
Figure 3.2: Concatenated light curves for the *XMM* OM sources. From top to bottom panel they are central nucleus, background region and field stars 1, 2 and 3 respectively.

the online XRT Products Builder (Evans et al., 2009). This performs all the necessary processing and provides background subtracted light curves.

3.2 Data Analysis

3.2.1 Quantifying variability

The values of the variability estimators (see Section 2.2) for the OM and UVOT sources are listed in Table 3.2. The variability statistics calculated over the whole ~ 45 day *XMM-Newton* observation show there is significant variability in NGC 4051, with $F_{\mathrm{var}} \approx 8\%$. On timescales within each observation, the variability is weaker than on long timescales.

In 11 of the *XMM-Newton* observations the excess variance in the nucleus and star 1 values are almost identical. This indicates that there is a "floor" in the excess variance, that isn't accounted for by the errors. We refer to this as a systematic error but are
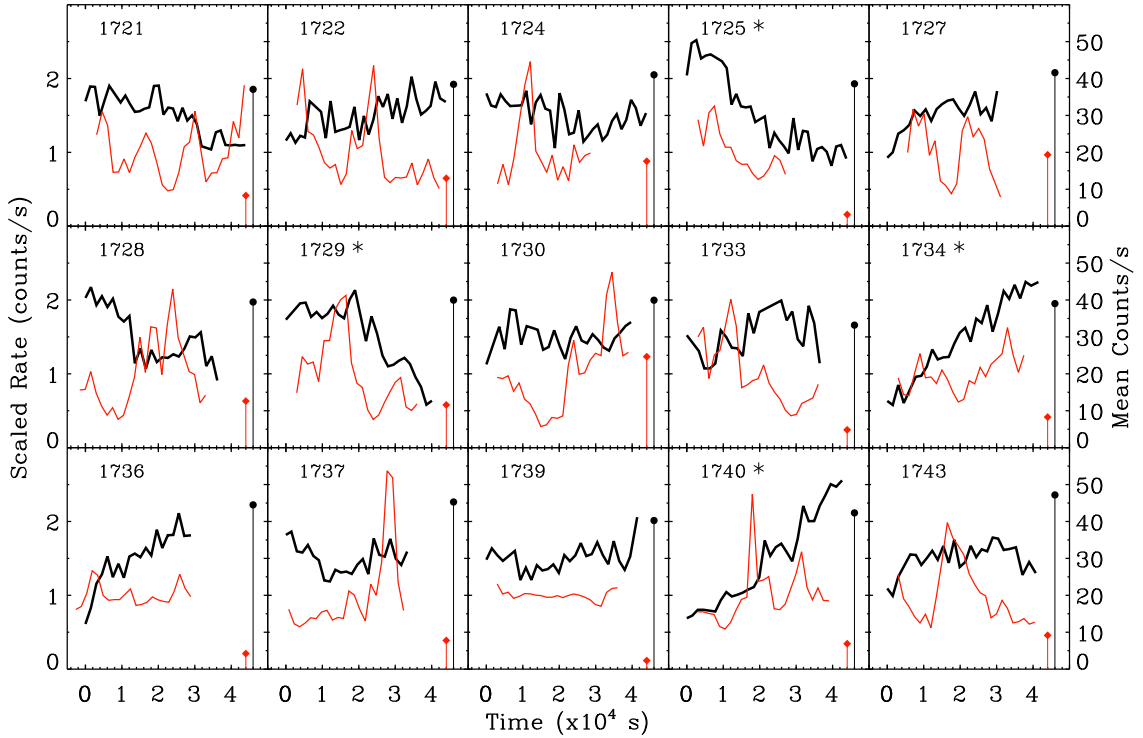
Figure 3.3: Within-observation X-ray and UV variability from the 15 *XMM-Newton* observations. To better represent the light curves the OM (thick black) has been scaled to some arbitrary value and shifted to a mean of 1.5 ct/s. The EPIC-pn (thin red) has been normalised to a mean rate of 1 ct/s. The circle and diamond markers represent the mean observation count rate, given by the right ordinate, for the OM and EPIC-pn respectively. The four "good" OM observations are indicated by the asteriks next to the revolution number.

unable to account for it. In the 11 observations this systematic error is too large to detect any intrinsic variability from the nucleus. The variability estimators in Table 3.2 show the nucleus in the remaining 4 "good" observations clearly posses significant variability compared to the field stars, and as such will be treated separately form the the "poor" 11 observations in the correlation analysis in Section 3.3. The "good" UV observations are revolutions 1725; 1729; 1734; and 1740, and are indicated by an asterisk in Fig. 3.3.

3.2.2 The UV Power Spectrum

The UV power spectrum was estimated from the 15 individual OM observations using standard methods (e.g van der Klis 1989). A 30 ks segment (equal to the shortest observation length) was taken from each observation. Within each *XMM-Newton* observation the individual OM exposures are approximately evenly sampled in time, although the exposure times do differ between observations (from 1200 to 1500 s). The basic periodogram requires evenly sampled data, and so we interpolated all OM data onto a grid
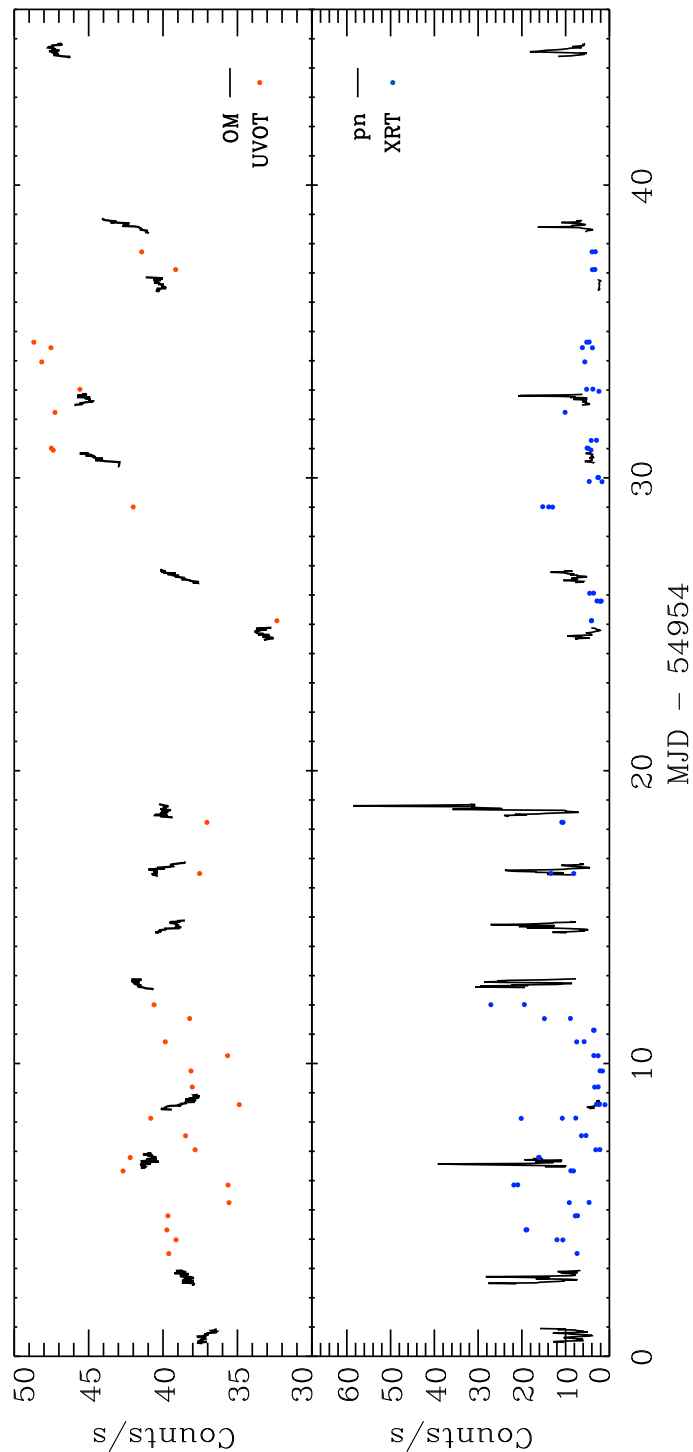
Figure 3.4: Between-observation variability for UV (top) and X-ray (bottom) from *XMM* and *Swift*. In the top panel the black lines are the OM data and the red circles are the UVOT. In the bottom panel the black lines are the EPIC-pn data and the blue dots the XRT. In both panels the *Swift* count rates have been scaled up to account for different effective areas (see Section 3.3.2 for details).

evenly sampled at $\Delta t = 1500\,\mathrm{s}$ – the smoothness of the OM light curves means that linear interpolation should not affect the shape of the time series in any significant manner.

Table 3.2: Quantifying source UV variability. The columns give the following information: (1) source name, (2) mean count rate, (3) sample standard deviation, (4) excess variance, (5) fractional, excess rms amplitude (F_{var}). The upper table shows the values obtained by combining all 15 *XMM-Newton* OM observations. The second and third tables show the values obtained by averaging the results from each of the 4 "good" and 11 "poor" *XMM-Newton* OM observations respectively. The lower table shows the results from the *Swift* UVOT observations.

Object	Mean rate	σ	σ_{XS}^2	F_{var}
	ct/s	ct/s	$[\mathrm{ct/s}]^2$	percent
XMM-Newton total				
Nucleus	40.5	3.19	10.1	7.9
Star 1	86.2	0.55	0.24	0.6
Star 2	1.6	0.05	0.0005	1.5
Star 3	4.6	0.09	0.003	1.2
Background	0.4	0.14	0.015	2.6
XMM-Newton "good" 4 observation averages				
Nucleus	40.0	0.84	0.69	2.1
Star 1	86.3	0.37	0.09	0.3
Star 2	1.6	0.05	0.0005	0.2
Star 3	4.7	0.08	0.001	0.6
Background	0.4	0.006	0.005	1.0
XMM-Newton "poor" 11 observation averages				
Nucleus	40.7	0.40	0.14	0.9
Star 1	86.2	0.42	0.13	0.4
Star 2	1.6	0.05	0.0004	0.1
Star 3	4.6	0.08	0.003	0.9
Background	0.4	0.007	0.007	1.8
Swift total				
Nucleus	40.1	4.39	19.2	10.8
Star 1	48.5	1.06	1.01	0.02
Star 2	1.1	0.04	-0.001	0.02
Star 3	3.1	0.09	0.002	0.01

Fig. 3.5 shows the power spectrum for the NGC 4051 nucleus, star 1, star 3 and the background for the 15 *XMM-Newton* OM observations. Periodograms were computed with absolute normalisation and the Poisson noise level is estimated using the formula in Vaughan et al. (2003); Appendix A. The background power spectrum is computed for the light curve from the background region (the same background region used in the source background subtraction) subtracted by a second background region on the opposite side of the CCD. In all sources, some power above the noise level is present. This is most likely the result of the background subtraction issues described in Section 3.1.2. Star 1 shows a similar red-noise slope, albeit with less power, to the nucleus. A cross-correlation test (see Section 3.3) between the nucleus and star 1 revealed no significant correlation between the two sources. This indicates that the variations in star 1 are either intrinsic to
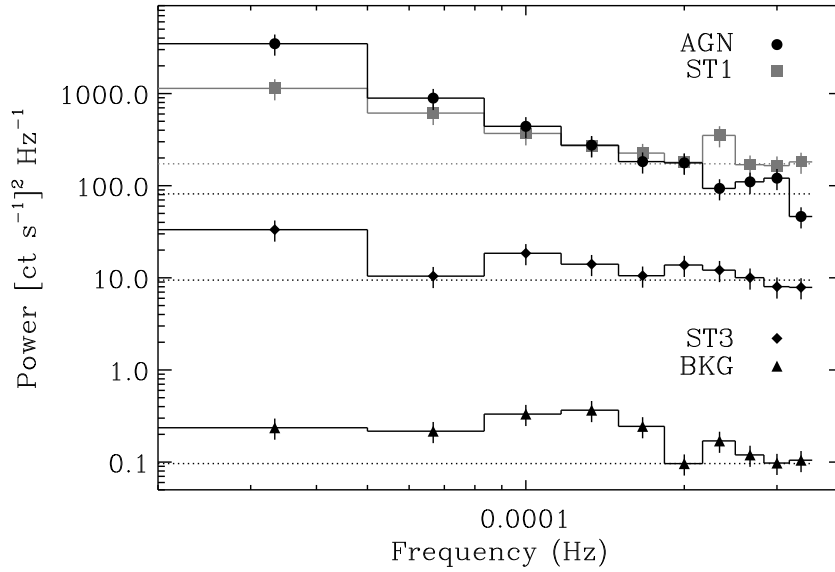
Figure 3.5: UV power spectrum in absolute units for the background subtracted OM sources, produced from the 15 *XMM* observations. The circles, squares, diamonds represent NGC 4051, star 1 and star 3 respectively. The triangles are the power spectrum estimate for the background light curves subtracted by a background region on the opposite side of the CCD, see text for details. The dotted lines are the Poisson noise estimates for each source.

the star or caused by the problems in the background subtraction.

Fig. 3.6 shows the resulting NGC 4051 power spectrum from the "good" and "poor" OM data, and a two component model is fit to the "good" data. Periodograms were computed with fractional rms normalisation (see Section 2.2). We did not subtract the expected contribution from Poisson noise but instead included this in the model fitting. The simple model comprises a power law plus constant to account for the Poisson fluctuations in the count rate: $P(\nu) = A\nu^{-\alpha} + P_N$ (where ν is the temporal frequency, A is a normalisation term, α is the power law index and P_N is the power density due to Poisson noise). This was fitted to the data using XSPEC v12.6.0 (Arnaud, 1996). The P_N level was allowed to vary freely. Using a χ^2 statistic the best fit to the data is found to have $\alpha = 2.62 \pm 0.48$ and $P_N = 0.059 \pm 0.023$, with $\chi^2 = 3.7$ for 7 degrees of freedom (*dof*). The Poisson noise level can also be estimated from the formula given in Vaughan et al. (2003) which we compute to be $P_N = 0.05$, in agreement with the value derived from the PSD. As expected, fitting the model assuming a fixed $P_N = 0.05$ value gave consistent results for the index parameter ($\alpha = 2.50 \pm 0.35$), with $\chi^2 = 3.9$ for 8 *dof*. Errors on the model parameters correspond to a 90 per cent confidence level for each interesting parameter (i.e. a $\Delta\chi^2 = 2.7$ criterion). For comparison, the X-ray PSD from Vaughan et al. (2011) is plotted in Fig. 3.6.
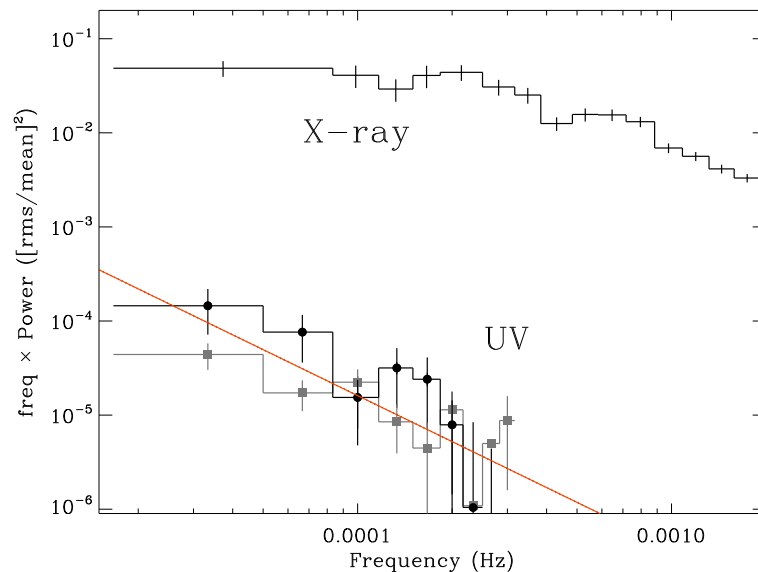
Figure 3.6: UV power spectrum produced from the *XMM* OM observations. The black circles are the average of the 4 "good" periodograms and the grey squares are the average of the 11 "poor" periodograms, prior to subtraction of Poisson noise. The red solid line is the power law fit to the "good" data. The upper solid black line is the Poisson noise subtracted X-ray ($0.2 - 10$ keV) power spectrum from Vaughan et al. 2011.

3.3   Correlation Analysis

In this section we discuss tests for X-ray/UV correlations on short timescales within each observation (*within -observations*) and longer timescale (*between-observations*). Treated individually, each of the 15 *XMM* observations allowed us to probe time scales of $\sim 2-40$ ks. Combining the *XMM* and *Swift* light curves allowed us to look for any long term trends in correlation between the two bands over the ~ 45 days.

3.3.1   Within-observation correlations

Standard time series analysis methods (c.f Box & Jenkins 1976; Priestley 1981) require the two light curves to be simultaneous and evenly sampled. This requirement is complicated by the the OM and EPIC-pn not always starting and ending at the same time, the irregular sampling of the OM, the read out time of the OM CCD, and any bad OM exposures. Where the two light curves are simultaneous we linearly interpolate the OM onto an uniformly-sampled regular grid. Given that the OM light curves vary smoothly within each observation, linear interpolation should not have a significant effect on the intrinsic variability. The EPIC-pn X-ray counts are re-binned to be contiguous and simultaneous with the OM bins by taking the average count rate within the new bin width. We chose a bin width of 1500 s to be consistent with the mean sampling rate of the OM

(1502 s) across the 15 *XMM* observations. The simultaneous light curve lengths range from 28.5-43.5 ks.

3.3.1.1   The Correlation Function

We estimated the cross-correlation function CCF for each *XMM-Newton* observation individually using the IDL function C_CORRELATE, shown in panel *a* of Fig. 3.7, where a positive lag in the plot indicates the UV variations are lagging those of the X-rays. A large spread in the CCF value for any computed time lag is seen. Panel *b* of Fig. 3.7 shows the average CCF for all 15 *XMM* observations. The strongest feature is the peak in the CCF around ~ 4.5 ks, although with a correlation of ~ 0.1, which falls within the confidence intervals. Confidence intervals on the average CCF are estimated using Monte Carlo simulations, where the 95% and 99% confidence intervals are shown in Fig. 3.7. These show the expected range of CCF values under the assumption that the X-ray and UV processes are independent, i.e. in the absence of a real correlation. The full details of these simulations is given in Section 2.7. The error on the average CCF is given by the standard error for N observations at each time-lag t.

Panel *c* in Fig. 3.7 shows the average CCF plot for the 4 "good" observations (see Section 3.2). A distinct broad peak can be seen around ~ 3 ks with a correlation of ~ 0.5, which lies outside the 99% confidence interval. Confidence intervals are calculated the same as above except 4 simulated light curves are averaged over in each CCF estimate. The small error bars on the averaged "good" CCF shows there is little scatter in the individual CCF measurements.

A correlation between optical light curves and X-ray photon index has been detected in some sources (e.g. Nandra et al. 2000), despite there being a weak correlation between the optical and X-ray light curves. We therefore cross-correlated the UV light curves with the 0.7–2/2–10 keV hardness ratio (a proxy for photon index) but find a CCF shape similar to that between the UV and X-ray light curves. This is most likely due to the X-ray spectral shape changes being strongly correlated with the overall X-ray flux.

3.3.1.2   The Cross-Spectrum

The cross-spectrum contains the same information as the CCF but represents the time-lags and strength of correlation in terms of phase difference and coherence as a function of temporal (Fourier) frequency. The phase lag $\Delta\phi$ can be expressed as a time-lag at a given frequency ν: $\tau = \Delta\phi/2\pi\nu$. Under quite general conditions the phase delay estimates are approximately independent at each frequency; by contrast, adjacent values of the CCF tend to be correlated due to the autocorrelation of the individual time series. Here we have estimated the cross spectrum using the "good" OM data, except
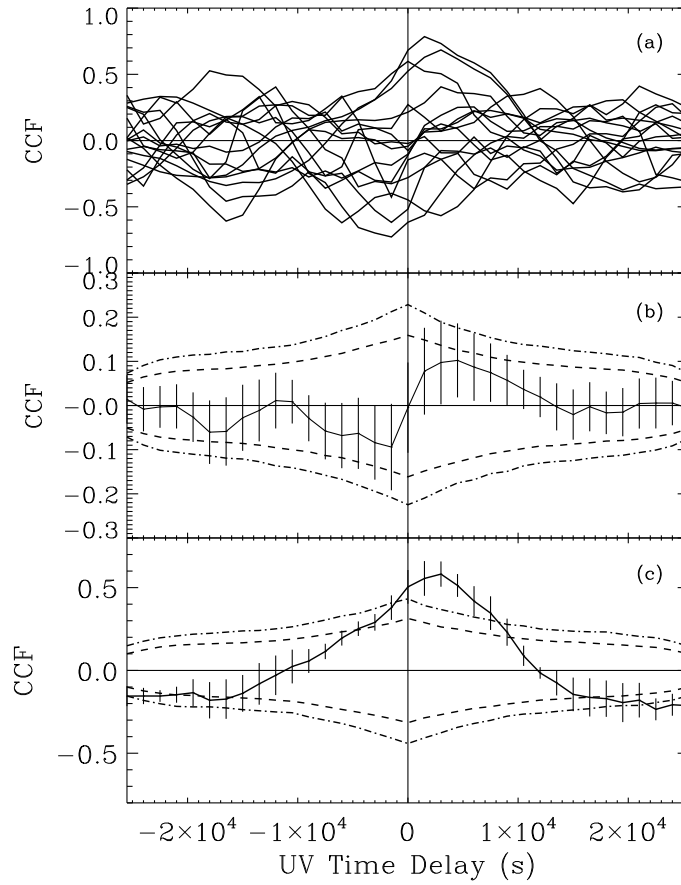
Figure 3.7: The Cross-correlation function (CCF) for the 15 *XMM* observations. The top panel is the individual CCF for each observation, the middle panel is the average CCF of all 15 observations, whilst the bottom panel is the average CCF for the 4 "good" observations. The dashed and dot-dashed lines are the 95% and 99% confidence intervals respectively, calculated individually for each data subset. Confidence intervals were estimated using Monte Carlo simulations of light curves assuming no correlation (see Section 2.7)

that the segments have been trimmed to equal length (28.5 ks), corresponding to the shortest simultaneous light curve. The resulting coherence and phase parts of the cross-spectrum are shown in Fig. 3.8. Errors were estimated using standard formulae (Vaughan & Nowak, 1997), and confidence intervals were estimated using simulated light curves (see Section 2.7 for details).

The coherence between the two bands is found to be low (≤ 0.2) at all frequencies. The average time-lag of the lowest 5 frequency bins is ~ 3 ks, consistent with what is seen in the CCF. A low coherence means that the errors on the time delay estimates are most likely underestimated using standard formulae, which can increase the apparent significance of lags when the errors are estimated using the standard formula and the intrinsic coherence is very low (e.g. Bendat & Piersol 2010). The cross spectrum is also computed for the combined 15 *XMM* observations which gives a coherence consistent with zero for
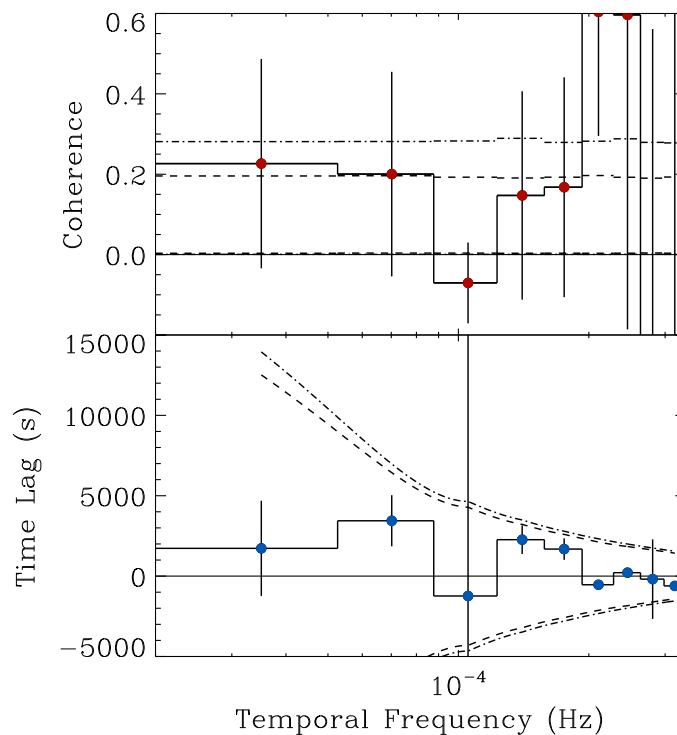
Figure 3.8: The Coherence and Phase-lag parts of the Cross-spectrum for the combined 4 "good" *XMM* observations. The dashed and dot-dashed lines are the 95% and 99% confidence intervals respectively. Confidence intervals were estimated using Monte Carlo simulations of light curves assuming no correlation (see Section 2.7).

each frequency bin, and the average time-lag in the lowest 5 bins is consistent with that found with the 4 "good" observations.

3.3.1.3 Pre-processing the light curves

The OM light curves tend to be dominated by slow, quasi-linear trends, and these can affect the CCF estimation (Welsh 1999). We have repeated the CCF and cross-spectrum analysis after 'end-matching' the OM light curves (i.e. removing a linear trend such that the first and last points are level - see Fougere 1985). This 'end-matching' removes, to a large extent, linear trends from the data, and alleviates the problem caused by circularity of the Fourier transform when estimating the cross spectrum.

We end-matched the *XMM* OM light curves individually and computed the CCF and cross-spectrum using the same X-ray light curves as before. The CCF for both the "good" and *all* the data remains mostly unchanged. In the cross-spectrum the phase-lag follows the same distribution and the coherence remains low in both cases. As this reanalysis did not substantially alter the results we do not show the CCF and cross-spectrum plots here.

3.3.2   Between-observation correlations

Given the extended period and sampling of the *XMM* and *Swift* observations, we are able to search for possible correlations and time lags on longer time scales. The *XMM-Newton* data (EPIC-pn and OM) and *Swift* data (XRT and UVOT) were first treated separately, then combined to produce one X-ray and one UV light curve. In either case the time sampling between observations is highly uneven, and so the Discrete Correlation Function (DCF; Edelson & Krolik 1988) was used to estimate the CCF. We use all the *XMM-Newton* OM data in this part of the analysis, as the variations within each OM observation will have little affect on the DCF.

For the *XMM* dataset, the midpoint of each original OM exposure was used. The EPIC-pn data were binned to be contiguous from the start of each revolution, with a bin size of 1500 s to be consistent with the mean OM sampling rate. A 10 ks DCF bin width is adopted to be consistent with the mean OM sampling rate over the extended observation. Although the OM exposure length varied between 1200–1500 s from revolution to revolution, we treat the source count rate in each exposure as a representative of the average count rate. As the source varies smoothly in the UVW1 filter we do not expect this to have any effect on the shape of the DCF. We test this by computing the DCF using the OM data that was binned onto a 1500 s even grid, and find no change in the shape of the DCF. The DCF for the *XMM* dataset for the range $-40 < \mathrm{lag} < +40$ days is shown in Fig. 3.9, where a positive lag means the UV are lagging the X-rays. Some peaks can be seen in the DCF but all lie within the confidence intervals. The peaks are most likely the result of the DCF binning used, combined with the underlying shape of the uncorrelated red-noise light curves.

For the *Swift* dataset, the UVOT exposures from each snapshot were used to represent the mean source count rate in the middle of each exposure bin. Again the exposure lengths varied from ~ 300–800 s with a mean of ~ 500 s, but due to the steepness of the red-noise power spectrum this will have no effect on the shape of the DCF as long as the DCF bin size is much greater than the mean UVOT exposure length. The XRT counts are taken from each snapshot and have a mean exposure length of ~ 500 s. The DCF for the *Swift* data is plotted in Fig. 3.9. The plotted 95% and 99% confidence intervals are calculated using simulated light curves following the method outlined in Section 2.7.

To make the most of the observational coverage we combine the *XMM* and *Swift* datasets and recompute the DCF. As the effective areas of the UV and X-ray instruments on either telescope are not identical the count rates from one telescope need to be scaled before the DCF can be computed. We estimate this scale factor using the 3 occasions the observations overlap and find OM $\approx 1.1\times$UVOT, and EPIC-pn $\approx 15\times$XRT. The
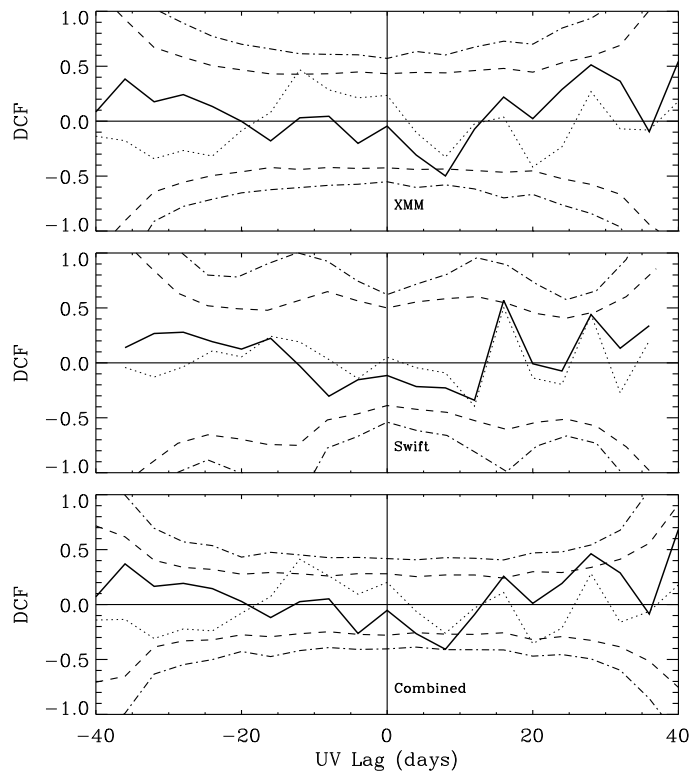
Figure 3.9: The discrete correlation function (DCF) for the between-observations (solid black line). The dotted black line is the DCF for the end-matched data. The dashed and dot-dashed lines represent the 90% and 95% confidence intervals respectively.

scaling factor for the X-ray cameras is consistent with that calculated by WebPIMMS[7]. No reference for a scaling factor between the UV cameras could be found, but we find the choice of scaling factor within the range $\sim 0.5 - 1.5$ has no effect on the shape of the DCF.

In Fig. 3.4 it can be seen that the UV light curves show a gradual increase in counts over the extended observation. To account for any underlying long-term trends in the UV variability we 'end-match' the overall UV light curve and recompute the DCF for the individual and combined datasets. These are shown as the dotted black lines in Fig. 3.9.

3.4 Discussion

3.4.1 Summary of results

Using UV and X-ray data from *XMM-Newton* and *Swift* we have analysed the light curves of NLS1 galaxy NGC 4051 to search for correlations in the variability between the two bands. UV variability is detected on short and long time scales, however the fractional

---

[7]http://ledas-www.star.le.ac.uk/pimms/w3p/w3pimms.html

rms amplitude is smaller than that in the X-rays. On days-weeks timescales the fractional variability of the UV is $F_{\mathrm{var}} \sim 8\%$, and on short ($\sim$ hours) timescales $F_{\mathrm{var}} \sim 2\%$ (from the "good" OM observations).

The excess variance in 4 of the 15 *XMM-Newton* OM observations is found to be considerably greater than the remaining 11. The "poor" 11 observations show there is a "floor" to the excess variance that isn't accounted for in the errors. In the "poor" observations any intrinsic source variations are masked by the errors, and inclusion of these observations will weaken the detection of any correlated emission. Although 4 out of the 15 observations is a relatively small subset, we find the variability statistics of the 4 "good" observations clearly very different from the remaining 11 "poor". The similarity in the overall shape of the CCF for the 4 "good" observations is hard to explain as arising by chance if the they were all representative of uncorrelated emission. Nevertheless, the interpretation of the time lag is still treated with some caution.

Analysis of the UV power spectral density reveals a red-noise light curve with a power-law slope of index $\alpha = 2.62 \pm 0.48$ for the 4 "good" OM observations. We searched for correlations between the two bands on time scales up to ~ 40 ks, treating all the *XMM-Newton* and the 4 "good" observations separately. The CCF for the 4 good observations revealed a significant peak of ~ 0.5 at a lag of ~ 3 ks. Using all 15 *XMM-Newton* observations the CCF revealed a weak correlation (~ 0.1) with a peak at ~ 3 ks. The cross-spectrum showed the lowest 5 frequency bins to have a low mean coherence of ~ 0.2 and a mean phase-lag of ~ 3 ks in both cases. Combining the *XMM-Newton* and *Swift* datasets we searched for correlated emission on timescales up to 40 days and find no significant correlations. The lag significance in the above results was estimated using simulated light curves. A correlation coefficient of $r \sim 0.5$ means the amount of UV variance predictable from the X-ray variance is $r^2 \sim 0.25$. As the coherence is a "square" quantity, this value is consistent with the ~ 0.2 form the coherence.

From a ~ 12 yr monitoring campaign on NGC 4051 using ground based optical photometry Breedt et al. (2010) estimated the PSD in the frequency range $\sim 10^{-8} - 10^{-3}$Hz. In their Fig. 4 they fit an unbroken power law to the PSD with $\alpha = 1.4^{+0.6}_{-0.2}$. In the paper Breedt et al. (2010) fitted a single-bend power-law model to the PSD, as is observed for X-rays (e.g. McHardy et al. 2004; Vaughan et al. 2011). Whilst they do not rule out the single-bend model, they find their data is more consistent with an unbroken power law. Their Fig. 5 shows the acceptance probabilities for the single-bend model as a function of high frequency slope α_{H} and bend frequency ν_{B}. Taking our value of $\alpha \approx 2.5$ as the high frequency slope this would give a break frequency $\nu_{\mathrm{B}} \approx 10^{-6.5}$ Hz. Our PSD is better constrained in the high-frequency range ($\sim 10^{-5} - 10^{-3}$Hz) and so the slope value $\alpha = 2.62 \pm 0.48$ is consistent with their single-bend model.

Table 3.3: UV and X-ray rms luminosity for the 15 *XMM-Newton* observations.

Band	$\bar{L}$ 10^{41}erg/s	L_{rms} 10^{41}erg/s
UVW1	3.4	0.3
0.2–10 keV X-ray	7.3	3.9
1–1.2 keV X-ray	0.3	0.2
5–6 keV X-ray	0.5	0.2

In a sample of 4 AGN using *Kepler* data, Mushotzky et al. 2011 estimated power spectral slopes (assuming a single power law model) of ~ 2.6–3.3 to the optical PSD in the $\sim 10^{-6.5} - 10^{-3.5}$Hz range. They do not attempt to fit a single-bend power-law model to their PSDs, but the break frequency for the larger black hole masses ($\sim 10^7 \text{M}_\odot$) in their sample would likely occur at lower frequencies than they estimate in the PSD.

The X-ray PSD in Fig. 3.6 shows orders of magnitude more variability power than the UV. This is consistent with what is seen in optical PSDs, where the high-frequency power is much less than in the X-rays, although the amplitudes can be similar (or even greater) at low frequencies (e.g, NGC 3783, Arévalo et al. 2009). A study with simultaneous UV and X-ray coverage on longer timescales is still lacking. A bend can be seen in the X-ray PSD at $\sim 2 \times 10^{-4}$ Hz (Vaughan et al. 2011). If a break was present in the UV PSD, it would be seen to occur at much lower frequencies that of the X-ray due to the radius of UV emission being much greater than that of the X-rays.

3.4.2 UV and X-ray rms luminosity

To assess whether the observed X-ray variations are significant enough to produce the variations seen in the UV band, we compare the root-mean-square luminosity variations in both bands. If the luminosity variations in the UV band are greater than the luminosity variations in the $0.2 - 10.0\,\text{keV}$ band, then this would in effect rule out the 0.2–10.0 keV X-ray variations being the dominant cause of variations in the UV band. The values in Table 3.3 show the integrated X-ray luminosity is greater than in the UVW1 band, and the X-ray luminosity variations are a factor ~ 10 greater. It is worth noting here that the UVW1 filter is very narrow compared to the X-rays. The X-ray band covers a factor of ~ 50 in wavelength, the UVW1 band covers only a factor 1.3. This largely explains the apparently low luminosity in the UWV1 compared to X-rays. The ratio of the FWHM to the central wavelength of the UVW1 filter is 620Å/2910Å≈ 0.2. Table 3.3 gives the rms luminosity for X-ray bands of comparable fractional energy range to the UVW1 filter. The rms luminosity in the narrower X-ray bands is now comparable to that of the UV band, albeit with lower mean luminosity. This shows that, in principle, the X-ray variations could drive variations in the UV band.

3.4.3 UV/X-ray correlation

Given the published black hole mass ($M_{BH} \approx 1.7 \pm 0.5 \times 10^6 M_\odot$ Denney et al. 2009) it is possible to make predicted lag estimates for each reprocessing scenarios based on standard disc equations to find the distance of the UV emitting (see Section 1.4.3). In the Compton up-scattering scenario the lags can be expected to be seen in the $\sim 1.5 - 7$ ks range for assumed accretion rate as a fraction of Eddington of 0.01–0.1. In the thermal reprocessing scenario the time-lags depend on the luminosity of the X-ray band and are expected to be ~ 7 ks. The direction and magnitude of our lag from the "good" data is consistent with the thermal reprocessing scenario.

Although the expected thermal reprocessing delay of ~ 7 ks is predicted from the toy model, the model assumes that the disc is heated solely from the incident X-rays, which are themselves coming from a radius $r = 0$. Both these assumptions are not likely to be true for a real AGN. An extended corona will increase R_X and a viscously heated disc will decrease R_{UV} and hence the light travel time between the two emitting regions. In the propagating accretion rate fluctuation model (Arévalo & Uttley 2006) the timescale of mass flow is dictated by the viscous timescale. This is dependent on the assumed viscosity parameter and scale height of the geometrically thin, optically thick accretion disc (Czerny 2006). We estimate this to be in the region of $\sim$ weeks—years.

Given the quality of the UV data in the 4 "good" observations, a lag in the region of ~ 1.5–7 ks would have manifested itself in the cross-correlation analysis. If the lag estimate from the 4 "good" observations is to be believed, then crudely speaking $\sim 25\%$ of the UV and X-ray variance are correlated on timescales of days. This is consistent with the Breedt et al. (2010) result, where an optical—X-ray correlation of $\sim 30\%$ is reported on timescales of $\sim$ weeks. Assuming the X-rays are produced at a radius $r = 0$ the observed ~ 3 ks time delay places the UV emitting region at $\sim 300 R_g$.

It doesn't matter how beautiful your theory is, it doesn't matter how smart you are. If it doesn't agree with experiment, it's wrong.

Richard Feynman

4

Flux dependent X-ray reverberation lags in NGC 4051

4.1 Introduction

In this chapter I investigate the reverberation signal in NGC 4051 with respect to source flux. These are time-lags *within* the X-ray band, in contrast to *inter-band* UV/X-ray time lags in Chap. 3. Soft X-ray lags have now been detected in many other sources (e.g. De Marco et al. 2011; Emmanoulopoulos et al. 2011; Zoghbi et al. 2012; Cackett et al. 2013; De Marco et al. 2013a) and even a source flux dependence on the soft lag has been seen (Kara et al. 2013). This builds on the now well-established X-ray time lags observed at lower frequencies (e.g. Papadakis et al. 2001; Vaughan et al. 2003; McHardy et al. 2004; Arévalo et al. 2006). Soft lags have also been uncovered in black hole X-ray binaries (XRBs; Uttley et al. 2011). However, at present, the interpretation of the lags remains controversial (Miller et al.; Zoghbi & Fabian 2011, hereafter M10a and Z11), see Section 1.4.1.

NGC 4051 displays rapid and high amplitude X-ray spectral variability, including occasional prolonged periods of low flux and variability (e.g. Green et al. 1999; Uttley et al. 1999; Vaughan et al. 2011). McHardy et al. (2004) revealed hard X-ray lags using a long *XMM* observation taken in 2001, while De Marco et al. (2013a) recently demonstrated the existence of soft X-ray lags at higher frequencies from more recent observations. Modeling how the lag spectrum changes over different flux levels, with different spectral appearance, could provide valuable insight into the geometry of the reverberating medium, responsible for the soft band lags.

The rest of this chapter is organised as follows. Section 4.2 discusses the observa-

tions of NGC 4051 and extraction of the X-ray light curves. Section 4.3 describes the method of producing frequency domain products and modeling of the lag spectrum. The implications of these results are discussed in Section 4.5. The results of simulations used to assess the reliability of the recovered lag-frequency spectrum are described in Section 4.4.

4.2 Observations and data reduction

Here we make use of the same 15 *XMM-Newton* observations of NGC 4051 discussed in Chap. 4. This chapter uses data from the EPIC-pn camera (Strüder et al., 2001) only, due to its higher throughput and time resolution. The raw data were processed from Observation Data Files (ODFs) following standard procedures using the *XMM* Science Analysis System (SAS v12.0.1), using the conditions PATTERN 0–4 and FLAG = 0. The X-ray data reduction followed that of Section 3.1.3 except that we used a 20 arcsec circular extraction region for the source. This extraction region decreases the contribution from the background in the source aperture, increasing the signal-to-noise (see Section 2.1.1). The EPIC observations were made using small window (SW) mode; the fast CCD readout helps to mitigate event pile-up (Ballet 1999; Davis 2001). We assessed the potential impact of pile-up using the SAS task EPATPLOT, and found only the highest flux revolution (rev 1730) showed significant signs of pile-up effects during the highest flux periods. The data were filtered for high background flares, and the background was visually inspected for rises towards the end of each observation. Strong background flares can introduce spurious time lags, so particular care has been taken to remove the influence of background variations (typically worse at the end of each observation).

The total duration of the useful data from the 2009 campaign is ≈ 572 ks, giving $\sim 6 \times 10^6$ EPIC-pn source counts. NGC 4051 was also observed for ~ 120 ks in 2001 and ~ 50 ks in 2002. We do not include these data in the present analysis to avoid problems caused by systematic changes during the intervening ~ 8 years.

4.3 Lag measurements

We estimated cross-spectral products by first averaging the complex $C_{xy}(f)$ values over non-overlapping segments of time series, and then averaging in geometrically spaced frequency bins (each bin spanning a factor ~ 1.3 in frequency). For the analysis in this paper we use segment sizes of 10 ks and time bins of 10 s. Accounting for observations that don't last an integer multiple of 10 ks, this leaves 490 ks of data from the 2009 observations.
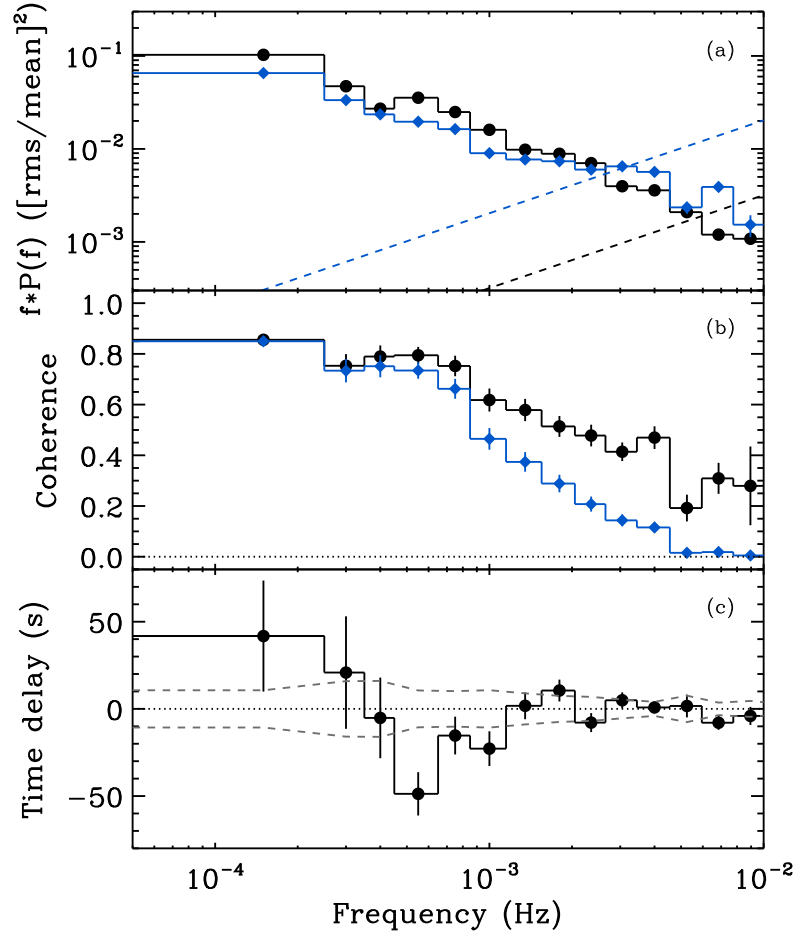
Figure 4.1: Cross-spectral products for the soft (0.3–1.0 keV) and hard (2.0–5.0 keV) energy bands. Panel (a) shows power spectral density for the soft (black circles) and hard (blue diamonds) bands. The dashed lines are the Poisson noise estimates. Panel (b) shows the raw (blue diamonds) and Poisson noise corrected (black circles) coherence, see Section 4.3 for details. Panel (c) shows the time lag between the hard and soft band, where a positive values indicate the hard band lags. The grey dashed line is the Poisson-noise lag estimate, see Section 4.3 for details.

Fig. 4.1 shows the power and cross-spectral products for the 0.3–1.0 keV (soft) and 2.0–5.0 keV (hard) bands, with mean count rates 5.8 and 0.8 $ct\,s^{-1}$ respectively. The power spectral density (PSD) is plotted for each band in panel (a), where the hard band shows a flatter spectrum, as found in Vaughan et al. (2011). Panel (b) shows the raw and noise corrected coherence. The noise corrected coherence is high (~ 0.6) for frequencies up to $\sim 10^{-3}$ Hz, above which it is seen to drop off smoothly.

Panel (c) in Fig. 4.1 shows the time lag as a function of Fourier frequency (here-

after 'lag-frequency spectrum'). Here we follow the convention of indicating a soft band lagging behind the hard band with a negative time lag (hereafter 'soft lags'). The lag-frequency spectrum shape is similar to that seen in other sources, and seems to be quite common in low-redshift, X-ray variable AGN (e.g. Fabian et al. 2009; Emmanoulopoulos et al. 2011 (hereafter E11); De Marco et al. 2013a). At frequencies less than $\approx 4 \times 10^{-4}$ Hz a hard lag is seen, whereas between $\approx 5 \times 10^{-4}$ and 1×10^{-3} the soft emission lags the hard, with a maximum soft lag of $\sim 50\,$s at $\sim 6 \times 10^{-4}$ Hz.

The effect of Poisson noise is to contribute an independent, random element to each phase difference measurement. This makes small time lags difficult to detect at high frequencies where the Poisson noise begins to dominate over intrinsic source variations. This effect can be estimated using equation 30 of Vaughan et al. (2003), which provides an estimate of the uncertainty on the time lag estimates due to the Poisson noise. This is plotted in Fig. 4.1 (panel c); we do not expect to recover reliable lags inside this range. The PSD for the hard band was used in this calculation, as this has the lowest signal-to-noise of the two bands concerned. For frequencies above $\sim 3 \times 10^{-3}$ Hz the Poisson noise dominates the lag.

The effects of spectral 'leakage' (e.g. van der Klis 1989; Uttley et al. 2002) on the lag-frequency spectrum were investigated using simulations (see Section 4.4). We found a bias in the size of the observed lag at a given frequency, such that the magnitude of the observed lag is reduced. This implies that in the absence of such a bias the lags would be larger than currently estimated.

4.3.1 Flux resolved time lags

It is already known that the shape of the energy spectrum and the rms vary with flux level (e.g. Vaughan et al. 2011). Here we investigate changes in the lag-frequency spectrum as a function of flux. The time series segments were sorted by their average flux level and the cross-spectrum estimated in three flux bins, using an approximately equal number of light curve segments in each flux bin. The total band (0.2–10 keV) mean count rate is 17.1, 7.8 and 4.5 ct s^{-1} for the high, medium and low flux levels respectively, with 15, 15 and 19 segments (of 10 ks) in each flux bin, respectively. The soft (0.3–1.0 keV) and hard (2.0–5.0 keV) band light curves are shown in Fig. 4.2, where the segments used in each flux level are indicated. The segment length was chosen to be 10 ks as a compromise between having a wide range of fluxes (smaller duration segments give a wider range of mean fluxes) and having better low frequency coverage and reduced bias (longer segments give better low frequency coverage). In Sec 4.4 we explore the effect of using longer length segments. The segment length is longer than the the timescale on which the PSD bends ($f \sim 2 \times 10^{-4}$ Hz; Vaughan et al. 2011) which also helps reduce
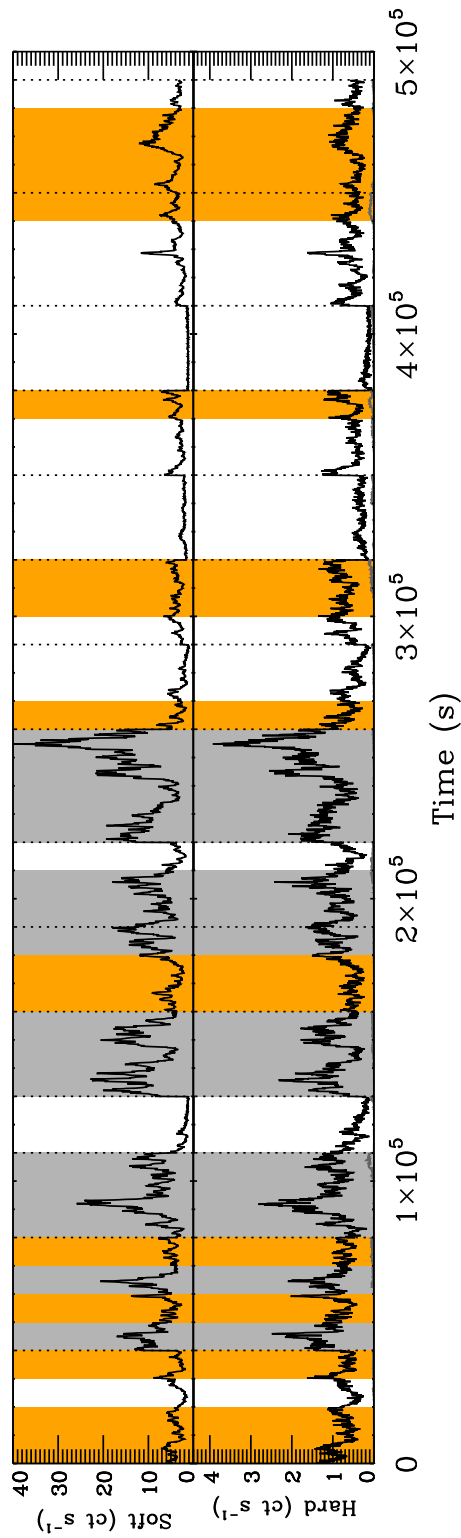
Figure 4.2: Plot of soft (0.3–1.0 keV) and and hard (2.0–5.0 keV) band light curve segments used in the fluxed analysis. The grey, orange and clear sections represent the high medium and low flux segments respectively, with a total band $(0.2 - 10.0\,\text{keV})$ mean flux of 17.1, 7.8, and 4.4 ct s^{-1}. The vertical dotted lines separate the individual observations. The dark grey curve is the background level in each band.
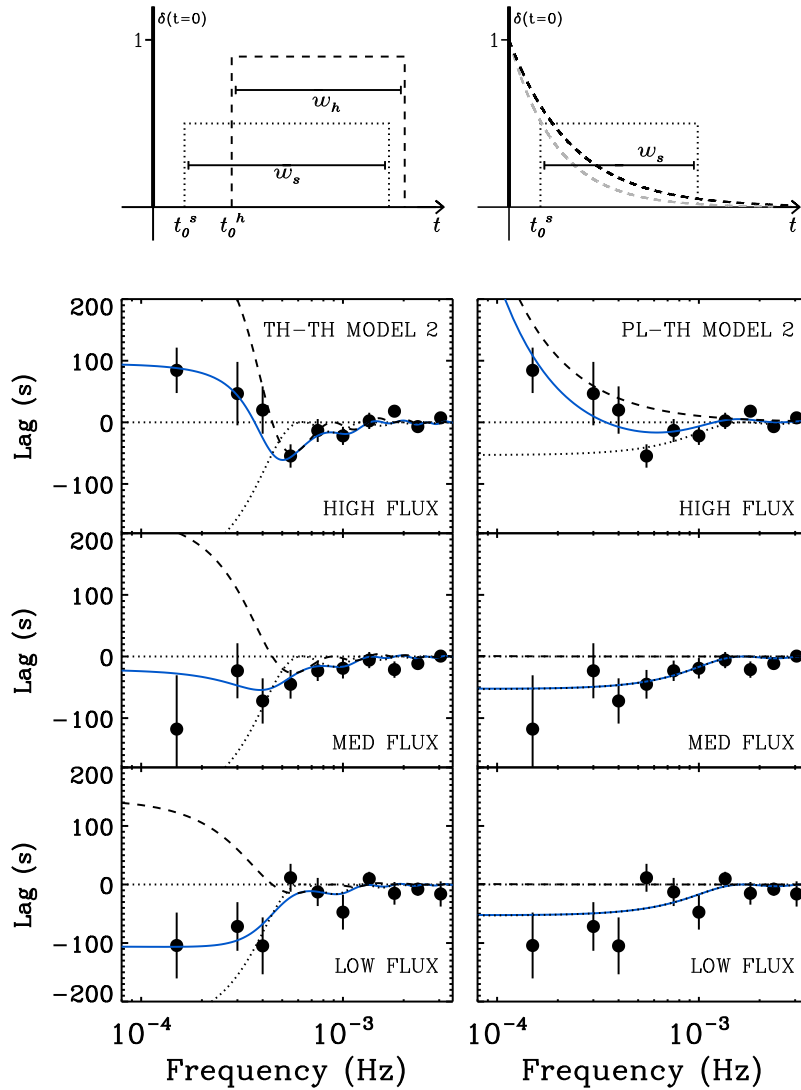
Figure 4.3: Lag-frequency spectrum as a function of source flux between the soft (0.3–1.0 keV) and hard (2.0–5.0 keV) bands. The data in the left and right hand panels are the same, with the panels from top to bottom showing the high, medium and low flux lag-frequency spectra respectively. The solid blue lines are the results of fitting the response function models described in Section 4.3.2. Left: TH-TH model 2 of Table 4.1 (upper section), consisting of a top hat in the hard band (dashed) and a top hat in the soft band (dotted). Right: PL-TH model 2 of Table 4.1 (lower section), consisting of a power law for the hard band (dashed) plus a top hat in the soft band (dotted). The upper panels illustrate (since they are only schematic) the corresponding time response functions for the plotted models. In the PL-TH model (right), the black and grey dashed lines represent the propagation of fluctuations between some initial fluctuations and the soft and hard emitting regions respectively. The difference of the Fourier transforms of these two functions is approximately constant, giving lags between the two bands that have a power-law dependence on frequency.

the bias from very low frequencies.

Fig. 4.3 shows the lag-frequency spectrum, for the high, medium and low flux levels.

The high flux lag-frequency spectrum is consistent with that of the total flux shown in Fig. 4.1. This is to be expected since the high flux intervals are also the most highly variable (Vaughan et al. 2011), so tend to have the higher Fourier amplitudes, and dominate the average cross-spectrum. A clear change in the lag-frequency spectrum shape with source flux can be seen.

We ignore any frequency bins where the raw coherence is consistent with zero (see Fig. 4.1). This leaves 10 frequency bins per lag-frequency spectrum after applying the frequency averaging. The noise corrected coherence is high ($\gtrsim 0.6$) for these 10 frequency bins in all three flux ranges. No significant changes in the coherence spectrum were seen across the flux levels.

4.3.2 Modelling the lag

In this section we attempt to fit the lag spectra for the high, medium and low fluxes using simple analytical models. We assume the time series obtained from each band is actually some underlying 'source' variability $z(t)$ convolved with a linear impulse response function[8]: $x(t) = \psi_x(t) \otimes z(t)$ and $y(t) = \psi_y(t) \otimes z(t)$ (see Section 2.5). This is clearly a simplification but allows us to test some 'toy models' for the origin of the time lags[9]. The phases obtained from the cross-spectrum $C_{xy}(f)$, which give the time lag-frequency spectrum, are (on average) the differences between the phases of the Fourier transforms of each response, i.e. $\phi(f) = \arg \Psi_y(f) - \arg \Psi_x(f)$.

Previous work (e.g. M10a, E11, Z11) has made use of two types of time lag model: a power law dependence of the time lag with frequency, or the delay due to a top hat impulse response. A roughly power law (PL) frequency dependence of the hard X-ray time lag is well established in X-ray binaries (e.g. Miyamoto et al. 1988; Nowak et al. 1999; Pottschmidt et al. 2000), at least at low frequencies, and consistent results from AGN have been reported several times (e.g. Papadakis et al. 2001; Vaughan et al. 2003; McHardy et al. 2004; Arévalo et al. 2006). We therefore consider a PL model of the form $\tau(f) = N f^{-\alpha}$ with $\alpha \approx 1$. The time domain representation of this function is shown in Fig. 4.3. This may represent the effects of variations propagating through and modulating an extended emission region (e.g. Kotov et al., 2001; Arévalo & Uttley, 2006). But a PL lag-frequency spectrum does not show a reversal in the direction of the lag (as seen in the data), meaning alternative or additional terms are required to explain the negative lag.

---

[8]We use 'impulse response' or 'response function' to indicate the function as applied in the time domain (by convolution), and 'transfer function' to represent its Fourier counterpart, as these terms are standard in the signal processing literature.

[9]We note that the response function models discussed here or elsewhere in the literature are linear, which give unity coherence between the input and output time series, and therefore fail to reproduce the coherence spectrum (see Fig. 4.1).

A simple alternative model is provided by a 'top hat' (TH) impulse response, as might be produced by reverberation from an extended medium. The TH is characterised by three parameters: start time t_0, width w, and scaling fraction S. In practice we fit the time-lag spectrum using the time lags extracted from the Fourier transform of a TH plus a δ-function. The δ-function corresponds to direct (not delayed or smoothed) emission, and the parameter S sets the intensity of delayed emission relative to the direct emission. The start time (t_0) of the top hat component was allowed to be negative to allow for time lags of the direct component, as is found in Wilkins & Fabian (2013). As discussed in M10a and Z11, a TH response function applied to the hard band alone can produce both a hard lag at low frequencies and an apparent soft lag at higher frequencies due to 'ringing' caused by the sharp edges of the response function in the time domain. However, as pointed out by Z11, such a model predicts a frequency range for the soft lag that is narrower than typically observed.

We fitted various combinations of PL and TH-based time lag models to our data. As the time lags were estimated by averaging the cross-periodograms from multiple segments their distributions should be approximately Normal, and hence we can use standard $\min(\chi^2)$ fitting techniques. The lag-frequency spectra from the three flux levels were fitted simultaneously. Some parameters were 'tied' such that the same value applies to the model at all three flux levels, and other parameters were 'untied' meaning that the parameter was allowed to take on different values for each flux level. During the fitting we experimented with different combinations of tied and untied parameters, as summarised in Table 4.1.

As expected, the simple PL model and the simple hard-band TH model do not provide acceptable fits to our data (with $p < 10^{-4}$ in a χ^2 goodness-of-fit test). We therefore consider in detail two more complex models. The first is based on TH plus δ-function responses in the soft and hard bands, the second model adds lags from a TH plus δ-function response in soft band to a PL lag in the hard band. We refer to these as the TH-TH and TH-PL models, respectively (they correspond to models 2 and 3 of E11). A model with PL-like responses in both bands (PL-PL model) can in principle generate hard lags on long timescales and soft lags on short timescales, if the PL index in the hard band is steeper than the soft band. We did not attempt to fit such a model as it necessarily gives only a very smooth lag-frequency spectrum, which is inconsistent with the relatively sharp transition from hard to soft lags observed.

Ignoring flux-dependence, the TH-TH model has six parameters (three for each TH component). Table 4.1 shows the results of fitting the model with variants of tied and untied parameters. The simplest acceptable fit to the data was provided by letting only the scaling factor S_h vary with flux (this is listed as TH-TH 2 in Table 4.1; 8 free parameters).

Table 4.1: Results of simultaneous model fitting to the three lag spectra, for variants of tied (T) and untied (U) parameters. Column (1) is the model variant, columns (2-7) are the model parameters, column (8) is the χ^2 fit and degrees of freedom, and column (9) is the null hypothesis probability. The h, s sub/super-scripts indicate the parameter is for the transfer function in the hard and soft band respectively.

Variant	Parameters: Tied / Untied						χ^2 / dof	p value
	TH-TH Model							
	t_0^{h}	w_{h}	S_{h}	t_0^{s}	w_{s}	S_{s}		
1	T	T	T	T	T	T	39/24	0.02
2	T	T	U	T	T	T	19/22	0.66
3	T	T	T	T	T	U	21/22	0.52
4	T	T	U	T	T	U	17/20	0.60
5	U	T	T	U	T	T	24/20	0.24
6	U	U	T	U	U	T	14.5/16	0.56
	PL-TH Model							
	N_{h}	α_{h}	t_0^{s}	w_{s}	S_{s}			
1	T	T	T	T	T		39/25	0.04
2	U	T	T	T	T		25.6/23	0.32
3	T	T	T	T	U		35/23	0.05
4	U	T	T	T	U		22.6/21	0.37
5	U	U	T	T	U		22.5/19	0.22
6	T	T	U	U	U		34/19	0.02
7	T	U	U	U	U		24/17	0.14

In this case a good fit is obtained if the S_h parameter, indicating the strength of the delayed component in the hard band, decreases with decreasing flux and is consistent with there being no delayed component at low fluxes. This is to be expected given the disappearance of the hard lag at low frequencies in the lower flux data (Fig 3; left panels). Allowing only the S_s parameter to vary (model TH-TH 3 in Table 4.1 gives a worse, but still acceptable fit to the data. Keeping the S_s and S_h constant with flux, but allowing the start times (t_s and t_h) to vary with flux provided a rather worse, but still acceptable, fit to the data (model TH-TH 5 in Table 4.1). Allowing the top hat widths (w_s and w_h) to also vary independently with flux gave a very good fit (model TH-TH 6 in Table 4.1) but with the largest number of free parameters (14). The fit parameter values for TH-TH models 2 and 3 are listed in Table 4.2.

Again ignoring flux-dependence the PL-TH model has five parameters: N_h, α_h, t_0^s, w_s, S_s. The results of fitting this model to the three lag-frequency spectra are displayed in Table 4.1. As with the previous model, the simplest variant providing an acceptable fit allowed only the hard band scaling factor N_h to vary with flux (PL-TH model 2 in Table 4.1). In particular, the parameter N_h, representing the normalisation of the PL lag in the hard band, is positive for the high flux data and consistent with zero for medium and low flux data, which accounts for the disappearance of the hard lag at low frequencies

Table 4.2: Parameter values for the simplest model fits to the three flux lag-frequency spectra. These correspond to the TH-TH variants 2 and 3, and PL-TH variants 2 and 3 from Table 1. Column (1) is the model parameter, where the h and s sub/super-scripts indicate the parameter is for the transfer function in the hard and soft band respectively. Columns (2-4) are the tied or untied parameter values, where '-' means the parameter was tied for all fluxes (see Section 4.3.2 and Table 4.1 for the model variant details).

Parameter	High / all	Medium	Low
	TH-TH variant 2		
t_0^{h}	1120 ± 120	-	-
w_{h}	560 ± 60	-	-
S_{h}	0.45 ± 0.09	0.26 ± 0.08	0.14 ± 0.07
t_0^{s}	60 ± 180	-	-
w_{s}	1530 ± 230	-	-
S_{s}	0.44 ± 0.09	-	-
	TH-TH variant 3		
t_0^{h}	1130 ± 100	-	-
w_{h}	570 ± 70	-	-
S_{h}	0.28 ± 0.07	-	-
t_0^{s}	-10 ± 110	-	-
w_{s}	1630 ± 130	-	-
S_{s}	0.23 ± 0.10	0.53 ± 0.13	0.66 ± 0.15
	PL-TH variant 2		
N_{h}	0.0005 ± 0.0001	0.0 ± 0.0002	0.0 ± 0.0002
α_{h}	1.44 ± 0.07	-	-
t_0^{s}	-10 ± 110	-	-
w_{s}	610 ± 120	-	-
S_{s}	0.22 ± 0.05	-	-
	PL-TH variant 3		
N_{h}	0.0002 ± 0.002	-	-
α_{h}	1.42 ± 0.10	-	-
t_0^{s}	10 ± 80	-	-
w_{s}	610 ± 100	-	-
S_{s}	0.16 ± 0.11	0.29 ± 0.12	0.25 ± 0.12

in the lower flux data (Fig 3; right panels). Allowing only S_s to vary with flux (PL-TH model 3 in Table 4.1 did not give an acceptable fit. The fit parameter values for PL-TH models 2 and 3 are listed in Table 4.2.

We have also tried a model combining features of both the above models, namely TH plus δ-function applied to the soft band, and a TH plus δ-function applied to the hard band, with additional hard lags from a PL component. In this case the power-law normalisation is always consistent with zero (for various combinations of tied/untied parameters), and so the model reduces to the TH-TH model above.

The models were refitted after re-parametrising the scaling factors such that the TH component normalised to unity and the normalisation of the delta function was a free parameter. This is mathematically equivalent, but allows us to monitor any changes in

the direct component with flux. The results are consistent with our model fits in Table 1, where we found the scaling fraction on the δ-function in the soft band to be constant with flux.

An extreme variation on this model has direct component in the soft band vanishing at low fluxes. We explicitly tested this by fixing the δ-function scaling factor in the soft band at low flux to zero. For the TH-TH and PL-TH model variants described in Table 1, we again simultaneously fit across all flux levels. We find fixing the δ-function scaling factor to zero did not provide an acceptable fit ($p < 0.01$ for all model variants).

4.4 Bias in time lag estimation

The X-ray PSD of NGC 4051 shows substantial power, and is still rising to lower frequencies, below 10^{-4} Hz, the lowest frequency used in our cross-spectrum analysis (due to the choice of 10 ks segments). One side-effect of observing a low-frequency dominated noise process using short segments is known as 'spectral leakage' (see Section 2.3.1). This is known to distort PSD estimates, but similarly distorts the phase estimates, and hence the cross-spectrum of two time series. In this section we briefly explore the origin and consequences of this 'leakage' on the lag-frequency spectrum.

4.4.1 Origin of the phase bias

It is possible to understand the origin of the phase (time) lag bias in terms of the finite segment length, or *sampling window* (see Section 2.3.1), used to make each cross-spectrum estimate. The following analysis sketches out the origin of the bias on the phase lag between two time series $x(t)$ and $y(t)$.

If $X(f)$ and $Y(f)$ are the Fourier Transforms of $x(t)$ and $y(t)$, then the complex-valued cross-spectrum is formed from the ensemble average of their product:

$$\langle C(f) \rangle = \langle X^*(f)Y(f) \rangle \tag{4.1}$$

and the phase lag-frequency spectrum $\phi(f)$ is obtained from its argument:

$$\phi(f) = \arg\langle C(f) \rangle = \arctan\left(\frac{\langle q(f) \rangle}{\langle c(f) \rangle} \right) \tag{4.2}$$

where $q(f)$ and $c(f)$ are the estimated 'quadrature-spectrum' and 'co-spectrum', the imaginary and real components of C, respectively. These are each real-valued and may be computed from:

$$q(f) = \Re(X)\Im(Y) - \Im(X)\Re(Y)$$
$$c(f) = \Re(X)\Re(Y) + \Im(X)\Im(Y) \tag{4.3}$$

where $\Re(\cdot)$ and $\Im(\cdot)$ indicate the real and imaginary components of some variable.

Real time series have finite length and sampling, $x_n(t_i)$ where $i = 1, 2, \ldots, n$ and $t_i = i\Delta t$. We can understand the effect of finite length time series by treating the observed time series $x_n(t_i)$ as the product of an infinitely long series $x(t)$ with a window function $w(t)$ that is zero everywhere except $-T/2 \leq t \leq T/2$, where $w(t) = 1$ and $T = n\Delta t$. (We shall neglect the effect of the finite time resolution Δt, but the following results are approximately correct for small Δt.)

$$x_n(t) = x(t)w(t) \tag{4.4}$$

and by the convolution theorem this leads to the relationship between the observed and asymptotic Fourier components:

$$X_n(f_j) = \int_{-T/2}^{T/2} X(f)W(f - f')df' \tag{4.5}$$

at Fourier frequencies $f_j = j/T$ ($j = 1, 2, \ldots, n/2$). Here, $W(f)$ is the Fourier transform of the function $w(t)$, with the form $W(f) = \mathrm{sinc}(\pi T f)$ for a rectangular window. More generally, for discretely sampled series this is the *Dirichlet kernel*. See Priestley (1981) and Jenkins & Watts (1969) for detailed discussion of the effect of window functions on Fourier products such as auto- and cross-spectral densities. This convolution of $X(f)$ with $W(f)$ distorts the real and imaginary components of $X_n(f_j)$, and likewise for $Y_n(f_j)$. In practice, when we estimate the phase lags using $x_n(t)$ and $y_n(t)$ we replace the Fourier transforms in equations 4.3 with those of equation 4.5. The distortion of each of the components – $\Re(X_j)$, $\Im(X_j)$, $\Re(Y_j)$, $\Im(Y_j)$ – generally leads to a bias on the estimated co- and quadrature spectra. The consequence is that if the phase difference $\phi(f)$ changes with f the distortion on co- and quadrature spectrum will be different, and lead to a bias on the phase lag $\phi_n(f_j)$ calculated from their ratio. The bias of the Fourier transforms, and hence the phase difference between them, decreases as $W(f) \to \delta(f)$, i.e. as $T \to \infty$.

If one or more of the PSDs are rising steeply to low frequencies, this can lead to a 'leakage' of the Fourier components from low (unobserved) to higher (observed) frequencies, through the side-lobes of the kernel. But even if the PSDs are flat towards lower frequencies, Fourier components at nearby frequencies influence $X_n(f_j)$ and $Y_n(f_j)$ and so, even in the absence of 'red noise leakage' of the power density there can be a non-trivial bias on the phase lags. This is strongest when the phase spectrum $\phi(f)$ changes rapidly with f, i.e. has large curvature $|d^2\phi(f)/df^2|$. By contrast, when the phase spectrum is very smooth (approximately constant or linear over $\sim$fewΔf, where $\Delta f = 1/n\Delta t$) the phases at nearby frequencies are sufficiently similar that the distortion on the co- and quadrature spectrum is similar and cancels when computing the phase lag, leading to small bias.
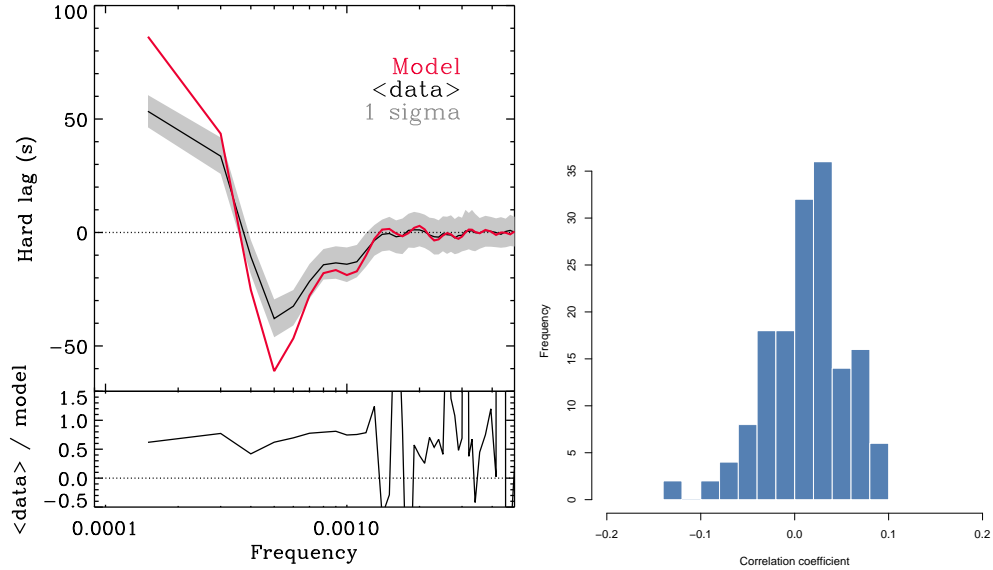
Figure 4.4: The effect of leakage on the measured lag-frequency spectrum. Left: The upper panel shows the lag-frequency spectrum for simulated pairs of light curves with a frequency-dependent time lag. The red curve is the model time lag, the black line is the mean measured lag and the grey shaded region is the 1 sigma confidence intervals from the simulations. The model shown is the best fit TH-TH (see Section 4.3.2). The lower panel shows the ratio between the mean measured lag and the model. Right: Covariance between lag estimates in adjacent frequency bins.

4.4.2 Simulations of leakage

To assess the level of phase bias in the observed lag-frequency spectra we simulated 1000 pairs of random time series. For each pair we used the Timmer & König (1995) method to generate a pseudo-random, Gaussian time series of length 50 days and 10 s binsize, corresponding to much longer and shorter timescales than is measured in the lag-frequency spectrum. The PSD used to generate the time series was a bending power-law with low frequency slope -1.1, high frequency slope -2.0 and break frequency $\nu_{\rm B} = 2 \times 10^{-4}$ Hz (Vaughan et al., 2011). For each of these simulations a second time series was produced using the same Fourier amplitudes and phases, except for an additional frequency-dependent phase shift derived from the time lag models described in Section 4.3.2. For each pair of time series, 15 intervals were extracted using the sampling pattern as the real *XMM-Newton* observations. The rms-flux relation (see Uttley et al. 2005) was added to the simulated time series using the static exponential transformation, although we note the results are largely insensitive to this. Observational noise was added to each time series by drawing a Poisson random deviate with mean equal to the mean count-per-bin in the real light curves.

Fig. 4.4 shows the input model of the time delays (TH-TH model in this case) com-

pared to the average lag-frequency spectrum from the simulated data, clearly revealing a bias in the estimates. The effect of leakage is to suppress the magnitude of the observed time lag. The ratio plot in Fig. 4.4 shows there is a $\sim 30\%$ reduction in the recovered lag for frequencies $\lesssim 2 \times 10^{-3}$ Hz. One implication is that the measured time lags would be larger if the bias towards zero could be removed. We find that changing the top-hat width or start-time (w; t_0) has little effect on the magnitude of the bias. A slightly smaller bias towards zero lag is observed in simulations with the PL-TH model.

4.4.3 Covariance between lag estimates

Another consequence of leakage is covariance between lag estimates in adjacent frequencies (Jenkins & Watts, 1969, chap. 9). The simulations performed here were used to constrain the degree of covariance. In the limit of very long observations (and in the absence of biases due to spectral leakage) the covariance between lag estimates at different frequencies tends to zero, but for finite length time series there will remain some small covariance. From the covariance matrix of the simulated time lags as a function of frequency, the correlation between adjacent frequency bins can be calculated. The lowest frequency bins show the highest correlation with each other (but with values $\lesssim 0.25$). A histogram of the correlation between adjacent frequencies shows a Gaussian distribution centred on $\sim$zero. This shows that, whilst some degree of covariance exists between adjacent frequencies, treating the lag measurements at each frequency as independent should not substantially distort the results of any $\min(\chi^2)$ fitting techniques. The scatter in the simulated lags was used to check the magnitude of the standard error estimates (e.g. Vaughan & Nowak 1997; Bendat & Piersol 1986), which show consistent results.

4.4.4 Reducing leakage bias

We have explored variations of the lag estimation procedure to reduce the bias caused by spectral leakage. We computed the lag-frequency spectrum using $20\,\mathrm{ks}$ segments (not shown here). Again the mean source rate in each segment was chosen to give an approximately equal number of segments for 3 flux levels. The segments used therefore differ from those shown in Fig. 4.2, and the range of mean fluxes is reduced compared to the shorter segments used in the above analysis. However, the same change in the lag-frequency spectrum is observed with source flux. We have also computed the lag-frequency spectrum using whole observations ($25 - 40\,\mathrm{ks}$) as the segment length, before binning in frequency space over segments of differing length. This includes more data in the lag-frequency estimate, but gives a much smaller range of mean fluxes. We can therefore only compute this for two flux levels, which still show the same change in the

lag-frequency spectrum with source flux. We conclude that the systematic change in the lag-frequency spectrum with source flux is robust to the details of the analysis.

Leakage bias can be reduced by 'end-matching' the data, whereby a linear trend is removed such that the first and last points are level (Fougere 1985). This 'end-matching' removes, to a large extent, linear trends from the data, and alleviates the problem caused by circularity of the Fourier transform when estimating the cross-spectrum. It removes the bias coming from lower frequencies "leaking" in, but does not remove the bias from nearby frequencies. We computed the lag-frequency spectrum for the three flux levels using 10 ks segments, where each segment is end-matched individually. The resulting lag-frequency spectra and response function model fits are consistent with the results of Section 4.3.

4.5 Discussion and conclusions

4.5.1 Summary and comparison with previous work

We have studied the frequency dependent time delays in the Seyfert galaxy NGC 4051 using a series of *XMM* observations made in 2009. We found the lag-frequency spectrum varies significantly and systematically with source flux. At high fluxes there is a hard ('positive') lag at the lowest frequencies and a soft ('negative') lag confined to a narrow range of frequencies around $\approx 5 \times 10^{-4}$ Hz, but at lower fluxes the low frequency lag reverses direction, becoming a soft lag. The lag-frequency spectra in three flux bins can be modelled simultaneously using simple response function models. The simplest acceptable fits have all parameters tied between the flux levels, except for the parameter that determines the magnitude of the delayed component in the hard band light curve. Allowing just the scaling fraction in the soft band to vary provides an acceptable fit in the TH-TH model, but not in the PL-TH model.

Previous work by McHardy et al. (2004), M10b and Legg et al. (2012) on X-ray time lags in NGC 4051 found hard lags increasing to lower frequency, but did not identify a soft ('negative') lag. This may reflect genuine differences in the variability between observations, but might also be due to differences in the data quality and/or analysis methods that meant a soft lag went undetected. We note that these papers all used data obtained during times when NGC 4051 was relatively bright, and our analysis shows that at high fluxes the soft lag occurs over a relatively narrow range of frequencies. M10b and Legg et al. (2012) used data from *Suzaku* which contain periodic gaps (due to the ~ 96 min Low Earth orbit), and used a much longer time bins (256 s) than our analysis. It may well be the case that the data or analysis used by these authors are less sensitive to the

short (~ 50 s) lag we observe with *XMM-Newton*. Recently, De Marco et al. (2013a) published a lag-frequency spectrum for a sample of unabsorbed, radio-quiet AGN including NGC 4051. Their lag-frequency spectrum represents an average over *XMM* observations taken during 2001, 2002 and 2009, and is consistent with the lag-frequency spectrum we show for high flux periods (which will tend to dominate such an average, as discussed above).

4.5.2 Understanding the time delays

The changes in lag-frequency behaviour with flux could be linked to the strong change in spectral shape with flux (see e.g. Vaughan et al. 2011) if the hard and soft lag components are linked to the components which make up the energy spectrum, and these components change in relative strength. A detailed comparison of the energy-dependent behaviour is beyond the scope of this paper, however. But we note here that the lack of positive lags at low fluxes could indicate a change in the circum-nuclear structure, and also be responsible for the dramatic change in the energy spectrum.

For the purpose of the present discussion we assume the cause of the very lowest fluxes is no different from the X-ray variability in general, simply the lowest point in a continuum of spectral variability. This seems most natural given the rms-flux relation for NGC 4051 (Uttley et al. 2005; Vaughan et al. 2011) appears as a single linear track from highest to lowest fluxes, and the PSD shape remains constant in shape for high and low fluxes (Vaughan et al. 2011)[10]. If the soft band emission was dominated by reprocessed emission at low fluxes we would expect to see a change in the PSD (the reprocessor acts as a low-pass filter). The optical and X-ray variations (including low flux periods) are correlated on timescales of $\gtrsim 1$ day (Breedt et al. 2010), and the UV and X-ray variations are correlated on timescales of ~ 1 hr (Alston et al. 2013b). These correlation results are independent of X-ray flux, and support the model where X-ray variability on the timescales that soft lags are observed is dominated by intrinsic X-ray luminosity variations.

We fitted the lag-frequency spectrum using two simple kinds of impulse response models: a top hat (TH) response in the time domain and a time lag that varies with frequency as a power law (PL). The soft band lag of about $\sim 50 - 100$ s can be explained by a single TH response function spanning lags from 0 s to $\sim 10^3$ s. The observed time lag is diluted by the direct (zero delay) component included in the response function. The hard band lag can be explained either in terms of a top hat response with a minimum

---

[10]The flux-resolved PSD analysis of Vaughan et al. (2011) was carried out using a broad (0.3-10 keV) energy band. But, as the count spectrum of NGC 4051 is dominated by soft (<2 keV) photons, this is effectively tracks the soft X-ray PSD with flux, which should be most sensitive to changes in absorption.

lag of $\sim 10^3$ s, or a power law-like frequency dependence with an index of $\alpha \approx 1.5$. These two models give similar quality fits over the observed frequency range, but diverge strongly at lower frequencies where these observations provide little sensitivity.

If the time lags from the response function models are interpreted simply as the result of light travel time differences, the maximum time lag in each band gives a distance to the most distant parts of the reprocessor of $\tau \sim (1 - \cos\theta)R/c$ where R is the distance between source and reprocessing region, and θ is the angle between source-reprocessor line and the line-of-sight to the source. Assuming $\theta > \pi/2$ (i.e. the reprocessor is not concentrated entirely on the near side of the source), the maximum lag corresponds to $\sim R/c$. The best fitting TH-TH models have the maximum time lag in the hard and soft band consistent with each other at a value ~ 1600 s, placing the outer region of the reprocessor at $\sim 160R_\mathrm{g}$ for NGC 4051 (assuming $M_\mathrm{BH} \sim 2 \times 10^6$ M$_\odot$; Denney et al. 2009). In the best fitting PL-TH model the soft band response extends out to ~ 600 s, placing the reprocessor at $\sim 60R_\mathrm{g}$.

Models using a single delayed component, i.e. contributing to either the hard or soft band but not both, give unacceptable fits to the lag-frequency spectrum. This, combined with the apparent flux-dependence of the contribution of the hard lag but not soft lag components, supports the need for at least two components causing time lags, one affecting each band. This is consistent with a more complex model in which time lags are caused by a combination of propagating fluctuations and reflection (e.g. E11; Z11). It could also be the case that a single lagging component contributes to both bands, but its spectral shape changes with flux (so that it appears as a constant fraction of variable emission in the soft band but decreasing with flux in the hard band).

The apparent change in direction of the lag at low fluxes can be explained by a change in the responses: as the flux decreases the skew towards lagging values becomes weaker in the hard band, relative to that in the soft band. This could occur either if the hard lagging component gets weaker compared to the hard direct light, or if the soft lagging component gets stronger relative to the soft direct light. If the direct emission, with a power law energy spectrum, contains 'intrinsic' hard time delays, as supposed in e.g. the propagating fluctuations model (Kotov et al. 2001; Arévalo & Uttley 2006) there will be hard delays even in the absence of reprocessing. The 'external' reprocessing then adds a second source of delays, contributing a short lag extending up to higher frequencies. In this scheme the efficiency of the 'external' reprocessing remains constant with flux, but the fraction of delayed light making up the intrinsic emission must decrease with flux.

If the lower fluxes are due to a low intrinsic (isotropic) luminosity, and the properties of the reprocessing medium remain constant, then the time lags should be relatively constant with flux. On the other hand if the low flux is a result of increasing absorption

along the line-of-sight (with a relatively constant isotropic luminosity) then the contribution of the delayed components in the light curves should increase (relative to the direct components) as the flux decreases. This is one way to interpret the TH-TH 3 model.

An extreme variation on this idea is that the periods of low flux and variability are the result of absorption completely obscuring the direct component in the soft band, but not the (more extended) reprocessing region. The low flux lag spectrum may well be reproduced by the lack of a δ-function at $t = 0$ in the soft band response function. However, we found this model, in which the direct (zero delay) contribution to the soft band disappears at low fluxes, did not give a good fit to the lag-frequency data.

M10a proposed to explain both hard and soft time lags in terms of scattering of X-rays in a spherical shell of material located at tens to thousands of r_g from the central source. If the reprocessing in each band is the result of scattering within the shell, and hard X-rays penetrate deeper into the shell as suggested by M10a, then the maximum lag in the response function due to the reprocessed component should be larger for the harder band, while the minimum lag should be the same in the two bands. Our best fitting TH-TH models (variants 2 and 3) are at odds with these predictions; the best fits have similar maximum lag in the two bands, but a larger minimum lag in the hard band.

The universe is not required to be in perfect harmony
with human ambition

Carl Sagan

5

Flux dependent X-ray time delays in a sample of Narrow Line Seyfert 1 galaxies

In this chapter I model the lag-frequency spectra in a small sample of NLS1 galaxies, as well as systematically exploring the flux dependence of the lag-frequency in each source. The growing number of NLS1s showing soft X-ray lags (e.g. De Marco et al. 2013b) and the increasing exposure time many objects are receiving, means that we can systematically explore the time delays as a function of source flux. De Marco et al. (2013b) presented lag-frequency data comparing a soft and hard band, but made no attempt to model the data. In Chap. 4 I demonstrated the flux-dependence of the low frequency lags in NGC 4051. Kara et al. (2013) also found some flux-dependence for the lags in IRAS 13224–3809. Understanding if, and how, the lag-frequency changes with flux in similar, low mass, highly X-ray variable sources, will help us better understand the origin of the lags.

As we saw in the previous chapter on NGC 4051, the X-ray spectral shape typically hardens as the source flux drops (e.g. Vaughan & Edelson 2001). However we note that the opposite behaviour (softening of the spectrum as the flux decreases) has been observed in a few LLAGN (e.g. NGC 7213; Emmanoulopoulos et al. 2012). The change in shape could be caused by a flux-correlated change in the emission or absorption spectrum of a component, or by a change in the relative strengths of components with differing spectral shapes (e.g. Shih et al. 2002; Fabian & Vaughan 2003). Studying the lag-frequency as a function of flux then provides valuable information that can be

used to associate the lagging components at a given frequency with spectral components.

5.1   Sample and data reduction

We select sources with significant soft lag detections from the literature. The sources are all radio quiet and X-ray unobscured ($N_{\mathrm{H}} < 2 \times 10^{22}$ cm^{-2}). The sources are selected based on high amplitude variability, low black hole mass ($\lesssim 10^7 \mathrm{M}_\odot$), and have at least 300 ks of available *XMM-Newton* data as of June 2013. The high variability amplitude ensures that the data will exhibit significant flux changes, and be a good candidate for lag-frequency analysis. The soft-lag—M_{BH} scaling relation observed in De Marco et al. (2013b) means that the segment sizes can be kept short while still giving sufficient frequency coverage to recover the soft lags (e.g. 20 ks) to give a large as possible range of flux, whilst keeping the soft lag within the frequency range of the segment length.

The properties and observation details of the objects used in this sample are shown in Table 5.1. We also include the NGC 4051 *XMM-Newton* data used in Chap. 3 and 4 for comparison and consistency with any new analysis methods used in this chapter.

5.1.1   Data reduction

As in Chap. 4 we use only the EPIC pn data from each observation and process them in a similar manner. The majority of the EPIC observations were made using small window (SW) mode; the fast CCD readout helps to mitigate event pile-up (Ballet 1999; Davis 2001). The window mode for each observation are listed in Table 5.1. EPIC observations taken in large window (LW) are more likely to be affected by pile-up. We assessed the potential impact of pile-up using the SAS task EPATPLOT, and found all but one object to be unaffected. In the case of Ark 564 the count rate is such that pile-up becomes an issue in the EPIC-pn. We therefore remove a 5 arcsecond circle from the central region of the circular aperture, following the analysis procedure for Ark 564 by Legg et al. (2012) and Kara et al. (2013). Strong background flares can introduce spurious time lags, so particular care has been taken to remove the influence of background variations (typically worse at the end of each observation).

The light curves for the total (0.2–10 keV) band for each object are shown in shown in Figs. 5.1 through 5.5.

5.2   All flux lag-frequency

In this section we explore the lag-frequency using the entire dataset for each object. We calculate the lag-frequency using a soft and hard energy band following the procedure

Table 5.1: Observation details and sample properties. (1) Name; (2) *XMM-Newton* Obs ID; (3) Observation duration; (4) Log black hole mass, uncertainty, estimate technique (R: reverberation mapping, S: stellar velocity dispersion, L: $L_{5100\text{\AA}}$ versus R_{BLR}) with references (a: Denney et al. 2009; b: Bentz et al. 2009; c: Zhang & Wang 2006; d: Oliva et al. 1999; e: Bian & Zhao 2003; f: Zhou et al. 2010; (5) soft/hard X-ray energy bands.

| Name	Obs ID	Duration (ks)	Log (M_{BH})	Esoft/hard (keV)
(1)	(2)	(3)	(4)	(5)
NGC 4051	-	-	6.24 ± 0.14 R, a	0.3-1/2-5
Mrk 766	0109141301	130	6.25 ± 0.35 R, b	0.3-0.7/1.5-4
	0304030301	99		
	0304030401	99		
	0304030501	96		
	0304030601	99		
	0304030701	35		
Ark 564	0206400101	102	6.27 ± 0.50 L, c	0.3-1/1.2-4
	0670130201	59		
	0670130301	55		
	0670130401	63		
	0670130501	67		
	0670130601	60		
	0670130701	64		
	0670130801	58		
	0670130901	55		
MCG-6-30-15	0111570101	47	6.30 ± 0.40 S/E, d,f	0.3-1.0/1.2-4
	0111570201	66		
	0029740101	89		
	0029740701	129		
	0029740801	130		
1H 0707-495	0110890201	47	6.31 ± 0.50 L, e	0.3-1/1.2-4
	0148010301	79		
	0506200301	40		
	0506200201	40		
	0506200501	46		
	0506200401	42		
	0511580101	123		
	0511580201	123		
	0511580301	122		
	0511580401	121		
	0653510301	116		
	0653510401	128		
	0653510501	127		
	0653510601	129		
	0554710801	95		
IRAS 13224-3809	0110890101	64	6.76 ± 0.50 L, e	0.3-1.0/1.2-4
	0673580101	133		
	0673580201	132		
	0673580301	129		
	0673580401	134		
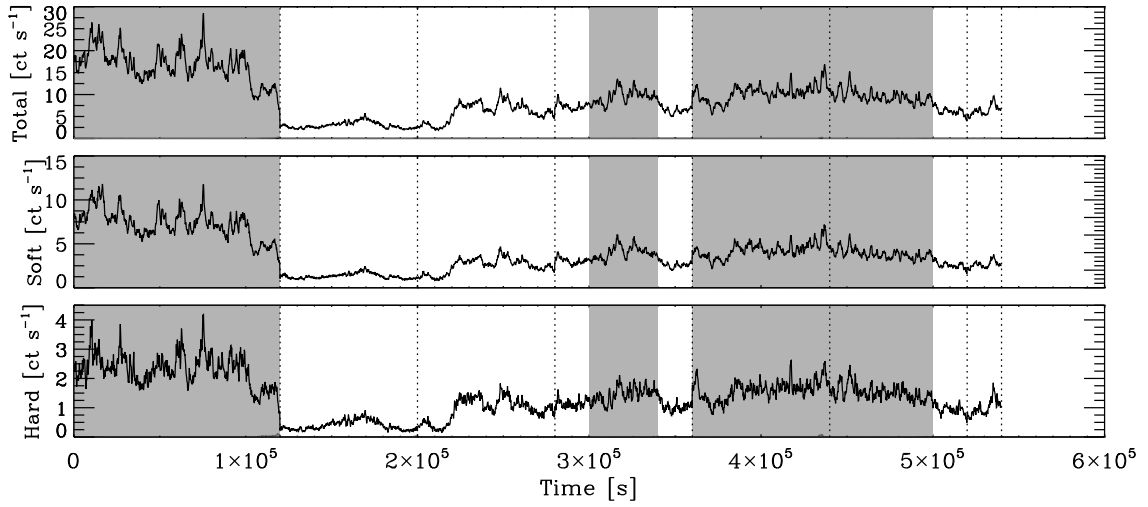
Figure 5.1: Light curves for Mrk 766, showing the total, soft and hard band light curve segments used in the fluxed analysis. The grey bands are the high flux segments. The vertical dotted lines separate the individual observations. The dark grey curve is the background level in each band.
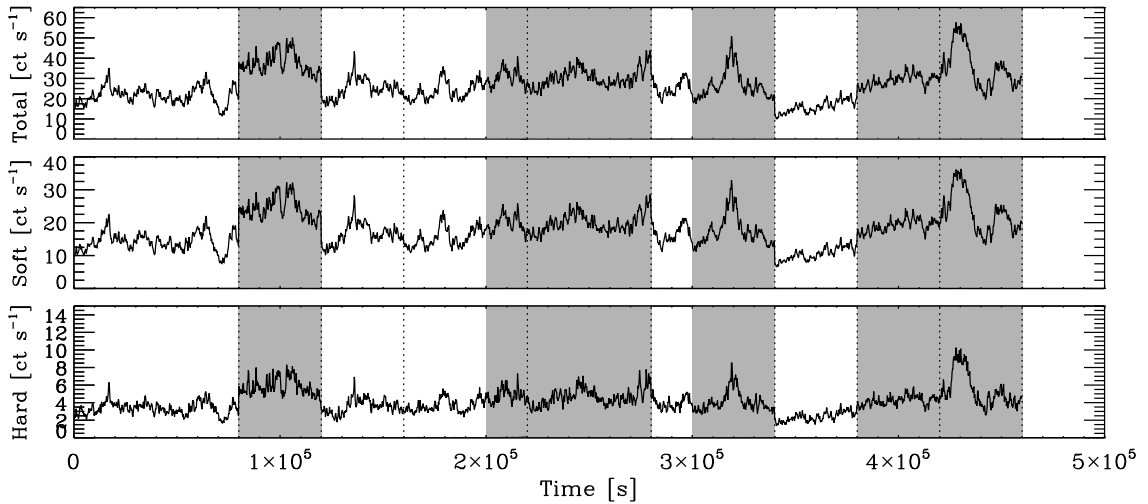
Figure 5.2: Light curves for Ark 564, showing the total, soft and hard band light curve segments used in the fluxed analysis. The grey bands are the high flux segments. The vertical dotted lines separate the individual observations. The dark grey curve is the background level in each band.

laid out in Section 2.4. The exact energy range for each object is listed in Table 5.1, and is slightly different for each object. The energy bands are chosen to best pick out the soft lag, and are in approximate agreement with the energy bands used in the literature (De Marco et al. 2013b; Emmanoulopoulos et al. 2011; Kara et al. 2013). The hard energy band is chosen to best pick out the primary power-law continuum, and be free from any the red wing of the broad iron Kα emission. No data above 5 keV was included, in order to avoid the Kα line.

The time series are split up in to segments for the averaging process of the cross-
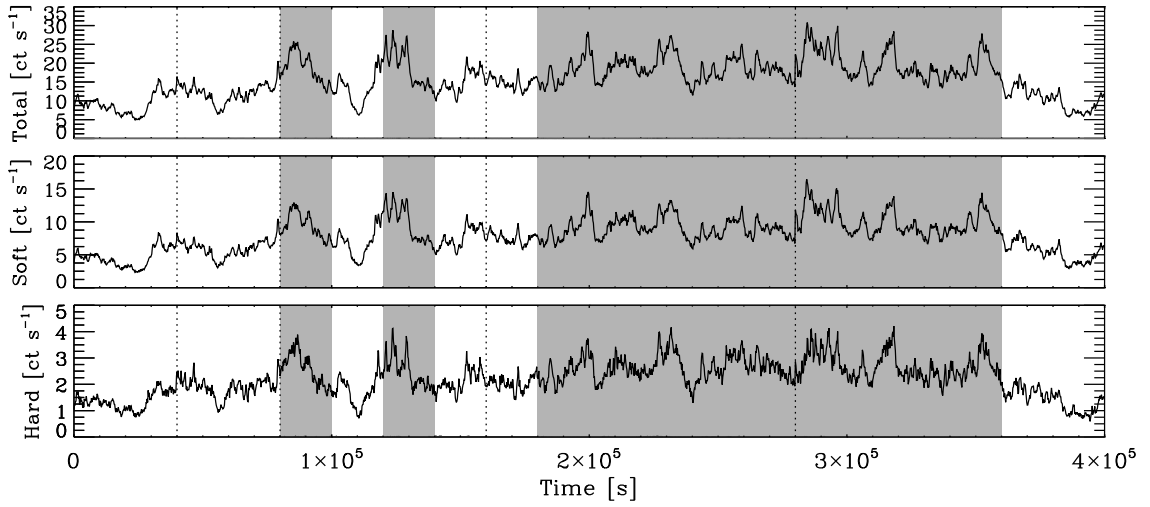
Figure 5.3: Light curves for MCG–6-30-15 , showing the total, soft and hard band light curve segments used in the fluxed analysis. The grey bands are the high flux segments. The vertical dotted lines separate the individual observations. The dark grey curve is the background level in each band.
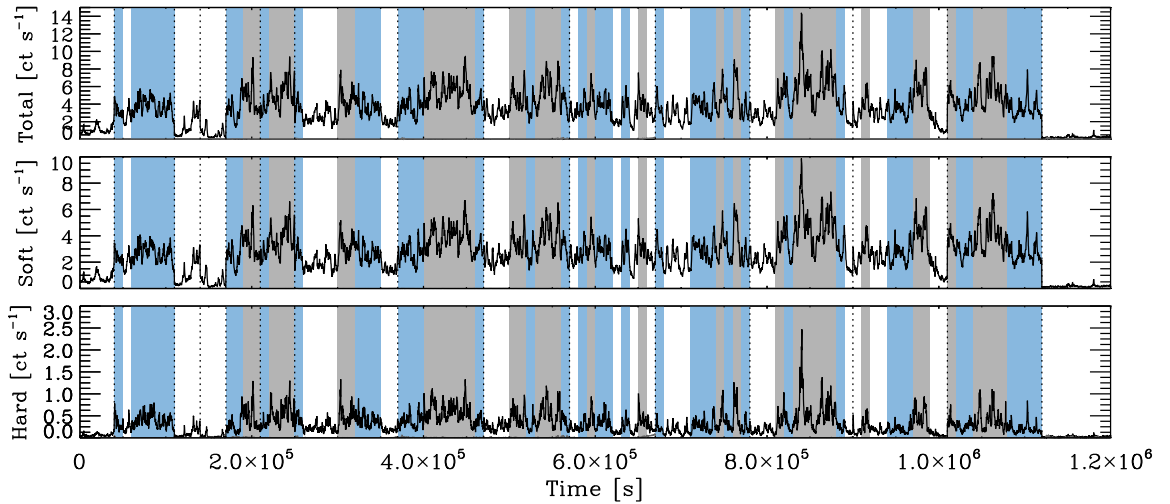

Figure 5.4: Light curves for 1H0707-495, showing the total, soft and hard band light curve segments used in the fluxed analysis. The grey and blue bands are the high and medium flux segments respectively. The vertical dotted lines separate the individual observations. The dark grey curve is the background level in each band.

spectrum, and are typically 20–40 ks. The segment size is chosen in order to maximise the the hard lag at low frequencies, whilst maintaining as larger number of segments, M, to average over, thus keeping the error bars approximately Gaussian. The resulting lag-frequency spectra were rebinned by averaging over geometrically space frequency bins, increasing with frequency by a factor, n, where $n = 1.2 - 1.6$, depending on the quality of the data. A time bin of $dt = 20$ seconds was used throughout. The *raw* and *noise-corrected* coherence (Section 2.4) was used to determine the highest frequency a meaningful lag estimate can be made. We took values of raw coherence >0.1 or noise-
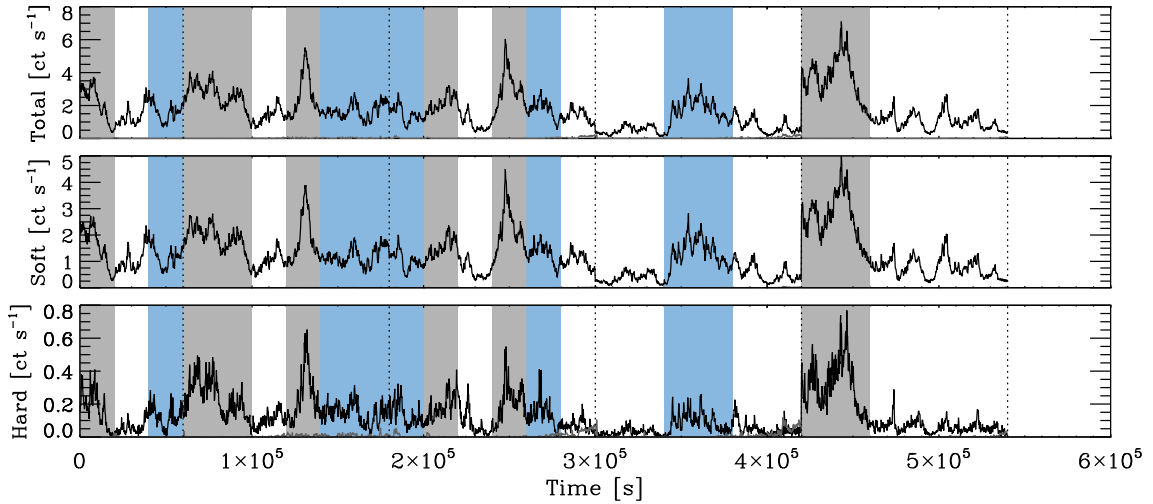
Figure 5.5: Light curves for IRAS 13224–3809, showing the total, soft and hard band light curve segments used in the fluxed analysis. The grey and blue bands are the high flux segments respectiveluy. The vertical dotted lines separate the individual observations. The dark grey curve is the background level in each band.

corrected coherence >0.3.

The resulting lag-frequency spectra are presented in Figs. 5.6 and 5.7 (same data in each figure. The modelling presented in these figures is discussed in Section 5.3. The lag-spectra are in good agreement with previous findings in the literature (e.g. Zoghbi & Fabian 2011; Emmanoulopoulos et al. 2011; De Marco et al. 2013b; Kara et al. 2013).

5.3 Modelling the lag

We model the lag-frequency using the same simple analytical response functions as in Chap. 4 (see also Section 4.3.2). As before, we make use of a top hat plus δ response function (TH), and a power-law (PL) dependence on lag-frequency (see Section 4.3.2)

In the previous chapter, the time lag τ was generated as a function of frequency for each version of the given model. The model was then fitted to the lag at each frequency bin centre using $\min(\chi^2)$ optimisation. In this chapter, however, we extend the modelling of the previous chapter in a number of ways. First, we compute the lags predicted for a given response function in a different manner. We compute the real and imaginary parts of the complex analytical transfer function for a given model. This is then integrated and averaged over each frequency bin to produce an average phase lag for that frequency bin. This more closely parallels the process of estimating the lags from data, and better handles cases where the transfer function changes rapidly within a frequency bin. Second, the model parameter space is explored using Markov Chain Monte Carlo simulations (see Section 2.8). A flat prior distribution on each parameter is used as well
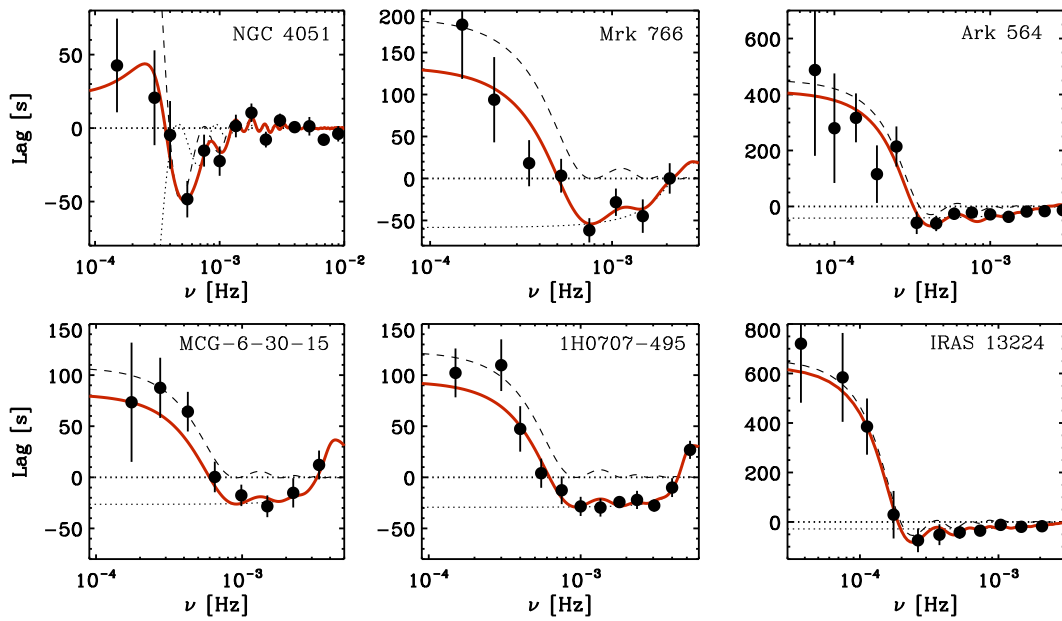
Figure 5.6: Best fitting TH-TH model (red) to the *all*-flux lag-frequency spectra for the sample. The dashed and dotted lines show the transfer function in the hard and soft energy bands respectively.
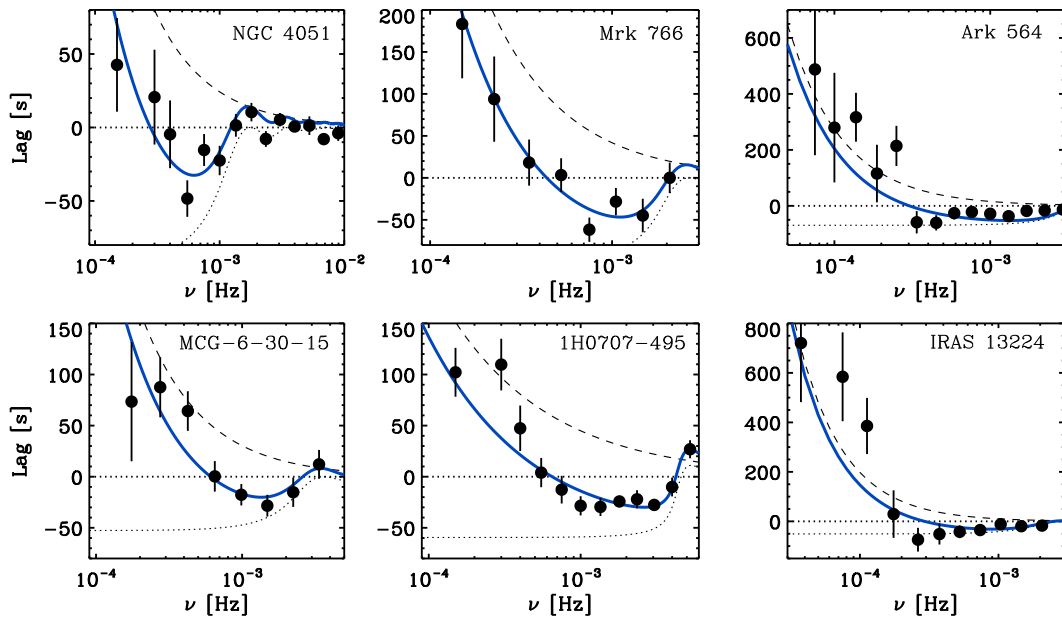

Figure 5.7: Best fitting PL-TH model (blue) to the *all*-flux lag-frequency spectra for the sample. The dashed and dotted lines show the transfer function in the hard and soft energy bands respectively.

Table 5.2: Model fits and parameters for TH-TH model and PL-TH model to the all flux lag-spectra. (1) Object; (2) χ^2 / degrees-of-freedom; (3) p-value; (4), (5), (6) hard band parameters; (7), (8), (9) soft band parameters.

Object	χ^2 / dof	p value			Params			
(1)	(2)	(3)	(4)	(5)	(6)	(7)	(8)	(9)
					TH-TH model			
			S_h	t_0^h	w_h	S_s	t_0^s	w_s
NGC 4051	10/8	0.25	0.47 ± 0.09	1370 ± 75	575 ± 45	0.64 ± 0.16	-145 ± 50	2290 ± 110
Mrk 766	5.1/2	0.08	0.35 ± 0.22	60 ± 540	1220 ± 580	0.34 ± 0.11	225 ± 235	10 ± 465
Ark 564	15.6/10	0.11	0.46 ± 0.05	490 ± 75	1860 ± 135	0.25 ± 0.03	130 ± 850	1530 ± 230
MCG–6-30-15	1.5/2	0.46	1.77 ± 0.72	135 ± 170	1120 ± 120	5.21 ± 1.71	-135 ± 20	320 ± 50
1H 0707–495	5.3/6	0.51	0.31 ± 0.26	-30 ± 705	1095 ± 230	6.17 ± 1.74	-80 ± 10	230 ± 15
IRAS 13224-3809	1.4/5	0.9	0.35 ± 0.05	1035 ± 230	3020 ± 525	0.29 ± 0.56	60 ± 180	251 ± 210
					PL–TH model			
			N_h	α_h		S_s	t_0^s	w_s
NGC 4051	24.7/11	0.25	0.026 ± 0.025	0.99 ± 0.11		0.46 ± 0.15	0 ± 95	565 ± 105
Mrk 766	5.1/3	0.16	0.034 ± 0.075	1.02 ± 0.25		1.16 ± 3.33	0 ± 490	380 ± 490
Ark 564	24.7/11	0.01	0.003 ± 0.003	1.24 ± 0.11		0.56 ± 0.23	0 ± 60	275 ± 60
MCG–6-30-15	10.6/3	0.01	0.022 ± 0.034	1.04 ± 0.17		0.61 ± 0.28	0 ± 50	275 ± 90
1H 0707–495	14.3/7	0.05	0.054 ± 0.066	0.64 ± 0.14		1.21 ± 0.63	45 ± 30	130 ± 60
IRAS 13224-3809	16.1/7	0.01	0.0015 ± 0.0027	1.28 ± 0.18		0.45 ± 0.27	0 ± 130	330 ± 145

as a Gaussian proposal distribution.

We start by fitting a PL response function to the hard band only. We find this gives a inadequate description of the data, due to the model giving only positive lag values at all frequencies.

We next model the data using a TH in the hard band only, and show the fitting results in Table 5.2. Again, this gives a poor fit to the data. A single TH in the hard band has been used to model the lag in NGC 4051 (Miller et al. 2010) and Ark 564 (Legg et al. 2012). However, our model fitting is at odds with this claim, as was found for NGC 4051 in Chap. 4. This means that, for each object with a well-detected soft lag, the lag is not well explained as an artifact of a lag in the hard band resulting from a sharp impulse response function.

Due to the unacceptable fits using a single transfer function in the hard band only, we move to a more complicated model by including a response in the soft band. We start with a top hat in each band (TH-TH model), which has six parameters, three for each band. The results of the TH-TH model fitting are displayed in Table 5.2. We find this model provides a good fit to all the objects, and show the best fit model in Fig. 5.6. The results for NGC 4051 are consistent with Alston et al. 2013a (see Section 4.3.2). The results for Mrk 766 and MCG-6-30-15 are also consistent with E11. We note that in NGC 4051 , Ark 564 and IRAS 13224 , the hard band t_0 is significantly shifted away from zero. These objects also do not display as broad (in frequency) soft lags as the other objects in the sample.

We next try a model variant with a PL in the hard band, and TH plus δ-function response in the soft band (PL-TH model). The results are displayed in Table 5.2. This model gives acceptable fits to the data in all objects, and we show the best fit model in Fig. 5.7.

5.4 Fluxed lag-frequency

In this section we explore the flux dependence on the lag frequency spectrum. The data for each object is divided into equal length segments, and the mean count rate in the total band (0.2–10 keV) was computed for each. The segments are then sorted by flux into a number of bins. In MCG–6-30-15 , Mrk 766 and Ark 564 the data can be split into 2 flux bins, whereas in NGC 4051 , IRAS 13224 and 1H 0707-495 the data can be split into 3 flux bins. The lag-spectra as a function of source flux are shown in Figs. 5.8 to 5.13.
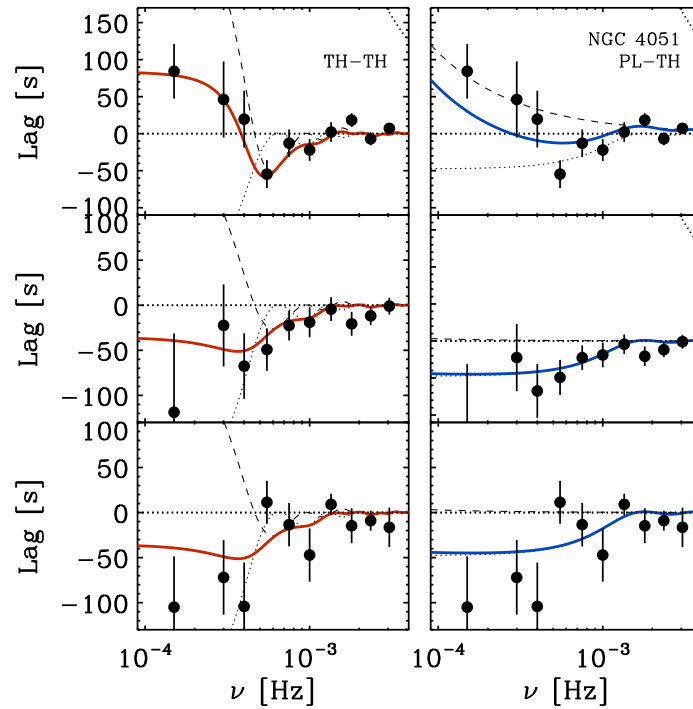
Figure 5.8: Model fits to the lag-frequency spectra in NGC 4051 as a function of source flux. The panels from top to bottom show the high to low flux bins respectively. The left panels show the total model fit (red) for the TH-TH model. The right panels show the total fit (blue) for the PL-TH model. The dashed and dotted lines show the hard and soft transfer function respectively in each model.
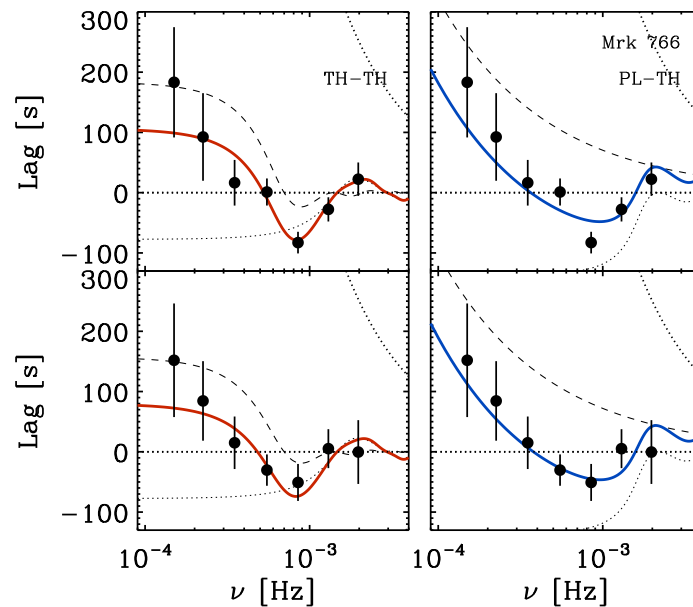
Figure 5.9: Model fits to the lag-frequency spectra in Mrk 766 as a function of source flux. The panels from top to bottom show the high to low flux bins respectively. The left panels show the total model fit (red) for the TH-TH model. The right panels show the total fit (blue) for the PL-TH model. The dashed and dotted lines show the hard and soft transfer function respectively in each model.
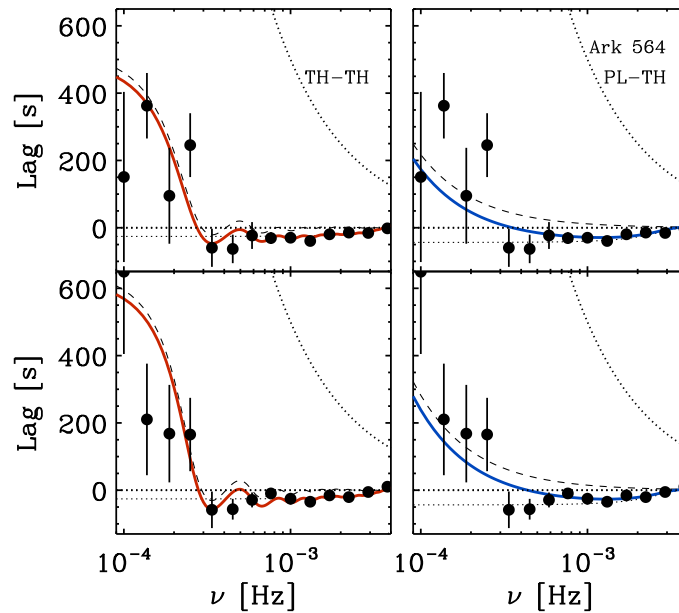
Figure 5.10: Model fits to the lag-frequency spectra in Ark 564 as a function of source flux. The panels from top to bottom show the high to low flux bins respectively. The left panels show the total model fit (red) for the TH-TH model. The right panels show the total fit (blue) for the PL-TH model. The dashed and dotted lines show the hard and soft transfer function respectively in each model.
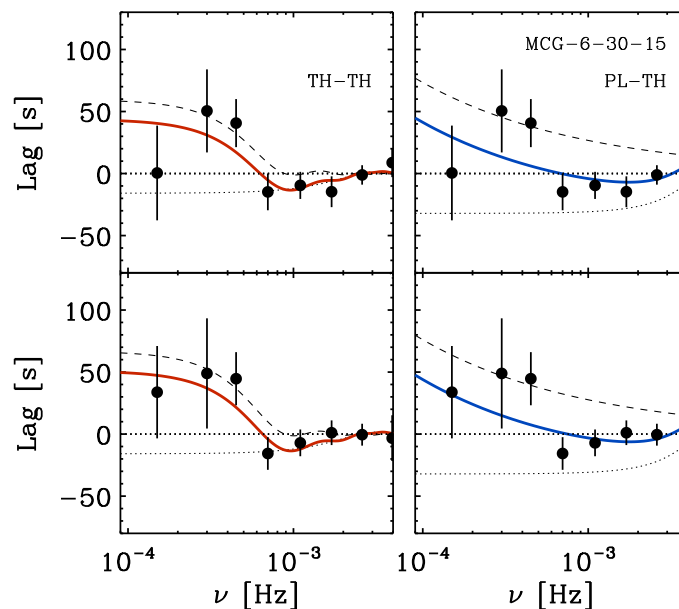

Figure 5.11: Model fits to the lag-frequency spectra in MCG–6-30-15 as a function of source flux. The panels from top to bottom show the high to low flux bins respectively. The left panels show the total model fit (red) for the TH-TH model. The right panels show the total fit (blue) for the PL-TH model. The dashed and dotted lines show the hard and soft transfer function respectively in each model.
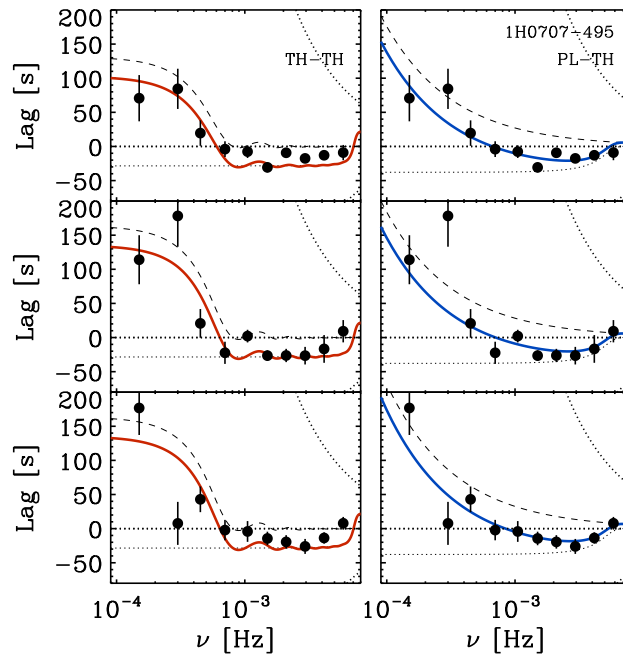
Figure 5.12: Model fits to the lag-frequency spectra in 1H 0707-495 as a function of source flux. The panels from top to bottom show the high to low flux bins respectively. The left panels show the total model fit (red) for the TH-TH model. The right panels show the total fit (blue) for the PL-TH model. The dashed and dotted lines show the hard and soft transfer function respectively in each model.
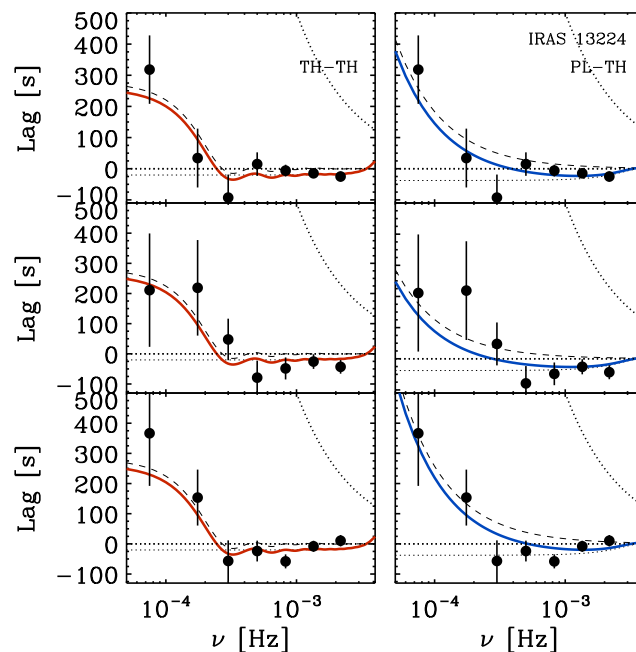
Figure 5.13: Model fits to the lag-frequency spectra in IRAS 13224-3809 as a function of source flux. The panels from top to bottom show the high to low flux bins respectively. The left panels show the total model fit (red) for the TH-TH model. The right panels show the total fit (blue) for the PL-TH model. The dashed and dotted lines show the hard and soft transfer function respectively in each model.

5.5 Modelling the flux dependence

We model the lag-frequency as a function of source flux using the same transfer functions described in Section 5.3. As a single transfer function in the hard band gave an unacceptable fit ($p < 10^{-4}$) to the all-flux data, we concentrate on the TH-TH and PL-TH models only. The fitting procedure is the same as that in Section 5.3.

The models are simultaneously fit to the lag-frequency spectra at each flux level. We start with the TH-TH model. Only the scaling fraction of the hard band S_h is free to vary with flux, whereas the remaining parameters are tied across flux level. In Table 5.3 we show the best fit TH-TH model The model was fitted to each flux level, with all parameters tied across flux level. This tells us the goodness of fit assuming no change with flux level. In Table 5.3 we show the $\Delta \chi^2$ between the tied and free scaling fraction variants of the model. We can see that only NGC 4051 and Ark 564 show a significant change with flux, in the sense that the χ^2 of the best-fitting model was substantially reduced when the scaling factor was allowed to vary with flux. In the case of Ark 564 the $\Delta \chi^2 \sim 5$ corresponds to a $\sim 2.5\sigma$ change with flux for two interesting parameters. In Fig. 5.14 we show the high and low flux S_h parameter from the MCMC chain output for Ark 564. Plotted against each other in this way we can see that a change with flux is preferred over no change with flux. The fraction of the points above the line is $\sim 90\%$. If there was no change with flux, the points would be centered on the line of $y = x$ shown in Fig. 5.14.

We investigated the TH-TH model variant where only the soft-band scaling-fraction S_s is untied across flux. The only object to show any change with source flux is NGC 4051, in agreement with the results found in Chap. 4. In the remaining sources, the error bars on this parameter are too large to detect any change with source flux.

We repeat the fitting procedure for the PL-TH model, this time allowing only the hard-band normalisation N_h to vary with flux. The fit results are shown in Table 5.4, as well as the $\Delta \chi^2$ for an *all tied* model. The model gives an acceptable fit to each source. However, the only source to show any flux dependence on N_h is NGC 4051, in agreement with the results found in Alston et al. (2013a) (see Section 4.3.2). Unlike in the TH-TH model, Ark 564 shows no significant change with flux.

The variant of the PL-TH model where the soft-band scaling-fraction S_s is untied across flux was also investigated. This model also gave acceptable fits to each source. Again, the only source to show a significant change with flux was NGC 4051.

Table 5.3: Fit results to the lag-frequency spectra for TH-TH model with S_h untied. (1) Object; (2) χ^2 / degrees-of-freedom; (3) $\Delta\chi^2$ between all tied model variant; (4) High; (5) Medium; (6) Low flux S_h parameter.

| Object | χ^2/dof | $\Delta\chi^2$ | S_h | | |
| | | | High | Medium | Low |
(1)	(2)	(3)	(4)	(5)	(6)
NGC 4051	19.3/22	-	0.43 ± 0.09	0.23 ± 0.08	0.15 ± 0.07
Mrk 766	5.4/9	0.5	0.58 ± 0.45	-	0.37 ± 0.26
Ark 564	30.9/25	4.8	0.45 ± 0.07	-	0.62 ± 0.07
MCG–6-30-15	8.4/9	0.1	0.11 ± 0.05	-	0.13 ± 0.05
1H 0707–495	16/16	2.0	0.27 ± 0.10	0.36 ± 0.13	0.29 ± 0.09
IRAS 13224–3809	13.1/13	2.3	0.17 ± 0.05	0.18 ± 0.08	0.26 ± 0.07

Table 5.4: Fit results to the lag-frequency spectra for PL-TH model with N_h untied. (1) Object; (2) χ^2 / degrees-of-freedom; (3) $\Delta\chi^2$ between all tied model variant; (4) High; (5) Medium; (6) Low flux N_h parameter.

| Object | χ^2/dof | $\Delta\chi^2$ | N_h | | |
| | | | High | Medium | Low |
(1)	(2)	(3)	(4)	(5)	(6)
NGC 4051	28/23	-	0.038 ± 0.007	$< 0.001 \pm 0.001$	$< 0.001 \pm 0.001$
Mrk 766	5.4/9	0.5	0.75 ± 0.63	-	0.76 ± 0.65
Ark 564	30.9/25	4.8	0.0017 ± 0.0014	-	0.0022 ± 0.0017
MCG–6-30-15	8.4/9	0.1	1.28 ± 1.12	-	1.32 ± 1.18
1H 0707–495	16/16	2.0	0.09 ± 0.07	0.1 ± 0.07	0.1 ± 0.07
IRAS 13224–3809	13.1/13	2.3	0.004 ± 0.002	0.003 ± 0.002	0.003 ± 0.002
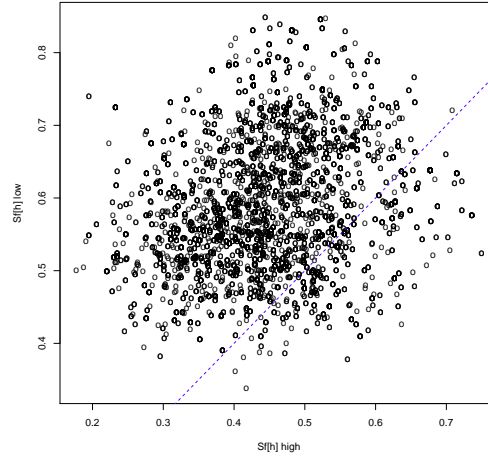
Figure 5.14: MCMC output for S_h parameters for the TH-TH model fit to the high and low flux lag-frequency of Ark 564. S_h for each flux level is plotted against each other, and a line of $y = x$ is shown in blue (we show only the last 5000 MCMC chain iterations for clarity). The distribution of points is evenly distributed, and away from the line of $y = x$, indicating a clear change in this parameter with flux.

5.6 Understanding the flux changes

In this section we look at how the results from the transfer function fitting in Section 5.5 compare with the properties of the source as a function of flux. First we compare the change in scaling fractions ($S_\mathrm{h}, S_\mathrm{s}$) in the TH-TH model with the mean source flux of the segments used to compute the lag-frequency at each flux level, where $f/ < f >$ is the rate of each segment relative to the mean rates over all segments. This is shown in panels (c) and (f) of Fig. 5.15. Whilst a general change in S_s with source flux can be seen in panel (f), the error bars are too large to confirm this result. We can see in panel (c) that only NGC 4051 and Ark 564 show any significant change in S_h with flux level, in agreement with the fitting from Section 5.5. However, there is a notable difference in the change of S_h with source flux between these two objects. NGC 4051 shows and increase in S_h as flux decreases, whilst NGC 4051 shows the opposite behaviour, with an increase in S_h in source flux.

In panels (a) and (d) of Fig. 5.15 we compare the hardness ratio $H_\mathrm{X} = X_\mathrm{hard}/X_\mathrm{soft}$ of the energy bands used to calculate the lag-frequency spectrum in each source, with the $S_\mathrm{h}, S_\mathrm{s}$ values from the model fitting. We can see now that the change in S_h with hardness ratio is the same between NGC 4051 and Ark 564 , although the change in hardness ratio in Ark 564 is very small. Again the errors on S_h in the remaining sources, and S_s in all sources, are consistent with no change with source flux.

In panels (b) and (e) of Fig. 5.15 we compare the ratio of the variance between the hard and soft energy bands used compute the lag-frequency spectra. This is like a hard-
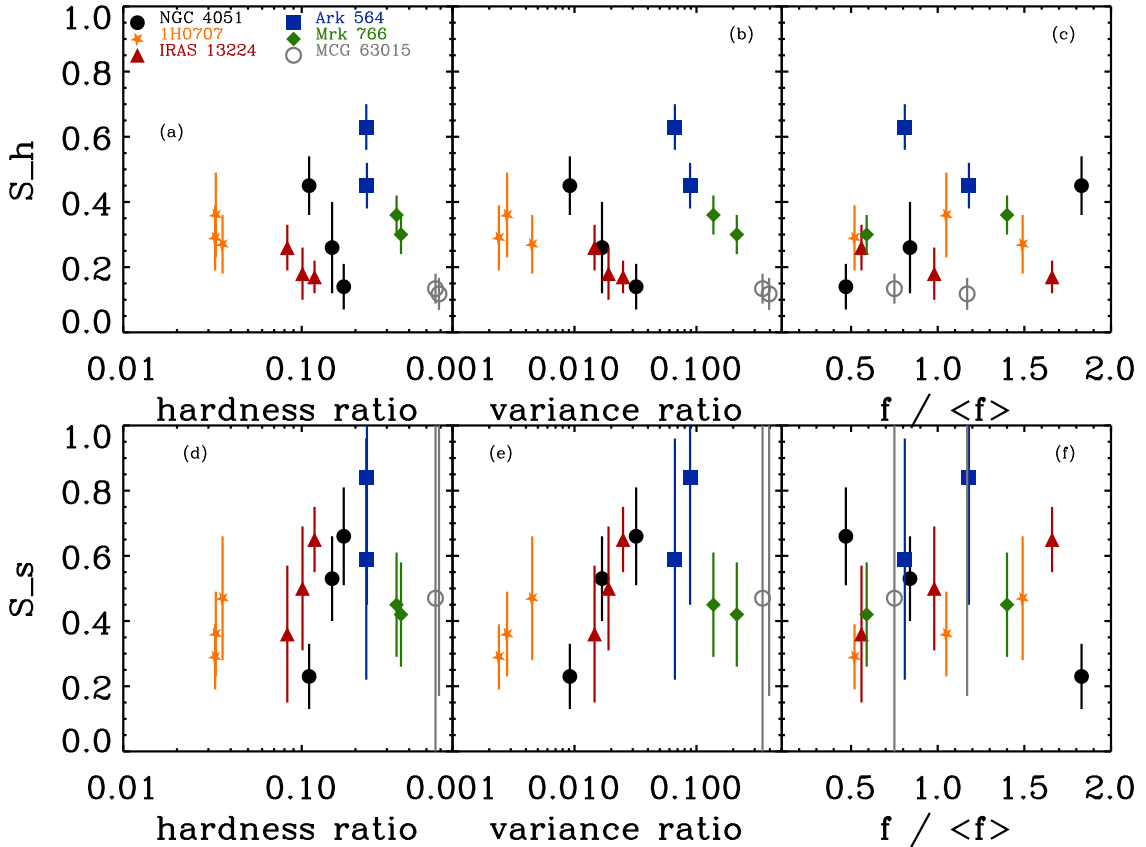
**Figure 5.15:** Change of scaling fraction with flux in TH-TH model. The top panels show the change in S_h hardness ratio (a), variance ratio (b) and mean flux level (c). The bottom panels show the change in S_s hardness ratio (d), variance ratio (e) and mean flux level (f).

ness ratio derived from the rms spectrum. In panel (b) we can see that the change in S_h with the variance ratio is the same in NGC 4051 and Ark 564. Although the remaining objects do show a change in variance ratio with source flux, the error bars on S_h are too large to detect a significant change. The only object to show a significant change with S_s is NGC 4051.

Excluding NGC 4051, no significant change is detected with source flux in the PL-TH model, so we do not show the same comparison with hardness ratio and variance ratio.

5.6.1 Source spectra

In Figs. 5.16 to 5.21 we show the mean, rms and covariance spectra for the high and low flux levels in each source. For sources that were divided into 3 flux levels, we do not show the medium flux spectra. The rms is calculated from the time domain, and the covariance spectra is determined from the Fourier domain method (see Section 2.6). The

rms and covariance spectrum are calculated for the total frequency range, i.e. from the $1/2dt$ to $1/Ndt$, where Ndt is the length of the segments used in the flux analysis for each source. The lower panels in Figs. 5.16 to 5.16 show the ratio between the low and high spectra. At energies $\gtrsim 2$ keV, each of the spectra is seen to harden at lower fluxes, whereas below ~ 2 keV, the spectrum is either flat or softens with decreasing flux.

NGC 4051 and Ark 564 were the only objects to show a significant change in S_h with source flux. The ratio of the variability in NGC 4051 (lower panel of Fig. 5.16) shows the soft band (0.3-1 keV) variability is suppressed more than the hard band (2-5 keV) as the flux drops. The ratio plot for Ark 564 (lower panel of Fig. 5.18) shows the opposite behaviour, where the hard band (1.2-4 keV) is suppressed more than the soft band (0.3-1 keV) as the flux drops. Similar changes are observed in the spectra with source flux in the remaining sources, however no significant change in the lag-frequency is detected in these sources.
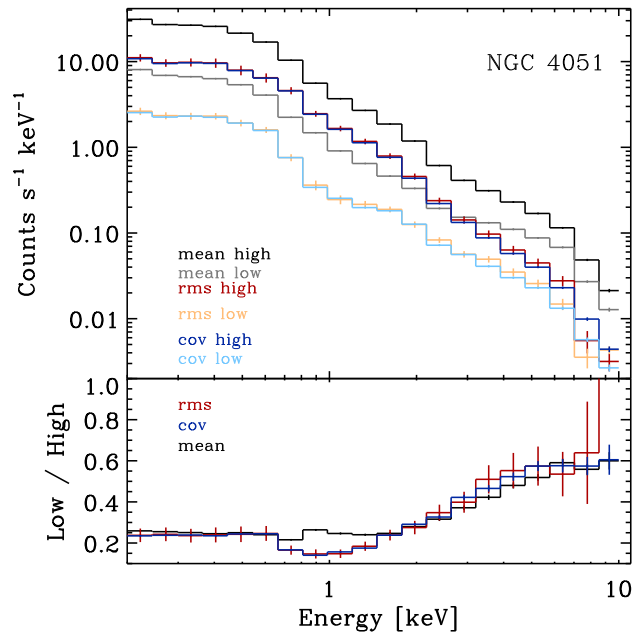
Figure 5.16: Time-integrated, rms and covariance spectra for NGC 4051, for the high and low flux segments. The ratio between high and low spectra can be seen in the lower panel.
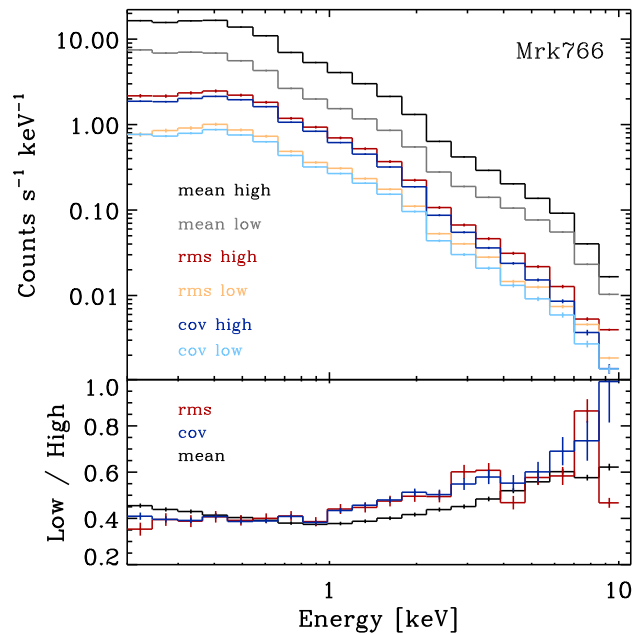

Figure 5.17: Time-integrated, rms and covariance spectra for Mrk 766, for the high and low flux segments. The ratio between high and low spectra can be seen in the lower panel.
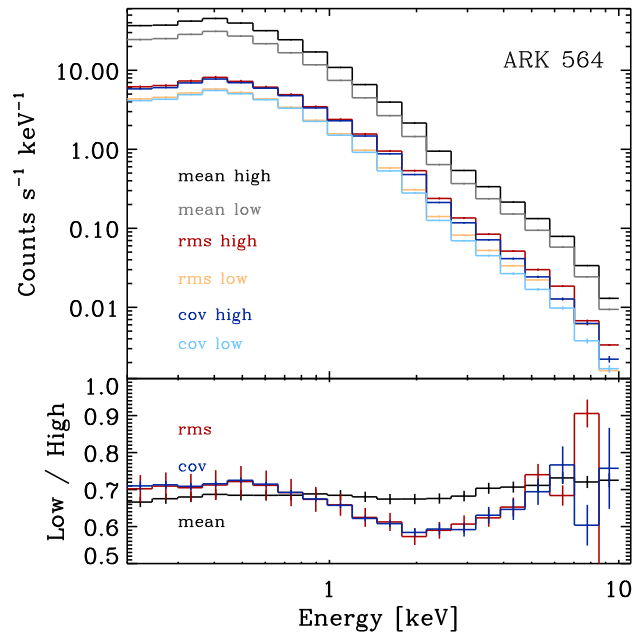
Figure 5.18: Time-integrated, rms and covariance spectra for Ark 564, for the high and low flux segments. The ratio between high and low spectra can be seen in the lower panel.
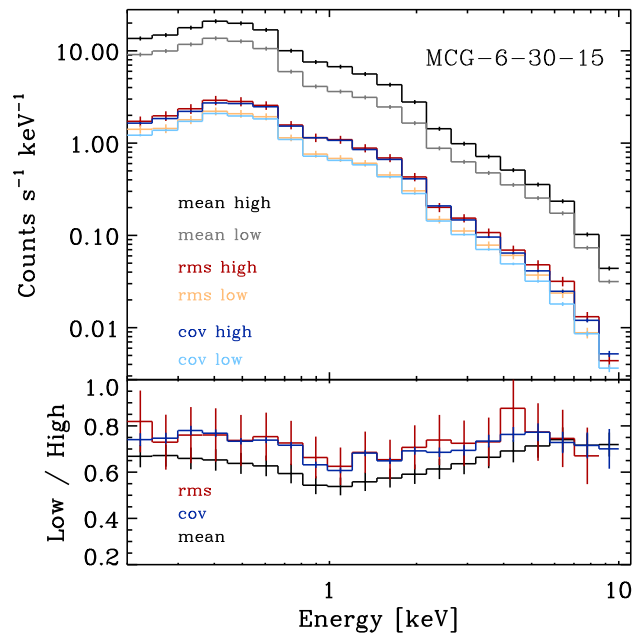

Figure 5.19: Time-integrated, rms and covariance spectra for MCG–6-30-15 , for the high and low flux segments. The ratio between high and low spectra can be seen in the lower panel.
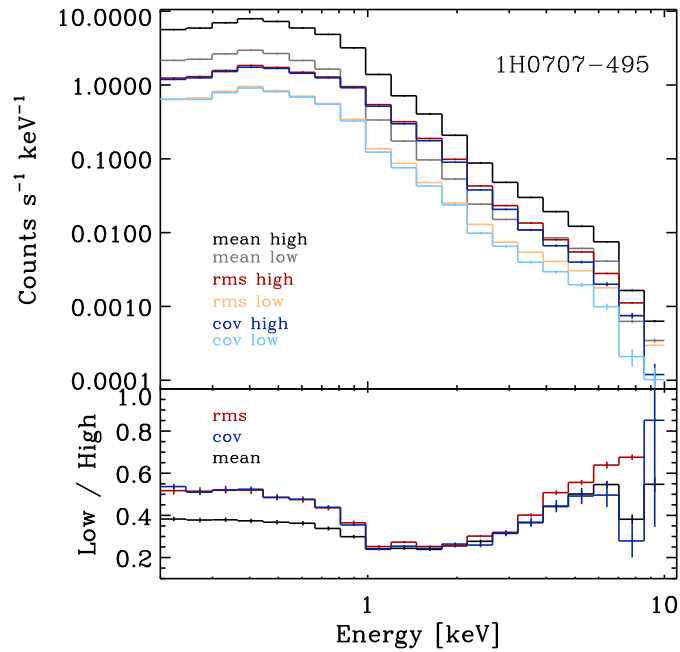
Figure 5.20: Time-integrated, rms and covariance spectra for 1H0707-495, for the high and low flux segments. The ratio between high and low spectra can be seen in the lower panel.
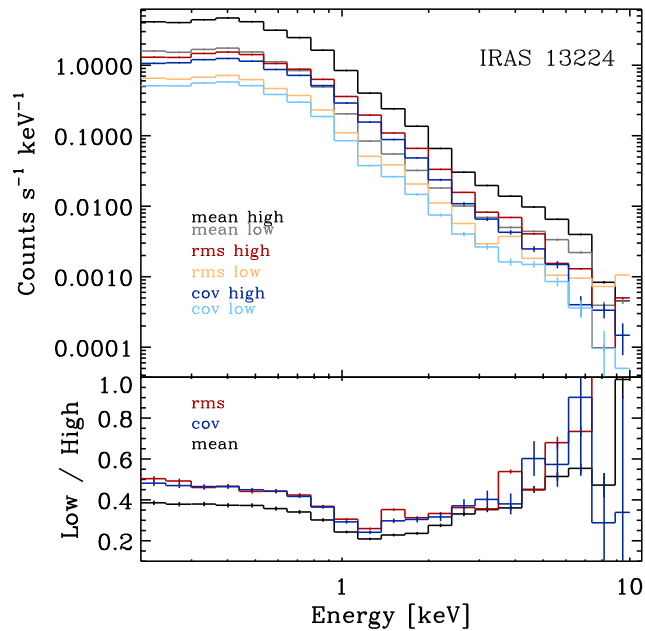

Figure 5.21: Time-integrated, rms and covariance spectra for IRAS 13224-3809, for the high and low flux segments. The ratio between high and low spectra can be seen in the lower panel.

5.7   Discussion and conclusions

We have studied the frequency dependent time delays in a sample of highly variable NLS1 galaxies. The lag-frequency was first explored using all the available data. We find consistent results with the shape of the lag-frequency spectra and frequency and magnitude of the soft lag reported for NGC 4051 (De Marco et al., 2013b), Mrk 766 (Emmanoulopoulos et al. 2011; De Marco et al. 2013b), Ark 564 (De Marco et al. 2013b; Kara et al. 2013), MCG–6-30-15 (Emmanoulopoulos et al. 2011; De Marco et al. 2013b), 1H0707-495 (Zoghbi & Fabian 2011; De Marco et al. 2013b), IRAS 13224–3809 (Kara et al., 2013).

Legg et al. (2012) reported on hard lags in NGC 4051 and Ark 564, but did not identify a soft ('negative') lags. Miller et al. (2010) also reported only hard band lags in NGC 4051. Miller et al. (2010) and Legg et al. (2012) both used a different analysis method, and data from *Suzaku* which contain periodic gaps (due to the ~ 96 min Low Earth orbit), and used a much longer time bins (256 s) than our analysis. In Legg et al. (2012) *XMM-Newton* data on Ark 564 were used, however these authors use a different analysis method for producing lag-frequency spectra than is presented in this work. As noted in Section 4.5, it may well be the case that the data or analysis used by these authors are less sensitive to the short (~ 50 s) lag we observe with *XMM-Newton*.

The lag-frequency data, averaged over all fluxes, was fitted using using two simple kinds of impulse response models: a top hat (TH) response in the time domain and a time lag that varies with frequency as a power law (PL), following on from the modelling of NGC 4051 in Chap. 4. We find that a single TH or PL in the hard band does not give an acceptable description of the data in any source. This finding is at odds with the claims of Miller et al. (2010) and Legg et al. (2012) who consider only a time-delayed respond in the hand band, e.g. a single TH. However, as previously noted these data are possibly not sensitive enough to the soft lag signature at higher frequencies. These authors also did not test models with an explicit soft lag, rather, they performed a simplistic comparison using a hard-lag only model.

More complicated models with a response in each band (TH-TH; PL-TH) give acceptable fits to the (all flux) lag-frequency data of all sources, with no model preferred over the other. The high frequency soft lags previously observed in the objects in this sample are most commonly interpreted as the signature of reverberation by some authors (e.g. Zoghbi & Fabian 2011; Emmanoulopoulos et al. 2011; Kara et al. 2013). Although high frequency soft lags have been claimed in Ark 564 and IRAS 13224–3809, in these papers the lag-frequency data were presented but no attempt was made to model the data in terms of impulse response functions, which is a goal of the present work. The require-

ment of a soft lagging component in these two sources provides strong evidence for the soft emission resulting from the reprocessing of a hard intrinsic spectrum.

The requirement for two lagging components in all sources in the present sample has strong implications for the distant reflector interpretation of the soft lags. Miller et al. (2010) introduced an additional soft lagging component to account for the broad frequency range of the soft lags in 1H0707–495. To broaden the soft lag frequencies the width of the soft band transfer function has to be much narrower than the hard band transfer function. In the distant reflector model this requires the soft lagging component to lie close to the line of sight. Such a geometry is conceivable in one object, but to be seen in many objects requires a high degree of fine tuning. A more natural interpretation of the soft lagging component is a small-scale reflector/reprocessing model, where the hard and soft lagging components results from two separate processes.

An aim of this study was to assess whether the unusual flux-dependence of the time lags observed in NGC 4051 (Chap. 4) were unique to that object or common to NLS1s. We therefore divided each observation into two or three distinct flux ranges, and allowed the strengths of the delayed components (e.g. TH) to vary as a function of flux (in either hard or soft bands). The only other source in the present study to show a dependence on source flux was Ark 564. The hard band scaling fraction S_h showing the opposite dependence on mean flux level to NGC 4051. However, when comparing the dependence on hardness ratio and variance ratio in these sources, the same dependence is seen in these two objects.

Fig. 5.15 shows that for NGC 4051 the observed change in the lags can be modelling by allowing the relative strength of the hard band TH (S_h) to decrease as the source becomes fainter (panel c), the rms spectrum becomes harder (panel b), and time averaged spectrum becomes harder (panel a). The other sources do not show the same trend with average flux (panel c). However, NGC 4051 shows the most dramatic change in the hardness of the rms spectrum with flux (the rms spectrum is dominated by harder energies when the source flux is low, Fig. 5.16). It remains possible that other sources follow a similar anti-correlation between rms hardness and hard lag strength, but the observations do not span a sufficient range of rms hardness to provide clear detections.

The strong change in the rms spectrum with flux in NGC 4051 (Fig. 5.16) could indicate that the variations in the hard band are dominated by some other emission component at the lowest fluxes, one that contributes flux and variability power to the hard band, but is swamped by the softer (power law) continuum at higher fluxes.

The majority of the sources in this sample showed no flux dependence on the lag. This could be an effect of not sampling as broad enough flux range to be sensitive enough to any flux changes. That we are unable to detect any changes in the soft lag for the majority

of the source has consequences for the soft-lag—M_{BH} relation seen in De Marco et al. 2013b. If there is a real flux dependence in these sources, then this could add to the scatter seen in the soft-lag—M_{BH} relation. On the other hand, if the majority of sources do not show a strong soft-lag dependence on flux then the mass scaling law inferred from this property remains valid.

*The world is full of magical things patiently waiting for
our wits to grow sharper.*

<div align="center">Bertrand Russell</div>

6

An energy- and flux-dependent timing analysis of NGC 4051

X-ray time lags have now been studied as a function of Fourier frequency in ~ 20 AGN (e.g. De Marco et al. 2013b). At low frequencies, hard energy bands (e.g. 2–5 keV) are observed to lag behind soft energy bands (e.g 0.3–1 keV). At high frequencies, the softer energies are observed to lag behind the harder. A consistent picture is beginning to emerge where the low frequency hard lags result from the propagation of mass accretion rate fluctuations through a stratified corona.

In a handful of sources, the time lags have been explored as a function of energy (hereafter *lag-energy spectrum*) for a given frequency range (e.g. Zoghbi et al. 2011; Zoghbi & Fabian 2011; Kara et al. 2013; Kara et al. 2013), allowing us to study the spectral shape of the time lags. This technique has revealed time lags in the iron Kα (6.4 keV) band on very short timescales in a small, but growing, sample of Seyfert 1s (e.g. Zoghbi et al. 2012; Zoghbi et al. 2013; Kara et al. 2013), which has been interpreted as a signature of disc reflection within $\sim 10R_{\mathrm{g}}$ of the illuminating source.

In Zoghbi et al. (2011) the 1H0707-495 lag-energy spectrum was modelled with the lag at each energy a weighed average of the lag of each component, with the weights taken to be the flux of each component in the energy band, which gave a good description of the data. A similar approach was adopted for 1H0707-495 by Kara et al. (2013), using simulated time-series, which were time-shifted, and weighted by the time-integrated spectra. Again, this gave a reasonable description of the data, but did not capture all of

the details of the iron Kα lag and the lag at soft excess energies. However, using the weightings (flux) of the spectral components from the time-integrated spectra is a simplified approach. The time-integrated spectra is likely to be affected by components that are constant at the frequencies where the lags are observed.

A better estimate of the strength of the spectral components is likely to be gained from the rms or covariance spectra (Wilkinson & Uttley 2009). The power in any energy band is the sum of the powers for each component, weighted not by their strengths in the time average spectrum, by in the rms spectrum. Similarly, the phase is the average phase shift from adding the Fourier transforms of each component. The phase of this average is the phase of each component weighted by their amplitudes.

The NLS1 galaxy NGC 4051 shows a soft lag in the lag-frequency spectra (Alston et al. 2013a hereafter A13; De Marco et al. 2013b; see also Chap. 4). In A13 the soft lag was observed to vary in frequency and magnitude with source flux. The X-ray PSD of NGC 4051 was studied in Vaughan et al. (2011). The 0.2–10 keV band PSD was described well by a bending power-law, with bend frequency $\nu_{\mathrm{bend}} \sim 2 \times 10^{-4}$ Hz. Vaughan et al. (2011) found the high frequency slope to flatten for at higher energies. A clear decrease in the 0.2–10 keV PSD amplitude, but not shape, was found with decreasing flux level. From fitting with a narrow Lorentzian component, no strong evidence was found for quasi-periodic oscillations (QPOs).

In this chapter we explore the energy dependent X-ray timing properties in NGC 4051. We explore the lag-energy as a function of frequency and flux. This is modelled using the weightings of the spectral components from fitting simple spectral models to the frequency-dependent covariance spectra. We also the explore the energy dependence of the PSD, as this provides vital information about the underlying variable components.

6.1 Observations and data reduction

In this chapter we use the 15 *XMM-Newton* observations of NGC 4051 taken in 2009 (see Section 4.2). We also make use of a ~ 120 ks *XMM-Newton* observation from 2001 (OBSID: 0109141401). The Observation Data Files (ODFs) were processed following standard procedures using the *XMM-Newton* Science Analysis System (SAS v13.0.0), using the conditions `PATTERN` 0–4 and `FLAG = 0`.

6.2 The frequency resolved lag-energy spectrum

We examine how the lag varies with respect to energy for a particular frequency range. The exact frequency range for each lag-energy spectra is guided by the frequencies at
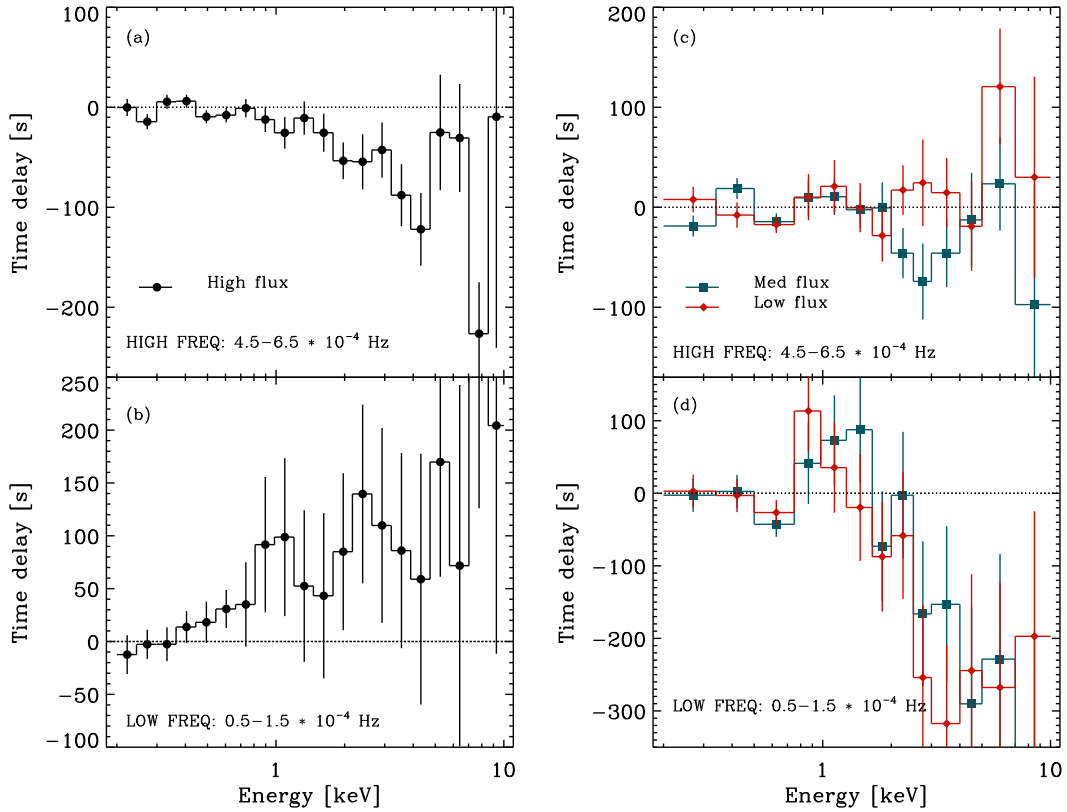
Figure 6.1: Lag-energy spectra for the flux selected 2009 observations of NGC 4051. Left: high flux intervals for high (a) and low (b) frequencies. Right: medium and low flux intervals for high (c) and low (d) frequencies. The lag-energy spectra are computed using a the 0.2–0.4 keV band as a reference.

which the hard and soft lags are observed in the lag-frequency spectrum (see Fig. 4.1), in order to highlight the spectral shape of the leading/lagging component(s). Following e.g. Zoghbi et al. (2011), for each energy band we compute the lag between the energy band and a broad reference band. The reference band is chosen to have a high signal-to-noise (S/N), in order to pick out any correlated variations and time delays in bands with weaker S/N. The lag is then computed between the comparison energy band and the broad reference band (or band with high S/N) *minus* the comparison energy band, if it happens to fall inside the reference band. Removing the comparison band from the reference band removes any correlated noise between the bands (Zoghbi et al. 2011). A more positive lag indicates the comparison energy-band lags the reference band. We do not shift the lag to a zero level, so the lag represents the average energy-band lag or lead relative to the reference band.

We start by looking at the 2009 data only. As with the lag-frequency analysis in Chap. 4, the data are divided into 10 ks segments (giving 490 ks of total data) with dt = 10 s, and sorted into 3 flux intervals. Fig. 6.1 shows the lag as a function of energy

for low $(0.5 - 1.5 \times 10^{-4} \, \text{Hz})$ and high $(4.5 - 6.5 \times 10^{-4} \, \text{Hz})$ frequencies for the high, medium and low flux intervals. We use the 0.2–0.4 keV band as the reference, as this has a high S/N. As the soft energies dominate the count rate in NGC 4051, we find the choice of reference band over a wider band (e.g 0.2–10 keV) has little effect on the shape of the lag-energy spectra, the only change being where the data are shifted relative to zero lag.

For the high flux intervals we compute the lag-energy for 20 approximately logarithmically spaced energy bins. At low frequencies (panel (b) Fig. 6.1) harder bands lag softer ones, with an increase in lag with increasing energy separation. The increase with energy is approximately log-linear and is consistent with results found in BH-XRBs (e.g Miyamoto & Kitamoto 1989; Nowak et al. 1999) and AGN (e.g. Arévalo et al. 2008; Zoghbi & Fabian 2011; Kara et al. 2013). At high frequencies (panel (a) Fig. 6.1), softer bands lag harder ones, however the shape of the lag-energy spectra is different than observed at low frequencies. There appears to be a positive lag between the 5–7 keV bands and the energy bands directly higher or lower. A feature of this type has been associated with iron Kα reverberation in a number of sources (e.g. Kara et al. 2013). The average lag between the 5–7 keV band and adjacent energy bands is ~ 150 s.

For the low and medium flux intervals we compute the lag-energy for 13 approximately logarithmically spaced energy bins, due to the worse S/N at these fluxes. The lag-energy spectrum is seen to change direction at certain energies, compared to the high flux intervals. For the low frequency range (panel (d) Fig. 6.1), at energies above ~ 2 keV the energy band is seen to lead the reference band, with the band lead increasing with energy. In the high frequency range (panel (c) Fig. 6.1), the medium flux shows a positive lag between $\sim 2 - 3$ keV and energy bands below ~ 2 keV. There is also a positive lag between ~ 3 keV and higher energies up to the 5–7 keV band. This feature is similar in shape to a broadened iron Kα feature, although we note the large error bar on the 7-10 keV band. The low flux lag is consistent with zero lag at all energies, except for a positive lag in the 5–7 keV band. However, this feature is only 2σ detection.

Clear changes in the lag-energy spectrum with source flux are evident in Fig. 6.1. We investigate this change further by computing the lag as a function of energy in 15 non-overlapping frequency bins over the $1 - 14 \times 10^{-4} \, \text{Hz}$ range. The frequency bins used are equivalent to the geometrically spaced bins, which increase in bin width by a factor ~ 1.1, used in the lag-frequency analysis in Section 4.3. In Fig. 6.2 we show the lag as a function of energy and frequency for the high, medium and low flux intervals. The 0.3–10 keV band is used as a a reference band to maximise the S/N, so the lag represents the average energy band lag/lead, where a more positive value denotes a band lag. The grid has been smoothed in order to make the changes in lag magnitude with energy and frequency more clear. These results agree with the lag-energy at the frequency bands
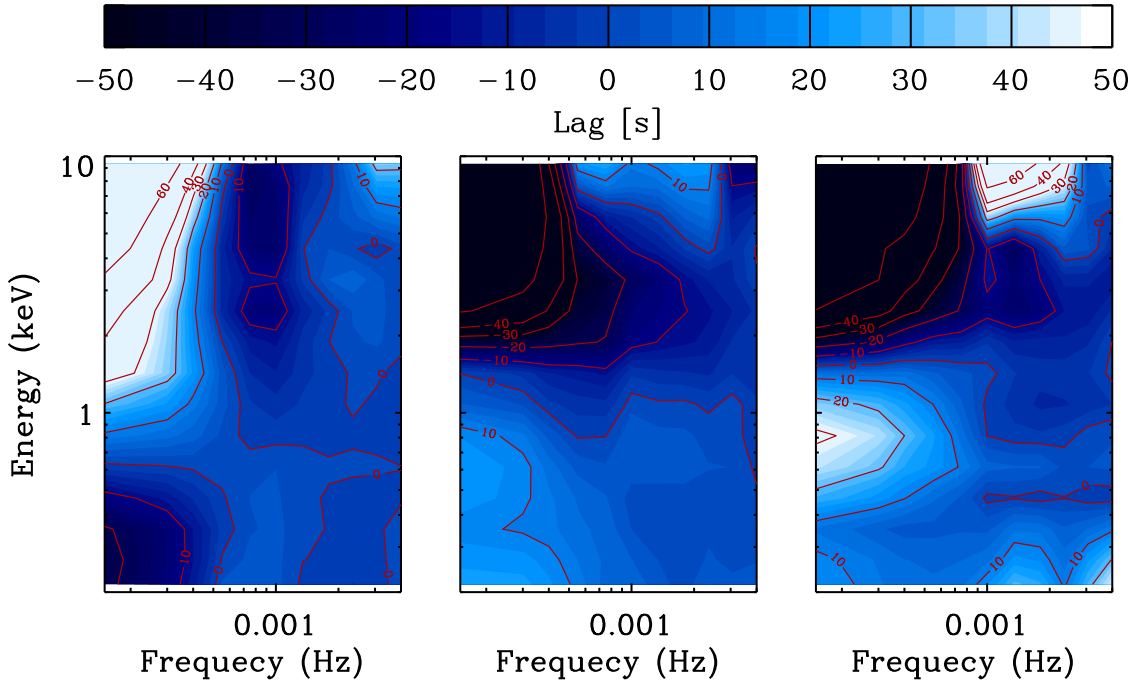
Figure 6.2: The X-ray time lag as a function of energy and frequency for the three flux levels in NGC 4051. The 0.3–10 keV band is used as a a reference band, so the lag represents the average energy band lag/lead, where a more positive value denotes a lag.

used in Fig. 6.1, and show that we are not missing any important feature. The possible features seen around iron in Fig. 6.1 are not observed in Fig. 6.2, most likely due to the smoothing of the grid.

We now explore the lag-energy in the 2001 *XMM-Newton* data. This observation has a mean count rate of 17.8 ct/ s^{-1}. A time binsize of 10 s and segment size of 10 ks is used, providing 11 segments in total for the averaging process. We treat this observation separately from the 2009 data, due to any structural changes that may have occurred in the system over the ~ 8 year period. The high count rate of the 2001 data means we can treat this as a separate flux level (very high), which we show in the top panels of Fig. 6.3. We now compute the lag energy at 13 logarithmically spaced energy bins for 4 different frequency bands, as shown in Fig. 6.3. We also show the high, medium and low flux level lag-energy spectra for the 2009 observations in Fig. 6.3. Each row is a different flux level, and each column a different frequency band.

The very high (2001) at the lowest frequency band shows the well established trend of increasing lag magnitude with increasing energy separation. The trend is approximately log-linear. The magnitude of the lag is greater for a given energy band, than in the high flux data, although with large error bars. At high frequency bands in the very high flux data, no obvious features are visible, except for a negative lag between $\sim 3 - 4$ keV and

lower energy bands. There is also a slowly rising positive lag from the $\sim 3 - 4$ keV band to increasingly higher energies.

When comparing all flux levels at a given frequency band, there appears to be a 'pivoting' of the lag-energy spectra at energies of ~ 1 keV and higher. This is most apparent in the lowest frequencies (left most column in Fig. 6.3). As the flux drops the lag above 1 keV switches from a more positive lag with increasing with energy, to a more negative lag with increasing energy. This is also seen at higher frequencies to some extent, after accounting for any possible iron Kα features.
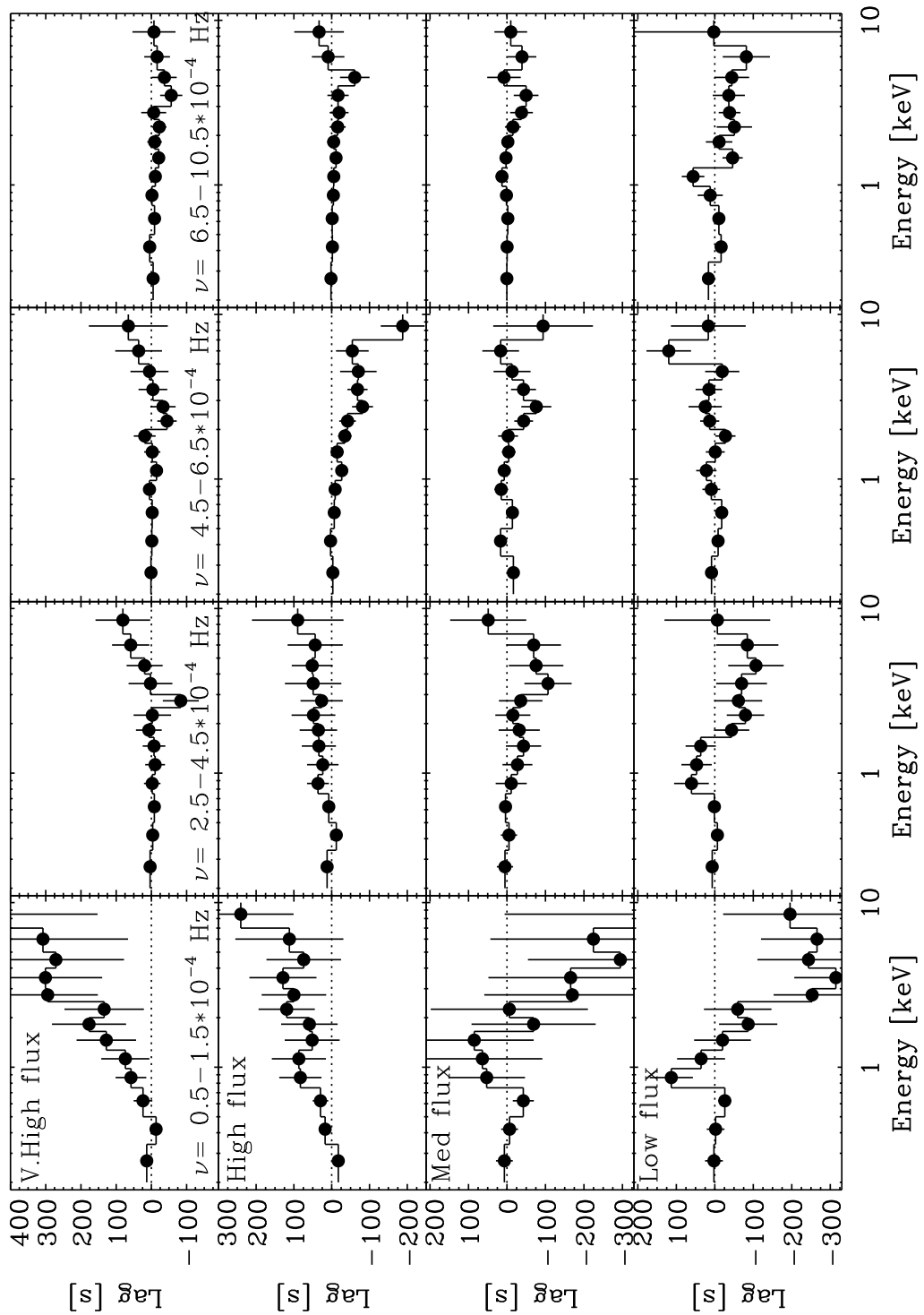
Figure 6.3: Exploring the lag-energy spectra as a function of flux and frequency in NGC 4051. Each row represents a different flux level, and each column is the lag-energy spectra for a given frequency band. The 2009 data is divided into the high, medium and low flux (second, third and bottom rows), whilst the very high flux (top row) is solely the 2001 data.
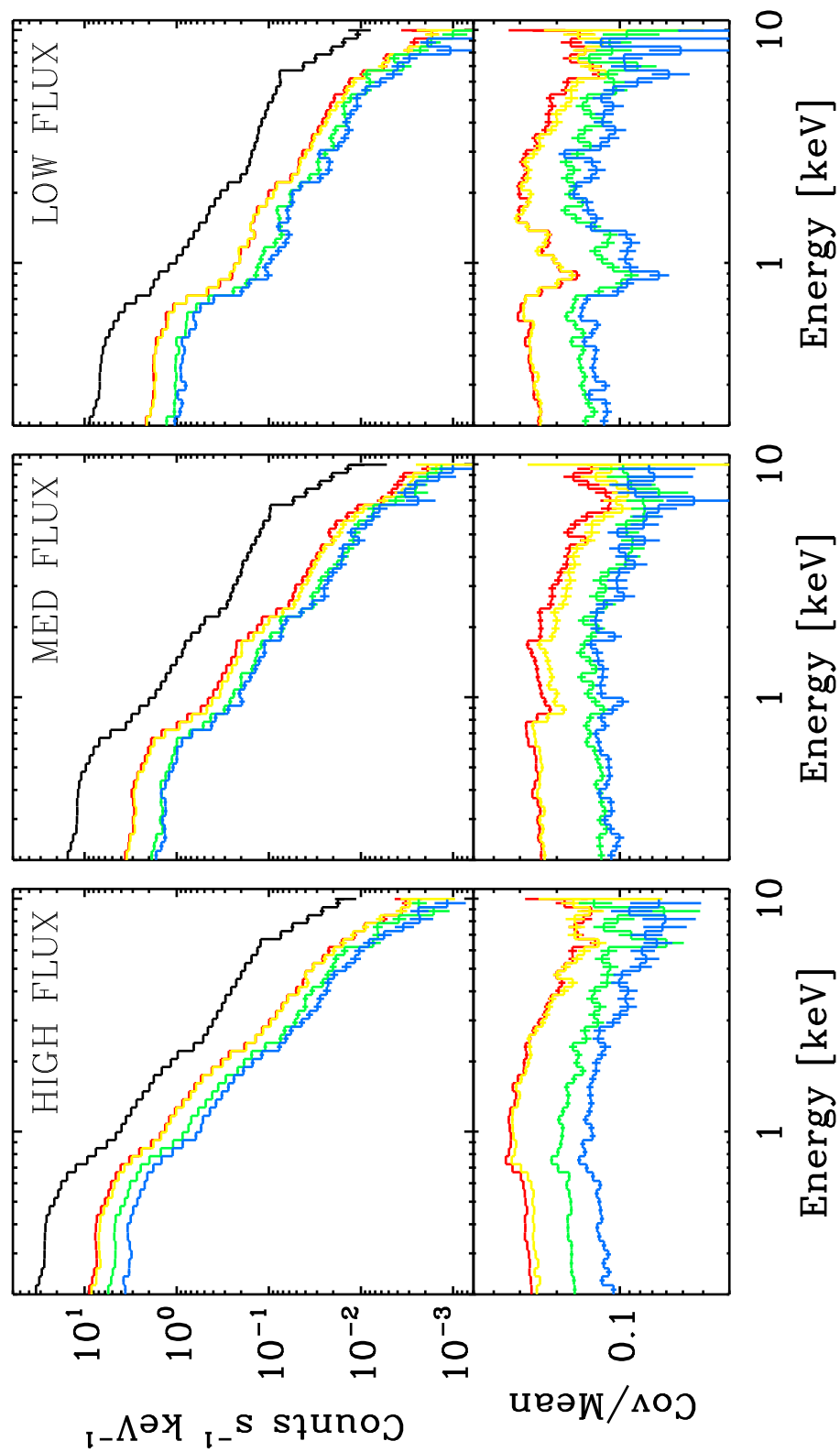
Figure 6.4: Covariance and time-integrated spectra for the high, medium and low flux levels. For each flux level we show the time-integrated (black), total frequency band covariance spectrum (red), and covariance spectrum for the frequency bands: $0.5 - 1.5 \times 10^{-4}$ Hz (yellow); $2.5 - 4.5 \times 10^{-4}$ Hz (green); $4.5 - 6.5 \times 10^{-4}$ Hz (blue). The lower panels show the covariance/time-integrated (F_{covar}).

6.3 Covariance spectrum

In this section we look at the variability spectrum, in order to understand which spectral components are dominating the variability at different timescales. The rms-spectrum shows the total variance in an energy band for a given variability timescales. However the S/N can be limited in low count rate data, particularly at hard energies. Instead, we use the covariance spectrum Wilkinson & Uttley (2009) calculated in the frequency domain (see Section 2.6).

In the previous section we found a frequency dependence to the lag-energy spectrum. The covariance spectrum can be used to study the strength of the variable components as a function of frequency. We estimate the mean (time-integrated) and covariance spectrum for each flux level using the same segment length and time binsize as in the previous section. The spectra are estimated in 50 non-overlapping energy bins. In Fig. 6.4 we show the mean (black), total frequency band covariance spectrum (red), and covariance spectrum for the frequency bands: $0.5 - 1.5 \times 10^{-4}$ Hz (yellow); $2.5 - 4.5 \times 10^{-4}$ Hz (green); $4.5 - 6.5 \times 10^{-4}$ Hz (blue). The yellow and green curves therefore represent the covariance spectrum at the frequency bands used for the lag-energy spectra in Fig. 6.1.

The lower panels in Fig. 6.4 show the covariance/mean (F_{covar}), analogous to the *fractional* rms spectrum (F_{var}; e.g. Vaughan et al. 2003). A drop in F_{covar} can be seen around ~ 6 keV in all fluxes, and a drop around ~ 1 keV can be seen in the medium and low fluxes. The F_{covar} spectrum also appears to harden as the flux drops. This agrees with the F_{var} spectrum from the 2001 and 2002 NGC 4051 data by Ponti et al. (2006). However, the high flux $4.5 - 6.5 \times 10^{-4}$ Hz F_{covar} (blue curve in Fig. 6.4 lower left panel) does not show the drop at ~ 6 keV.

6.4 Modelling the covariance spectrum

In this section we model the covariance spectra for the two frequency bands used for the lag-energy in Fig. 6.1, i.e low ($0.5 - 1.5 \times 10^{-4}$ Hz; LF) and high ($4.5 - 6.5 \times 10^{-4}$ Hz; HF). The models are simplistic descriptions of the data, trying only to capture the components that could be responsible for causing and delayed emission. For a given frequency band, we simultaneously fit each model across the three flux levels. All models give a reasonable fit to the data. In the we do not show the full details of the model fits. In each model we use an XSTAR grid (Bautista & Kallman 2001) to model the warm absorption. The column density is tied across flux, but the ionisation parameter ξ is free to vary with flux. An angle of $30°$ is assumed for all reflection models. All components are absorbed by a galactic column of $N_{\mathrm{H}} = 4 \times 10^{20} \mathrm{cm}^{-2}$ using TBABS (Wilms et al.

2000) in XSPEC v12.8.1 (Arnaud 1996).

6.4.0.1 Neutral reflection and a separate soft X-ray excess

This model consists of a blackbody (BBODY), a separate soft X-ray excess component (COMPTT; Titarchuk & Lyubarskij 1995) as thermal Compton scattering of the blackbody seed photons, and then in turn provides seed photons to produce the coronal emission from Compton upscattering (NTHCOMP). This coronal emission illuminates the disc and produces a neutral reflection spectrum. The reflection is modelled with PEXMON (Nandra et al. 2007) convolved with KDBLUR (Laor 1991; Fabian et al. 2002) for the blurring from a region with inner radius fixed at $10R_{\mathrm{g}}$. The resulting fit of this model to the LF and HF covariance spectra is shown in Fig. 6.5. This corresponds to model COMP-COMPTT in Jin et al. (2013) and is intended to represent a physical situation in which there is an optically thick comptonising medium between the cool disc and hot corona, which produces a smooth soft excess. For both the LF and HF covariance spectra the contribution of the COMPTT component relative to intrinsic power-law emission increase as the flux decreases.

6.4.0.2 Ionised reflection

This model consists of blackbody which provides the seed photons for the primary coronal component. The reflection is ionised (REFLIONX; Ross & Fabian 2005), which also produces the soft-excess component (from e.g. N, O, Ne and Fe L emission lines). The inner disc radius is fixed at $3R_{\mathrm{g}}$ using the KDBLUR convolution model. The resulting fit of this model to the LF and HF covariance spectra is shown in Fig. 6.6. This corresponds to model REFL of Jin et al. 2013 and is intended to represent a physical situation in which the bulk of the soft excess flux is produced by reflection off a highly ionised accretion disc close to the black hole. For the LF covariance spectra, the contribution of the ionised reflection at soft energies increases as the flux drops. This is also evident in the HF covariance spectra.

6.4.0.3 Composite model

This model is identical to the *ionised reflection* model, except now we include an additional cooler Comptonisation component (COMPTT) to model the soft excess. The resulting fit of this model to the LF and HF covariance spectra is shown in Fig. 6.7. For both the LF and HF covariance spectra the relative contributions of the COMPTT and the primary power-law remain approximately constant as the flux decreases. The contribution of the ionised reflection increases as the flux level drops.
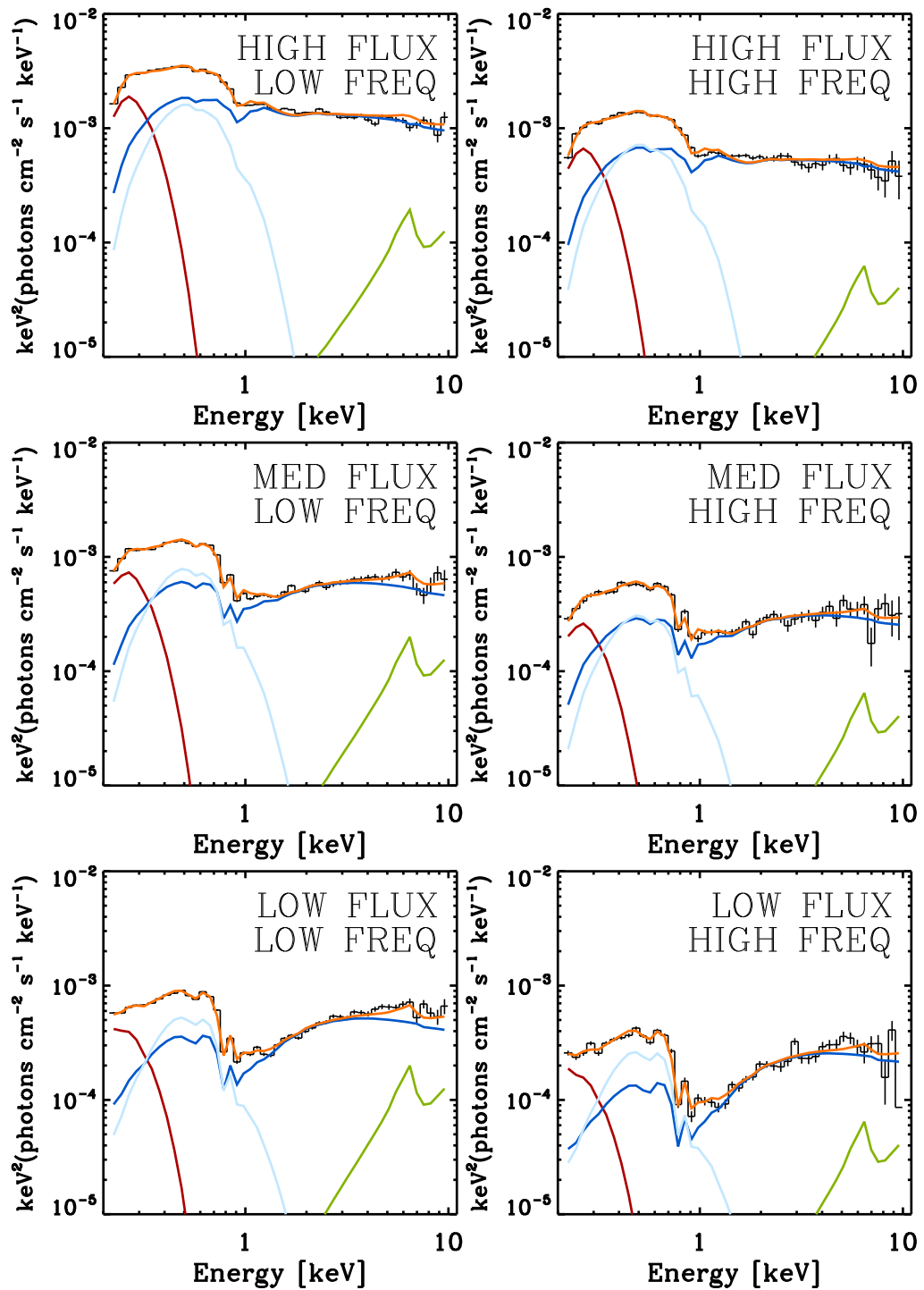
Figure 6.5: Neutral reflection model fits to covariance spectra as a function of frequency and source flux. The models are 'unfolded' using XSPEC and are plotted in E*F(E) style. The model consist of a blackbody (red), absorbed power-law (blue), neutral reflection (green) and a cooler comptonising component (light blue). The left panels are the LF and the right panels are the HF, with high to low flux from top to bottom.
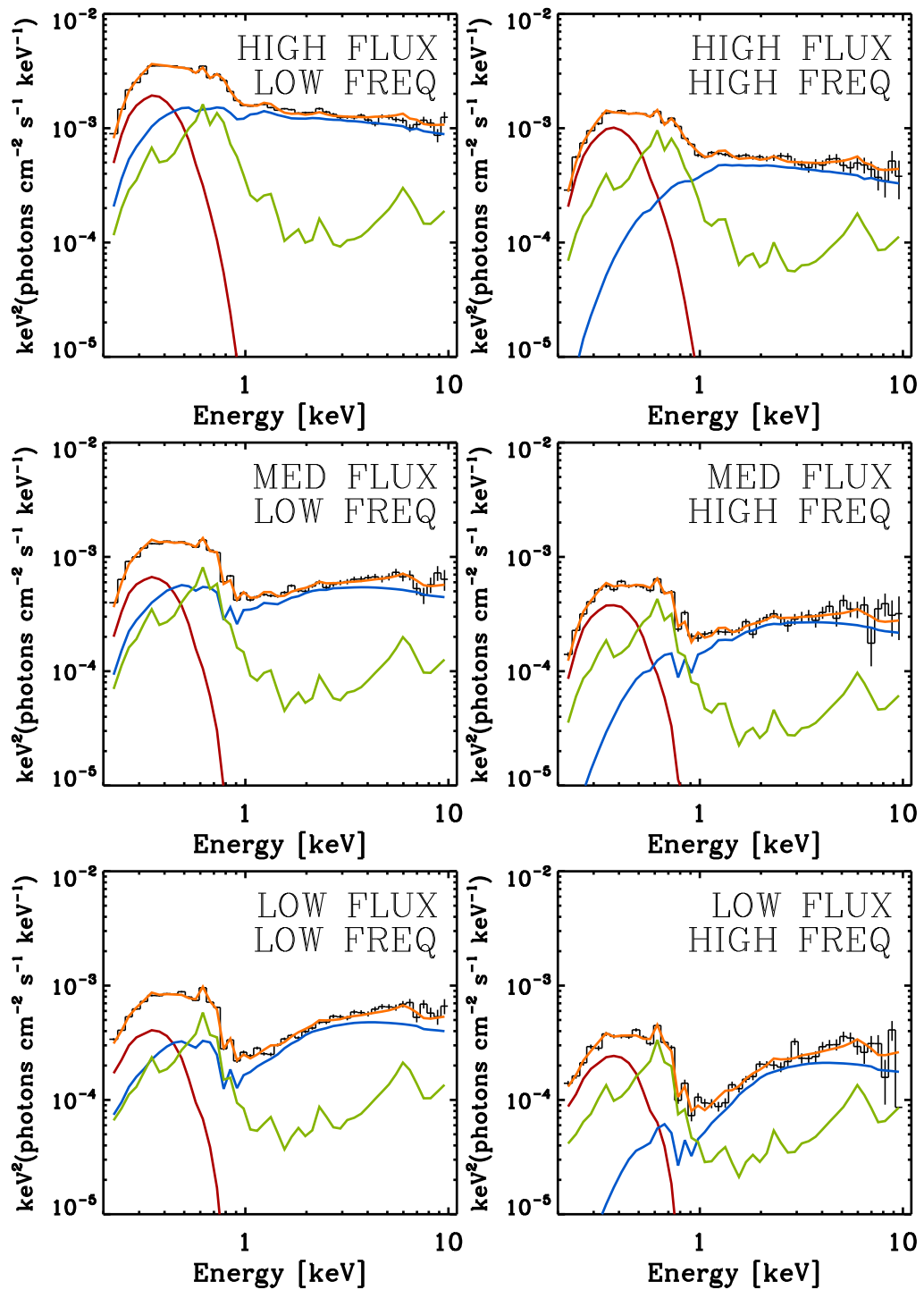
Figure 6.6: Ionised reflection model fits to covariance spectra as a function of frequency and source flux. The models are 'unfolded' using XSPEC and are plotted in E*F(E) style. The model consist of a blackbody (red), absorbed power-law (blue) and ionised reflection (green). The left panels are the LF and the right panels are the HF, with high to low flux from top to bottom.
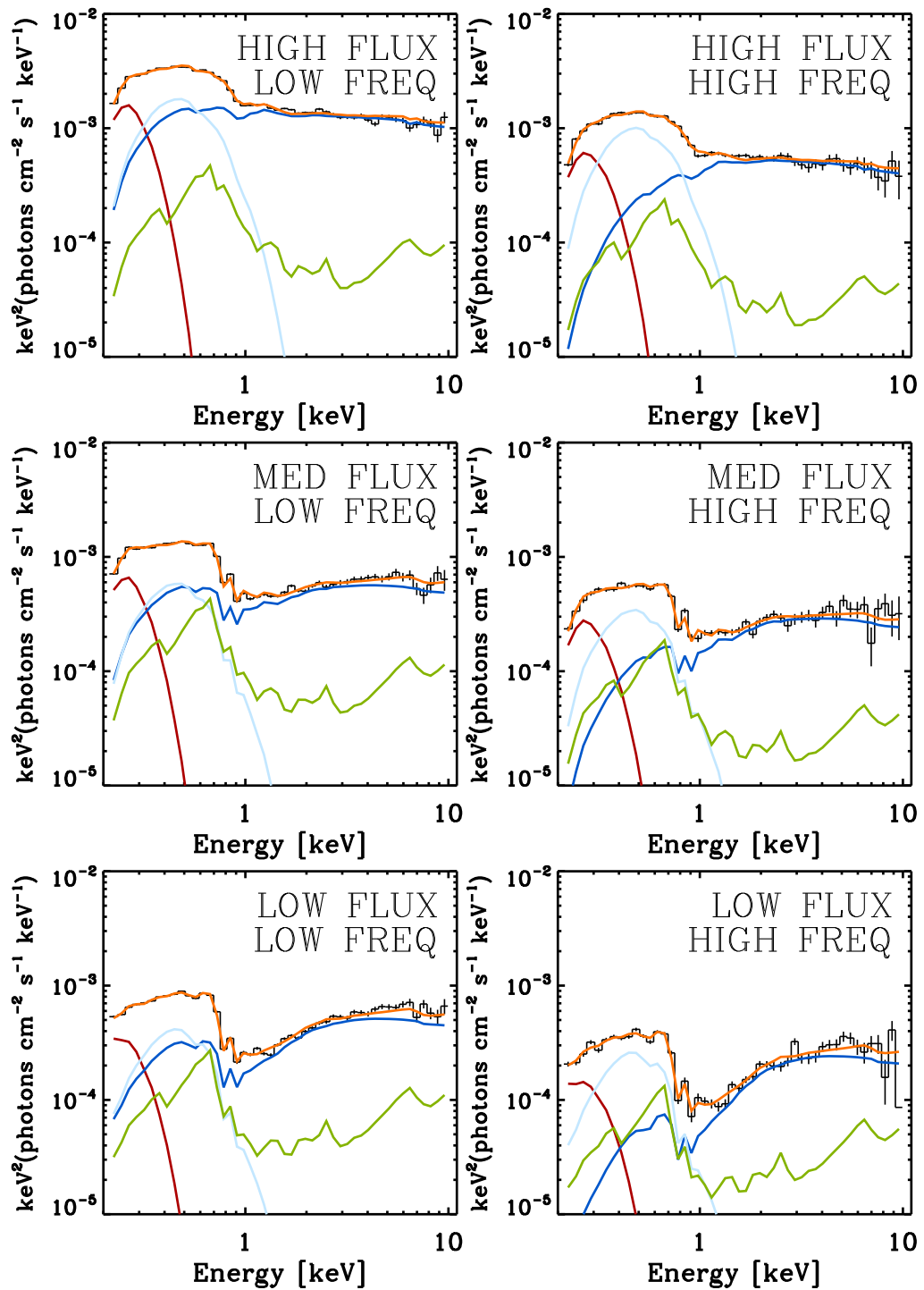
Figure 6.7: Composite model fits to covariance spectra as a function of frequency and source flux. The models are 'unfolded' using XSPEC and are plotted in E*F(E) style. The model consist of a blackbody (red), absorbed power-law (blue), ionised reflection (green) and a cooler comptonising component (light blue). The left panels are the LF and the right panels are the HF, with high to low flux from top to bottom.

6.5 Modelling the lag-energy

In this section we model the low and high frequency lag-energy spectra using the spectral models used to fit the covariance spectra. For each model we take the fractional contribution of each component to the covariance spectrum. Each component is then scaled by some average lag in order to match the observed lag-energy spectra. We note that no lag-energy model fitting is performed here, the lag-energy models simply represent the lag prediction we would expect to see for the given spectral models. The predicted lag magnitudes for each component are adjusted to give the best description of the lag-energy data.

Fig. 6.8 shows the fractional contribution of each component for the neutral reflection model and the resulting lag-energy model for the LF data. For the high flux data the COMPTT component lags the BB by 100 s, with the power-law (PL) component 100 s after that. The reflection component lags the PL by a further 300 s. We can see that this model gives a reasonable description of the data. For the medium and high flux data (middle and right panels of Fig. 6.8) the softer energies are seen to lag the harder energies. As the PL dominates the harder energies assume therefore assume that the PL variations occur first, followed by the BB 150 s later, and the COMPTT component 100 s after that. Again the reflection follows the PL by 300 s. The data are described well at energies below ~ 0.7 keV and above ~ 2 keV. However, the model fails to reproduce the lag at energies between $\sim 0.7 - 2$ keV.

Fig. 6.9 shows the lag-energy model for the HF data. For the high and medium flux levels we assume the PL variations are followed by the BB with a 60 s lag, the COMPTT component follows 50 s after that and the reflection is 100 s behind the PL. Again, this model fails to describe the lags in the $\sim 0.7 - 2$ keV band. At low fluxes the BB and COMPTT follow the PL by 10 s, and the reflection follows the PL by 300 s.

The ionised reflection model prediction of the LF lag-energy spectra is shown in Fig. 6.10. We use the same lag magnitudes to the neutral reflection model, except no COMPTT component is used. The high flux data don't appear to be described very well by this model at energies above 2 keV. Increasing the lag between the PL and reflection component produces too great a lag around 1 keV. The medium and low flux data are described reasonably well by this model, although again the model isn't quite describing the lag at energies between $\sim 0.7 - 2$ keV. Fig. 6.11 shows the predicted ionised reflection lag-energy model for the HF data. The data are reasonable well described by the model, although the $\sim 0.7 - 2$ keV band in the high flux are not matched by the model. The magnitude of the lag at ~ 0.6 keV in the low flux data is too large, resulting from the large contribution of the reflection component at these energies.

Fig. 6.12 shows the composite model prediction for LF lag-energy data. Each component is given the same average lag as in the neutral reflection model. The high flux data is described quite well by this model, although the lag at high energies is not as long as in the neutral reflection model. The medium and low fluxes are well described, except around $\sim 0.7 - 2$ keV. Fig. 6.13 shows the composite model prediction for HF lag-energy data. At high and medium fluxes, the $\sim 0.7 - 2$ keV band is not well described by the data. At low fluxes, this model seems to predict a too long lag at at ~ 0.6 keV and the lag in the iron Fe Kα band is not large enough.
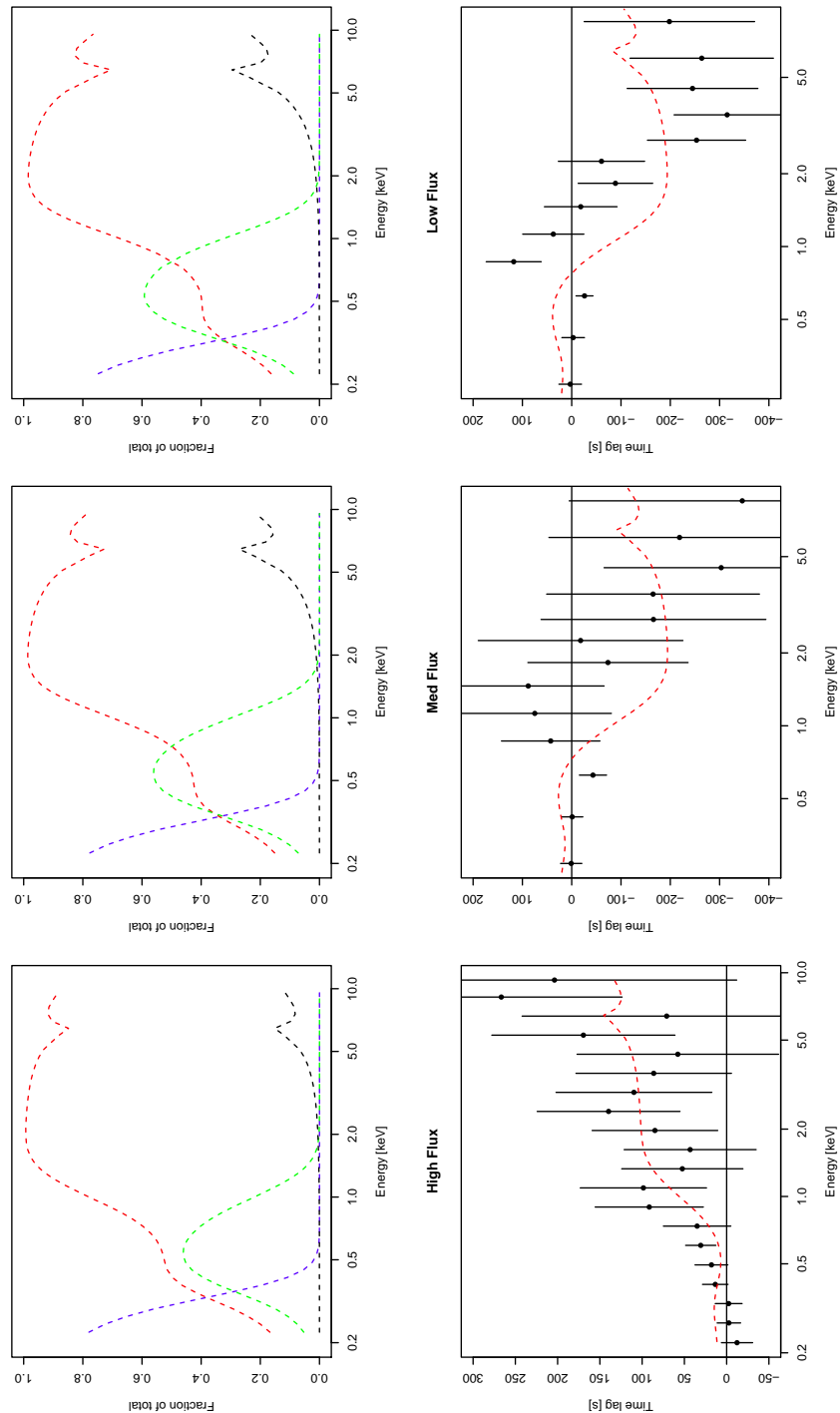
Figure 6.8: Neutral reflection model to low frequency lag-energy spectrum. The upper panels show the fraction of each component to the covariance spectrum fit, for the PL (red), BB (blue), COMPTT (green) and reflection (black). The lower panels show the resulting lag-energy model.
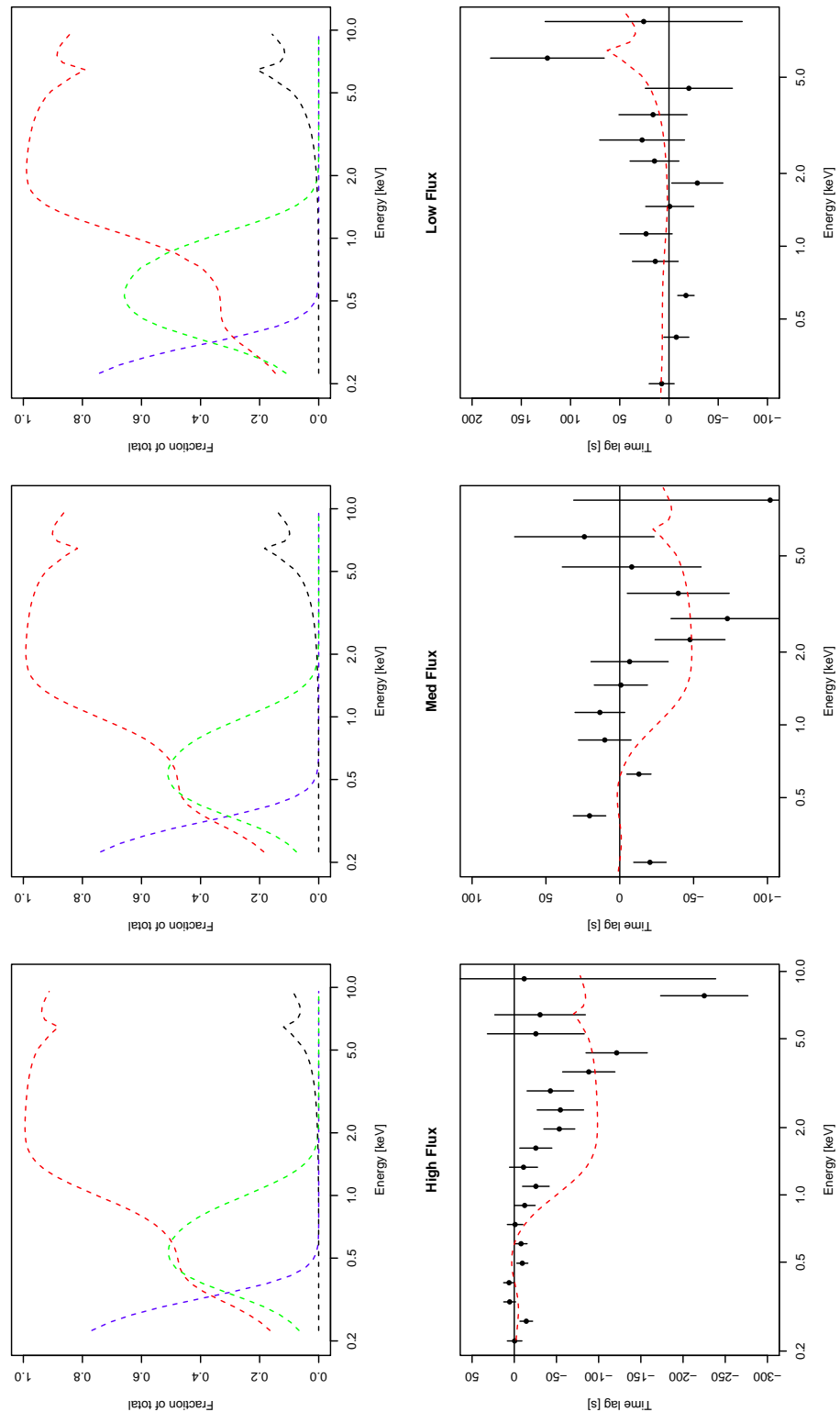
Figure 6.9: Neutral reflection model to high frequency lag-energy spectrum. The upper panels show the fraction of each component to the covariance spectrum fit, for the PL (red), BB (blue), COMPTT (green) and reflection (black). The lower panels show the resulting lag-energy model.
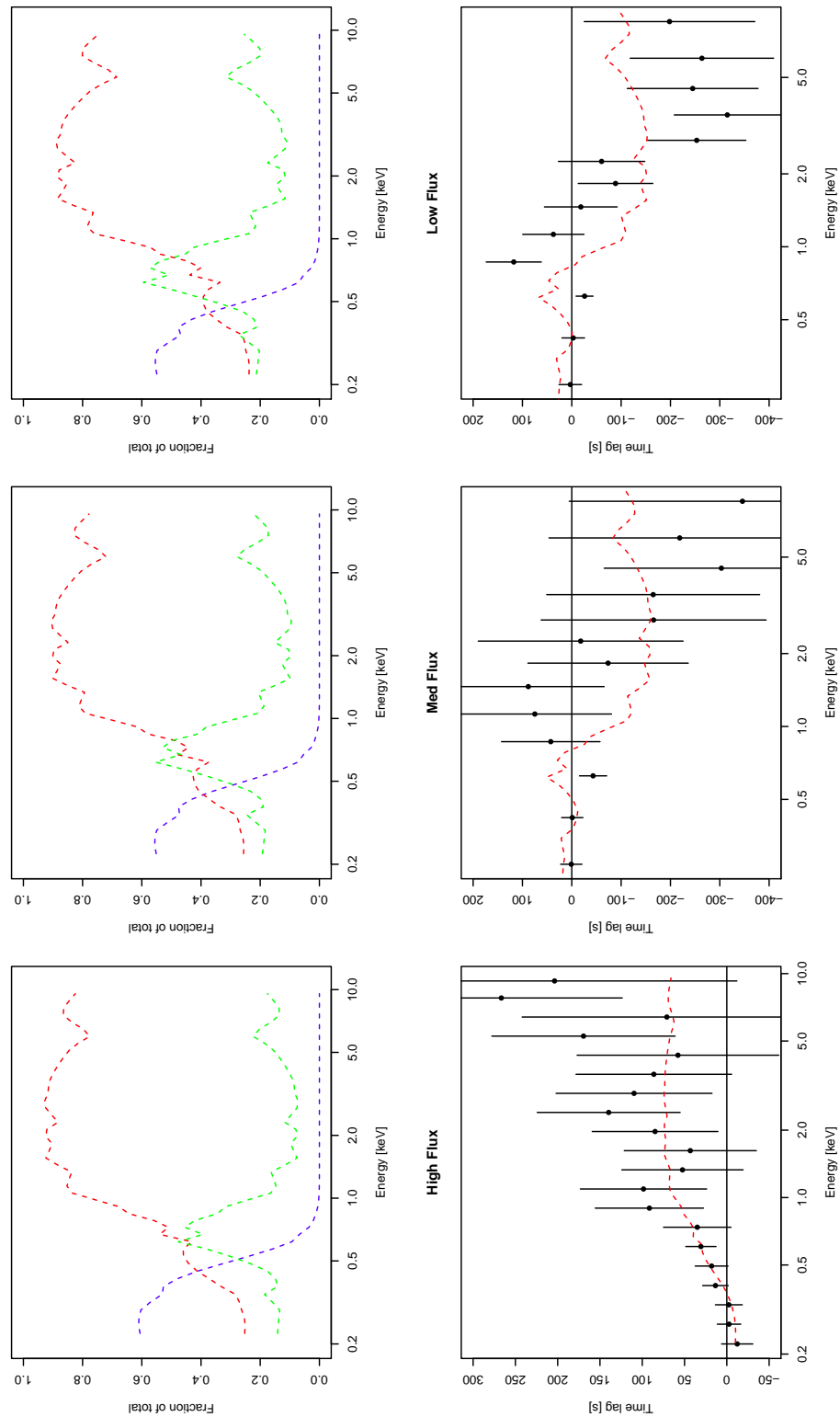
Figure 6.10: Ionised reflection model to low frequency lag-energy spectrum. The upper panels show the fraction of each component to the covariance spectrum fit, for the PL (red), BB (blue) and reflection (green). The lower panels show the resulting lag-energy model.
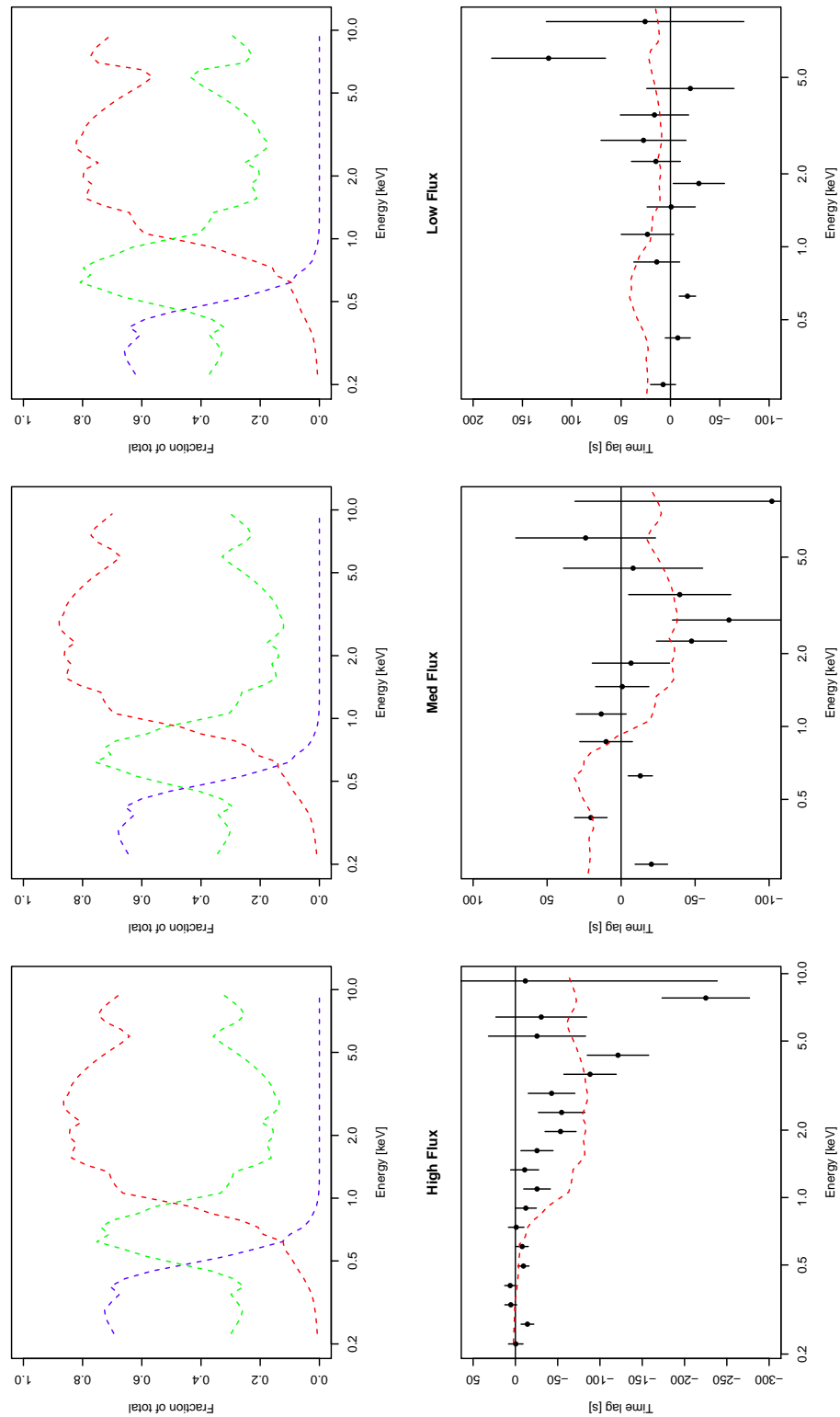
Figure 6.11: Ionised reflection model to high frequency lag-energy spectrum. The upper panels show the fraction of each component to the covariance spectrum fit, for the PL (red), BB (blue) and reflection (green). The lower panels show the resulting lag-energy model.
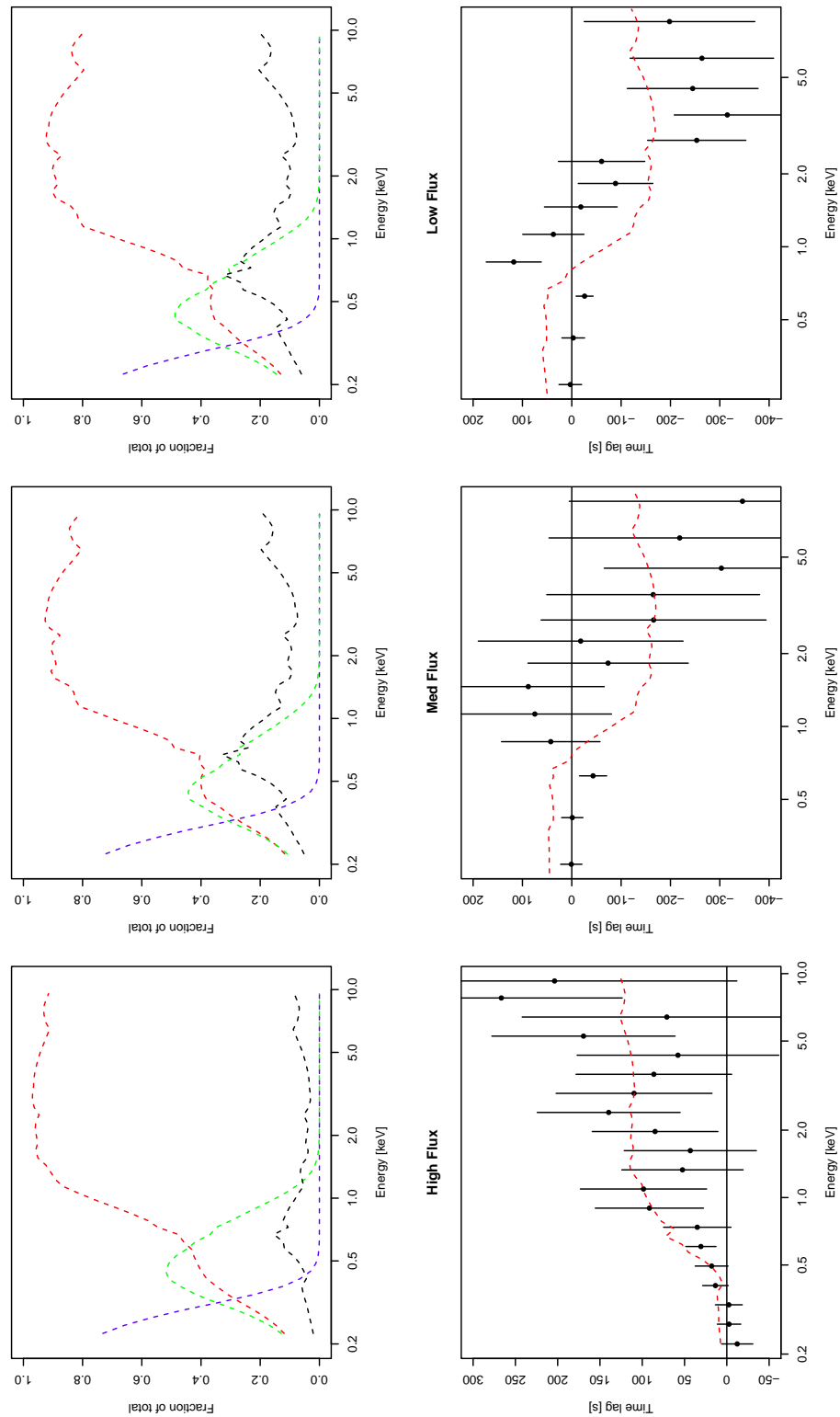
Figure 6.12: Composite model to low frequency lag-energy spectrum. The upper panels show the fraction of each component to the covariance spectrum fit, for the PL (red), BB (blue), COMPTT (green) and reflection (black). The lower panels show the resulting lag-energy model.
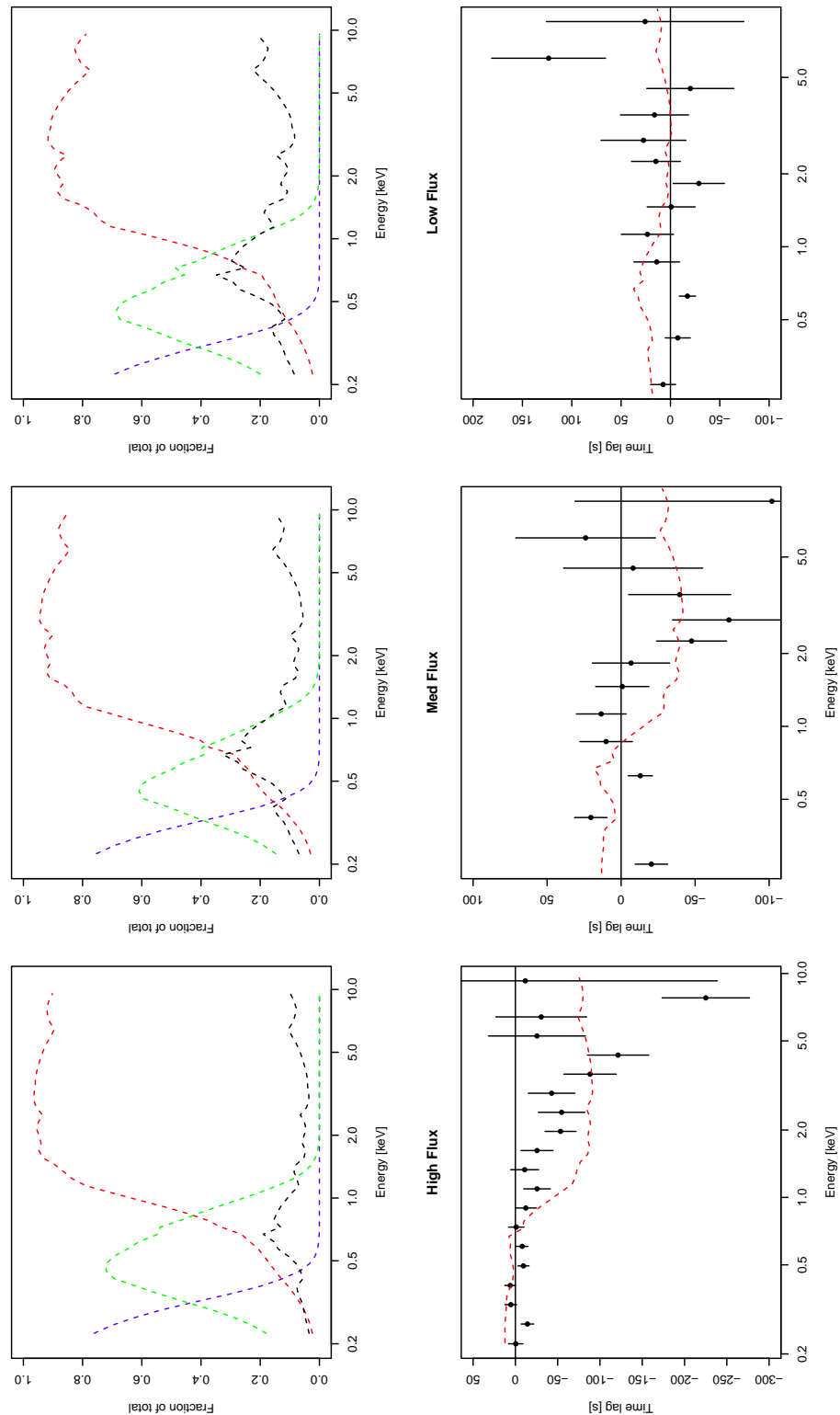
Figure 6.13: Composite model to high frequency lag-energy spectrum. The upper panels show the fraction of each component to the covariance spectrum fit, for the PL (red), BB (blue), COMPTT (green) and reflection (black). The lower panels show the resulting lag-energy model.
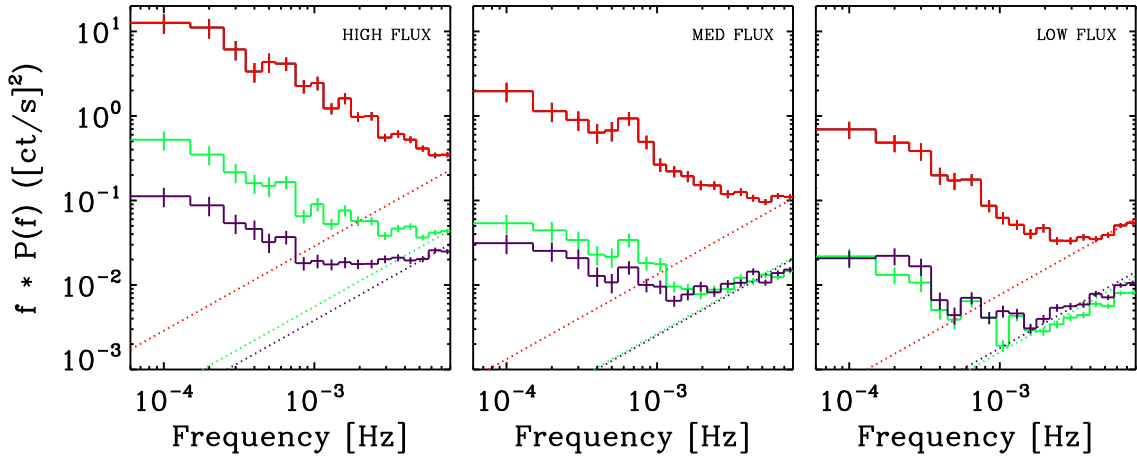
Figure 6.14: Power spectra (PSD) in absolute units as a function of energy and flux for NGC 4051. PSD is shown for the 0.2–1 keV (red), 1–2 keV (green) and 2–10 keV (purple) energy bands.

6.6   Energy and flux resolved PSD

The PSD of the 2009 data was estimated using standard techniques (van der Klis 1989, see Section 2.3). The segment length (10 ks), binning (10 s) and count rate selection of flux intervals was the same as the lag-energy analysis in Section 6.2. Fig. 6.14 shows the resulting PSD estimates with absolute normalisation for 3 energy bands: 0.2–1 keV, 1–2 keV and 2–10 keV. The PSDs have been rebinned in geometrically spaced frequency bins which increase by a factor of 1.2. A higher frequency resolution is used for the PSD in order to pick out any structure that may be present. The Poisson noise was estimated as described in Table. 2.1. For a given energy band, a clear change in the amplitude can be seen (in absolute units), however there is little change in shape. A peaked feature can be seen in the PSD at $\nu \sim 6.5 \times 10^{-4}$ Hz, which is most obvious in the medium flux PSD (middle panel of Fig. 6.14). The location of this peak is approximately consistent with the frequency at which the soft lags are observed in the high flux intervals (see Fig. 4.1). The significance of this peak is explored in Section 6.7.

In Fig. 6.15 we show the same data but with rms normalisation. The Poisson noise is again estimated as described in Table. 2.1. Here we can clearly see how the power in the 0.2–1 keV band drops with source flux.

6.7   Bending power-law and Lorentzian profile fit to PSD

Motivated by the presence of a peak in the PSD we explore this feature with model fitting. Peaks in the power spectra of XRBs and AGN are QPOs, which are typically modelled in terms of Lorentzian line profiles in addition to a smooth continuum. In order
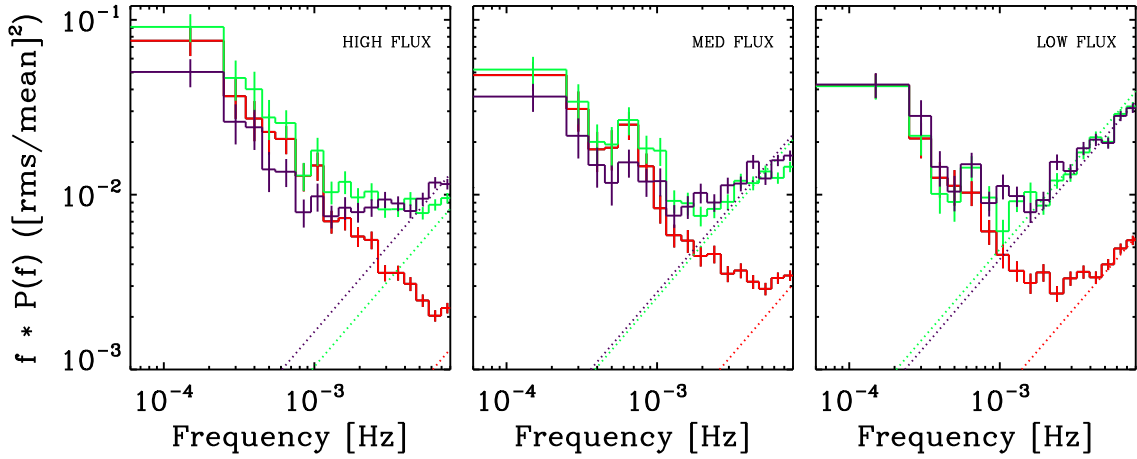
Figure 6.15: Power spectra (PSD) in rms units as a function of energy and flux for NGC 4051. PSD is shown for the 0.2–1 keV (red), 1–2 keV (green) and 2–10 keV (purple) energy bands.

to asses the significance of the peak we first fit a continuum model PSD. We fit only the 0.2–1 keV from the medium flux interval, as this shows the strongest evidence for this feature. McHardy et al. (2004) and Vaughan et al. (2011) found an adequate description to the data with a bending power law

$$p(\nu) = \frac{N\nu^{\alpha_{\text{low}}}}{1 + (\nu/\nu_{\text{bend}})^{\alpha_{\text{low}} - \alpha_{\text{high}}}} \qquad (6.1)$$

where α_{low} is the low frequency slope, α_{high} is the high frequency slope, ν_{bend} is the bend frequency and N is a normalisation constant.

The model fitting was performed in XSPEC v12.8.1 using a χ^2 fit statistic. Errors quoted on parameters correspond to 90 per cent confidence intervals. We first fit just the bending power-law model plus a constant component for the Poisson noise to the data. We fix α_{low} at -1.1, since this has been well constrained from *RXTE* observations (McHardy et al. 2004). The best fitting values for the bending power-law model free parameters were $\nu_{\text{bend}} = 1.77 \pm 1.10 \times 10^{-4}$ Hz and $\alpha_{\text{high}} = -2.28 \pm 0.10$. The fit statistic $\chi^2 = 46.17$ for 41 degrees of freedom (dof), giving a null hypothesis probability $p = 0.27$. These results are consistent with the PSD fitting in Vaughan et al. (2011).

We next add the Lorentzian component to the model, described by

$$l(\nu) = \frac{K(\sigma/2\pi)}{(\nu - \nu_{\text{L}})^2 + (\sigma/2)^2} \qquad (6.2)$$

where ν_{L} is the centroid frequency, σ is the FWHM of the line profile and K is a normalisation constant. We again fixed α_{low} at -1.1, and refit the free model parameters. The best fitting model parameters were $\nu_{\text{bend}} = 1.01 \pm 1.27 \times 10^{-4}$ Hz, $\alpha_{\text{high}} = -2.19 \pm 0.12$, $\nu_{\text{L}} = 6.6 \times 10^{-4}$ Hz, $\sigma = 1.04 \pm 0.93 \times 10^{-4}$ Hz and $K = 0.209 \pm 0.095$. The fit statistic
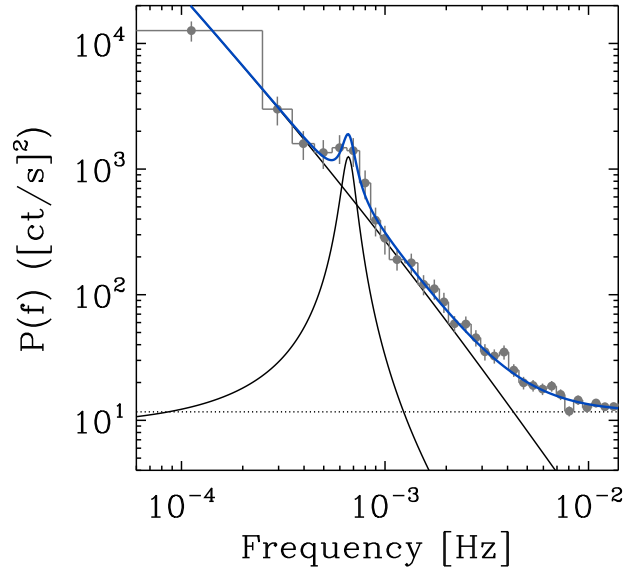
Figure 6.16: Model fit to PSD including a bending power law and Lorentzian profile.

was $\chi^2 = 38.18$ for 38 dof, giving a null hypothesis probability $p = 0.46$. The model including the Lorentzian profile therefore has a $\Delta\chi^2 \sim 8$ for three interesting parameters. To estimate the significance of QPO we use the error on the Lorentzian normalisation, showing a $\sim 2.2\sigma$ detection. The *quality factor* $Q = \nu_L/\sigma \sim 6$. Values of $Q \sim 5-10$ are typical values of high frequency QPOs in BH-XRBs (e.g. Remillard et al. 2002, 2003).

6.8 Discussion

We have studied the energy dependent X-ray time lags in the NLS1 galaxy NGC 4051. For a given frequency band, the lag-energy spectrum shows a strong dependence on source flux. At high flux and low frequencies, a positive (hard) lag is observed, with an approximately log-linear dependence on the lag with energy. This is characteristic of the low frequency lag-energy spectra observed in several AGN (e.g. Zoghbi et al. 2012; Zoghbi et al. 2013; Kara et al. 2013). As the flux drops, the direction of the lag above ~ 1 keV changes, now with softer bands lagging harder bands. At high frequencies, the high flux shows a more positive lag at softer energies and a possible iron Kα feature is observed. In the medium and low flux levels, the softer bands are also seen to lag harder bands. The observed changes in flux are consistent with the flux dependence on lag-frequency presented in Chap. 4.

A positive lag can be seen between the 5–7 keV energy bands and adjacent bands, with an average time lag of ~ 150 s (see Fig. 6.1). It is tempting to associate this feature with an iron Kα lag, as has been claimed in several sources (e.g. Kara et al. 2013). In Kara et al. (2013) they plot the observed magnitude of the iron Kα lag for several sources

as a function of black hole mass (see their Fig. 12). They find the sources are consistent with the reverberation taking place within the central $\sim 1 - 6R_{\rm g}$. If the lag in this band in NGC 4051 is interpreted as a signature of reverberation then for $M_{\rm BH} \sim 2 \times 10^6$ M$_\odot$ this corresponds to reverberation taking place on a size scale of $>6R_{\rm g}$.

We modelled the covariance spectrum at frequencies of the observed lag-energy spectra using the sum of spectral components (modified by absorption). These models had either a cooler comptonising component for the soft excess, or ionised reflection, or both. All three models gave acceptable fits to the covariance spectra at LF and HF ranges. For each spectral model, a clear increase in the relative strength of the soft excess component is found as the flux decreases. This is matched by a decrease in the strength of the power-law component, which dominates the spectrum above ~ 2 keV, as the flux decreases.

For the first time, we have modelled the lag-energy spectrum of an AGN using the weightings of the components from fitting the covariance spectra, albeit in a simplified manner. Kara et al. (2013) and Zoghbi et al. (2011) constructed model lag-energy curves based on spectral components fitted to the time-average spectrum. Here we use model components based on fitting to the covariance spectrum, since this direct represents the spectra of the correlated, variable components. The three spectral models used all gave an equally good description of the data. The largest discrepancies in the lag-energy modelling occurs at energies around $\sim 0.7 - 2$ keV. One explanation for these discrepancies could be the fact that we use a constant time delay as a function of energy for the power-law spectral component. This component is likely to have a frequency and energy-dependent time lag, if these are intrinsic lags from the propagation of mass accretion rate fluctuations model (e.g. Arévalo & Uttley 2006). Increasing the time delay as a function of energy for the power-law component in the model may account for the observed discrepancy. This simplistic approach highlights the need to account for any lags that increase as a function of energy in the power law component, when using the weightings of spectral components to model the lag-energy spectrum.

The PSD in Fig. 6.15 shows evidence for two variability mechanisms, each with a different energy dependence. The process dominating at higher frequencies has a harder energy dependence. As we have known some time (e.g. Vaughan et al. 2003; Vaughan et al. 2011) that the PSD is flatter at higher energies. This is equivalent to saying the rms (or covariance) spectrum must get harder at high frequencies, as is observed in e.g. Fig. 6.7. This work is starting to disentangle the origin of this by explicitly modelling the covariance and lag-energy using spectral models. The strong change in the lag energy with flux could indicate that the variations in the hard band are dominated by some other emission component at the lowest fluxes. This component contributes flux and variability

power to the hard band, but is swamped by the softer (power law) continuum at higher fluxes.

The most exciting phrase to hear in science, the one that heralds new discoveries, is not 'Eureka!' but 'That's funny...'

Isaac Asimov

7

X-ray time delays in the Narrow Line Seyfert 1 galaxy PG 1244+026

7.1   Introduction

A subset of NLS1s (the 'complex' NLS1s; Gallo 2006) can also show much more dramatic variability than seen in broad line Seyfert 1s (BLS1s), with deep dips in their X-ray light curves where their spectra appear dominated by reflection (Fabian et al. 2004; 2009). Hence these should give the clearest detections of reverberation lags, contrasting with the 'simple' NLS1, which show only moderate reflection and variability amplitude Gallo 2006. NLS1s typically show stronger soft X-ray excesses than broad line AGN (e.g. Boller et al. 1996; Middleton et al. 2007), so the soft lag signature should be strong in all these systems if the soft excess is from reflection. However, detailed spectral decomposition shows that the majority of the strong soft X-ray emission in NLS1s can be attributed to direct emission from the accretion disc, itself extending into the soft X-ray bandpass. There is still a 'true' soft X-ray excess (which can again be made from either ionised reflection or an additional component) in addition to the disc and coronal components, but it is actually smaller than in broad line objects (Jin et al. 2012a;2012b; Done et al. 2012; Jin et al. 2013; hereafter J13, cf Ross et al. 1992).

PG 1244+026 is one such 'simple' NLS1. Using a 120 ks *XMM-Newton* observation, J13 used frequency resolved spectroscopy (e.g. Revnivtsev et al. 1999) to study the origin of the 'true' soft X-ray excess in this source. The fastest variability (timescales
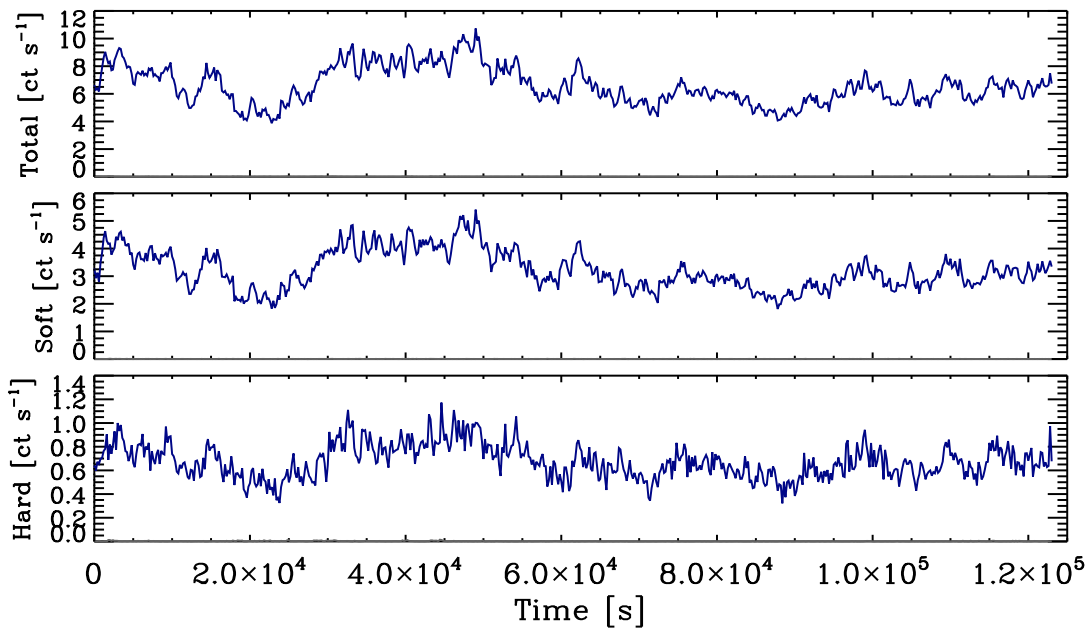
Figure 7.1: PG 1244+026 background subtracted light curves for the soft (0.3–7 keV), hard (1.2–4.0 keV) and total (0.2–10 keV) energy bands. The dark grey curve in each plot is the background count rate.

≤ 5000 s) has a spectrum in which the soft X-ray excess is less prominent than in the time averaged spectrum, as expected if the corona is closest to the black hole so has more rapid variability than the soft excess and disc emission (J13). However, little of this rapid variability of the soft X-ray excess is correlated with the 3–10 keV light curve. This seems to rule out an ionised reflection origin for the majority of the soft X-ray excess, since ionised reflection produces simultaneously the soft X-ray excess and the Fe Kα line and reflection continuum at higher energies (J13).

In this chapter we explore the time lags from PG 1244+026 as a function of frequency and of energy. We model the lag-frequency spectra using simple analytical transfer functions. The lag-energy spectra is modelled using simple simulations.

7.2   Observations and data reduction

PG 1244+026 was observed by *XMM* for $\sim$ 123 ks in December 2011 (OBS ID: 0675320101). The timing analysis in this chapter uses data from the EPIC-pn camera (Strüder et al., 2001) only, due to its higher throughput and time resolution. The raw data were processed from Observation Data Files following standard procedures using the *XMM* Science Analysis System (SAS v13.0.0) with a 20 arcsec circular extraction region.
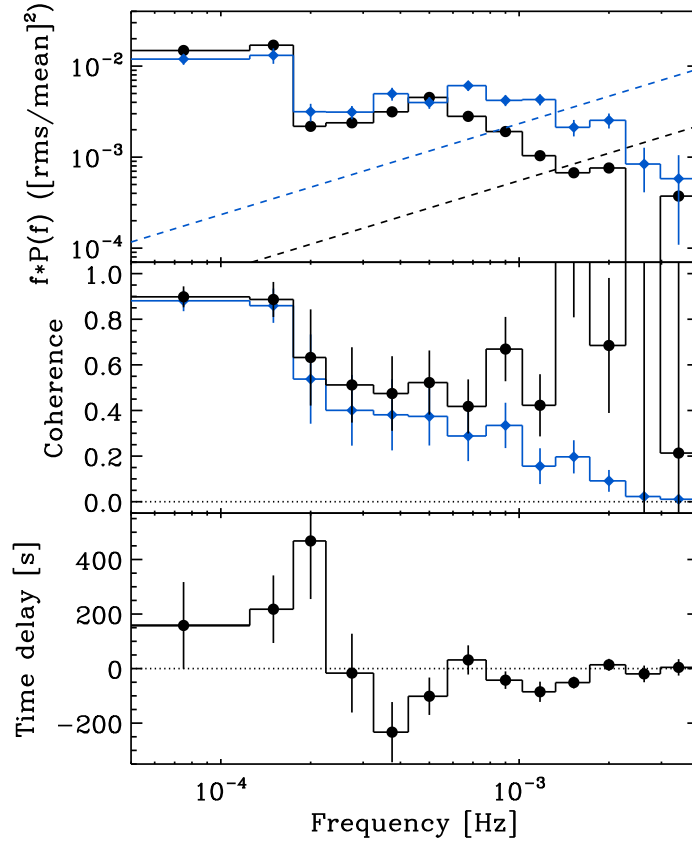
Figure 7.2: Cross-spectral products for the soft (0.3–7 keV) and hard (1.2–4.0 keV) energy bands. Panel (a) shows power spectral density for the soft (black circles) and hard (blue diamonds) bands. The dashed lines are the Poisson noise estimates. Panel (b) shows the raw (blue diamonds) and Poisson noise corrected (black circles) coherence, see Section 7.3 for details. Panel (c) shows the time lag between the hard and soft band, where a positive values indicate the hard band lags.

7.3 Lag as a function of frequency

7.3.1 The power spectrum

We use 0.3–0.7 keV as a soft band to maximise the disc and soft X-ray excess components, with little contamination from the hard X-ray coronal emission, and 1.2-4 keV as a hard band to maximise the coronal emission, with little contamination from the soft X-ray excess or reflected iron Kα emission (J13, see also Fig. 4a). These bands have mean count rates of 3.2 and 0.7 $\mathrm{ct\,s^{-1}}$ respectively. The total (0.2–10 keV) energy band has a mean count rate of 6.6 $\mathrm{ct\,s^{-1}}$. The light curve for the soft, hard and total (0. energy bands are shown in Fig. 7.1.

The upper panel in Fig. 7.2 shows the Poisson noise subtracted power spectra with rms normalisation for the hard (blue) and soft (black) bands, with the Poisson noise level
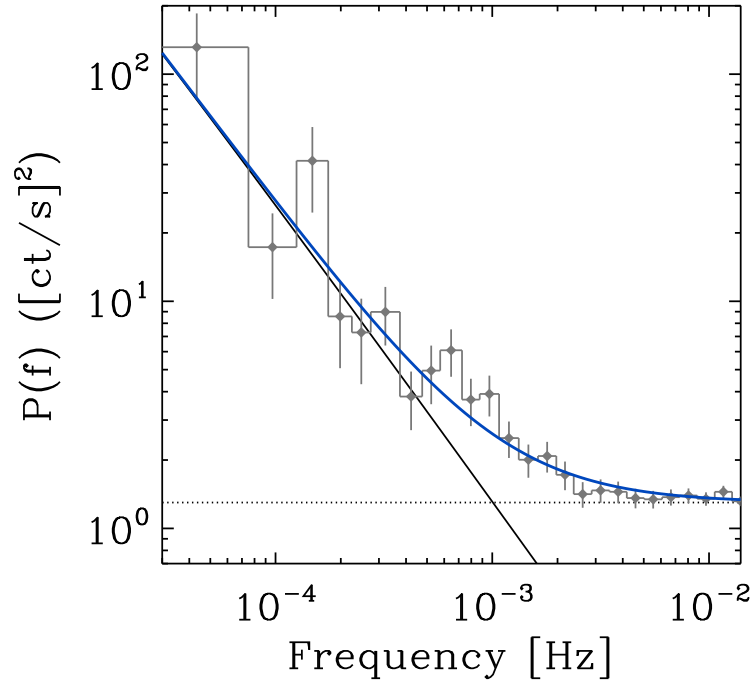
Figure 7.3: Model fit to hard band PSD using a power-law model. The solid black line is the power-law component and the dotted black line is the Poisson noise estimate from the model fitting.

indicated by the dashed lines. So that we can perform Monte Carlo simulations using the properties of the observed light curves, we estimate the PSD using a simple power-law plus constant to model the Poisson noise: $P(\nu) = A\nu^{-\alpha} + P_{\mathrm{N}}$. As the hard band suffers more from the effects of Poisson noise, we estimate the PSD in this band. The model fitting was performed in XSPEC v12.8.1 using a χ^2 fit statistic. Errors quoted on parameters correspond to 90 per cent confidence intervals. The best fitting values for the free parameters were $\alpha = 1.31 \pm 0.11$, $A = 1.4 \pm 1.15 \times 10^{-4}$ and $P_{\mathrm{N}} = 1.31 \pm 0.03$. The fit statistic $\chi^2 = 21.9$ for 24 degrees of freedom (dof), giving a null hypothesis probability $p = 0.58$. The best fit power-law model to the hard band PSD with absolute normalisation is shown in Fig. 7.3.

7.3.2 The observed lag-frequency

We compute cross spectra following the method outlined in Section 2.4. We estimated cross-spectral products by first averaging the complex cross-spectra values over non-overlapping segments of time series, and then averaging in geometrically spaced frequency bins (each bin spanning a factor ~ 1.3 in frequency). For the analysis in this paper we use segment sizes of 20 ks and time bins of 20 s, leaving 6 segments in total. We use these to calculate the coherence between the hard and soft both before (blue) and
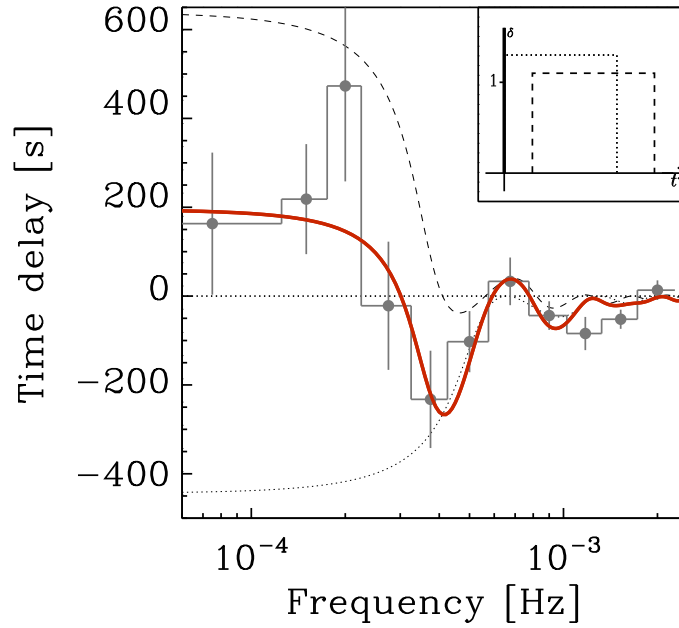
Figure 7.4: The TH-TH model fit to lag-frequency spectrum. The blue dashed line shows the model fit to the data. The red line is the model fit integrated over the frequency bin, matching the fitting procedure. The inset illustrates the TH and δ function in each band. See Section 7.4 for details.

after (black) Poisson noise correction. The noise corrected coherence is high (~ 0.9) for frequencies up to $\sim 1.5 \times 10^{-4}$ Hz, showing that soft and hard band variations are very well correlated on timescales longer than a few ks, but then drops to ~ 0.5 between $\sim 1.5 - 10 \times 10^{-4}$ Hz, and becomes well correlated again at frequencies higher than $\sim 1.5 \times 10^{-3}$ Hz.

The lower panel shows these frequency dependent time lags between the soft and hard bands, where we follow convention by using a negative time lag to indicate the soft band lagging behind the hard band (hereafter 'soft lags').

The lag-frequency spectrum shows a hard lag at frequencies below $\approx 2 \times 10^{-4}$ Hz, whereas between $\approx 3 \times 10^{-4}$ and 2×10^{-3} the soft emission lags the hard, with a maximum soft lag of $\sim 250\,\text{s}$ at $\sim 4 \times 10^{-4}$ Hz. This shape is similar to that seen in other sources, and seems to be quite common in low-redshift, X-ray variable AGN (e.g. Fabian et al. 2009; Emmanoulopoulos et al. 2011; De Marco et al. 2013b; Alston et al. 2013a).

7.3.3 Modelling the lag-frequency

In this section we model the lag-frequency spectra using simple analytical models. Following the approach of Alston et al. (2013a) (see also Chap. 6) we use a top hat (TH) response functions (or transfer functions when discussing the response function in the

Fourier domain), as well as a power law (PL) dependence on lag-frequency, to model the frequency dependent time delays. The response functions can be present in either the hard band, the soft band or both, together with a δ-function response to account for direct (unreprocessed) emission. We fit the lag-frequency data using standard $\min(\chi^2)$ fitting techniques, integrating the model over the bin width, rather than fitting just at the bin centre.

A roughly power law (PL) frequency dependence of the hard X-ray time lag is well established in X-ray binaries (e.g. Miyamoto et al. 1988; Nowak et al. 1999; Pottschmidt et al. 2000), at least at low frequencies, and consistent results from AGN have been reported several times (e.g. Papadakis et al. 2001; Vaughan et al. 2003; McHardy et al. 2004; Arévalo et al. 2006). We therefore consider a PL model of the form $\tau(f) = Nf^{-\alpha}$ with $\alpha \approx 1$. However, a power law response function alone (with no δ function) for the hard band gives an unacceptable fit to the lag-frequency data ($p < 10^{-8}$), as this predicts only positive (hard) lags.

We next model the response of the system assuming a δ function in the soft band, and a δ function plus TH in the hard band. The parameters of the TH are start time t_0, width w and area S (which sets the intensity of delayed emission relative to the direct emission). This was used to model distant reflection by Miller et al. (2010), but the physical picture here is that it models the propagation time delays, as there is probably little reflection contributing to our 'hard' (1.2-4 keV) bandpass (see Alston et al. 2013a, J13). However, irrespective of the way this is interpreted, this can reproduce both positive and negative lags from 'ringing' in the Fourier domain as a result of the sharp edges of the impulse response function (Miller et al., 2010). This model also gives a poor fit to the data ($p \sim 10^{-4}$) as the resulting negative lag from ringing is too sharp to explain the broad frequency range of the observed soft lag (see also Zoghbi & Fabian 2011; Emmanoulopoulos et al. 2011).

We next considered models including an additional TH response in the soft band response, where this soft TH is now physically modelling a reverberation response to the direct emission, whereas the TH in the hard band is modelling propagation lags. Thus the total model is a δ function plus TH in both hard and soft bands, giving a total of 6 free parameters (3 for each TH). We find a good fit to the data with $\chi^2 = 9 / 5$ d.o.f ($p = 0.1$). The full resolution model is shown as the red solid line (Fig. 7.4). The hard response parameters are: $t_0^h = 330 \pm 80$s, $w^h = 1780 \pm 220$s, and $S^h = 1.1 \pm 0.3$, while the soft response parameters are: $t_0^s = 0 \pm 100$s, width $w^s = 1520 \pm 140$s, and scaling fraction $S^s = 1.4 \pm 0.5$.

The effect of the response functions can be separated out by calculating the resulting lag-frequency model assuming that the response function in the other band is simply a δ

function. If the soft band response is replaced by a δ function then the TH in the hard causes the hard band variations to lag the soft band variations (dashed line). Conversely if the hard band response is replaced by a δ function then the TH in the soft band causes the soft to lag the hard (dotted line), but the soft lag extends to higher frequencies due to the narrower width of the TH in the soft band than in the hard. The total response is the sum of these two segments.

The typical propagation lags of the hard band behind the soft band are ~ 1000 s, while the typical reverberation timescale lags of the soft band behind the hard band are of order ~ 750 s. It is this timescale which gives the size scale of the reprocessor, not the lag of ~ 250 seconds as given from the cross-spectrum as the latter does not include the effect of dilution of the lagged flux (TH) by the direct flux (δ function) (see e.g. Miller et al. 2010; Wilkins & Fabian 2013). Hence the reprocessing typically occurs on size scales of $15 R_g$ for a black hole mass of $10^7 M_\odot$.

We note that the model still does not quite match the soft lags observed at the highest frequencies. We could improve the fit by adding another TH in the soft band, starting from $t_0^{s2} = 0$ with width of $\sim$ few hundred seconds. This would skew the response more towards shorter timescales i.e. to weight the reverberation towards smaller distance material. Given the limited frequency resolution, such a complex model will over-fit the data.

7.3.4 Flux dependence of the lag-frequency

A dependence of the lag-frequency with source flux has been observed in the highly variable NLS1 galaxies NGC 4051 (Alston et al. 2013a) and IRAS 13224-3809 (Kara et al. 2013). In NGC 4051 the change with flux level was attributed to different spectral components dominating the broadband X-ray spectra at different flux levels. In IRAS 13224-3809 the change in lag-frequency with flux level was interpreted as arising from changes in the coronal geometry.

A flux dependence on the lag-frequency has been reported in several objects (NGC 4051; Alston et al. 2013a, IRAS 13224-3809; Kara et al. 2013; Ark 564; Chap. 5). In Fig. 7.5 we show the flux dependence on lag-frequency for PG 1244+026 . The total (0.2–10 keV) energy band mean count rate is 6.2 and 5.1 $\mathrm{ct\,s^{-1}}$ for the high and low fluxes respectively. Each flux bin contains only three 20 ks segments, and hence the large error bars. Despite this, a tentative change with flux is observed, with the frequency of the soft lag appearing to shift to higher frequencies as the flux level drops. Given the large error bars we do not attempt to model the lag-frequency spectra.
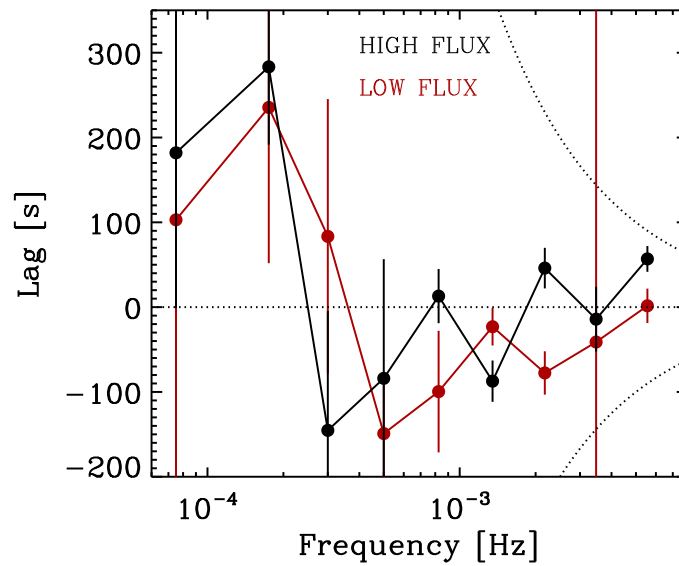
Figure 7.5: Flux dependence of the lag-frequency spectra. The high and low flux levels have a total (0.2–10 keV) energy band mean count rate of 6.2 and 5.1 $\mathrm{ct\,s}^{-1}$ respectively. The dotted line shows the time delay for a phase lag of π.

7.4 The frequency resolved lag-energy spectrum

7.4.1 The observed lag-energy spectra

A lag-energy spectrum can be calculated over a given range in frequency by estimating the cross-spectral lag between a light curve in each energy band with respect to the frequency resolved lightcurve over a broad reference band (e.g. Zoghbi & Fabian 2011). We take our reference band as the hard band in the previous lag-frequency work i.e. the 1.2–4.0 keV light curve *minus* the energy band for which the lag is being computed so that we never have correlated Poisson noise. A positive lag indicates the given energy bin lags the broad reference band (so soft lags are now positive). The lag has not been shifted to a zero level, so the lag represents the average lag or lead of that energy band to variability over this frequency range.

Motivated by the lag-frequency plot, we calculate the lag-energy over three frequency ranges, one focused on the hard lags ($0.8-2\times10^{-4}$ Hz, low frequency, hereafter LF), one centred around the most negative (soft) lags ($3-5\times10^{-4}$ Hz, high frequency, hereafter HF), and one spanning the remaining negative (soft) lags ($8-16\times10^{-4}$ Hz, very high frequency, hereafter VHF).

Fig. 7.6 shows the lag as a function of energy for the LF, HF and VHF frequencies. At LF (lower panel) the soft energies lead the 1.2-4 keV reference band, with the delay increasing with energy separation. This is consistent with results found in BH-XRBs (e.g
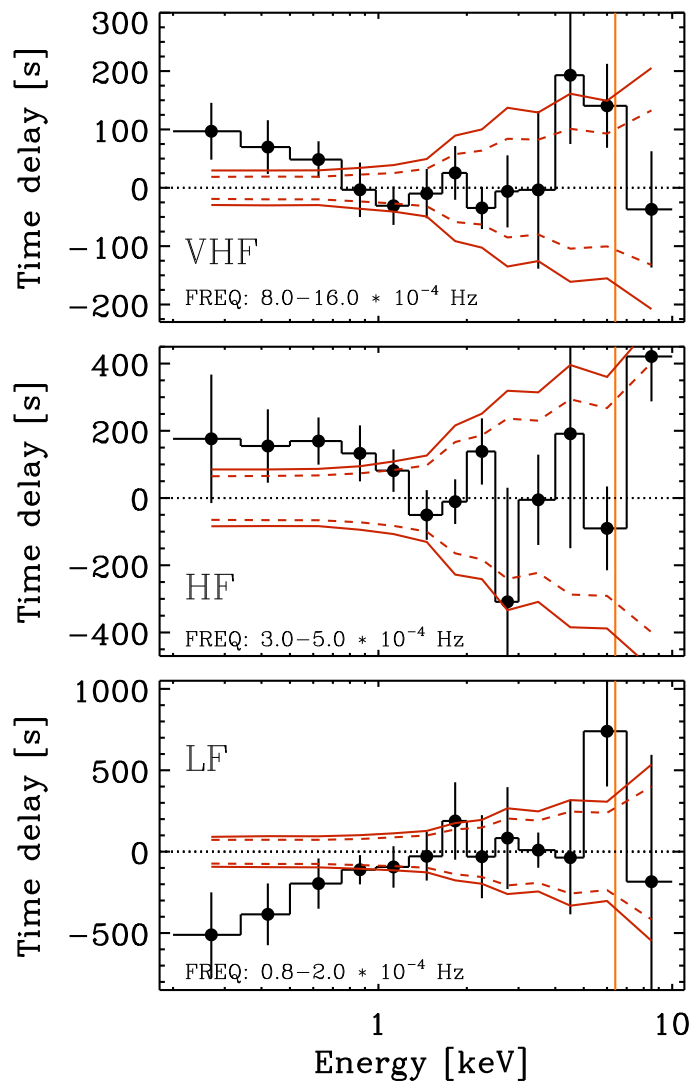
Figure 7.6: Lag-energy spectrum for low (LF; $0.8 - 2.0 \times 10^{-4}$ Hz), high (HF; $3 - 6 \times 10^{-4}$ Hz) and very high (VHF; $8 - 14 \times 10^{-4}$ Hz) frequencies. A 1.2–4.0 keV reference band was used. The red dashed and solid lines are the 90 and 95 per cent confidence intervals respectively, on the assumption of zero 'true' lag.

Miyamoto & Kitamoto 1989; Nowak et al. 1999) and AGN (e.g. Arévalo et al. 2008; Zoghbi & Fabian 2011; Kara et al. 2013). A possible (2σ significance) lag in the iron K band can be seen, which lags behind the 1.2–4.0 keV reference band by $\sim 500 - 1000$ s.

At HF (middle panel), the softer energies lag the reference band, in agreement with the lag-frequency spectrum in Fig. 7.4. The lag below ~ 1 keV is ~ 200 s behind the reference band. No iron Kα lag can be seen in the data.

At VHF (upper panel in Fig. 7.6) the soft energies (below ~ 0.6 keV) lag the reference band by up to 100 s. Also evident is a feature around iron Kα with a lag of ~ 150 s.

The difference in lag-energy between the two soft lag frequency ranges (HF and VHF)

is surprising. This is the first time that the soft lags have been examined as a function of frequency, and the differences indicate that different processes may be dominating at these two different timescales. We assess the significance of this result firstly by assessing the significance of the lags in the VHF as this regime is more susceptible to Poisson noise, particularly at high energies. We use 10^4 Monte Carlo simulations of well-correlated light curves with zero 'true lag', with the properties (power spectra, count rates) of the real data. The 90 and 95 per cent confidence intervals are shown as the red dashed and solid lines in Fig. 7.6. The low energy continuum (below 0.6 keV) and iron line lags are both detected at $\sim 2\sigma$ significance. We also show the 90 and 95 percent confidence intervals for the HF and LF in Fig. 7.6. The soft lag is detected at $> 2\sigma$ confidence at energies below 1 keV in the HF. At LF, the soft lead at energies below $\sim 0.8\,\mathrm{keV}$ is detected at $> 2\sigma$, as well as the lag in the iron Kα band.

7.4.2 Modelling the lag-energy spectra

J13 presented several spectral models to explain the time averaged spectrum and the co-variance spectra. In this section we re-examine these models in terms of their lag-energy predictions. We model the resulting lag-energy spectra using simulations, similar to the method of Kara et al. (2013). We simulated identical sets of light curves for each energy bin, including independent Poisson noise in each. The light curves of each component (at each energy) were time-shifted and then combined weighted by the strength of the component in the mean spectrum at a given energy. This is clearly a simplification of the effects of an impulse response function on each spectral component, but allows us to approximate the shape of the lag-energy spectrum resulting from the combined effects of multiple components.

7.4.2.1 Neutral reflection and a separate soft X-ray excess

We first use the spectral components identified in J13 (see Fig. 7.7a), where there is a blackbody from intrinsic disc emission (red), a separate soft X-ray excess component (green) which provides seed photons to produce the coronal emission from Compton up-scattering (blue). This coronal emission illuminates the disc and produces a (mostly) neutral reflection spectrum (black) from a region with inner radius of $\sim 15R_g$ (The spectral fitting shown here was performed by C. Done).

For slow variability, where we are seeing propagation time delays, we assume that the blackbody disc emission leads, followed by the soft X-ray excess, followed by the corona. This gives a good match to the LF lag-energy spectra if the soft excess lags 400 seconds behind the blackbody, and the corona lags by 1500 seconds behind the blackbody. The
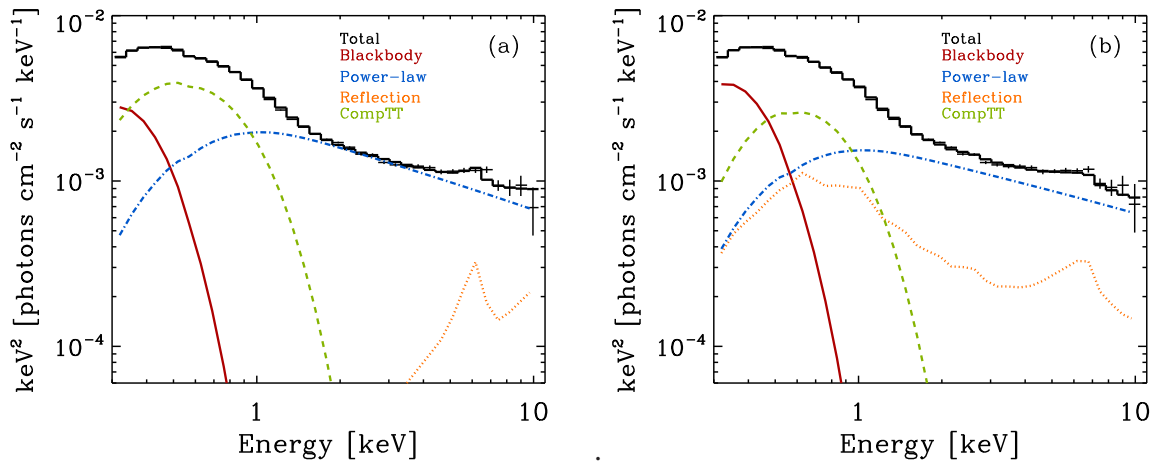
Figure 7.7: a) Left: neutral reflection model: blackbody (red solid), an absorbed power-law emission (blue dot-dashed), separate soft excess component (green dashed), and neutral reflection (orange dotted). b) Right: ionised reflection model including a blackbody (red solid), absorbed power-law emission (blue dot-dashed), a separate soft excess component (green dashed), and ionised reflection (orange dotted). The data are the 'unfolded' time-averaged EPIC spectra (see J13). The spectral fitting shown here was performed by C. Done.

soft band emission then leads the hard band by ~ 1000 seconds, as required by the lag-frequency fits (see Fig. 7.4). These simulated LF lag-energy spectra are shown in the lower panel of Fig. 7.8.

The HF lag energy can be matched by assuming that some part of the soft excess emission is reprocessed on short timescales, so that it lags behind the corona by 300 seconds (middle panel in Fig. 7.8). No iron Kα is seen in the data at this frequency, but we include a 300 second lag for this feature. If an iron Kα reflection feature is observed at VHF, and at LF with a longer delay than in the VHF, then we might also expect to see this feature at HF. Its presence in the LF suggests this feature has not been smeared out over the timescale of interest, and hence why we expect to observe it at HF.

An iron line is instead seen in the VHF lag-energy plot. This can be well described if some fraction of the reflected emission lags 200 seconds behind the fastest coronal variability. However, this cannot reproduce the low energy lag seen in the VHF (blue simulations in upper panel of Fig. 7.8). This is better fit by the shape of the blackbody disc. The green simulations in the upper panel of Fig. 7.8 show the VHF lag-energy prediction if both the blackbody and reflected emission lag 200 seconds behind the fastest coronal variability.
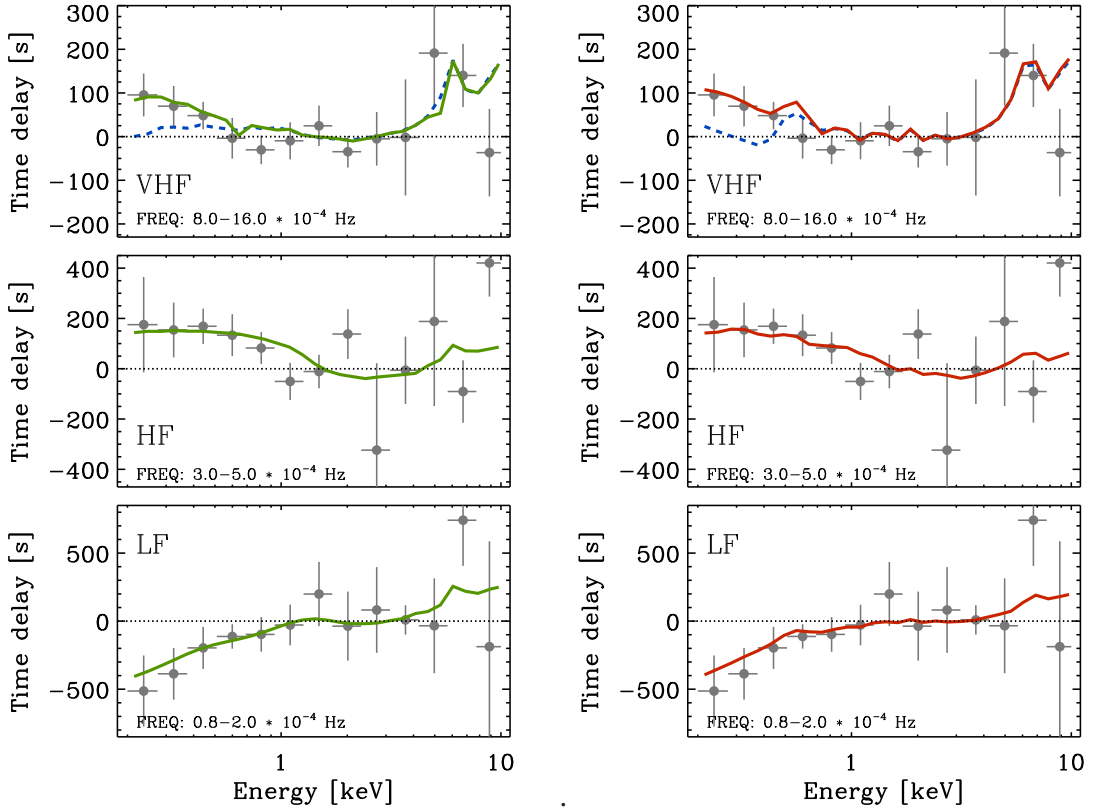
Figure 7.8: a) Left: simulated lag-energy spectra for the neutral reflection model, at low (LF; $0.8 - 2.0 \times 10^{-4}$ Hz), high (HF; $3 - 6 \times 10^{-4}$ Hz) and very high (VHF; $8 - 14 \times 10^{-4}$ Hz) frequencies. A 1.2–4.0 keV reference band was used. The green line represents the model including the black body, whereas the blue line does not include a lag from this component. b) Right: simulated lag-energy spectrum for the ionised reflection model, for the LF, HF and VHF ranges. The red line represents the models including the black body, whereas the blue line does not include a lag from this component.

7.4.2.2 Ionized reflection and a separate soft X-ray excess

The model above is an extreme interpretation of the spectrum. The reflector is likely to be ionized to some extent, so we explore how this might change the reverberation predictions. We allow reflection to be ionised in the fits. We describe this using the RFXCONV model (Kolehmainen et al. 2011), which is a convolution version of the Ross & Fabian (2005) ionized reflection models, but also include an additional soft X-ray excess as is required by the fast covariance spectra (J13). However, this gives a best fitting model to the time average spectrum for fairly low ionisation $\log \xi = 1.3$, which is again not highly smeared by relativistic effects ($R_{in} = 10R_g$ for standard emissivity of $\eta(r) \propto r^{-3}$). This does not produce much more low energy reflection than the original models, so instead we fix $\log \xi = 3$ to explore the impact of the maximal contribution of reflection at low energies. This requires $R_{in} = 3R_g$ in order to smooth the low energy

atomic features, and so implies high spin, in contrast to the intrinsic disc component in this source which implies low spin (Done et al. 2013). This spectral model is shown in Fig. 7.7b (The spectral fitting shown here was performed by C. Done).

The lag prediction from this maximal reflection model are shown in Fig. 7.8b, calculated using the same lags for each component as before. They are not dramatically different to those from neutral reflection, possibly because the ionised reflection is still a small fraction of the soft band flux, relative to the other components. The additional blackbody variability is still required in the VHF to match the soft lag seen in these data as the reflected emission follows the illuminating spectrum, and there is a downturn in the illuminating spectrum at low energies due to the seed photon energy for Compton upscattering being within the observed bandpass (J13). This downturn limits the amount of reflection at the lowest energies.

7.5 Discussion and Conclusions

We show that the X-ray time delays as a function of energy and Fourier-frequency can be constrained in the 'simple' NLS1 PG 1244+026 using a 120 ks XMM-Newton observation. The lag as a function of frequency between a hard (1.2–4.0 keV) and a soft (0.3-1 keV) energy band shows the now well established switch from a hard lag at low frequencies to a soft lag at high frequencies. The maximum soft lag of ~ 200 s is at $\sim 4 \times 10^{-4}$ Hz but there is also evidence for a second negative lag of ~ 100 s at $\sim 1.2 \times 10^{-3}$ Hz.

Modelling the lag-frequency spectrum with simple response functions gives an acceptable fit if both hard and soft bands contain both direct emission (modelled using a δ-function response) and a smoothed, time-delayed response (approximated by a top hat response function). We interpret the lagged response in two different ways in the two different bands, with the hard band lag being a result of propagation time delays while the soft band lag results from reprocessing of the primary X-ray spectrum. The soft band response function has a maximum time delay of ~ 1500 s. For a black hole mass of $\sim 10^7 M_{\rm BH}$, this corresponds to reprocessing within $\sim 20 R_g$ of the illuminating source.

We consider the lag as a function of energy in three frequency ranges. The lag-energy data are consistent with the interpretation above. The lowest frequency lag-energy spectra shows the long timescale variability has a lag which increases systematically with energy (Fig. 7.6). This is expected from propagating fluctuations through the accretion flow, where the disc, soft excess and harder X-ray emission from a spatially extended corona are produced at progressively smaller radii. The slow variability originates in the disc, propagates to the soft excess, then propagates to the corona. Each component has its own

lag, but the smoothly varying change in the contribution of each component with energy results in a smooth lag-energy spectrum.

On shorter timescales, we would not expect the propagating fluctuations to correlate at all across the spectrum, as the disc and soft X-ray excess probably cannot vary much intrinsically on these timescales. The soft lag at these frequencies is therefore interpreted as reprocessing of the intrinsic power-law emission. We split the frequency band over which the soft lag is seen into two, and find evidence for a change in the lag-energy spectra with frequency. The high frequency (HF) variability appears to show a stronger reprocessing response in the soft excess rather than in the reflected component; there is no significant lag at iron Kα, but only at energies below 1.2 keV. The VHF has a lag at iron (and redward) energies, but this is accompanied not by the soft excess but by the blackbody.

The hard X-ray emission from the corona is consistent with an origin in inverse-Compton scattering. The downturn below 0.8 keV in the covariance indicates that the source of seed photons is the soft X-ray excess (J13). This strongly limits the amount of reflection which can contribute to the spectrum below 1 keV. Thus reflection alone is not the only source of lags in this object. An obvious additional source is thermal reprocessing - the thermalisation of the non-reflected, absorbed emission, which leads to heating of the disc and soft X-ray excess regions as they respond to increased illumination. This could give a physical explanation as to why these components are seen to reverberate along with the reflection component. However, it is strange that the soft excess emission requires typically longer to respond to the coronal illumination than the blackbody and iron line. The propagation lags clearly show that the soft excess region lags the blackbody, so is smaller and closer in than the blackbody. We would expect its reprocessed signature to be more evident at higher frequencies than the blackbody as it is closer to the coronal emission region. It may be that the region producing the soft excess has little reflected or reprocessed flux (perhaps because it is too highly ionised), but that it responds to the corona via propagation lags on the blackbody disc response.

The hard band PSD (Fig. 7.2) shows weaker variability power than the soft band at frequencies below $\sim 2 \times 10^{-4}$ Hz (LF). At frequencies above $\sim 2 \times 10^{-4}$ Hz (HF) the power in each band is comparable, with the hard showing a slight excess in power. The hard band shows an obvious excess in power exactly where the VHF soft lag occurs. The coherence also drops to ~ 0.5 just above the HF band. This drop in coherence is most easily explained as due to the 'cross over' between two independently varying components with quite different energy spectra. At LF and VHF bands, where one component dominates the PSD in both bands, the coherence is high since each component is correlated with itself.

Only scientists and prostitutes get paid for doing what they love

Origin Unknown (from Hawking. S. memoir)

8

Conclusions and future work

8.1   Summary of work presented in this thesis

In this thesis I have presented several studies on the variability properties of Narrow Line Seyfert 1s (NLS1s). Here we briefly summarise the main results of each chapter.

In Chap. 3 we studied the correlated variability between the UV and X-ray emission in NGC 4051. UV variability is detected on short and long time scales, however the fractional rms amplitude is smaller than that in the X-rays. Fitting the UV PSD with a simple power-law model found a slope of index $\alpha = 2.62 \pm 0.48$. A ~ 3 ks UV time lag behind the X-ray variations was detected, indicating a scenario where $\sim 25\,\%$ of the UV variance is caused by thermal reprocessing of the incident X-ray emission, placing the UV reprocessing region at an annulus of $\sim 300R_{\mathrm{g}}$. However, the analysis was limited by the short lengths of each observation (which means the UV varies only a little within each observation) and uncertainties in the OM photometry.

In Chap. 4 we studied the inter-band X-ray time lags as a function of frequency between a soft and hard band as a function of source flux in NGC 4051, including modelling with simple analytical response functions. We found that in order to model the lag-frequency data we needed to include delayed components in the response functions for both hard and soft bands, and the weighting of the hard reprocessing component was found to decrease with source flux. This result is consistent with reprocessing/reflection on the disc within $\sim 60R_{\mathrm{g}}$ of the central illuminating power-law continuum source. The change in the reprocessing with source flux is consistent with the continuum of spectral variability observed in NLS1s.

In Chap. 5 we apply the response function modelling of Chap. 4 to a sample of NLS1. We found the lag-frequency spectra for each object require two lagging components, one in the hard band and one in the soft. This has strong implications for the distant reflector model, as this would require a response function with a narrow width to lie along the line

of sight in each object. We searched for a flux dependence on the lag-frequency spectra in each source. The only object, in addition to NGC 4051, to show a significant flux dependence was Ark 564.

In Chap. 6 we studied the energy dependence of the X-ray time lags in NGC 4051. As with the lag-frequency in Chap. 4, a strong dependence on source flux was observed. Using simple spectral models, we modelled the covariance spectra at frequencies where we compute the lag energy, and use the weightings of the spectral components to model the lag-energy. The model fitting indicates that the changes in the lag-energy spectrum with flux can be associated with the increase in the soft excess component, and subsequent decrease in the power law component as the flux level drops. This is also observed in the power spectrum, with the harder component dominating the variability as the flux drops. The lag energy models did not give a full description of the data, suggesting that the intrinsic energy dependence of the primary power law component needs to be accounted for.

In Chap. 7 we studied the X-ray time delays as a function of energy and Fourier-frequency in the NLS1 PG 1244+026, a source with $L/L_{\mathrm{Edd}} \sim 1$). We found remarkable time delay properties despite using only a 120 ks *XMM-Newton* observation. The lag-frequency spectra showed the now well established hard lags at low frequencies, with a switch to soft lags at higher frequencies. Modelling the lag-frequency with simple response functions we found the reprocessing to occur within $\sim 20R_{\mathrm{g}}$ of the illuminating source. The lag-energy spectra revealed lags consistent with the low-frequency intrinsic propagation delays. At higher frequencies only a soft lag is seen. At the highest frequencies, a soft lag is seen, along with tentative evidence for iron Kα reverberation. Simple modelling of the lag-energy spectra found that both ionised and neutral reflection was consistent with the data. A blackbody component was also required to model the lowest energies, as well as a component for the soft excess.

8.2 Future work

X-ray timing studies of AGN are proving to add valuable information to our understanding the emission processes from the inner regions of accreting black holes. Time delays between X-ray energy bands hold the key to decoding the causal connection between the various emission and absorption components, as well as understanding the geometry and location of the central source. Studies of this kind are vital if we wish to make precise spin measurements, and understand strong gravity near black holes. However, our understanding of the intrinsic time delays and reverberation signature is still in its infancy.

In this thesis I modelled the lag-frequency spectrum using simple response functions. To derive more physical insight from this data they need to be modelled with realistic response functions (e.g. Wilkins & Fabian 2013). Although, as we have seen, simple models are capable of describing the data well, meaning higher resolution lag-frequency spectra are required in order to distinguish more complex models. Ultimately, this relies on longer observations of the same sources with observatories such as *XMM-Newton* , to improve the signal to noise. The signal-to-noise of the lag-frequency is determined by the number of segments being averaged. Repeated, long observations are therefore needed to extend our coverage of the lag-frequency spectrum down to lower frequencies, and to increase the frequency resolution. As has been known for some time, the lower frequencies appear to be dominated by a different reprocessing mechanism. Having a better estimates of the time lags at these frequencies is essential for constraining the intrinsic reprocessing component, and performing detailed modelling of the reverberation signature signature at higher frequencies.

Different analysis methods may also prove valuable in understanding the low frequency time delays. Recently, Zoghbi et al. (2013) have developed the method of Miller et al. (2010) for producing time lags from 'gappy' data. This may result in better low-frequency time delay estimates from satellites in low-Earth orbits, such as *Suzaku* and *NuStar* , which are subject to more frequent orbital gaps. These methods may even be applicable to contiguous *XMM-Newton* observations.

The recently launched *NuStar* telescope (Harrison et al. 2013) provides X-ray coverage from $\sim 3 - 79$ keV. Combined *NuStar* and *XMM-Newton* observations could provide lag-frequency and lag-energy data at energies >10 keV. Understanding the X-ray time lags at higher energies will improve our understanding of the separate variability components. Constraining the shape of the lag-energy spectrum at higher energies will provide an additional way to distinguish between the distant reprocessor model and disc reprocessing model for the origin of the soft lags.

The *ASTROSAT* satellite is currently scheduled for launch in 2014. This will carry both soft and hard X-ray instruments, as well as twin UV/optical telescopes. This will provide an excellent resource for inter-band variability studies, such as was presented in Chap. 3. These studies prove to be an excellent tool for studying the constraining the origins of the origins of the variability, and probing the disc—corona geometry of the central engine.

Future missions such as *Athena+* (Nandra et al. 2013) would provide very high count rate light curves. This would enable lag-energy and lag-frequency studies at much higher energy and frequency resolution. The higher S/N means we will be able to studies up to much higher frequencies.

There is still much more insight that can be gained from existing and forthcoming *XMM-Newton* data. Understanding the soft lags in wider range of objects, with a broader range in $M_{\rm BH}$ and $L/L_{\rm Edd}$, will help explore the soft-lag–$M_{\rm BH}$ relation found in De Marco et al. (2013b), providing more insight into the reverberation origin. A flux dependence has been confirmed in three sources (NGC 4051; Alston et al. 2013a, IRAS 13224–3809; Kara et al. 2013, Ark 564; Chap. 5) and tentatively seen in PG 1244+026 (Chap. 7). As we saw in Chap. 4, this improves the modelling of the lag-frequency spectra, particularly when the frequency resolution is low. Longer exposure on these sources is required to capture a broader range in flux levels, in order to fully understand this flux dependence.

As the exposure sources receive increases, this will also allow us to explore the energy dependence of the time lags at a higher frequency resolution. Indeed, this is currently possible with some of the sources presented in Chap. 5. I plan to follow up the lag-frequency sample study with a detailed systematic look at the lag-energy spectra in these sources. Of course, better techniques to model the lag-energy spectra are required before more physical insight can be gained, and allowing us to break the degeneracies in spectral models.

As the reprocessing components have an energy-dependence as well as frequency dependence, response functions which account for this energy dependence are required for a complete description of the time delays across the whole X-ray band. The development of energy dependent response functions, $RESP(E, f)$, is currently work in progress. A number of related timing analysis diagnostics are currently used to understand the underlying variability in accreting black holes. A model which simultaneously makes predictions for the PSDs, lag-energy, lag-frequency and coherence would provide a valuable test of the variability process and reprocessing components.

8.3   A final remark

The work presented in this thesis highlights the use of time-delay studies in understanding the central engine in AGN. Simultaneous UV and X-ray variability studies provide an excellent probe of the disc—corona geometry, and the origins of the variable emission. The time lags between X-ray bands reveal the causal connection between the X-ray emission components, and help break the degeneracies in spectral modelling. A consistent picture is beginning to emerge in which the high frequency soft X-ray lags arise from the reprocessing of the primary X-ray emission in the innermost regions of the accretion disc. However, the exact details of the reprocessing remain uncertain. It is clear that the high frequency X-ray time delays offer a powerful, new probe of the direct vicinity of black holes, that which is affected most by strong gravity.

References

Abramowicz M. A., 1988, Advances in Space Research, 8, 151 8

Agol E., Krolik J. H., 2000, ApJ, 528, 161 5

Alston W. N., Vaughan S., Uttley P., 2013a, MNRAS, 435, 1511 86, 90, 102, 131, 132, 133, 144

Alston W. N., Vaughan S., Uttley P., 2013b, MNRAS, 429, 75 75

Antonucci R., 1993, ARA&A, 31, 473 9

Antonucci R. R. J., Miller J. S., 1985, ApJ, 297, 621 10

Arévalo P., 2013, in Zhang C. M., Belloni T., Méndez M., Zhang S. N., eds, IAU Symposium Vol. 290 of IAU Symposium, Accretion disc variability in AGN. pp 181–182 18

Arévalo P., McHardy I. M., Summons D. P., 2008, MNRAS, 388, 211 104, 135

Arévalo P., Papadakis I. E., Uttley P., McHardy I. M., Brinkmann W., 2006, MNRAS, 372, 401 60, 66, 132

Arévalo P., Uttley P., 2006, MNRAS, 367, 801 21, 22, 59, 66, 76, 125

Arévalo P., Uttley P., Kaspi S., Breedt E., Lira P., McHardy I. M., 2008, MNRAS, 389, 1479 23

Arévalo P., Uttley P., Lira P., Breedt E., McHardy I. M., Churazov E., 2009, MNRAS, 397, 2004 23, 58

Arnaud K. A., 1996, in G. H. Jacoby & J. Barnes ed., Astronomical Data Analysis Software and Systems V Vol. 101 of Astronomical Society of the Pacific Conference Series, XSPEC: The First Ten Years. p. 17 50, 110

Arnaud K. A., Branduardi-Raymont G., Culhane J. L., Fabian A. C., Hazard C., McGlynn T. A., Shafer R. A., Tennant A. F., Ward M. J., 1985, MNRAS, 217, 105 16

Awaki H., Kunieda H., Tawara Y., Koyama K., 1991, PASJ, 43, L37 10

Baade W., Zwicky F., 1934, Phys. Rev., 46, 76 2

Balbus S. A., Hawley J. F., 1991, ApJ, 376, 214 7

Balbus S. A., Hawley J. F., 1992, ApJ, 400, 610 7

Ballet J., 1999, A&AS, 135, 371 61, 79

Bardeen J. M., Press W. H., Teukolsky S. A., 1972, ApJ, 178, 347 2, 15

Barthel P. D., 1989, ApJ, 336, 606 9

Barthelmy S. D., Barbier L. M., Cummings J. R., Fenimore E. E., Gehrels N., Hullinger D., Krimm H. A., Markwardt C. B., Palmer D. M., Parsons A., Sato G., Suzuki M.,

Takahashi T., Tashiro M., Tueller J., 2005, Space Science Rev., 120, 143 28

Bartlett M., 1948, Nature, 161, 686 31

Bautista M. A., Kallman T. R., 2001, ApJS, 134, 139 109

Beckmann V., Shrader C., 2012a, in Proceedings of "An INTEGRAL view of the high-energy sky (the first 10 years)" The AGN phenomenon: open issues 10

Beckmann V., Shrader C. R., 2012b, Active Galactic Nuclei 5, 9, 11, 12

Begelman M. C., 2003, Science, 300, 1898 3

Belloni T. M., 2010, in Belloni T., ed., Lecture Notes in Physics, Berlin Springer Verlag Vol. 794 of Lecture Notes in Physics, Berlin Springer Verlag, States and Transitions in Black Hole Binaries. p. 53 18, 19

Bendat J., Piersol A., 1986, Random data: analysis and measurement procedures. A Wiley-Interscience publication, Wiley 36, 73

Bendat J. S., Piersol A. G., 2010, Random data: analysis and measurement procedures. John Wiley & Sons, Inc. 34, 35, 36, 53

Bentz M. C., Walsh J. L., Barth A. J. e. a., 2009, ApJ, 705, 199 80

Berti E., Volonteri M., 2008, ApJ, 684, 822 5

Bian W., Zhao Y., 2003, MNRAS, 343, 164 80

Blaes O., 2013, Space Science Rev. 7

Blandford R. D., McKee C. F., 1982, ApJ, 255, 419 4

Blandford R. D., Znajek R. L., 1977, MNRAS, 179, 433 5

Boller T., Brandt W. N., Fink H., 1996, A&A, 305, 53 10, 127

Box G. E. P., Jenkins G. M., eds, 1976, Time series analysis. Forecasting and control 51

Breedt E., Arévalo P., McHardy I. M., Uttley P., Sergeev S. G., Minezaki T., Yoshii Y., Gaskell C. M., Cackett E. M., Horne K., Koshida S., 2009, MNRAS, 394, 427 23

Breedt E., McHardy I. M., Arévalo P., Uttley P., Sergeev S. G., Minezaki T., Yoshii Y., Sakata Y., Lira P., Chesnok N. G., 2010, MNRAS, 403, 605 42, 57, 59, 75

Brenneman L., 2013, Measuring the Angular Momentum of Supermassive Black Holes 3

Brooks S., 1998, Journal of the Royal Statistical Society: Series D (The Statistician), 47, 69 40

Burrows D. N., The Swift XRT Team 2004, in AAS/High Energy Astrophysics Division #8 Vol. 36 of Bulletin of the American Astronomical Society, The Swift X-ray Telescope. pp 929–+ 28

Cackett E. M., Fabian A. C., Zogbhi A., Kara E., Reynolds C., Uttley P., 2013, ApJL, 764, L9 60

Cackett E. M., Horne K., Winkler H., 2007, MNRAS, 380, 669 23

Cameron D. T., McHardy I., Dwelly T., Breedt E., Uttley P., Lira P., Arevalo P., 2012,

MNRAS, 422, 902 23

Carter B., 1968, Phys. Rev., 174, 1559 2

Cassatella P., Uttley P., Maccarone T. J., 2012, MNRAS, 427, 2985 39

Chandrasekhar S., 1931a, MNRAS, 91, 456 2

Chandrasekhar S., 1931b, ApJ, 74, 81 2

Colbert E. J. M., Mushotzky R. F., 1999, ApJ, 519, 89 3

Collin S., 2001, in Aretxaga I., Kunth D., Mújica R., eds, Advanced Lectures on the Starburst-AGN Accretion and Emission Processes in AGN. p. 167 17

Collin S., Kawaguchi T., 2004, A&A, 426, 797 10

Courvoisier T. J.-L., 2013, High Energy Astrophysics 9

Crummy J., Fabian A. C., Gallo L., Ross R. R., 2006, MNRAS, 365, 1067 14, 16

Cui W., Zhang S. N., Focke W., Swank J. H., 1997, ApJ, 484, 383 20

Cunningham C. T., 1975, ApJ, 202, 788 3

Czerny B., 2006, in C. M. Gaskell, I. M. McHardy, B. M. Peterson, & S. G. Sergeev ed., Astronomical Society of the Pacific Conference Series Vol. 360 of Astronomical Society of the Pacific Conference Series, The Role of the Accretion Disk in AGN Variability. p. 265 8, 22, 59

Czerny B., Elvis M., 1987, ApJ, 321, 305 12

Czerny B., Nikołajuk M., Różańska A., Dumont A.-M., Loska Z., Zycki P. T., 2003, A&A, 412, 317 16

Davis J. E., 2001, ApJ, 562, 575 61, 79

de Laplace P., 1796, Exposition du système du monde. No. v. 2 in Exposition du système du monde, Impr. du Cercle-Social 2

De Marco B., Ponti G., Cappi M., Dadina M., Uttley P., Cackett E. M., Fabian A. C., Miniutti G., 2013a, MNRAS 60, 63, 75

De Marco B., Ponti G., Cappi M., Dadina M., Uttley P., Cackett E. M., Fabian A. C., Miniutti G., 2013b, MNRAS, 431, 2441 78, 79, 81, 83, 98, 100, 101, 102, 131, 144

De Marco B., Ponti G., Uttley P., Cappi M., Dadina M., Fabian A. C., Miniutti G., 2011, MNRAS, 417, L98 60

De Rosa A., Piro L., Fiore F., Grandi P., Maraschi L., Matt G., Nicastro F., Petrucci P. O., 2002, A&A, 387, 838 14

den Herder J. W., Brinkman A. C., Kahn S. M., Branduardi-Raymont G., Thomsen K., Aarts H., de Vries C. P., Welch S., Zehnder A., 2001, A&A, 365, L7 26

Denney K. D., Watson L. C., Peterson B. M., 2009, ApJ, 702, 1353 42, 59, 76, 80

Dewangan G. C., Griffiths R. E., Dasgupta S., Rao A. R., 2007, ApJ, 671, 1284 16

Done C., 2007, Progress of Theoretical Physics Supplement, 169, 248 16

Done C., 2010, ArXiv e-prints 17

Done C., Davis S. W., Jin C., Blaes O., Ward M., 2012, MNRAS, 420, 1848 127

Done C., Gierliński M., 2005, Ap&SS, 300, 167 9

Done C., Jin C., Middleton M., Ward M., 2013, MNRAS, 434, 1955 139

Done C., Nayakshin S., 2007, MNRAS, 377, L59 17

Done C., Ward M. J., Fabian A. C., Kunieda H., Tsuruta S., Lawrence A., Smith M. G., Wamsteker W., 1990, MNRAS, 243, 713 22, 42

Dressler A., Richstone D. O., 1988, ApJ, 324, 701 4

Eckart A., Genzel R., 1997, MNRAS, 284, 576 4

Edelson R. A., Alexander T., Crenshaw D. M., Kaspi S., Malkan M. A., Peterson B. M., Warwick R. S., Clavel J., Filippenko A. V., Horne K., Korista 1996, ApJ, 470, 364 6

Edelson R. A., Krolik J. H., 1988, ApJ, 333, 646 55

Edelson R. A., Krolik J. H., Pike G. F., 1990, ApJ, 359, 86 30

Einstein A., 1915, Sitzungsberichte der Königlich Preußischen Akademie der Wissenschaften (Berlin), Seite 778-786., pp 778–786 2

Emmanoulopoulos D., McHardy I. M., Papadakis I. E., 2011, MNRAS, 416, L94 60, 63, 81, 83, 98, 131, 132

Emmanoulopoulos D., Papadakis I. E., McHardy I. M., Arévalo P., Calvelo D. E., Uttley P., 2012, MNRAS, 424, 1327 78

Evans P. A., Beardmore A. P., Page K. L., 2009, MNRAS, 397, 1177 46

Fabian A. C., 2005, Ap&SS, 300, 97 14

Fabian A. C., 2012, ARA&A, 50, 455 5

Fabian A. C., Ballantyne D. R., Merloni A., Vaughan S., Iwasawa K., Boller T., 2002, MNRAS, 331, L35 22, 110

Fabian A. C., Iwasawa K., Reynolds C. S., Young A. J., 2000, PASP, 112, 1145 5, 15

Fabian A. C., Miniutti G., Gallo L., Boller T., Tanaka Y., Vaughan S., Ross R. R., 2004, MNRAS, 353, 1071 127

Fabian A. C., Rees M. J., Stella L., White N. E., 1989, MNRAS, 238, 729 5, 15

Fabian A. C., Vaughan S., 2003, MNRAS, 340, L28 16, 78

Fabian A. C., Zoghbi A., Ross R. R., Uttley P., Gallo L. C., Brandt W. N., Blustin A. J., Boller T., Caballero-Garcia M. D., Larsson J., Miller J. M., Miniutti G., Ponti G., Reis R. C., Reynolds C. S., Tanaka Y., Young A. J., 2009, Nature, 459, 540 16, 20, 63, 131

Feigelson E. D., 1997, Time series problems in astronomy: an introduction. p. 161 28

Fender R., 2010, in Belloni T., ed., Lecture Notes in Physics, Berlin Springer Verlag Vol. 794 of Lecture Notes in Physics, Berlin Springer Verlag, 'Disc-Jet' Coupling in Black Hole X-Ray Binaries and Active Galactic Nuclei. p. 115 8, 18

Ferrarese L., Merritt D., 2000, ApJL, 539, L9 5

Fougere P. F., 1985, *JGR* , 90, 4355 54, 74

Frank J., King A., Raine D. J., 2002, Accretion Power in Astrophysics: Third Edition 7, 8, 12

Gallo E., Treu T., Marshall P. J., Woo J.-H., Leipski C., Antonucci R., 2010, ApJ, 714, 25 11

Gallo L. C., 2006, MNRAS, 368, 479 127

Garofalo D., Evans D. A., Sambruna R. M., 2010, MNRAS, 406, 975 11

Gaskell C. M., McHardy I. M., Peterson B. M., Sergeev S. G., eds, 2006, AGN Variability from X-Rays to Radio Waves Vol. 360 of Astronomical Society of the Pacific Conference Series 17

Gebhardt K., Bender R., Bower G., Dressler A., Faber S. M., Filippenko A. V., Green R., Grillmair C., Ho L. C., Kormendy J., Lauer T. R., Magorrian J., Pinkney J., Richstone D., Tremaine S., 2000, ApJL, 539, L13 5

Gehrels N., Chincarini G., Giommi P., Mason K. O., 2004, ApJ, 611, 1005 27

Gelman A., Rubin D. B., 1992, Statistical Science, 7, pp. 457 40, 41

Genzel R., Eisenhauer F., Gillessen S., 2010, Reviews of Modern Physics, 82, 3121 4

George I. M., Fabian A. C., 1991, MNRAS, 249, 352 14

Ghez A. M., Salim S., Weinberg N., Lu J., Do T., Dunn J. K., Matthews K., Morris M., Yelda S., Becklin E. E., 2008, in Jin W. J., Platais I., Perryman M. A. C., eds, IAU Symposium Vol. 248 of IAU Symposium, Probing the properties of the Milky Way's central supermassive black hole with stellar orbits. pp 52–58 4

Gierliński M., Done C., 2004, MNRAS, 349, L7 16, 17

Gierliński M., Middleton M., Ward M., Done C., 2008, Nature, 455, 369 19

Gillessen S., Eisenhauer F., Trippe S., Alexander T., Genzel R., Martins F., Ott T., 2009, ApJ, 692, 1075 4

Gladstone J. C., 2013, ArXiv e-prints 3

Gladstone J. C., Roberts T. P., Done C., 2009, MNRAS, 397, 1836 4

González-Martín O., Vaughan S., 2013, in Zhang C. M., Belloni T., Méndez M., Zhang S. N., eds, IAU Symposium Vol. 290 of IAU Symposium, X-ray variability of 104 active galactic nuclei. pp 37–40 19

Green A. R., McHardy I. M., Done C., 1999, MNRAS, 305, 309 60

Guilbert P. W., Rees M. J., 1988, MNRAS, 233, 475 13, 22

Haardt F., Maraschi L., 1991, ApJL, 380, L51 12, 22

Halpern J. P., 1984, ApJ, 281, 90 17

Harrison F. A., Craig W. W., Christensen F. E., Hailey C. J., Zhang W. W., Boggs S. E., Stern D., Cook W. R., Forster K., Giommi P., Grefenstette B. W., 2013, ApJ, 770, 103 143

Hastings W. K., 1970, Biometrika, 57, 97 40

Hawking S. W., 1974, Nature, 248, 30 3

Heckman T. M., 1980, A&A, 87, 152 8

Hubeny I., Agol E., Blaes O., Krolik J. H., 2000, ApJ, 533, 710 12

Ingram A., Done C., 2010, MNRAS, 405, 2447 21

Inoue H., Matsumoto C., 2003, PASJ, 55, 625 16

Jansen F., Lumb D., Altieri B., Clavel J., Ehle M., Erd C., Gabriel C., Guainazzi M., Gondoin P., Much R., Munoz R., Santos M., Schartel N., Texier D., Vacanti G., 2001, A&A, 365, L1 25

Jenkins G., Watts D., 1969, Spectral analysis and its applications. Holden-Day series in time series analysis, Holden-Day 71, 73

Jin C., Done C., Middleton M., Ward M., 2013, ArXiv e-prints 19, 110, 127

Jin C., Ward M., Done C., 2012a, MNRAS, 422, 3268 127

Jin C., Ward M., Done C., 2012b, MNRAS, 425, 907 127

Kalogera V., Baym G., 1996, ApJL, 470, L61 3

Kara E., Fabian A. C., Cackett E. M., Miniutti G., Uttley P., 2013, MNRAS, 430, 1408 60, 78, 81, 83, 98, 101, 133, 144

Kara E., Fabian A. C., Cackett E. M., Steiner J. F., Uttley P., Wilkins D. R., Zoghbi A., 2013, MNRAS, 428, 2795 101, 104, 125, 135, 136

Kara E., Fabian A. C., Cackett E. M., Uttley P., Wilkins D. R., Zoghbi A., 2013, MNRAS, 434, 1129 79, 98, 101, 104, 124

Kaspi S., Brandt W. N., Netzer H., George I. M., Chartas G., Behar E., Sambruna R. M., Garmire G. P., Nousek J. A., 2001, ApJ, 554, 216 17

Kelly B. C., Sobolewska M., Siemiginowska A., 2011, ApJ, 730, 52 21

Kerr R. P., 1963, Phys. Rev. Lett., 11, 237 2

King A. R., Pringle J. E., West R. G., Livio M., 2004, MNRAS, 348, 111 21

Kolehmainen M., Done C., Díaz Trigo M., 2011, MNRAS, 416, 311 138

Koratkar A., Blaes O., 1999, PASP, 111, 1 11

Kormendy J., Ho L. C., 2013, ARA&A, 51, 511 3, 5

Kormendy J., Richstone D., 1995, ARA&A, 33, 581 5

Kotov O., Churazov E., Gilfanov M., 2001, MNRAS, 327, 799 21, 66, 76

Laor A., 1991, ApJ, 376, 90 5, 15, 110

Laor A., Netzer H., 1989, MNRAS, 238, 897 12

Lasota J.-P., Abramowicz M. A., Chen X., Krolik J., Narayan R., Yi I., 1996, ApJ, 462, 142 8

Lawrence A., Elvis M., 1982, ApJ, 256, 410 10

Leahy D. A., Darbro W., Elsner R. F., Weisskopf M. C., Kahn S., Sutherland P. G., Grindlay J. E., 1983, ApJ, 266, 160 32

Lee J. C., Ogle P. M., Canizares C. R., Marshall H. L., Schulz N. S., Morales R., Fabian A. C., Iwasawa K., 2001, ApJL, 554, L13 17

Legg E., Miller L., Turner T. J., Giustini M., Reeves J. N., Kraemer S. B., 2012, ApJ, 760, 73 74, 79, 86, 98

Lightman A. P., White T. R., 1988, ApJ, 335, 57 13, 14

Lynden-Bell D., 1964, ApJ, 139, 1195 6

Lyubarskii Y. E., 1997, MNRAS, 292, 679 21

Magorrian J., Tremaine S., Richstone D., Bender R., Bower G., Dressler A., Faber S. M., Gebhardt K., Green R., Grillmair C., Kormendy J., Lauer T., 1998, AJ, 115, 2285 5

Marshall H. L., Edelson R. A., Vaughan S., Malkan M., O'Brien P., Warwick R., 2003, AJ, 125, 459 16

Mason K. O., Breeveld A., Much R., Carter M., Cordova F. A., Cropper M. S., Fordham J., Huckle H., Ho C., Kawakami H., Kennea J., Kennedy T., Mittaz J., Pandel D., Priedhorsky W. C., Sasseen T., Shirey R., Smith P., Vreux J.-M., 2001, A&A, 365, L36 26

Mason K. O., McHardy I. M., Page M. J., Uttley P., Córdova F. A., Maraschi L., Priedhorsky W. C., Puchnarewicz E. M., Sasseen T., 2002, ApJL, 580, L117 42

Matt G., Perola G. C., 1992, MNRAS, 259, 433 16

Matt G., Perola G. C., Piro L., 1991, A&A, 247, 25 14

McClintock J. E., Remillard R. A., 2006, Black hole binaries. pp 157–213 3

McHardy I., 2010, in Belloni T., ed., Lecture Notes in Physics, Berlin Springer Verlag Vol. 794 of Lecture Notes in Physics, Berlin Springer Verlag, X-Ray Variability of AGN and Relationship to Galactic Black Hole Binary Systems. p. 203 17, 18

McHardy I. M., Arévalo P., Uttley P., Papadakis I. E., Summons D. P., Brinkmann W., Page M. J., 2007, MNRAS, 382, 985 19, 20

McHardy I. M., Papadakis I. E., Uttley P., Page M. J., Mason K. O., 2004, MNRAS, 348, 783 18, 57, 60, 66, 74, 123, 132

Meier D. L., 2003, NewA Rev., 47, 667 11

Metropolis N., Rosenbluth A. W., Rosenbluth M. N., Teller A. H., Teller E., 1953, J. Chem. Phys, 21, 1087 40

Michell J., 1784, Royal Society of London Philosophical Transactions Series I, 74, 35 2

Middleton M., Done C., Gierliński M., 2007, MNRAS, 381, 1426 127

Middleton M. J., Sutton A. D., Roberts T. P., 2011, MNRAS, 417, 464 4

Miller J. M., 2007, ARA&A, 45, 441 15

Miller L., Turner T. J., Reeves J. N., 2008, A&A, 483, 437 15

Miller L., Turner T. J., Reeves J. N., 2009, MNRAS, 399, L69 15

Miller L., Turner T. J., Reeves J. N., Braito V., 2010, MNRAS, 408, 1928 20, 99

Miller L., Turner T. J., Reeves J. N., Lobban A., Kraemer S. B., Crenshaw D. M., 2010, MNRAS, 403, 196 20, 60, 86, 98, 132, 133, 143

Miniutti G., Fabian A. C., Goyder R., Lasenby A. N., 2003, MNRAS, 344, L22 16

Miniutti G., Fabian A. C., Miller J. M., 2004, MNRAS, 351, 466 16

Misner C. W., Thorne K. S., Wheeler J. A., 1973, Gravitation 2, 3

Miyakawa T., Ebisawa K., Terashima Y., Tsuchihashi F., Inoue H., Zycki P., 2009, PASJ, 61, 1355 15

Miyamoto S., Kimura K., Kitamoto S., Dotani T., Ebisawa K., 1991, ApJ, 383, 784 32

Miyamoto S., Kitamoto S., 1989, Nature, 342, 773 20, 104, 135

Miyamoto S., Kitamoto S., Mitsuda K., Dotani T., 1988, Nature, 336, 450 20, 66, 132

Miyoshi M., Moran J., Herrnstein J., Greenhill L., Nakai N., Diamond P., Inoue M., 1995, Nature, 373, 127 4

Mushotzky R. F., Done C., Pounds K. A., 1993, ARA&A, 31, 717 5, 6, 17

Mushotzky R. F., Edelson R., Baumgartner W., Gandhi P., 2011, ApJL, 743, L12 58

Mushotzky R. F., Marshall F. E., Boldt E. A., Holt S. S., Serlemitsos P. J., 1980, ApJ, 235, 377 12

Nandra K., Barret D., Barcons X., Fabian A., den Herder J.-W., Piro L., Watson M., Adami C., Aird J., Afonso J. M., et al. 2013, ArXiv e-prints 143

Nandra K., Clavel J., Edelson R. A., George I. M., Malkan M. A., Mushotzky R. F., Peterson B. M., Turner T. J., 1998, ApJ, 505, 594 23

Nandra K., George I. M., Mushotzky R. F., Turner T. J., Yaqoob T., 1997, ApJ, 477, 602 14, 16

Nandra K., Le T., George I. M., Edelson R. A., Mushotzky R. F., Peterson B. M., Turner T. J., 2000, ApJ, 544, 734 52

Nandra K., O'Neill P. M., George I. M., Reeves J. N., 2007, MNRAS, 382, 194 14, 110

Nandra K., Pounds K. A., 1992, Nature, 359, 215 17

Nandra K., Pounds K. A., 1994, MNRAS, 268, 405 22

Narayan R., McClintock J. E., 2012, MNRAS, 419, L69 5

Narayan R., Yi I., 1995, ApJ, 452, 710 8

Nemmen R. S., Storchi-Bergmann T., Eracleous M., Yuan F., 2010, in Peterson B. M., Somerville R. S., Storchi-Bergmann T., eds, IAU Symposium Vol. 267 of IAU Symposium, Advection-Dominated Accretion, Jets, and the Spectral Energy Distribution of LINERs. pp 313–318 8

Nowak M. A., Vaughan B. A., Wilms J., Dove J. B., Begelman M. C., 1999, ApJ, 510, 874 19, 34, 36, 66, 104, 132, 135

Nowak M. A., Wilms J., Vaughan B. A., Dove J. B., Begelman M. C., 1999, ApJ, 515, 726 20

Oliva E., Origlia L., Maiolino R., Moorwood A. F. M., 1999, A&A, 350, 9 80

Oppenheimer J. R., Volkoff G. M., 1939, Physical Review, 55, 374 2

Papadakis I. E., Lawrence A., 1993, MNRAS, 261, 612 33

Papadakis I. E., Nandra K., Kazanas D., 2001, ApJL, 554, L133 60, 66, 132

Patrick A. R., Reeves J. N., Lobban A. P., Porquet D., Markowitz A. G., 2011, MNRAS, 416, 2725 16

Percival D., Walden A., 1993, Spectral Analysis for Physical Applications. Cambridge University Press 29

Peterson B. M., 1997, An Introduction to Active Galactic Nuclei 11

Peterson B. M., 2008, NewA Rev., 52, 240 4

Peterson B. M., 2011, in Narrow-Line Seyfert 1 Galaxies and their Place in the Universe Masses of Black Holes in Active Galactic Nuclei: Implications for Narrow-Line Seyfert 1 Galaxies 10

Peterson B. M., McHardy I. M., Wilkes B. J., Berlind P., Bertram R., Calkins M., Collier S. J., Huchra J. P., Mathur S., Papadakis I., Peters J., Pogge R. W., Romano P., Tokarz S., Uttley P., Vestergaard M., Wagner R. M., 2000, ApJ, 542, 161 42

Ponti G., Miniutti G., Cappi M., Maraschi L., Fabian A. C., Iwasawa K., 2006, MNRAS, 368, 903 109

Poole T. S., Breeveld A. A., Page M. J., Landsman W., 2008, MNRAS, 383, 627 28, 45

Pottschmidt K., Wilms J., Nowak M. A., Heindl W. A., Smith D. M., Staubert R., 2000, A&A, 357, L17 66, 132

Pounds K. A., Done C., Osborne J. P., 1995, MNRAS, 277, L5 10

Pounds K. A., Turner T. J., 1989, in Osterbrock D. E., Miller J. S., eds, Active Galactic Nuclei Vol. 134 of IAU Symposium, The EXOSAT Spectral Survey of Emission Line AGN. p. 155 16

Press W. H., 1978, Comments on Astrophysics, 7, 103 21

Priestley M., 1981, Spectral analysis and time series. No. v. 1 in Probability and mathematical statistics, Academic Press 29, 31, 34, 51, 71

Pringle J. E., 1981, ARA&A, 19, 137 7

Quataert E., Di Matteo T., Narayan R., Ho L. C., 1999, ApJL, 525, L89 8

Remillard R., Muno M., McClintock J. E., Orosz J., 2003, in Durouchoux P., Fuchs Y., Rodriguez J., eds, New Views on Microquasars X-ray QPOs in black-hole binary systems. p. 57 124

Remillard R. A., McClintock J. E., 2006, ARA&A, 44, 49 5

Remillard R. A., Muno M. P., McClintock J. E., Orosz J. A., 2002, ApJ, 580, 1030 19, 124

Revnivtsev M., Gilfanov M., Churazov E., 1999, A&A, 347, L23 127

Reynolds C. S., 1997, in Arav N., Shlosman I., Weymann R. J., eds, Mass Ejection from Active Galactic Nuclei Vol. 128 of Astronomical Society of the Pacific Conference Series, Warm Absorbers in Seyfert 1 Galaxies. p. 173 17

Reynolds C. S., 2000, ApJ, 533, 811 15

Reynolds C. S., Fabian A. C., 2008, ApJ, 675, 1048 15

Reynolds C. S., Fabian A. C., Brenneman L. W., Miniutti G., Uttley P., Gallo L. C., 2009, MNRAS, 397, L21 15

Reynolds C. S., Nowak M. A., 2003, Phys. Rep., 377, 389 5, 15

Reynolds C. S., Young A. J., Begelman M. C., Fabian A. C., 1999, ApJ, 514, 164 16

Roming P. W. A., Kennedy T. E., Mason K. O., 2005, Space Science Rev., 120, 95 28

Ross R. R., Fabian A. C., 1993, MNRAS, 261, 74 14

Ross R. R., Fabian A. C., 2005, MNRAS, 358, 211 14, 110, 138

Ross R. R., Fabian A. C., Mineshige S., 1992, MNRAS, 258, 189 127

Ross R. R., Fabian A. C., Young A. J., 1999, MNRAS, 306, 461 14, 15

Russell D. G., 2002, ApJ, 565, 681 42

Rybicki G. B., Lightman A. P., 1979, Radiative processes in astrophysics 13

Sako M., Kahn S. M., Behar E., Kaastra J. S., Brinkman A. C., Boller T., Puchnarewicz E. M., Starling R., Liedahl D. A., Clavel J., Santos-Lleo M., 2001, A&A, 365, L168 17

Salpeter E. E., 1964, ApJ, 140, 796 6

Saxton R. D., Turner M. J. L., Williams O. R., Stewart G. C., Ohashi T., Kii T., 1993, MNRAS, 262, 63 16

Schreier E., Gursky H., Kellogg E., Tananbaum H., Giacconi R., 1971, ApJL, 170, L21 3

Schurch N. J., Done C., 2006, MNRAS, 371, 81 17

Schurch N. J., Done C., 2008, MNRAS, 386, L1 17

Schutz B., 2003, Gravity from the Ground Up 2, 3

Schwarzschild K., 1916, Abh. Konigl. Preuss. Akad. Wissenschaften Jahre 1906,92, Berlin,1907, pp 189–196 2

Shakura N. I., Sunyaev R. A., 1973, A&A, 24, 337 7

Shang Z., Brotherton M. S., Wills B. J., Wills D., Cales S. L., Dale D. A., Green R. F., Runnoe J. C., Nemmen R. S., Gallagher S. C., Ganguly R., Hines D. C., Kelly B. J., Kriss G. A., Li J., Tang B., Xie Y., 2011, ApJS, 196, 2 11

Shapiro S. L., Lightman A. P., Eardley D. M., 1976, ApJ, 204, 187 8

Shemmer O., Uttley P., Netzer H., McHardy I. M., 2003, MNRAS, 343, 1341 42

Shih D. C., Iwasawa K., Fabian A. C., 2002, MNRAS, 333, 687 78

Shu X. W., Yaqoob T., Wang J. X., 2010, ApJS, 187, 581 14

Silk J., Rees M. J., 1998, A&A, 331, L1 5

Smartt S. J., 2009, ARA&A, 47, 63 3

Smith R., Vaughan S., 2007, MNRAS, 375, 1479 42

Stella L., 1990, Nature, 344, 747 16

Stella L., Arlandi E., Tagliaferri G., Israel G. L., 1994, ArXiv Astrophysics e-prints 33

Strohmayer T. E., 2001, ApJL, 552, L49 5

Strüder L., Briel U., Dennerl K., Hartmann R., 2001, A&A, 365, L18 26, 61, 128

Sun W.-H., Malkan M. A., 1989, ApJ, 346, 68 12

Tadhunter C., 2008, NewA Rev., 52, 227 11

Tanaka Y., Nandra K., Fabian A. C., Inoue H., Otani C., Dotani T., Hayashida K., Iwa-sawa K., Kii T., Kunieda H., Makino F., Matsuoka M., 1995, Nature, 375, 659 15

Thorne K. S., 1974, ApJ, 191, 507 2, 6

Timmer J., König M., 1995, A&A, 300, 707 40, 72

Titarchuk L., Lyubarskij Y., 1995, ApJ, 450, 876 110

Turner M. J. L., Abbey A., Arnaud M., Balasini M., Barbera M., Belsole E., Bennie P. J., Bernard J. P., 2001, A&A, 365, L27 25

Uttley P., 2006, in C. M. Gaskell, I. M. McHardy, B. M. Peterson, & S. G. Sergeev ed., Astronomical Society of the Pacific Conference Series Vol. 360 of Astronomical Society of the Pacific Conference Series, The Relationship Between Optical and X-ray Variability in Seyfert Galaxies. p. 101 22, 23

Uttley P., Edelson R., McHardy I. M., Peterson B. M., Markowitz A., 2003, ApJL, 584, L53 23

Uttley P., McHardy I. M., 2001, MNRAS, 323, L26 21

Uttley P., McHardy I. M., Papadakis I. E., 2002, MNRAS, 332, 231 33, 40, 63

Uttley P., McHardy I. M., Papadakis I. E., Guainazzi M., Fruscione A., 1999, MNRAS, 307, L6 60

Uttley P., McHardy I. M., Vaughan S., 2005, MNRAS, 359, 345 21, 40, 72, 75

Uttley P., Wilkinson T., Cassatella P., Wilms J., Pottschmidt K., Hanke M., Böck M., 2011, MNRAS, 414, L60 60

van der Klis M., 1989, in H. Ögelman & E. P. J. van den Heuvel ed., Timing Neutron Stars Fourier techniques in X-ray timing. pp 27–+ 19, 33, 47, 63, 122

van der Klis M., 1997, in Babu G. J., Feigelson E. D., eds, Statistical Challenges in Modern Astronomy II Quantifying Rapid Variability in Accreting Compact Objects. p. 321 32

Vaughan B. A., Nowak M. A., 1997, ApJL, 474, L43 19, 34, 35, 36, 53, 73

Vaughan S., 2013, ArXiv e-prints 28

Vaughan S., Boller T., Fabian A. C., Ballantyne D. R., Brandt W. N., Trümper J., 2002,

MNRAS, 337, 247 16

Vaughan S., Edelson R., 2001, ApJ, 548, 694 15, 78

Vaughan S., Edelson R., Warwick R. S., Uttley P., 2003, MNRAS, 345, 1271 18, 19, 29, 32, 33, 34, 49, 50, 60, 63, 66, 109, 125, 132

Vaughan S., Fabian A. C., Ballantyne D. R., De Rosa A., Piro L., Matt G., 2004, MN-RAS, 351, 193 16

Vaughan S., Uttley P., 2007, Proc. SPIE, 6603, 660314 21

Vaughan S., Uttley P., 2008, ArXiv e-prints 40

Vaughan S., Uttley P., Pounds K. A., Nandra K., Strohmayer T. E., 2011, MNRAS, 413, 2489 44, 50, 51, 57, 58, 60, 62, 63, 66, 72, 75, 102, 123, 125

Volonteri M., Rees M. J., 2005, ApJ, 633, 624 5

Webster B. L., Murdin P., 1972, Nature, 235, 37 3

Welsh W. F., 1999, PASP, 111, 1347 54

Wilkins D. R., Fabian A. C., 2013, MNRAS, 430, 247 67, 133, 143

Wilkinson T., Uttley P., 2009, MNRAS, 397, 666 39, 102, 109

Wilms J., Allen A., McCray R., 2000, ApJ, 542, 914 109

Worrall D. M., 2009, A&AR, 17, 1 11

Yaqoob T., Murphy K. D., Miller L., Turner T. J., 2010, MNRAS, 401, 411 15

Zdziarski A. A., 2005, MNRAS, 360, 816 21

Zdziarski A. A., Fabian A. C., Nandra K., Celotti A., Rees M. J., Done C., Coppi P. S., Madejski G. M., 1994, MNRAS, 269, L55 12

Zdziarski A. A., Johnson W. N., Done C., Smith D., McNaron-Brown K., 1995, ApJL, 438, L63 12

Zhang E.-P., Wang J.-M., 2006, ApJ, 653, 137 80

Zhou H., Wang T., Yuan W., Lu H., Dong X., Wang J., Lu Y., 2006, ApJS, 166, 128 10

Zhou X.-L., Zhang S.-N., Wang D.-X., Zhu L., 2010, ApJ, 710, 16 80

Zoghbi A., Fabian A. C., 2011, MNRAS, 418, 2642 60, 83, 98, 101, 104, 132, 134, 135

Zoghbi A., Fabian A. C., Reynolds C. S., Cackett E. M., 2012, MNRAS, 422, 129 60, 101, 124

Zoghbi A., Reynolds C., Cackett E. M., 2013, ApJ, 777, 24 143

Zoghbi A., Reynolds C., Cackett E. M., Miniutti G., Kara E., Fabian A. C., 2013, ApJ, 767, 121 101, 124

Zoghbi A., Uttley P., Fabian A. C., 2011, MNRAS, 412, 59 101, 103, 125

Życki P. T., 2004, MNRAS, 351, 1180 15